Direct Numerical Simulation of Turbulent Flow and Heat Transfer in a Square Duct Roughened with Transverse or V-shaped Ribs

by

Seyyed Vahid Mahmoodi Jezeh

A thesis submitted to
The Faculty of Graduate Studies of
The University of Manitoba
in partial fulfillment of the requirements
of the degree of

Doctor of Philosophy

Department of Mechanical Engineering
The University of Manitoba
Winnipeg, Manitoba, Canada
June 2021

© Copyright 2021 by Seyyed Vahid Mahmoodi Jezeh

Abstract

This integrated thesis documents a series of complementary numerical investigations aimed at an improved understanding of turbulent flows and heat transfer in a square duct with ribs of different shapes mounted on one wall. Direct numerical simulation (DNS) is used to accurately resolve the spatial and temporal scales of the simulated flows. The first DNS investigates the turbulent flow in a ribbed square duct of different blockage ratios. The results are compared with those of a smooth duct flow. It is observed that an augmentation of the blockage ratio concurrently generates stronger turbulent secondary flow motions, which drastically alter the turbulent transport processes between the sidewall and duct center, giving rise to high-degrees of non-equilibrium states. The dynamics of coherent structures are studied by examining characteristics of the instantaneous velocity field, swirling strength, spatial two-point auto-correlations, and velocity spectra. The impact of the blockage ratio on the turbulent heat transfer is investigated in the second numerical study. The results show that owing to the existence of the ribs and confinement of the duct, organized secondary flows appear as large streamwise-elongated vortices, which have profound influences on the transport of momentum and thermal energy. This study also shows that the spatial distribution and magnitude of the drag and heat transfer coefficients are highly sensitive to the rib height.

The final study focuses on a comparison of highly-disturbed turbulent flows in a square duct with inclined and V-shaped ribs mounted on one wall. The turbulence field is highly sensitive to not only the rib geometry but also the boundary layers developed over the side and top walls. Owing to the difference in the pattern of the cross-stream secondary flow motions of these two ribbed duct cases, the flow physics in the inclined rib case is significantly different from the V-shaped rib case. It is found that near the leeward and windward faces of the ribs, the mean inclination angle of

turbulence structures in the V-shaped rib case is greater than that of the inclined rib case, which subsequently enhances momentum transport between the ribbed bottom wall and the smooth top wall.

Contents

List of Figures

List of Tables

Acknowledgments

First and foremost, I would like to thank my supervisor, Professor Bing-Chen Wang, for his guidance in the area of fluids science, encouragement on creative thinking and his trust in me. I really appreciate that the door of his office was always open to me, and I was able to stop by any time and discuss academic and non-academic areas with him.

I extend my gratitude to my Ph.D. committee members from University of Manitoba, Professor Mark Tachie, for his excellent course on the turbulence, and Professor Karen Dow, for her helpful and constructive comments on my project.

I would like to thank Professor Vahid Esfahanian, my adviser at University of Tehran, for teaching me the fundamentals of Computational Fluid Dynamics.

Special Thanks to my brother, Hesam Shoori, and my friends for their unconditional support and love during this time.

Last and most of all, I would like to thank my parents, Seyyed Hossein Mahmoodi Jezeh and Tahereh Sharifi Jezeh, for their never-ending love. They have taught me the importance of education and have been supporting me every step of my life.

Nomenclature

English Symbols:

Br	blockage ratio: $Br = H/D$
C_f	skin friction coefficient: $C_f = \tau_w/(\rho U_b^2/2)$
C_k	convection term for TKE
C_p	pressure coefficient: $C_p = \langle p \rangle/(\rho U_b^2/\,2)$
D	side length (or, hydraulic diameter) of the duct: $D = 2\delta$
D_v, D_p, D_t	viscous, pressure and total drag forcing terms, respectively
D_k	viscous diffusion for TKE
d_0	virtual origin
E_{ii}	temporal energy spectra
H	height of a rib
H^+	Reynolds number based on the rib height: $H^+ = Hu_{\tau R}/\nu$
J	Jacobian of the $\partial x_i/\partial \xi_j$ tensor
k	turbulence kinetic energy: $\langle u_i' u_i' \rangle/2$
k_t	instantaneous turbulent kinetic energy: $k_t = (u'^2 + v'^2 + w'^2)/2$
L_x, L_y, L_z	computational domain sizes in the x, y and z directions, respectively
L_{xx}	streamwise integral length scale: $L_{xx} = \int_0^\infty R_{uu}(x)dx$
L_x^+	streamwise domain length based on wall friction velocity of the ribbed bottom wall in the central vertical plane: $L_x^+ = L_x u_{\tau R}/\nu$
N	total number of rib elements
Nu	Nusselt number
Nu_{av}	average Nusselt number

P	streamwise distance between ribs
p	pressure
P_k	production term for TKE
P_t	production term for temperature variance
P_{ka}	active production component
P_{ki}	inactive production component
q_w	heat flux through ribbed bottom wall
Re_b	Reynolds number based on bulk velocity: $U_b\delta/\nu$
$Re_{\tau S}$	Reynolds number based on wall friction velocity of the smooth top wall in the central vertical plane: $Re_{\tau S} = u_{\tau S}\delta/\nu$
$Re_{\tau R}$	Reynolds number based on wall friction velocity of the ribbed bottom wall in the central vertical plane: $Re_{\tau R} = u_{\tau R}\delta/\nu$
R_{ii}	two-point autocorrelation coefficient of velocity fluctuation u_i'
$R_{u\theta}$	two-point cross-correlations of u' and θ'
$R_{\phi\phi}$	temporal autocorrelations for velocity and temperature fluctuations
S	secondary flow strength
T	temperature
T_b, T_{in}, T_w	bulk, inlet and ribbed bottom temperature, respectively
T_k	turbulent diffusion for TKE
t	time
u_i	velocity components: $i = 1, 2, 3$
$u_{\tau R}$	wall friction velocity of the ribbed bottom wall in the central vertical plane
$u_{\tau S}$	wall friction velocity of the smooth top wall in the central vertical plane
$u_{\tau P}$	peripherally-averaged wall friction velocity of a smooth duct flow
U_b	bulk velocity
x, y, z	streamwise, vertical and spanwise coordinates, respectively
W	width of a rib

Greek Symbols:

α	molecular diffusivity of the scalar
ξ_1, ξ_2 and ξ_3	generalized curvilinear coordinate system
β	cofactor of the $\partial x_i/\partial \xi_j$ tensor
Δ	maximal dimension of a grid cell in all three directions
δ	half channel height: $\delta = D/2$
δ_{ij}	Kronecker delta
ϵ_{ijk}	Levi-Civita symbol
ε_k	dissipation term for TKE
ε_t	dissipation term for temperature variance
η	Kolmogorov length scale
λ_{ci}	swirl strength
ν	kinematic viscosity
Π	mean streamwise pressure gradient
Π_k	pressure diffusion for TKE
ρ	density
θ	instantaneous temperature difference: $\theta = (T - T_{in})/(T_w - T_{in})$
θ_d	bulk and inlet temperature difference: $\theta_d = (T_b - T_{in})$
ω_x	instantaneous streamwise vorticity fluctuations: $\partial w/\partial y - \partial v/\partial z$
ω_z	instantaneous spanwise vorticity fluctuations: $\partial v/\partial x - \partial u/\partial y$
τ_w	wall shear stress
τ_{12}	mean viscous shear stress: $\tau_{12} = \mu \partial \langle u \rangle / \partial y$
σ	normalized fluctuating velocity

Subscripts and Superscripts:

$(\cdot)^+$	wall coordinates
$(\cdot)_1$, $(\cdot)_2$, $(\cdot)_3$	streamwise, vertical, and spanwise components, respectively
$(\cdot)'$	fluctuating component
$(\cdot)_{in}$	value at the inlet of the duct
$(\cdot)_{lee}$	value on the leeward side of a rib
$(\cdot)_w$	value at the ribbed bottom wall
$(\cdot)_{wind}$	value on the windward side of a rib
$\langle\cdot\rangle$	averaging over time and rib periods for the velocity field and time-averaging for the temperature field
$(\cdot)_{rms}$	root mean square

Abbreviations:

2-D	two-dimensional
3-D	three-dimensional
AMG	algebraic multi-grid
BFM	body-fitted mesh
CFL	Courant-Friedrichs-Lewy
CPU	central processing unit
DNS	direct numerical simulation
FFT	fast Fourier transform
FVM	finite volume method
IBM	immersed boundary method
JPDF	joint probability density function
LES	large-eddy simulation
MPI	message passing interface
PETSc	portable, extensible toolkit for scientific computation
RANS	Reynolds-averaged Navier-Stokes
RMS	root-mean-squares
TKE	turbulent kinetic energy

Chapter 1

Introduction

1.1 Background and motivation

The physical argument of the non-equilibrium three-dimensional (3-D) turbulent flow confined within a ribbed square duct has important practical implications in many engineering applications, such as turbine blade cooling, heat exchangers, and mixing chambers (Yaglom and Kader, 1974; Han et al., 2012; Casarsa and Arts, 2005; Borello et al., 2015). Turbulent flow inside a ribbed duct is three-dimensional (3-D), characterized by not only the existence of multiple turbulent separations but also the interaction of four boundary layers developed over the four sidewalls. These characteristics greatly complicate the flow physics and make turbulence characteristics drastically different from those of a two-dimensional (2-D) rough-wall boundary layer flow over a flat plate. These interesting physical features lead to the motivation of this thesis, which aims to expound the influence of rib elements on the mechanism underlying the organized secondary flows and their effects on the turbulence structures in a ribbed square duct.

Notwithstanding the rib-induced variations in the near-wall mean flow and turbulence statistics are commonly encountered in engineering applications; however, the number of detailed DNS study of turbulent heat and fluid flows inside a ribbed square duct is currently lacking. Indeed, no DNS results on the ribbed square duct flows have been published thus far. In view of this, this thesis aims at investigating the effects of both the sidewalls and rib geometry on (i) the non-equilibrium turbulent flow, (ii) transport of turbulent heat fluxes, (iii) the role of coherent structures in heat transfer through characteristics of the instantaneous velocity and temperature fields, swirling strength, temporal auto-correlations, spatial two-point auto-correlations and velocity and temperature spectra, as well as (iv) the transfer of the energy between different velocity fluctuating components through a budget analysis of the transport equation of turbulent kinetic energy. The DNS study of turbulent flow and heat transfer in square ribbed ducts is conducted at relatively low Reynolds numbers, with an emphasis on the fundamental physics of turbulence theory.

1.2 Literature review

1.2.1 Conventional 2-D riblet flow

In the current literature, studies of 2-D turbulent boundary-layer flows over rough walls are relatively abundant. For instance, Krogstad and Antonia (1994) studied the effects of k-type rough walls on large-scale structures of a turbulent boundary layer using X-wires in a wind tunnel. They found that turbulence structures were profoundly influenced in the outer region by the transverse ribs. Wang et al. (2010) measured 2-D riblet flows using particle image velocimetry (PIV), and the rib height was up to 20% of their channel. There are many reported DNS studies of 2-D riblet flows, well represented by the works of Choi et al. (1993), Bhaganagar et al. (2004), Leonardi et al. (2004), Orlandi et al. (2006), Ikeda and Durbin (2007), Liu et al. (2008), Burattini et al. (2008), and Chan et al. (2015). For instance, Leonardi et al. (2004) conducted DNS of a fully-developed 2-D turbulent channel flow with square bars mounted on the bottom wall. They showed that the coherence of streaky structures decreased in the streamwise direction with an increasing pitch-to-height ratio P/H, as a result of intense ejections of fluid from cavities. Here, P and H denote the streamwise rib separation and the rib height, respectively.

According to Perry et al. (1969) and Bandyopadhyay (1987), the type of roughness switches from the k- to d-type when the pitch-to-height ratio becomes less than three (i.e. $P/H \leq 3$). For the k-type roughness, unstable vortices generated by the ribs and shed upwards to form roughness sublayer structures (Shafi and Antonia, 1997). Conversely, for the d-type roughness, stable vortices recirculate within cavities between two nearby ribs. These prototypical physical features have been clearly visualized by Bandyopadhyay (1987) who conducted experiments to investigate the effects of surface roughness on the vortex-shedding pattern in a low-speed wind tunnel, and by Leonardi et al. (2003) who studied turbulent boundary-layer flow developed over a plate roughened with transverse ribs using DNS. The classical works reviewed here (e.g., Perry et al., 1969; Bandyopadhyay, 1987) were conducted primarily based on the 2-D rib-roughened boundary layers. If we follow the convention of these classical papers, the present work would deal only with k-type riblet roughness mounted on the bottom wall of a square duct. However, strictly speaking, the classical definitions of k- or d-type roughnesses established based on the 2-D boundary layers are not entirely applicable to the current 3-D flow, and it would be of interest to investigate the riblet effect on the turbulent flow pattern confined peripherally within a duct.

1.2.2 Three dimensional smooth and ribbed duct flows

In contrast to 2-D ribbed flows briefly reviewed above, the flow inside a ribbed duct is inhomogeneous in all directions, influenced by not only the ribs but also the confinement of four sidewalls of the square duct. In a smooth square duct, mean and turbulent secondary flow structures appear in the cross-stream directions. Gavrilakis (1992) investigated the mechanism leading to secondary flow generation through the analysis of the transport of mean streamwise vorticity in a smooth square duct at a Reynolds number of $Re_b = DU_b/\nu = 4410$ (based on the duct width D and bulk mean velocity U_b). Following this study, Mompean et al. (1996) performed Reynolds-averaged Navier–Stokes (RANS) simulations using a non-linear $k - \varepsilon$ model. Their approach was capable of modelling mean secondary flows observed in the DNS study of Gavrilakis (1992). Recently, Pirozzoli et al. (2018) conducted DNS study of a fully-developed turbulent flow in a smooth square duct with a wide range of Reynolds numbers, and observed that the mean flow characteristics (such as local skin friction coefficient) were insensitive to the secondary flows. Similar to the flow pattern in a smooth duct briefly reviewed above, dominant secondary flows also occur in the cross-stream directions in a ribbed duct. This is evidenced by the studies of Casarsa and Arts (2005) and Lohász et al. (2006), who investigated ribbed duct flows using PIV and large-eddy simulation (LES), respectively. Since the generation of secondary flow motions is strongly associated with the anisotropy of turbulent stresses, it is expected that the strength and the pattern of secondary flows are noticeably altered in a transversely rib-roughened duct due to the disturbances from the ribs. Hirota et al. (1992) measured fully-developed turbulent flows in square and rectangular ducts with perpendicular ribs mounted on one wall using a hot-wire anemometer. They showed that the secondary flow appeared as a large streamwise-elongated vortex adjacent to each vertical sidewall, which transports high momentum fluid from the duct center towards the duct corner. To study the effect of secondary flow on the statistics of the velocity field, Yokosawa et al. (1989) measured the mean velocities and Reynolds stresses in a square duct with the bottom and top walls roughened by transverse ribs and compared their results against measurements taken in a smooth square duct. They showed that in comparison with the smooth duct, owing to the presence of ribs and strong secondary flows, the spatial distribution of turbulent shear stress is significantly altered in the rib-roughened duct. Liou et al. (1993) conducted laser-Doppler velocimeter (LDV) measurements of a fully-developed duct flow with square ribs mounted on the bottom and top walls. They observed that due to the appearance of the mean secondary flow, the impingement region close to the vertical sidewalls resulted in high heat transfer rates. This research finding of Liou et al. (1993), was later confirmed by Sewall et al. (2006) and Labbé (2013) using LES. Sewall et al. (2006) also concluded that both the skin friction and form drags were less sensitive to the secondary flow than the heat transfer coefficient on the ribbed wall. Coletti et al. (2013) measured the turbulent flow confined in a rectangular duct using PIV. In their experiment, transverse square ribs were mounted on the bottom wall of the duct with a blockage ratio of $Br = 0.1$. Besides their study of this stationary ribbed channel flow, Coletti et al. (2012, 2014) also conducted detailed PIV experiments to investigate the effects of spanwise system rotation on turbulent flow in a transverse rib-roughened rectangular duct. In their experiments, the measurement results of rotating duct flows were compared against those of a stationary smooth duct flow. The PIV experiments of Coletti et al. (2012, 2014) on rotating and non-rotating rib-roughened duct flows were later reproduced using a hybrid RANS/LES approach by Xun and Wang (2016), who used the PIV measurement data to validate a new forcing model applied to the RANS-LES interface.

1.2.3 Effects of rib height on the turbulent heat tranfer rate

In the current literature, extensive experimental measurements and numerical simulations were conducted to investigate the effects of rib elements on heat transfer in 2-D plane-channel flows. For example, Hetsroni et al. (1999) measured temperature field in turbulent channel and pipe flows using a hot-foil infrared technique, and a significant increase of heat transfer was observed near the ribbed wall due to the destruction of the thermal streaky structures. Nagano et al. (2004) conducted DNS of a fully-developed turbulent channel flow to investigate the effects of transverse ribs on both the velocity and temperature fields. Their results showed that k-type roughness has optimal heat transfer performance due to the promotion of turbulent mixing in the downstream region of the ribs. Hattori and Nagano (2012) performed DNS to study the mechanism of heat transfer in turbulent boundary-layer flow developed over a plate roughened with a rectangular rib. They observed that the streamwise and spanwise fluctuating vorticities had significant impacts on the near-wall heat transfer rate, which further led to an enhancement of the wall-normal turbulent heat flux. Leonardi et al. (2015) studied the effects of pitch-to-height ratios (P/H) and rib shapes on heat transfer enhancement in a turbulent plane-channel flow. They found that turbulent heat flux reaches its maximum at $P/H = 7.5$ for both square and circular ribs. More recently, Li et al. (2018) investigated the effects of cube heights on turbulence modulation and heat transfer enhancement in a channel flow using DNS and observed a distinct correlation between enhancement of heat transfer and increase of drag.

As reviewed above, studies of 2-D turbulent flow and heat transfer in ribbed plane channels are relatively abundant, however, research on turbulent heat transfer within 3-D rib-roughened ducts is yet limited in the literature. Hirota et al. (1997) measured temperature variance and turbulent heat fluxes in a smooth square duct using multiple-wire probes. They observed that due to the confinement of the four sidewalls of the duct, secondary flows appear as four pairs of counter-rotating vortices in the cross-stream direction, which have a significant impact on the characteristics of both the velocity and temperature fields. Furthermore, in a transversely rib-roughened duct, the strength and appearance of the secondary flow motions are noticeably altered, as the rib elements impose significant disturbances to the flow field. Fujita et al. (1989) measured turbulent flows in a rectangular duct with perpendicular ribs mounted on one wall using a hot-wire anemometer. They observed that secondary flows appeared as a pair of counter-rotating vortices, which exert a great influence on both momentum and heat transfer.

1.2.4 Influences of rib geometry on the turbulence structures

In addition to 2-D ribbed flows briefly reviewed above, numerous numerical and experimental works have also focused on the effects of secondary flows on the mean velocities and Reynolds stresses in either a smooth or a transverse rib-roughened duct (Yokosawa et al., 1989; Gavrilakis, 1992; Hirota et al., 1992; Mompean et al., 1996; Sewall et al., 2006; Lohász et al., 2006; Wang et al., 2007; Labbé, 2013; Coletti et al., 2012, 2014; Mahmoodi-Jezeh and Wang, 2020). For instance, Brundrett and Baines (1964) performed measurements of a smooth square duct flow using a hot-wire anemometer to investigate the mechanism of secondary flow motions. By analyzing the transport equation of the streamwise vorticity, they concluded that the gradients of Reynolds stress in the cross-stream directions played an important role in the generation of secondary flows. Hirota et al. (1992) performed measurement in a turbulent ribbed duct flow using hot-wire anemometers and observed that secondary flows drastically alter the distributions of TKE in the cross-stream directions. This research finding of Hirota et al. (1992) was recently confirmed by Mahmoodi-Jezeh and Wang (2020), who investigated the effects of rib height on turbulent flow structures in a square duct using DNS. Mahmoodi-Jezeh and Wang (2020) compared three straight transverse rib duct flows with a smooth duct flow, and concluded that secondary flows in a ribbed duct generate a high degree of non-equilibrium states in a region between the sidewalls and duct center. All these previous investigations have indicated that the appearance of the secondary flows in the cross-stream directions represents a major physical feature in a smooth or a ribbed 3-D duct flow, a mechanism that is absent in a conventional 2-D rough-wall boundary-layer flow over a flat plate.

While there is considerable research dedicated to turbulent flow in a transverse rib-roughened duct, much less is documented on turbulent flow in a duct with inclined ribs. Gao and Sundén (2004a) performed measurements of a flow in an angled rib-roughened rectangular duct using PIV and showed that the secondary flow appeared as one large longitudinal vortex in the cross-stream directions. In their follow-up study, Gao and Sundén (2004b) conducted PIV measurements in a rectangular duct with surface-mounted V-shaped ribs pointing towards both upstream and downstream directions. They observed that owing to the disturbances from the sharp-angled ribs and the presence of strong secondary flows, the magnitude of Nusselt number is significantly enhanced on the two vertical sidewalls of the duct. Fang et al. (2017) conducted a large-eddy simulation (LES) study of the turbulent flow in rib-roughened ducts with three different rib angles, and showed that the spatial distribution of main flow characteristics (such as the first- and second-order turbulence statistics) in the V-shaped rib case is greatly different from those in the perpendicular rib case. Recently, Ruck and Arbeiter (2018) performed detached eddy simulation (DES) to investigate the effects of secondary flows on the statistics of the velocity and temperature fields in V-shaped rib-roughened square ducts. They showed that the mean secondary flows greatly affected the spatial distribution of both friction and pressure drags on the ribbed bottom wall, resulting in an enhanced magnitude of Nusselt number.

1.3 Thesis objectives

The studies referenced in the preceding section indicate that the number of detailed numerical studies on turbulent flow and heat transfer in a duct with transverse or V-shaped ribs is still limited, and many questions regarding the fundamentals of the flow physics remain open. Furthermore, no DNS results on rib-roughened duct flows have been published in open literature thus far. In view of this, the proposed research aims at conducting a detailed DNS study of rib-roughened duct flow to investigate the effects of rib height and geometry on the mechanism underlying the organized secondary flows and their effects on turbulent flow structures and heat transfer in both physical and spectral spaces. The following outlines the objectives of the thesis research:

1. Further develop, test, validate, and optimize a finite volume method (FVM)

code based on an existing generalized curvilinear coordinate system for DNS of turbulent flows and heat transfer. This objective is to provide a proper tool to numerically study the effects of rib height and geometry on turbulent heat transfer.

2. Systematically investigate the effects of rib height on the statistical moments and premultiplied energy spectra of the turbulent velocity field, local non-equilibrium of turbulence, large- and small-scale flow anisotropy, transport of TKE, as well as the dynamics of mean and turbulent secondary flow motions. In order to identify the rib effects on the flow field, an additional DNS of a smooth duct flow has also been conducted at the same Reynolds number (as in the three rib cases), which is used as a baseline comparison case.

3. Systematically study the effects of rib height on the first- and second-order statistical moments of the temperature field, spectral characteristics of temperature fluctuations, and coherent structures that facilitate the turbulent transport of thermal energy. The characteristics of the temperature field of ribbed duct cases are compared with those of a heated smooth duct flow.

4. Investigate the influences of sidewalls and rib geometry (either inclined or V-shaped) on the statistical moments of different orders, including the mean flows, the pressure and viscous drag coefficients, Reynolds stresses, as well as the budget balance of TKE. Furthermore, the production TKE term, which is conventionally a function of Reynolds shear stresses and the mean velocity gradient, was decomposed into an "active" and an "inactive" components, following the proposal of Hinze (1972). This decomposition is effective for determining whether the difference in the magnitude of the TKE production term is caused by the large- or small-scale eddies.

5. Compile detailed benchmark data of turbulent duct flows disturbed by trans-

verse or V-shaped ribs mounted on one wall.

1.4 Outline

The remainder of this thesis is organized as follows:

In chapter 2, the computational approach, which includes a discussion of the governing equations, the method for discretizing the governing equations, and the method for solving the discretized system of equations are described. Also in this section, to examine the predictive accuracy of the numerical approach, two simulations are conducted based on two canonical test cases of (i) a 2-D ribbed plane-channel flow at $Re_b = 5600$, and (ii) a smooth duct flow at $Re_b = 4410$. The DNS results of these two additional test cases are validated against those reported in the literature.

In chapter 3, the turbulent flow in a ribbed square duct of different blockage ratios ($Br = 0.05$, 0.1 and 0.2) at a fixed Reynolds number of $Re_b = 5600$ is studied using DNS (major findings of Chapter 3 have been published in *J. Fluid Mech.*).

In chapter 4, the DNS study of turbulent heat transfer within a square duct with transverse ribs mounted on one wall is studied (major results of Chapter 4 have been published in *Int. J. Heat Fluid Flow*).

In chapter 5, highly-disturbed 3-D turbulent flow in a square duct with inclined or V-shaped ribs mounted on one wall is investigated using DNS. The Reynolds number based on the bulk mean velocity is fixed at $Re_b = 7000$ for both ribbed duct cases, while the Reynolds number based on the mean streamwise wall friction velocity of the ribbed bottom wall is $Re_{\tau R} = 642$ and 1294 for the inclined and V-shaped rib cases, respectively. (major findings of Chapter 5 have been submitted to *J. Fluid Mech.*).

In chapter 6, major conclusions of this thesis are summarized followed by comments on future studies.

Chapter 2

Numerical Method

2.1 Rib-roughened square ducts

In order to simulate the turbulent heat and fluid flow inside a square duct with transverse or V-shaped ribs mounted on one wall, a parallel in-house finite volume method (FVM) code is further developed and optimized to conduct DNS for chapters 3, 4 and 5. In addition, to examine the predictive accuracy of the numerical approach, two simulations have been conducted based on two canonical test cases of (i) a 2-D ribbed plane-channel flow at $Re_b = 5600$, and (ii) a smooth duct flow at $Re_b = 4410$. The DNS results of these two test cases are validated against those reported in the literature.

In this computer code, the continuity, momentum and thermal energy equations are discretized based on a general curvilinear coordinate system (ξ_1, ξ_2, ξ_3), which takes the following form for an incompressible flow:

$$\frac{1}{J}\frac{\partial\left(\beta_i^k u_i\right)}{\partial \xi_k} = 0 \quad , \tag{2.1}$$

$$\frac{\partial u_i}{\partial t} + \frac{1}{J}\frac{\partial}{\partial \xi_k}\left(\beta_j^k u_i u_j\right) = -\frac{1}{J\rho}\frac{\partial\left(\beta_i^k p\right)}{\partial \xi_k} - \frac{1}{\rho}\Pi\delta_{1i} + \frac{\nu}{J}\frac{\partial}{\partial \xi_p}\left(\frac{1}{J}\beta_j^p\beta_j^q\frac{\partial u_i}{\partial \xi_q}\right) \quad , \tag{2.2}$$

$$\frac{\partial T}{\partial t} + \frac{1}{J}\frac{\partial}{\partial \xi_k}\left(\beta_j^k T u_j\right) = \frac{\alpha}{J}\frac{\partial}{\partial \xi_p}\left(\frac{1}{J}\beta_j^p\beta_j^q\frac{\partial T}{\partial \xi_q}\right) \quad , \tag{2.3}$$

where u_i, p, T, ν, ρ, α and δ_{ij} represent the velocity, pressure, temperature, kinematic viscosity, density, thermal diffusivity, and Kronecker delta, respectively. Also, Π is the required streamwise pressure gradient that keeps a constant flow rate. Here, β_i^j and J denote the cofactor and Jacobian of tensor $\partial x_i/\partial \xi_j$, respectively. The above governing equations are expressed using tensor notations, and the streamwise (x), vertical (y) and spanwise (z) coordinates are denoted using x_i for i = 1, 2 and 3, respectively. Correspondingly, the velocity components u, v and w are denoted using u_i (for $i = 1$, 2 and 3, respectively). It should be indicated that this computer code is developed for the general purpose of dealing with complex computational domains of curved boundaries using body-fitted mesh. Specific to the present numerical simulation of the flow through a square duct with straight rectangular ribs mounted on the bottom wall, the cofactor and Jacobian degenerate to Kronecker delta and unity, respectively.

2.1.1 Spatial discretization of continuity and momentum equations

To make the code suitable for the general curvilinear system (ξ_i), all the derivatives are quantified in the curvilinear system, whereas the velocity, temperature and pressure components are kept as in the physical Cartesian system (x_i). The task of determining the new coordinate system is to appropriately conduct transformations: $\xi = \xi(x, y, z)$, $\eta = \eta(x, y, z)$ and $\zeta = \zeta(x, y, z)$. More generally, these transformations can be expressed as $\xi_i = \xi_i(x_1, x_2, x_3)$, for i = 1, 2 and 3. In the partial differential governing equations, $d\xi_i$ is given as

$$d\xi_j = \frac{\partial \xi_j}{\partial x_1}dx_1 + \frac{\partial \xi_j}{\partial x_2}dx_2 + \frac{\partial \xi_j}{\partial x_3}dx_3 \quad \text{or} \quad d\xi_j = \frac{\partial \xi_j}{\partial x_i}dx_i \quad \text{for } i = 1,2,3 \quad , \tag{2.4}$$

conversely,

$$dx_i = \frac{\partial x_i}{\partial \xi_1}d\xi_1 + \frac{\partial x_i}{\partial \xi_2}d\xi_2 + \frac{\partial x_i}{\partial \xi_3}d\xi_3 \quad \text{or} \quad dx_i = \frac{\partial x_i}{\partial \xi_j}d\xi_j \quad \text{for } i = 1,2,3 \quad . \tag{2.5}$$

The following coordinate transform between the curvilinear (ξ_i) and Cartesian (x_i) coordinate systems holds

$$\frac{\partial}{\partial x_i} = \frac{\partial \xi_j}{\partial x_i}\frac{\partial}{\partial \xi_j} \quad . \tag{2.6}$$

In matrix form, equation 2.4 becomes

$$\begin{bmatrix} d\xi_1 \\ d\xi_2 \\ d\xi_3 \end{bmatrix} = \begin{bmatrix} \frac{\partial \xi_1}{\partial x_1} & \frac{\partial \xi_1}{\partial x_2} & \frac{\partial \xi_1}{\partial x_3} \\ \frac{\partial \xi_2}{\partial x_1} & \frac{\partial \xi_2}{\partial x_2} & \frac{\partial \xi_2}{\partial x_3} \\ \frac{\partial \xi_3}{\partial x_1} & \frac{\partial \xi_3}{\partial x_2} & \frac{\partial \xi_3}{\partial x_3} \end{bmatrix} \begin{bmatrix} dx_1 \\ dx_2 \\ dx_3 \end{bmatrix} \quad . \tag{2.7}$$

Similarly,

$$\begin{bmatrix} dx_1 \\ dx_2 \\ dx_3 \end{bmatrix} = \begin{bmatrix} \frac{\partial x_1}{\partial \xi_1} & \frac{\partial x_1}{\partial \xi_2} & \frac{\partial x_1}{\partial \xi_3} \\ \frac{\partial x_2}{\partial \xi_1} & \frac{\partial x_2}{\partial \xi_2} & \frac{\partial x_2}{\partial \xi_3} \\ \frac{\partial x_3}{\partial \xi_1} & \frac{\partial x_3}{\partial \xi_2} & \frac{\partial x_3}{\partial \xi_3} \end{bmatrix} \begin{bmatrix} d\xi_1 \\ d\xi_2 \\ d\xi_3 \end{bmatrix} \quad . \tag{2.8}$$

Equations 2.4 and 2.5 can only be correct if the two three-by-three matrices that appear in these equations are inverses of each other, such that

$$\underbrace{\begin{bmatrix} \frac{\partial \xi_1}{\partial x_1} & \frac{\partial \xi_1}{\partial x_2} & \frac{\partial \xi_1}{\partial x_3} \\ \frac{\partial \xi_2}{\partial x_1} & \frac{\partial \xi_2}{\partial x_2} & \frac{\partial \xi_2}{\partial x_3} \\ \frac{\partial \xi_3}{\partial x_1} & \frac{\partial \xi_3}{\partial x_2} & \frac{\partial \xi_3}{\partial x_3} \end{bmatrix}}_{Matrix\ B} = \underbrace{\begin{bmatrix} \frac{\partial x_1}{\partial \xi_1} & \frac{\partial x_1}{\partial \xi_2} & \frac{\partial x_1}{\partial \xi_3} \\ \frac{\partial x_2}{\partial \xi_1} & \frac{\partial x_2}{\partial \xi_2} & \frac{\partial x_2}{\partial \xi_3} \\ \frac{\partial x_3}{\partial \xi_1} & \frac{\partial x_3}{\partial \xi_2} & \frac{\partial x_3}{\partial \xi_3} \end{bmatrix}^{-1}}_{Matrix\ A} \quad . \tag{2.9}$$

If matrix B is the inverse of matrix A then

$$B = A^{-1}, \text{ and} \qquad \frac{\partial \xi_j}{\partial x_i} = \frac{\beta_{ij}}{Det(A)} = \frac{(-1)^{j+i} M_{ij}}{Det(A)} \quad , \tag{2.10}$$

where M_{ij} denotes the minor determinant. The minor determinant is used to define the cofactor (i.e., $\beta_{ij} = (-1)^{j+i} M_{ij}$). The determinant of the matrix on the right hand side of equation 2.9 is known as the Jacobian determinant

$$J = Det\left(\frac{\partial x_i}{\partial \xi_j}\right) = \begin{bmatrix} \frac{\partial x_1}{\partial \xi_1} & \frac{\partial x_1}{\partial \xi_2} & \frac{\partial x_1}{\partial \xi_3} \\ \frac{\partial x_2}{\partial \xi_1} & \frac{\partial x_2}{\partial \xi_2} & \frac{\partial x_2}{\partial \xi_3} \\ \frac{\partial x_3}{\partial \xi_1} & \frac{\partial x_3}{\partial \xi_2} & \frac{\partial x_3}{\partial \xi_3} \end{bmatrix}$$

$$= \frac{\partial x_1}{\partial \xi_1}\frac{\partial x_2}{\partial \xi_2}\frac{\partial x_3}{\partial \xi_3} + \frac{\partial x_2}{\partial \xi_1}\frac{\partial x_3}{\partial \xi_2}\frac{\partial x_1}{\partial \xi_3} + \frac{\partial x_3}{\partial \xi_1}\frac{\partial x_1}{\partial \xi_2}\frac{\partial x_2}{\partial \xi_3} - \frac{\partial x_3}{\partial \xi_1}\frac{\partial x_2}{\partial \xi_2}\frac{\partial x_1}{\partial \xi_3} - \frac{\partial x_2}{\partial \xi_1}\frac{\partial x_1}{\partial \xi_2}\frac{\partial x_3}{\partial \xi_3} - \frac{\partial x_1}{\partial \xi_1}\frac{\partial x_3}{\partial \xi_2}\frac{\partial x_2}{\partial \xi_3} \quad . \tag{2.11}$$

Since all stored variables are at the centroids of adopted non-orthogonal control volumes, $\partial/\partial\xi_j$ can be calculated using the finite difference approach whereas $\partial/\partial x_j$ can only be quantified using equation 2.6. Therefore, the component of Jacobian, $\partial\xi_j/\partial x_i$, needs to be quantified for each control volume as

$$\begin{aligned}
\frac{\partial \xi_1}{\partial x_1} &= \frac{1}{J}\left[\frac{\partial x_2}{\partial \xi_2}\frac{\partial x_3}{\partial \xi_3} - \frac{\partial x_3}{\partial \xi_2}\frac{\partial x_2}{\partial \xi_3}\right] & \frac{\partial \xi_1}{\partial x_2} &= \frac{1}{J}\left[\frac{\partial x_1}{\partial \xi_3}\frac{\partial x_3}{\partial \xi_2} - \frac{\partial x_1}{\partial \xi_2}\frac{\partial x_3}{\partial \xi_3}\right] \\
\frac{\partial \xi_1}{\partial x_3} &= \frac{1}{J}\left[\frac{\partial x_1}{\partial \xi_2}\frac{\partial x_2}{\partial \xi_3} - \frac{\partial x_1}{\partial \xi_3}\frac{\partial x_2}{\partial \xi_2}\right] & \frac{\partial \xi_2}{\partial x_1} &= \frac{1}{J}\left[\frac{\partial x_2}{\partial \xi_3}\frac{\partial x_3}{\partial \xi_1} - \frac{\partial x_2}{\partial \xi_1}\frac{\partial x_3}{\partial \xi_3}\right] \\
\frac{\partial \xi_2}{\partial x_2} &= \frac{1}{J}\left[\frac{\partial x_1}{\partial \xi_1}\frac{\partial x_3}{\partial \xi_3} - \frac{\partial x_1}{\partial \xi_3}\frac{\partial x_3}{\partial \xi_1}\right] & \frac{\partial \xi_2}{\partial x_3} &= \frac{1}{J}\left[\frac{\partial x_1}{\partial \xi_1}\frac{\partial x_2}{\partial \xi_3} - \frac{\partial x_1}{\partial \xi_3}\frac{\partial x_2}{\partial \xi_1}\right] \\
\frac{\partial \xi_3}{\partial x_1} &= \frac{1}{J}\left[\frac{\partial x_2}{\partial \xi_1}\frac{\partial x_3}{\partial \xi_2} - \frac{\partial x_2}{\partial \xi_2}\frac{\partial x_3}{\partial \xi_1}\right] & \frac{\partial \xi_3}{\partial x_2} &= \frac{1}{J}\left[\frac{\partial x_1}{\partial \xi_2}\frac{\partial x_3}{\partial \xi_1} - \frac{\partial x_1}{\partial \xi_1}\frac{\partial x_3}{\partial \xi_2}\right] \\
\frac{\partial \xi_3}{\partial x_3} &= \frac{1}{J}\left[\frac{\partial x_1}{\partial \xi_1}\frac{\partial x_2}{\partial \xi_2} - \frac{\partial x_1}{\partial \xi_2}\frac{\partial x_2}{\partial \xi_1}\right] \quad .
\end{aligned} \tag{2.12}$$

which can be expressed in a general tensor form as

$$\frac{\partial}{\partial x_i} = \frac{1}{J}\beta_i^j \frac{\partial}{\partial \xi_j} \quad . \tag{2.13}$$

It should be noted that the equation (2.13) cannot be directly used to discretize terms (such as continuity, momentum convection and thermal energy convection

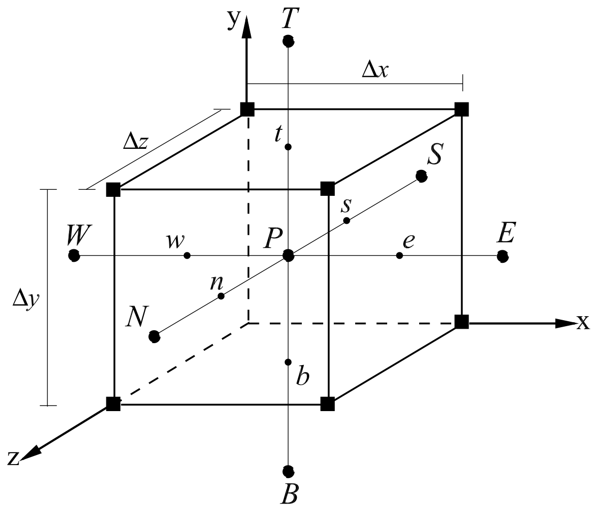

(a) 3-D view

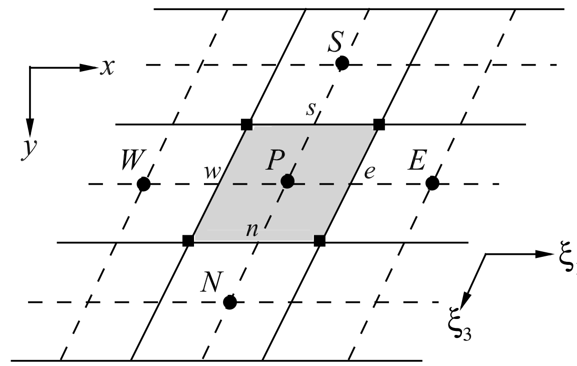

(b) 2-D view

Figure 2.1: Schematic of a computational cell, its node, faces, and neighbors in 2-D and 3-D configurations for the base grid.

terms) of a divergence form, as the conservation law would be broken in FVM. Therefore, equation 2.13 can be further expressed as

$$\frac{1}{J}\beta_i^j\frac{\partial u_i}{\partial \xi_j} = \frac{1}{J}\left(\frac{\partial \beta_i^j u_i}{\partial \xi_j} - u_i\frac{\partial \beta_i^j}{\partial \xi_j}\right) = \frac{1}{J}\frac{\partial \beta_i^j u_i}{\partial \xi_j} \quad . \tag{2.14}$$

To discretize equations (2.1), (2.2) and (2.3), the computation domain is divided into body-fitted control volumes. Figure 2.1 shows the schematic of a 3-D computational node and its neighbouring nodes.

In this thesis, a collocated second-order central differencing scheme was used to discretize the spatial derivatives for both the momentum and thermal energy equations. As such, all the physical variables (velocity components, temperature and pressure) were stored at the centroids of control volumes. Furthermore, interpolations were required to approximate the values at faces and edges of control volumes. In order to carefully control the variation of grid spacing in the computation domain, an arithmetic average was utilized to calculate the interpolations, *e.g.*, $u_e \approx (u_P + u_E)/2$ and $T_{sw} \approx (T_P + T_S + T_{SW} + T_W)/4$. In other words, this is to avoid the violation of energy conservation induced by the linear interpolation in non-uniform grids (Vasilyev, 2000; Fukagata and Kasagi, 2002). Here, upper-case letter subscripts ‘P’, ‘W’, ‘E’, ‘S’, ‘N’, ‘B’ and ‘T’ indicate the centroids of computational nodes. However, the lower-case letters ‘w’, ‘e’, ‘s’, ‘n’, ‘b’ and ‘t’ refer to the west, east, south, north, bottom and top faces of a control volume, respectively. In the simulations of V-shaped and inclined rib cases, the projection of a control volume onto the x-z plane is of a parallelogram shape (see figure 2.1(b)). Curvilinear coordinates ξ_1 and ξ_2 correspond to Cartesian coordinates x and y, respectively, and the angle between the ξ_3 and z axes is determined by the angle of V-shaped or inclined ribs (see figure 2.1(b)). In the curvilinear coordinate system (based on ξ_i), a control volume has a unit length in all three directions.

The integration of equation (2.1) within a control volume can be written as

$$\begin{aligned}
&\int_w^e \int_s^n \int_b^t \frac{1}{J}\frac{\partial(\beta_i^j u_i)}{\partial \xi_j} d\xi_1 d\xi_2 d\xi_3 = \\
&\quad \int_s^n \int_b^t \frac{1}{J}\frac{\partial(\beta_i^j u_i)}{\partial \xi_j} d\xi_2 d\xi_3\Big|_w^e + \\
&\quad \int_w^e \int_b^t \frac{1}{J}\frac{\partial(\beta_i^j u_i)}{\partial \xi_j} d\xi_1 d\xi_3\Big|_s^n + \\
&\quad \int_w^e \int_s^n \frac{1}{J}\frac{\partial(\beta_i^j u_i)}{\partial \xi_j} d\xi_1 d\xi_2\Big|_b^t = \\
&\frac{1}{J}\left(\beta_i^1 u_i|_w^e + \beta_i^2 u_i|_s^n + \beta_i^3 u_i|_b^t\right) = 0 \quad ,
\end{aligned} \tag{2.15}$$

and the mass flux through each face of the control volume can be derived as

$$\begin{aligned}
CW &= m_w = \rho\beta_i^1 u_i|_w \\
CE &= m_e = \rho\beta_i^1 u_i|_e \\
CS &= m_s = \rho\beta_i^2 u_i|_s \\
CN &= m_n = \rho\beta_i^2 u_i|_n \\
CB &= m_b = \rho\beta_i^3 u_i|_b \\
CT &= m_t = \rho\beta_i^3 u_i|_t \quad .
\end{aligned} \tag{2.16}$$

Term	Cartesian	Curvilinear
Velocity divergence	$\frac{\partial u_j}{\partial x_j}$	$\frac{1}{J}\frac{\partial(\beta_i^j u_i)}{\partial \xi_j}$
Temporal derivative	$\partial u_i/\partial t$	$\partial u_i/\partial t$
Convection	$\frac{\partial u_i u_j}{\partial x_j}$	$\frac{1}{J}\frac{\partial}{\partial \xi_k}\left(\beta_j^k u_i u_j\right)$
Pressure gradient	$-\frac{1}{\rho}\frac{\partial p}{\partial x_i}$	$-\frac{1}{J\rho}\frac{\partial\left(\beta_i^k p\right)}{\partial \xi_k}$
Viscosity	$\nu\frac{\partial^2 u_i}{\partial x_j \partial x_j}$	$\frac{\nu}{J}\frac{\partial}{\partial \xi_p}\left(\frac{1}{J}\beta_j^p\beta_j^q\frac{\partial u_i}{\partial \xi_q}\right)$
Driving force	Π	Π

Table 2.1: Coordinate transformation of terms in the continuity and momentum equations.

The momentum equation is more complex, which requires to be considered term by term. A detailed description of the discretization schemes used for the momentum equation are delivered in Appendix A. Table 2.1 summarizes the coordinate transformation of terms in the continuity and momentum equations.

2.1.2 Spatial discretization of advection-diffusion equation

With the above analysis, the convection term in equation (2.3) is discretized as

$$\begin{gathered}
\int_w^e\int_s^n\int_b^t \frac{1}{J}\frac{\partial(\beta_i^j T u_i)}{\partial \xi_j} d\xi_1 d\xi_2 d\xi_3 = \\
\int_s^n\int_b^t \frac{1}{J}\frac{\partial(\beta_i^j T u_i)}{\partial \xi_j} d\xi_2 d\xi_3\Big|_w^e + \\
\int_w^e\int_b^t \frac{1}{J}\frac{\partial(\beta_i^j T u_i)}{\partial \xi_j} d\xi_1 d\xi_3\Big|_s^n + \\
\int_w^e\int_s^n \frac{1}{J}\frac{\partial(\beta_i^j T u_i)}{\partial \xi_j} d\xi_1 d\xi_2\Big|_b^t = \\
\frac{1}{J}\left(\beta_i^1 T u_i|_e - \beta_i^1 T u_i|_w + \beta_i^2 T u_i|_n - \beta_i^2 T u_i|_s + \beta_i^3 T u_i|_t - \beta_i^3 T u_i|_b\right) \quad .
\end{gathered} \tag{2.17}$$

Term	Cartesian	Curvilinear
Temporal derivative	$\frac{\partial T}{\partial t}$	$\frac{\partial T}{\partial t}$
Convection	$\frac{\partial T u_i}{\partial x_i}$	$\frac{1}{J}\frac{\partial}{\partial \xi_j}\left(\beta_i^j T u_i\right)$
Diffusion	$\nu \frac{\partial^2 T}{\partial x_j \partial x_j}$	$\frac{\alpha}{J}\frac{\partial}{\partial \xi_p}\left(\frac{1}{J}\beta_j^p \beta_j^q \frac{\partial T}{\partial \xi_q}\right)$

Table 2.2: Coordinate transformation of terms in the advection-diffusion equation.

The diffusion term in equation (2.3) is discretized as

$$\begin{aligned}
&\int_w^e \int_s^n \int_b^t \alpha \frac{1}{J}\frac{\partial}{\partial \xi_p}\left(\frac{1}{J}\beta_j^p \beta_j^q \frac{\partial T}{\partial \xi_q}\right) d\xi_1 d\xi_2 d\xi_3 = \\
&\alpha \frac{1}{J}\left[\frac{1}{J}\beta_j^1 \beta_j^q \frac{\partial T}{\partial \xi_q}\bigg|_w^e + \frac{1}{J}\beta_j^2 \beta_j^q \frac{\partial T}{\partial \xi_q}\bigg|_s^n + \frac{1}{J}\beta_j^3 \beta_j^q \frac{\partial T}{\partial \xi_q}\bigg|_b^t\right] = \\
&\alpha \frac{1}{J}\left[\frac{1}{J}\beta_j^1 \beta_j^1 \frac{\partial T}{\partial \xi_1}\bigg|_w^e + \frac{1}{J}\beta_j^2 \beta_j^2 \frac{\partial T}{\partial \xi_2}\bigg|_s^n + \frac{1}{J}\beta_j^3 \beta_j^3 \frac{\partial T}{\partial \xi_3}\bigg|_b^t\right] + \\
&\alpha \frac{1}{J}\left[\frac{1}{J}\beta_j^1 \beta_j^2 \frac{\partial T}{\partial \xi_2}\bigg|_w^e + \frac{1}{J}\beta_j^2 \beta_j^1 \frac{\partial T}{\partial \xi_1}\bigg|_s^n + \frac{1}{J}\beta_j^3 \beta_j^1 \frac{\partial T}{\partial \xi_1}\bigg|_b^t\right] + \\
&\alpha \frac{1}{J}\left[\frac{1}{J}\beta_j^1 \beta_j^3 \frac{\partial T}{\partial \xi_3}\bigg|_w^e + \frac{1}{J}\beta_j^2 \beta_j^3 \frac{\partial T}{\partial \xi_3}\bigg|_s^n + \frac{1}{J}\beta_j^3 \beta_j^2 \frac{\partial T}{\partial \xi_2}\bigg|_b^t\right] \quad .
\end{aligned} \tag{2.18}$$

In this thesis, the derivatives in the third last brackets in equation (2.18) are discretized by employing a second-order finite difference method based on two adjacent control volumes, *e.g.*, $\partial T/\partial \xi_1|_e \approx T_E - T_P$. As for the derivatives in the last two brackets of equation (2.18), they need to be first evaluated at the centroids of control volumes, and then interpolated to the desired faces, *e.g.*, $\partial T_i/\partial \xi_3|_e \approx (T_S + T_{SE} - T_N - T_{NE})/4$. It should be indicated that the terms in the last two brackets are cross-derivative diffusion fluxes, which vanish in an orthogonal grid system. Table 2.2 summarizes the coordinate transformation of thermal equation.

2.1.3 Temporal discretization

An explicit two-step Runge-Kutta scheme (RK) was utilized to discretize the temporal derivative. Within each sub-step of the Runge-Kutta scheme, a fractional-step method is also implemented to enhance the accuracy. The advection-diffusion equation that governs the temperature field was implemented after the solution of the momentum equations at each time step. For the first sub-step, equation (2.3) is further evaluated as

$$
\begin{aligned}
&J\frac{T^{*}-T}{\Delta t}+Tu_i|_e-Tu_i|_w+Tu_i|_n-Tu_i|_s+Tu_i|_t-Tu_i|_b= \\
&\alpha\left(\frac{1}{J}\beta_j^1\beta_j^1\frac{\partial T}{\partial \xi_1}\bigg|_w^e+\frac{1}{J}\beta_j^2\beta_j^2\frac{\partial T}{\partial \xi_2}\bigg|_s^n+\frac{1}{J}\beta_j^3\beta_j^3\frac{\partial T}{\partial \xi_3}\bigg|_b^t\right) \\
&+\alpha\left(\frac{1}{J}\beta_j^1\beta_j^2\frac{\partial T}{\partial \xi_2}\bigg|_w^e+\frac{1}{J}\beta_j^2\beta_j^1\frac{\partial T}{\partial \xi_1}\bigg|_s^n+\frac{1}{J}\beta_j^3\beta_j^1\frac{\partial T}{\partial \xi_1}\bigg|_b^t\right) \\
&+\alpha\left(\frac{1}{J}\beta_j^1\beta_j^3\frac{\partial T}{\partial \xi_3}\bigg|_w^e+\frac{1}{J}\beta_j^2\beta_j^3\frac{\partial T}{\partial \xi_3}\bigg|_s^n+\frac{1}{J}\beta_j^3\beta_j^2\frac{\partial T}{\partial \xi_2}\bigg|_b^t\right) \quad .
\end{aligned}
\tag{2.19}
$$

Here, T^{*} denotes an updated preliminary temperature field. Equation 2.19 can be expressed in a more compact manner as

$$T^{*}=H-\frac{\Delta t}{J} \quad , \tag{2.20}$$

where H denotes all the explicit terms in equation (2.19). The first stage of any explicit Runge-Kutta method simply samples the temperature field at the current time-step as

$$
\begin{aligned}
T^{(1)}&=T^{n} \quad , \\
K_1&=H(T^{(1)}) \quad , \\
T^{(2)}&=T^{(1)}+K_1\Delta t \quad , \\
K_2&=H(T^{(2)}) \quad ,
\end{aligned}
\tag{2.21}
$$

and the second time-step as

$$T^{(n+1)*}=T^{n}+\Delta t(\frac{K_1+K_2}{2}) \quad . \tag{2.22}$$

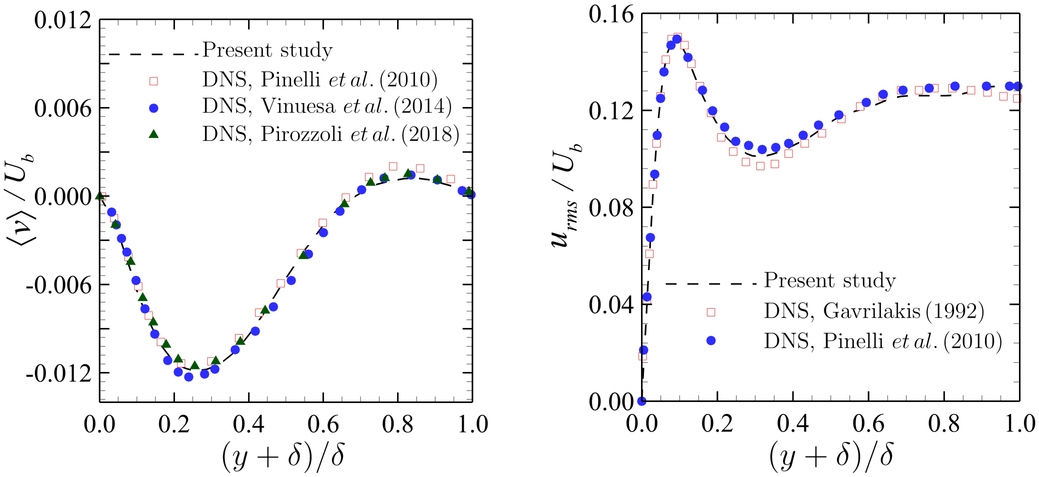

(a) Profiles of $\langle v \rangle$ at $z/\delta = -0.75$

(b) Profiles of u_{rms} at $z/\delta = -0.7$

Figure 2.2: Comparison of the vertical profiles of mean transverse velocity $\langle v \rangle$ and streamwise RMS velocity u_{rms} against the reported DNS data of Gavrilakis (1992), Pinelli et al. (2010b), Vinuesa et al. (2014) and Pirozzoli et al. (2018) for a smooth square duct flow of $Re_b = 4410$ in the off-center vertical planes located at $z/\delta = -0.75$ and -0.7, respectively.

2.1.4 Code validation

Prior to the DNS study of ribbed square duct flows, the computer code was validated based on two classical test cases of (1) a smooth square duct flow at $Re_b = 4410$, and (2) a 2-D ribbed plane-channel flow (with spanwise square bars mounted on one wall) at $Re_b = 5600$. The obtained DNS results were compared against the reported DNS data of Gavrilakis (1992), Pinelli et al. (2010b), Vinuesa et al. (2014), and Pirozzoli et al. (2018) on the smooth duct flow case, and against those of Orlandi et al. (2006) and Ismail et al. (2018) on the 2-D ribbed planed-channel flow case. The comparisons are shown in figures 2.2 and 2.3, respectively.

The DNS of the smooth duct flow was performed with a computational domain of $L_x \times L_y \times L_z = 6\pi\delta \times 2\delta \times 2\delta$. The streamwise computational domain was set to $L_x = 6\pi$, identical to that used in Pirozzoli et al. (2018). Periodic boundary condition was applied to the streamwise direction and no-slip boundary condition was prescribed at all four sidewalls. The number of grid points used in our DNS was $N_x \times N_y \times N_z = 512 \times 128 \times 128$, identical to that used for "case A" of the DNS study of Pirozzoli et al. (2018). As is evident in figure 2.2, the DNS results show an excellent agreement with the reported data in terms of the prediction of the non-dimensionalized the mean transverse velocity $\langle v \rangle / U_b$ and root-mean-squares (RMS) of the streamwise velocity fluctuations u_{rms}/U_b. Figure 2.2(a) clearly indicates the presence of the secondary mean flow in the cross-stream directions, as the magnitude of $\langle v \rangle / U_b$ is non-negligible, and the profile is characterized by a "S-shaped" pattern along the vertical direction. From figure 2.2(b), it is seen that the profile of non-dimensionalized streamwise RMS velocity u_{rms}/U_b manifests a primary peak near the sidewall, and again increases in value close to the duct center. Clearly, in a smooth duct flow, the presence of the secondary flow has a significant impact on the mean and turbulence fields. Later, it will be shown that the occurrence of the secondary flow is characteristic of both smooth and ribbed duct flows, which is due to the confinement of the four sidewalls of the duct.

For the second test case of a 2-D ribbed plane-channel flow, the DNS was performed in a computational domain of $L_x \times L_y \times L_z = 8\delta \times 2.2\delta \times \pi\delta$ consisting of five rib periods, identical to the setup of Orlandi et al. (2006). The same test case has also been investigated by Ismail et al. (2018), and their data are also used here in our comparative study. Periodic boundary condition was applied to both streamwise and spanwise directions, and no-slip boundary condition was applied to all surfaces. Following Orlandi et al. (2006), the range of the vertical coordinate is $-1.2 \leq y/\delta \leq 1.0$. The number of grid points used in our DNS was $N_x \times N_y \times N_z = 400 \times 160 \times 128$, identical to that used by Orlandi et al. (2006). Figure 2.3 compares the predicted mean streamwise velocity and mean viscous shear stress profiles against the DNS data of Orlandi et al. (2006) and Ismail et al. (2018). As shown in figure 2.3, the results are in an excellent agreement with the reported data. The effects of ribs on the velocity field is evident in both figures 2.3(a) and 2.3(b). The vertical profile of

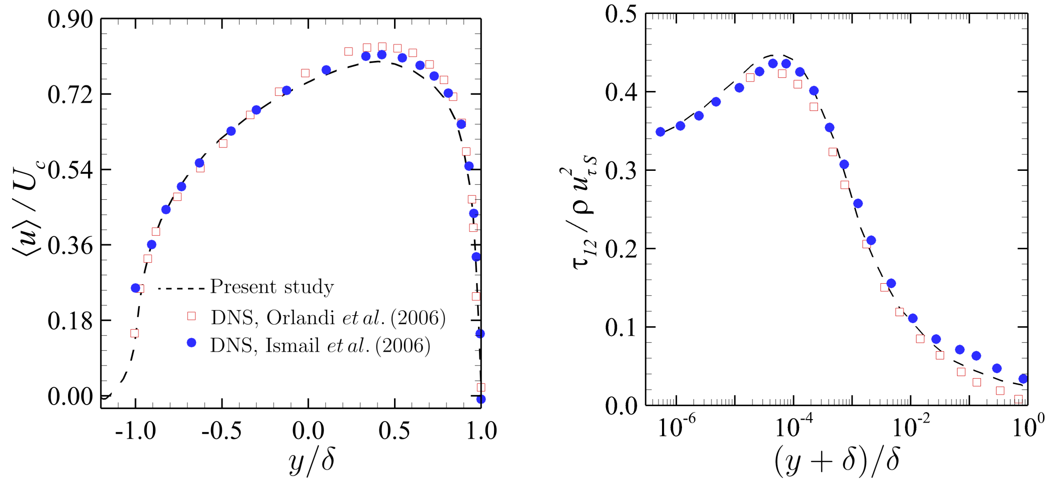

(a) Profiles of $\langle u \rangle$ (b) Profiles of τ_{12}

Figure 2.3: Comparison of the vertical profiles of mean streamwise velocity $\langle u \rangle$ and viscous shear stress τ_{12} against the DNS data of Orlandi et al. (2006) and Ismail et al. (2018) for 2-D turbulent plane-channel flow of $Re_b = 5600$ with transverse square ribs mounted on one wall.

$\langle u \rangle / U_c$ becomes asymmetrical in the vertical direction due to the presence of the ribs. Here, $U_c = 3U_b/2$ is the mean streamwise velocity at the center line of the channel (Orlandi et al., 2006; Ismail et al., 2018). From figure 2.3(a), it is also clear that the shear layer carrying the highest streamwise momentum is pushed towards the smooth top wall. These characteristics of the mean streamwise velocity profile further result in a viscous shear stress ($\tau_{12} = \mu \partial \langle u \rangle / \partial y$) profile that is special for a 2-D ribbed boundary-layer flow shown in figure 2.3(b). The viscous shear stress reaches its maximum near the rib crest and decreases as the channel center is approached.

2.2 High-performance computing

Numerical simulations for the following chapters were conducted on the Western Canada Research Grid (WestGrid) supercomputers, which encompasses 15 partner institutions and is one of four consortia that provides high-performance computational resources across Canada. The precursor simulation was run for an extended duration of 73 flow-through times (i.e., $930\delta/U_b$) until the turbulent flow field becomes fully-developed and statistically stationary. Then, turbulence statistics were collected for a time period over approximately 110 flow-through times (i.e., $1400\delta/U_b$). For each simulated case in chapters 3 and 4, 240-254 cores were used for performing DNS, and approximately 548,000 central processing unit (CPU) hours were spent for solving the velocity field and for collecting the flow statistics (after the precursor simulation).

Chapter 3

Direct numerical simulation of turbulent flow through a ribbed square duct

3.1 Introduction

In this chapter, a systematic DNS study of rib-roughened duct flows of three different blockage ratios ($Br = 0.05$, 0.1 and 0.2) is conducted to obtain detailed knowledge of the rib height effects on the statistical moments and premultiplied energy spectra of the turbulent velocity field, local non-equilibrium of turbulence, large- and small-scale flow anisotropy, transport of TKE, as well as the dynamics of mean and turbulent secondary flow motions. In order to identify the rib effects on the flow field, an additional DNS of a smooth duct flow has also been conducted at the same Reynolds number (as in the three rib cases), which is used as a baseline comparison case. This study also aims to bring new insights into the secondary flows and turbulence structures characteristic of a three-dimensional (3-D) ribbed duct flow, which are considerably different from those of a conventional two-dimensional (2-D) rough-wall boundary-layer flow.

The remainder of this chapter is organized as follows: in section 3.2, the numerical algorithm for conducting DNS is introduced together with a detailed study of the minimum computational domain required for capturing dominant turbulent flow structures in a ribbed duct with various blockage ratios. In section 3.3, the influence of rib height on the statistically averaged quantities is analyzed, including the mean flows, the pressure and viscous drag coefficients, Reynolds stresses, production and dissipation terms, budget balance of TKE, as well as the anisotropy of the turbulence field characteristic of the ribbed duct. Furthermore, the impact of rib height on sweep and ejection events is investigated. To this purpose, the third-order moments and the joint probability density functions (JPDF) of streamwise and vertical velocity fluctuations are studied. In section 3.4, the effect of rib height on the turbulent flow structures is analyzed based on multiple tools such as vortex identifiers, two-point correlation functions, and velocity spectra. Finally, in section 3.5, major conclusions of this chapter are summarized.

3.2 Test cases and numerical method

Figure 3.1 shows a schematic of the computational domain for the ribbed squared duct with a side length D (i.e., $L_y = L_z = D$). The streamwise domain is $L_x = 6.4D$ long and consists of eight rib periods (P), with $P = 0.8D$. The height and width of the rectangular bars are H and W, respectively. In our analysis, it is useful to define half side length ($\delta = D/2$), especially when the results are compared with those of 2-D plane-channel flow. In our comparative study, DNS is performed based on three different blockage ratios (for $Br = H/L_y = 0.05$, 0.1, and 0.2). The flow field is assumed to be fully-developed and periodic boundary conditions are applied to the inlet and outlet of the duct. A no-slip boundary condition is imposed on all solid walls. The Reynolds number is fixed at $Re_b = DU_b/\nu = 5600$, where U_b denotes the average bulk mean velocity over the streamwise direction of the ribbed

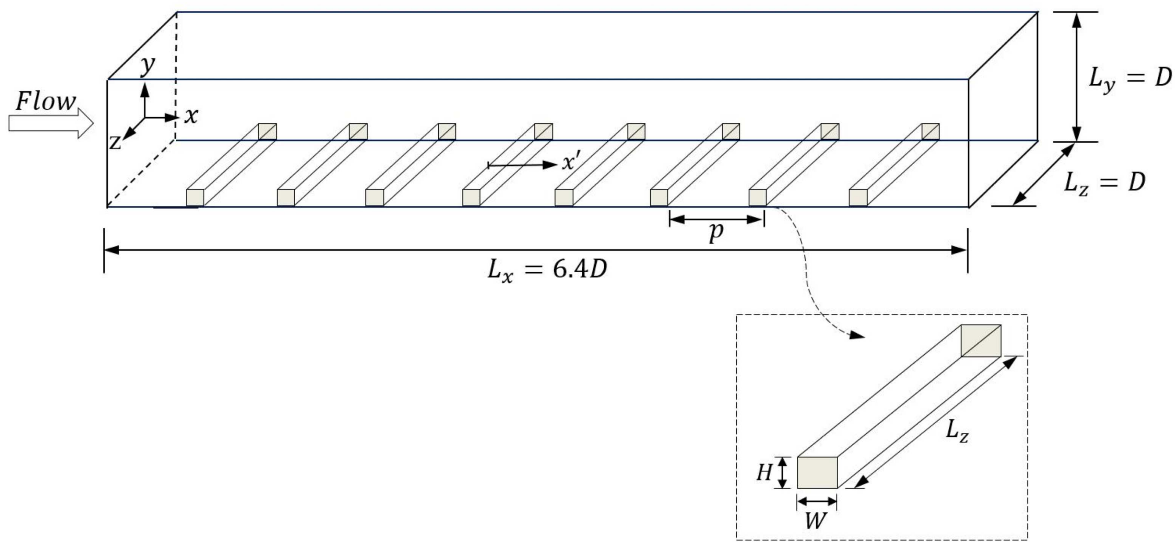

Figure 3.1: Schematic of a square duct with transverse ribs and coordinate system. The origin of the absolute coordinate system $[x, y, z]$ is located at the center of the inlet (y-z) plane. Eight rib periods are simulated in the DNS. To facilitate the analysis of each rib period, the relative streamwise coordinate x' is defined, with its origin located at the windward face of each rib.

duct. In comparison with a 2-D ribbed boundary-layer flow, more degrees of freedom are involved in the analysis of a 3-D ribbed duct flow. For instance, the restriction of spanwise homogeneity characteristic of a 2-D boundary-layer flow is lacking in a duct flow. Given the high blockage ratio, a common fixed-valued bulk Reynolds number Re_b is chosen, which facilitates a comparative study under a constant mass flow rate. This is similar to the study of Hirota et al. (1992) and Coletti et al. (2012), who conducted comparative experimental studies of rib-roughened duct flows based on bulk Reynolds number Re_b. The rib effects on the flow field are studied by comparing the DNS results of three rib cases against those of a baseline case of DNS of a smooth duct flow at the same Reynolds number Re_b. The geometrical setup of the smooth duct is similar to that described by figure 3.1, except that there are no ribs on the bottom wall and the streamwise length of the domain is $L_x = 6\pi\delta$ following the approach of Pirozzoli et al. (2018).

Table 3.1 compiles the flow parameters of three rib cases, including the Reynolds number based on the rib height (defined as $H^+ = Hu_{\tau R}/\nu$), streamwise domain length (defined as $L_x^+ = L_x u_{\tau R}/\nu$), elevation of the virtual origin (d_0) on the ribbed bottom wall side, and Reynolds numbers ($Re_{\tau S} = \delta u_{\tau S}/\nu$ and $Re_{\tau R} = \delta u_{\tau R}/\nu$) defined based on the mean streamwise wall friction velocities of smooth top and ribbed bottom walls (i.e., $u_{\tau S}$ and $u_{\tau R}$, respectively) in the central vertical (x-y) plane located at $z/\delta = 0$. The calculation of the value of $u_{\tau S}$ for the smooth top wall is straightforward, which is done based on the mean streamwise velocity gradient in the central (x-y) plane. The method for calculating the value of $u_{\tau R}$ for the ribbed bottom wall in the central (x-y) plane of the duct is analogous to that of Leonardi and Castro (2010) and Ismail et al. (2018) for a 2-D ribbed turbulent channel flow, viz. $u_{\tau R}^2 = D_p + D_v$. Here, term D_p and D_v are direct consequences of pressure and viscous drag forces in the central (x-y) plane, determined as $D_p = 1/(\rho L_x) \sum_{n=1}^{N} \int_0^H (\langle P_{wind}\rangle - \langle P_{lee}\rangle) dy$ and $D_v = \mu/(\rho L_x) \int_0^{L_x} (\partial\langle u\rangle/\partial y)_w \, dx$, respectively. In these equations, subscript 'w' denotes either the bottom wall or rib crest exposed to the streamwise flow, N is the total number of rib elements, $\langle\cdot\rangle$ denotes averaging over time and over the eight rib periods, and P_{wind} and P_{lee} represent the pressure on the windward and leeward faces of a rib, respectively. The position of the virtual origin in the central (x-y) plane can be determined analogously by following Thom (1971), Jackson (1981) and Chan et al. (2015) who studied 2-D rough-wall boundary-layer flows, viz. $d_0 = \int_0^H yD_t(y)dy / \int_0^H D_t(y)dy$, where $D_t = D_p + D_v$ is the total drag forcing term.

From table 3.1, it is clear that as the blockage ratio increases from $Br = 0.05$ to 0.2, the elevation of the virtual origin d_0/H increases monotonically as a result of an increasing rib height; meanwhile, both values of $Re_{\tau S}$ and $Re_{\tau R}$ also increase monotonically. The increasing trend in the elevation of the virtual origin in the central (x-y) plane of a 3-D square duct observed here is similar to the DNS results of Bhaganagar et al. (2004) and Chan et al. (2015) who systematically investigated 2-D roughness boundary-layer flow in a plane channel and a circular pipe, respectively.

Table 3.1: Flow parameters for DNS of three ribbed square duct flow cases of different blockage ratios.

Br	D_p (m^2s^{-2})	D_v (m^2s^{-2})	H^+	L_x^+	d_0/H	$Re_{\tau R}$	$Re_{\tau S}$
0.05	0.0095	0.00052	28	3587	0.38	280	183
0.1	0.0167	-0.00143	69	4428	0.69	346	208
0.2	0.0238	-0.00272	162	5203	0.84	406	236

The reason that the value of $Re_{\tau S}$ increases with the Br value is that this comparative study is conducted under the condition of a constant bulk Reynolds number Re_b. As the rib height increases, the mean streamwise velocity increases in order to maintain a constant mass flow rate. On the other hand, the physical mechanism underlying the monotonic increasing trend of $Re_{\tau R}$ with an increasing Br value is rather complicated. By definition, the value of $Re_{\tau R}$ is influenced by both values of D_p and D_v. From table 3.1, it is evident that the value of D_v is one order of magnitude smaller than that of D_p, indicating that the drag force is primarily contributed by the pressure drag term D_p, which increases as the rib height increases. It is interesting to observe that the value of the viscous drag term D_v transitions from being positive to being negative as the Br value increases. A negatively-valued viscous drag is a direct reflection of boundary-layer separation in the recirculation bubble behind a rib. The rib height effects on the pattern of the recirculation bubble and on the spanwise variation of the viscous and pressure drag coefficients will be detailed shortly in subsection 3.3.1.

It should be indicated here that the calculation of the values of D_p, D_v, $Re_{\tau S}$, $Re_{\tau R}$ and d_0 in the central vertical (x-y) plane (located at $z/\delta = 0$) follows the method of analysis for a conventional 2-D rough-wall boundary layer. Strictly speaking, the value of applying this method to the analysis for a 3-D ribbed duct flow is very limited, simply because a 2-D boundary layer is absent in a 3-D ribbed duct flow and the analysis is restricted to the selected central vertical (x-y) plane. Furthermore, given the large value of the blockage ratio (up to $Br = 0.2$ in a square duct), it would be more reasonable to treat the tall ribs as part of the domain geometry rather than

2-D roughness elements.

DNS was performed with an in-house computer code developed using the FORTRAN 90/95 programming language and parallelized following the message passing interface (MPI) standard. In this computer code, the continuity and momentum equations are discretized based on a general curvilinear coordinate system (ξ_1, ξ_2, ξ_3), and in the context of an incompressible flow, they are expressed as

$$\frac{1}{J}\frac{\partial\left(\beta_i^k u_i\right)}{\partial\xi_k} = 0 \quad , \tag{3.1}$$

$$\frac{\partial u_i}{\partial t} + \frac{1}{J}\frac{\partial}{\partial\xi_k}\left(\beta_j^k u_i u_j\right) = -\frac{1}{J\rho}\frac{\partial\left(\beta_i^k p\right)}{\partial\xi_k} - \frac{1}{\rho}\Pi\delta_{1i} + \frac{\nu}{J}\frac{\partial}{\partial\xi_p}\left(\frac{1}{J}\beta_j^p\beta_j^q\frac{\partial u_i}{\partial\xi_q}\right) \quad , \tag{3.2}$$

where u_i, p, ν, ρ, and δ_{ij} represent the velocity, pressure, kinematic viscosity, density, and Kronecker delta, respectively. In addition, Π denotes a constant streamwise pressure gradient that drives the flow, and β_i^j and J denote the cofactor and Jacobian of tensor $\partial x_i/\partial\xi_j$, respectively. It is worth noting that this computational code is developed to tackle curved surfaces based on body-fitted mesh. Specific to the current application to simulation of the flow through a square duct with straight rectangular shaped ribs mounted on one wall, the Jacobian degenerates to Kronecker Delta. The above governing equations are represented using tensor notations, and the streamwise (x), vertical (y), and spanwise (z) coordinates shown in figure 3.1 are denoted using x_i for $i = 1$, 2, and 3, respectively. Correspondingly, the three velocity components u, v and w are also denoted using u_1, u_2 and u_3. Eight rib periods are simulated in our DNS, and in our analysis of each rib period, we also use the relative streamwise coordinate x', with its origin located at the windward face of a rib (see figure 3.1).

The numerical algorithm of the computer code is based on the finite-volume method (FVM) in which a second-order accuracy is achieved with respect to both spatial and temporal discretizations. Within each sub-step of the second-order Runge-Kutta scheme, a fractional-step method is applied and a pressure correction equation is solved using the parallel algebraic multigrid solver (AMG), and the convergence of the solver is considered once the averaged residue of a discretized algebraic equation drops below 10^{-6}. For time advancement, the Courant-Friedrichs-Lewy (CFL) number is approximately 0.2. A momentum interpolation approach is used to obtain the cell-face velocity components and based on the velocity and pressure values in two adjacent control volumes in order to avoid the potential checkerboard problem of the pressure field. The simulation started with an initial laminar flow solution superimposed with artificial perturbations to trigger turbulence. The precursor simulation was run for an extended duration of 73 flow-through times (i.e., $930\delta/U_b$) until the turbulent flow field becomes fully-developed and statistically stationary. Then, turbulence statistics were collected for a time period over approximately 110 flow-through times (i.e., $1400\delta/U_b$). All the simulations were conducted using the WestGrid (Western Canada Research Grid) supercomputers. For each simulated case, 254 cores were used for performing DNS, and approximately 548,000 CPU hours were spent for solving the velocity field and for collecting the flow statistics (after the precursor simulation).

3.2.1 Streamwise integral length scale and domain size

In the current literature, there are controversies over the proper choice of the streamwise computational domain size (L_x) for transient simulation of ribbed turbulent duct flow. For instance, Sewall et al. (2006) performed LES to investigate the effects of transverse rib roughness on the turbulent flow and heat transfer within a square duct at a fixed Reynolds number. The streamwise domain in their LES was a single rib period (i.e., $L_x = P = 2\delta$) with a periodic boundary condition applied to the streamwise direction. Fang et al. (2017) studied turbulent flow and structures in a square duct with perpendicular and V-shaped ribs mounted on the bottom wall, and the streamwise domain size set to $L_x = 4.8\delta$. They showed that this domain size is insufficient for capturing the largest eddy structures in the duct center. In view of this, a larger value of $L_x = 6.4D$ (or, 12.8δ) is taken into account in the current DNS to ascertain that typical large-scale turbulent structures of the flow are properly captured. To confirm, streamwise two-point correlation (R_{uu}) is computed for different rib heights at various elevations. Note that since the flow in the vicinity of ribs experiences various separation and reattachment phenomena, ribbed duct flow is remarkably inhomogeneous in the streamwise direction. Consequently, the two-point correlation of the fluctuating velocity components cannot be computed via fast Fourier transform (FFT). In this regard, we follow the approach of Christensen and Adrian (2001), who calculated auto- and cross-correlations of the velocity field in the physical space at several points across the vertical direction. For a ribbed duct flow, the streamwise two-point auto-correlation coefficient is defined as (Townsend, 1980; Volino et al., 2009)

$$R_{uu}(x_{ref}, \Delta x) = \frac{\langle u'(x_{ref})u'(x_{ref} + \Delta x)\rangle}{\sqrt{\langle u'^2(x_{ref})\rangle\langle u'^2(x_{ref} + \Delta x)\rangle}} \quad , \tag{3.3}$$

where u' represents the streamwise fluctuating velocity, and Δx denotes the relative displacement from the reference point located at x_{ref}, such that $x = x_{ref} + \Delta x$.

Figure 3.2 compares the profiles of the normalized streamwise two-point auto-correlation coefficient at different elevations along the vertical line located at approximately the center of the domain of $(x_{ref}/\delta, z_{ref}/\delta) = (5.9, 0.0)$ for two rib cases of different blockage ratios. In terms of the relative streamwise coordinate measured from the windward face of the upstream rib, the reference points are at $x'_{ref}/\delta = 0.4$. It is evident from this figure that R_{uu} decays to zero over one-half the streamwise domain length at all three elevations, indicating that the streamwise computational domain size is sufficiently large to capture energetic turbulence structures. By comparing figures 3.2(a) with 3.2(b), it is observed that as the rib height increases, the spread of the peak becomes greater as a result of larger streamwise length scales. Indeed, the streamwise integral length scale (i.e., $L_{xx} = \int_0^\infty R_{uu}(x)dx$) of $Br = 0.2$ near the rib crest is 2.8 times that of $Br = 0.05$. From this figure, it is also clear that for the two rib cases of different Br values, the length scales of turbulent ed-

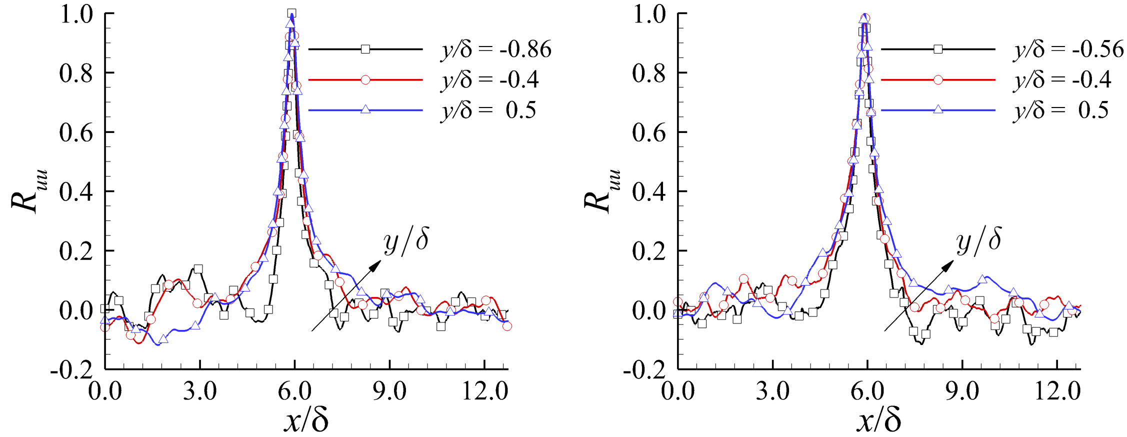

(a) $Br = 0.05$ (b) $Br = 0.2$

Figure 3.2: Streamwise profiles of two-point auto-correlations for ribbed duct flows of two different blockage ratios (Br) at different elevations (y/δ). The reference points are located approximately at the center of the computational domain (i.e., at $x_{ref}/\delta = 5.9$ and $z_{ref}/\delta = 0.0$). In terms of the relative streamwise coordinate measured from the windward face of the upstream rib, the reference points are at $x'_{ref}/\delta = 0.4$. In the vertical direction, the reference points at $y/\delta = -0.86$ and -0.56 coincide with the peaks positions of $\langle u'u' \rangle$ and $-\langle u'v' \rangle$ for $Br = 0.05$ and 0.2 cases, respectively (which will be demonstrated later in section 3.3.3).

dies slightly increase with an increasing distance from the rib crest in the vertical direction. Further from table 3.1, it is clear that as the blockage ratio increases from $Br = 0.05$ to 0.2, the non-dimensional domain length increases monotonically from $L_x^+ = 3587$ to 5203.

3.2.2 Grid resolution

In this study, we used body-fitted mesh (BFM) to resolve precisely each rib geometry, such that the entire flow field can be accurately calculated. The simulations were conducted using $N_x \times N_y \times N_z = 1280 \times 148 \times 152$ body-fitted grid points. The mesh is non-uniform in all three directions, and is refined near all solid surfaces. It should be mentioned that there are two popular meshing methods in the current literature that can be used for dealing with riblets. Besides BFM, the immersed boundary

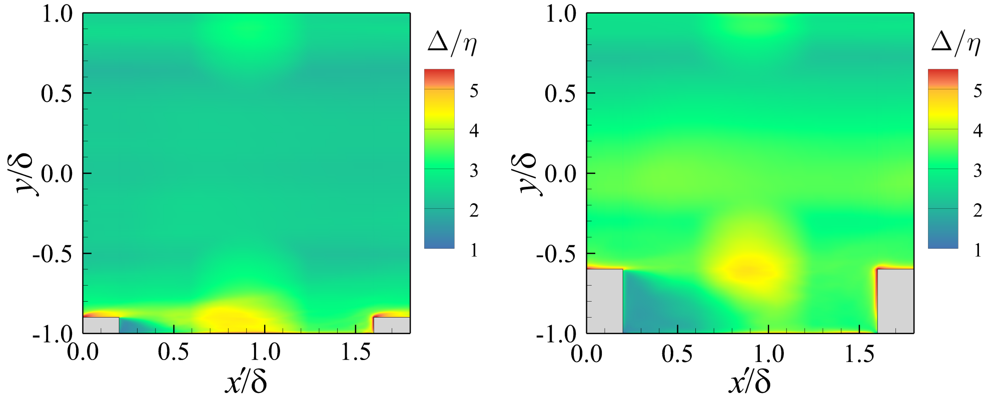

(a) $Br = 0.05$ (b) $Br = 0.2$

Figure 3.3: Contours of the ratio of the grid size to the Kolmogorov length scale (Δ/η) in the central plane at $z/\delta = 0.0$ for two different blockage ratios of $Br = 0.05$ and 0.2.

method (IBM) can be also considered. The IBM method started with Peskin (1972) and has been significantly developed since (Mittal and Iaccarino, 2005; Griffith and Patankar, 2020). The IBM method has been successfully applied to DNS and LES of turbulent flows over regular and irregular shaped roughness elements (Leonardi et al., 2003; Scotti, 2006; Orlandi et al., 2006; Pinelli et al., 2010a; Bhaganagar, 2008; Bhaganagar and Chau, 2015; Lee et al., 2011; Yuan and Piomelli, 2014; Rouhi et al., 2019). As two popular methods, both BFM and IBM have advantages and disadvantages. In comparison with the BFM method, the IBM method is computationally less expensive, but it relies on an additional roughness-forcing model. Given that the blockage ratio is relatively high (up to $Br = 0.2$), the tall ribs should be treated as part of the domain geometry rather than 2-D roughness elements. Furthermore, because the geometry of the square rib bars is regular and simple, we can use BFM to resolve precisely each rib geometry (without a need for roughness forcing model as in IBM), such that the flow field of the entire computation domain (including the rib neighborhood) can be accurately calculated. The BFM method used here is similar to those of Ikeda and Durbin (2007), Yang and Shen (2010), Philips et al. (2013), Chan

Table 3.2: Grid resolutions in wall units for all three directions based on the mean streamwise wall friction velocity ($u_{\tau S}$) along the intersection line of the smooth top wall (located at $y = \delta$) and the central vertical (x-y) plane (located at $z/\delta = 0$).

Br	$\Delta_x^+\|_{max}$	$\Delta_y^+\|_{max}$	$\Delta_z^+\|_{max}$	$\Delta_x^+\|_{min}$	$\Delta_y^+\|_{min}$	$\Delta_z^+\|_{min}$
0.05	6.5	5.4	5.9	0.65	0.48	0.61
0.1	7.7	6.5	7.2	0.69	0.57	0.69
0.2	8.9	7.9	8.1	0.73	0.68	0.76

et al. (2015), Wagner and Shishkina (2015), MacDonald et al. (2016), and Ismail et al. (2018), who directly resolved regularly-shaped roughness elements (e.g., ribs, cubes, and wavy surfaces) using body-fitted meshes.

To ensure that this mesh is sufficiently fine to capture the smallest scales of the turbulence as demanded by DNS, the ratio of the grid size to the Kolmogorov length scale is investigated. Based on their DNS study of turbulent channel flows, Moser and Moin (1987) indicated that the grid size requires to be of the same order as the Kolmogorov length scale (i.e., $O(\Delta/\eta) \sim O(1)$) in order to accurately capture the turbulence kinetic energy (TKE) dissipation pertaining to the smallest scales of turbulence. The grid size considered here is based on the maximal dimension of a grid cell in all three directions (i.e., $\Delta = \max(\Delta_x, \Delta_y, \Delta_z)$) and the Kolmogorov length scale is calculated as $\eta = (\nu^3/\varepsilon)^{1/4}$, where the local dissipation rate is defined as $\varepsilon = \nu\langle \partial u_i'/\partial x_j \partial u_i'/\partial x_j \rangle$.

The contours of Δ/η in the central (x-y) plane for two different rib cases are shown in figure 3.3. As indicated in figures 3.3(a) and 3.3(b), it is apparent that the value of Δ/η is of the order of one (i.e., $\Delta/\eta = O(1)$) in the two rib cases. Furthermore, as is seen in these figures 3.3(a) and 3.3(b), the maximum value of Δ/η is found to be around 6.2 at the leading corner of the rib. Other than this specific location, the value of Δ/η never exceeds 4.5 over the rest of the computational domain for all the simulations. This indicates that this grid spacing suffices for accurately performing DNS of turbulent flows in all three ribbed duct cases tested. Contours of non-dimensionalized grid size shown in figure 3.3 are comparable to those used by

Ikeda and Durbin (2007) who conducted DNS study of the 2-D turbulent boundary layer over periodic transverse rib roughness, and are finer than those employed for DNS of turbulent flow over cuboidal obstacles mounted on a wall conducted by Coceal et al. (2007). The spatial resolutions used in our DNS are summarized in table 3.2.

3.3 Statistics of the velocity field

3.3.1 Mean velocity field and mean flow structures

Figure 3.4 compares the time-averaged streamlines in the central plane located at $z/\delta = 0.0$ for three different rib blockage ratios. This figure clearly shows the effect of rib height on the mean flow structures. As is seen in figures 3.4(a)-3.4(c), the mean flow structures between the ribs consist of a large recirculation bubble (marked with "B"), and two small secondary vortices located at corners on the leeward side of the upstream rib and windward side of the downstream rib (marked with "A" and "E", respectively). By comparing these figures, it is clear that corner vortex A is not apparently observed at $Br = 0.05$ due to the fact that the rib is not high enough to cause a significant sudden expansion of the flow in the lee of the rib. The size of corner vortex A increases as the rib height increases. Owing to the relatively small velocity (roughly 15% of the free-stream velocity) within the recirculation zone B, an adverse pressure gradient is induced, causing the flow to reattach onto the bottom wall. Downstream of the reattachment point "C", a new boundary layer builds up and impinges on the next rib leading to the generation of the upstream vortex "E" (starting at point "D"). Clearly, the recirculation bubble B becomes increasingly elongated with an increasing rib height, which further leads to a reduction in the horizontal distance between points C and D. This phenomenon inevitably impacts both the local friction and form drags (which will be discussed in subsection 3.3.2). By comparing figures 3.4(a)-3.4(c), it is interesting to observe that the mean flow

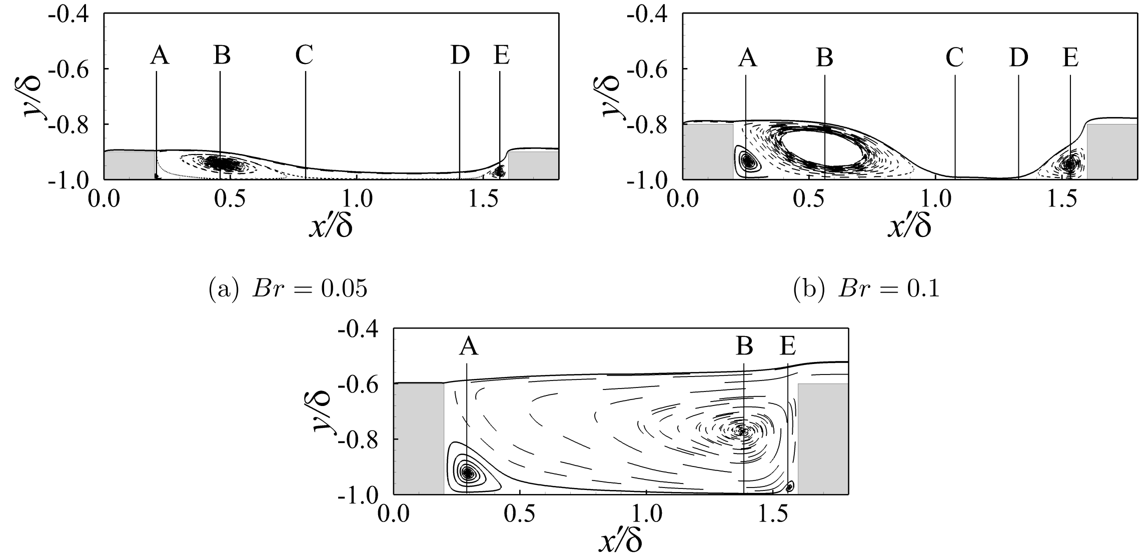

(a) $Br = 0.05$

(b) $Br = 0.1$

(c) $Br = 0.2$

Figure 3.4: Mean streamline pattern near the ribbed bottom wall in the central plane located at $z/\delta = 0.0$ for three different rib cases of $Re_b = 5600$.

patterns of cases of $Br = 0.05$ and 0.1 are typical of k-type rough-wall flows, but that of $Br = 0.2$ exhibits features that are characteristic of a d-type rough-wall flow. Specifically, as shown in figure 3.4(c), recirculation bubble B is well extended such that it occupies almost the entire “cavity” between two adjacent ribs, there is no touch point D, and the mean free-stream flow skims over the cavity. The pitch-to-height ratios of these three rib cases are $P/H = 16$, 8 and 4 (for $Br = 0.05$, 0.1 and 0.2), respectively. If we strictly follow the proposal of Perry et al. (1969) and Bandyopadhyay (1987) on 2-D rough-wall boundary layers, all these three rib cases should be considered as k-type rough-wall flows because their pitch-to-height ratios are larger than three. However, the 3-D rough-wall flow in a square duct under current investigation is qualitatively different from the classical case of 2-D rough-wall boundary-layer flow. As such, the case of $Br = 0.2$ features a d-type rough-wall flow pattern.

To assess the effects of the rib height on the velocity field, the non-dimensional

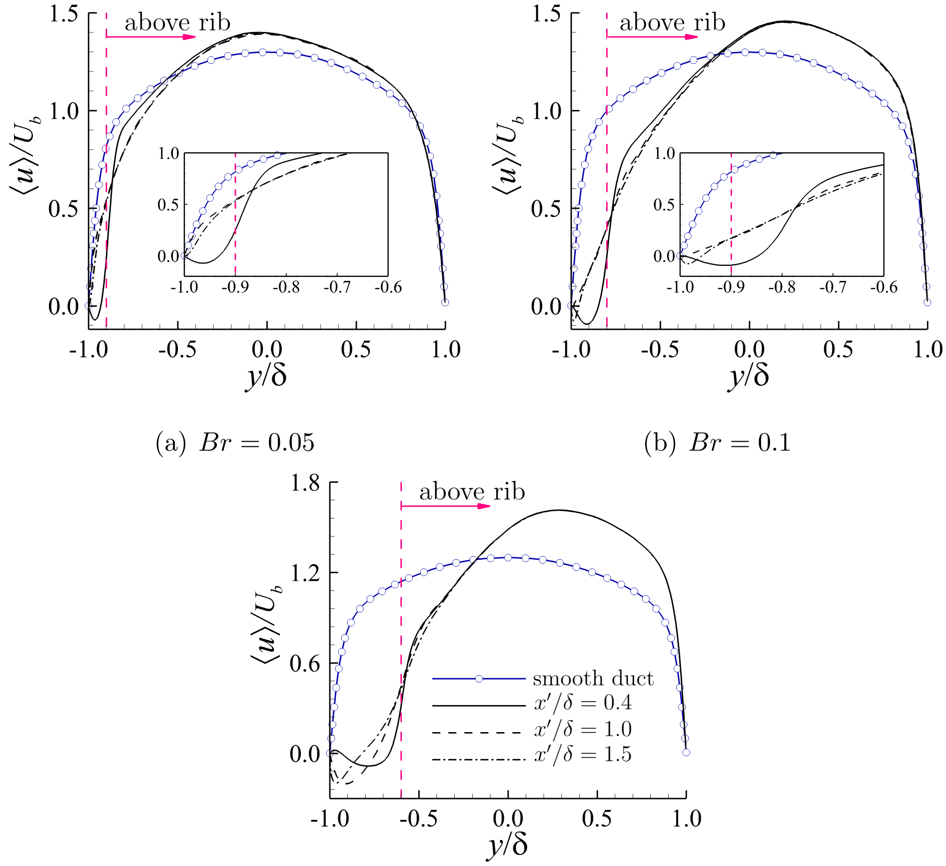

(a) $Br = 0.05$

(b) $Br = 0.1$

(c) $Br = 0.2$

Figure 3.5: Comparison of the non-dimensionalized mean streamwise velocity profiles at three relative streamwise locations (for $x'/\delta = 0.4$, 1.0 and 1.5) in the central plane (located at $z/\delta = 0$) of the ribbed square duct flows (of three blockage ratios for $Br = 0.05$, 0.1 and 0.2) with that of the smooth square duct flow at the same Reynolds number $Re_b = 5600$. The vertical pink dashed line demarcates the rib crest.

vertical profiles of the mean streamwise velocity at different relative streamwise locations ($x'/\delta = 0.4$, 1.0, and 1.5) are plotted in figure 3.5. The results of three rib cases are compared with that of the smooth duct in the central vertical plane (located at $z/\delta = 0$). As expected, the profile of $\langle u \rangle / U_b$ of the smooth duct flow is symmetrical in the vertical direction. By contrast, the profiles of all three rib case are 'skewed' towards the smooth top wall. By comparing figures 3.5(a)-3.5(c), it is seen that the vertical position corresponding to the maximum value of the mean streamwise velocity elevates from $y/\delta = -0.07$ to 0.28 as the blockage ratio increases from $Br = 0.05$ to 0.2. Owing to the presence of the ribs, the magnitude of the mean streamwise velocity $\langle u \rangle / U_b$ is smaller than that of the smooth duct flow on the ribbed bottom wall side. As the rib height increases, the profile of the mean streamwise velocity shifts downwards progressively, a pattern that is often seen in a 2-D rough-wall boundary-layer with spanwise homogeneity. By contrast, on the smooth top wall side, the magnitude of the mean streamwise velocity increases monotonically as the rib height increases. This is due to the need of maintaining a constant mass flow rate under the test condition of a constant bulk Reynolds number Re_b. Clearly, as the rib height increases, the flow convects downstream with higher momentum near the duct center associated with a decrease in the mean streamwise velocity in the near-wall region below the rib height. Furthermore, owing to the presence of the ribs, the mean streamwise velocity is bumped up around the rib crest. From figures 3.5(a)-3.5(c), it is apparent that the shear layer strength, as interpreted from the vertical gradient of the mean streamwise velocity, decreases monotonically in the region immediately above the rib crest as the rib height increases (i.e., the value of $|\partial \langle u \rangle / \partial y|$ at the rib crest decreases as the blockage ratio increases from $Br = 0.05$ to 0.2). These mean flow features directly influence the large-scale eddies induced by the roll-up of the shear layer near the rib crest, which have a significant impact on the turbulent transport processes.

The study of the mean streamwise velocity can be refined by further examining the effects of rib height on the mean viscous shear stress $\tau_{12} = \mu \partial \langle u \rangle / \partial y$ in the central vertical plane (located at $z/\delta = 0$), which is shown in figure 3.6. From the figure 3.6(a)-3.6(c), it is clear that the profile of τ_{12} is symmetrical for the smooth duct flow, but asymmetrical for all three ribbed duct cases at all three relative streamwise locations of $x'/\delta = 0.4$, 1.0 and 1.5. As indicated by the dominant peak of τ_{12} shown in figure 3.6(a)-3.6(c), it is clear that the shearing effect is the highest near the rib crest (in the vertical direction) and at $x'/\delta = 0.4$ relative to the windward face of

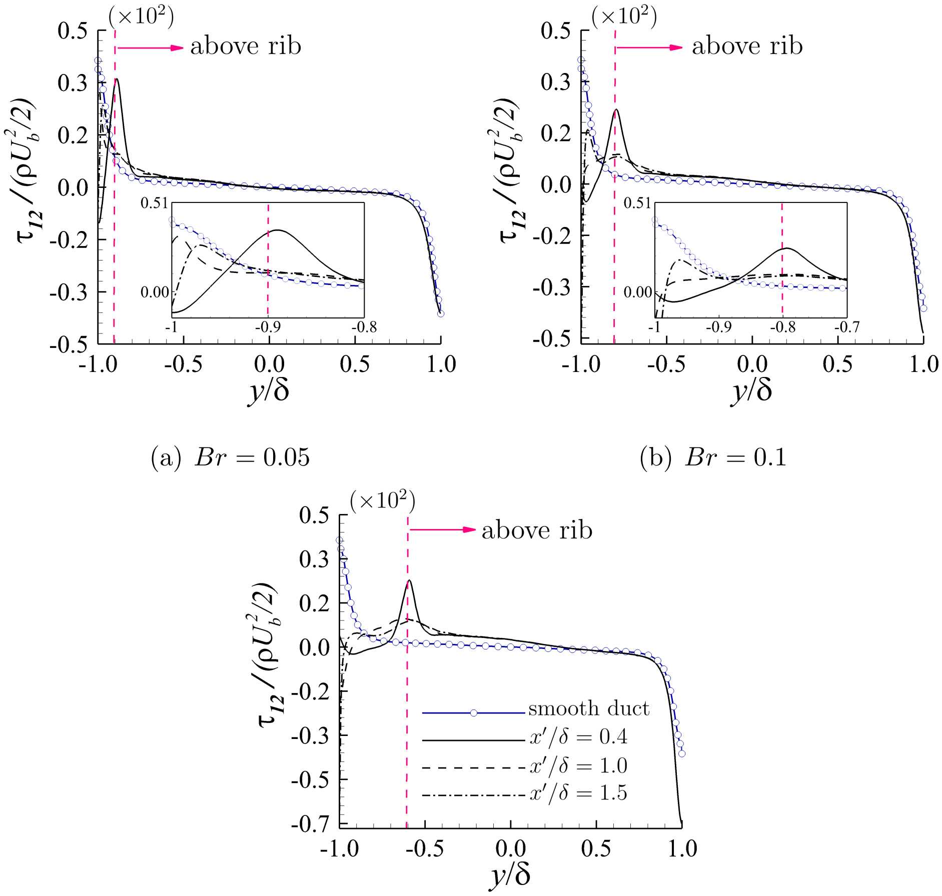

(a) $Br = 0.05$

(b) $Br = 0.1$

(c) $Br = 0.2$

Figure 3.6: Comparison of the non-dimensionalized mean viscous shear stress profiles at three relative streamwise locations (for $x'/\delta = 0.4$, 1.0 and 1.5) in the central plane (located at $z/\delta = 0$) of the ribbed square duct flows (of three blockage ratios for $Br = 0.05$, 0.1 and 0.2) with that of the smooth square duct flow at the same Reynolds number $Re_b = 5600$. The vertical pink dashed line demarcates the rib crest.

the upstream rib (in the streamwise direction) in all three rib cases. This feature is in sharp contrast to that of the smooth duct flow, in which the value of τ_{12} is the maximum at the two walls. From figures 3.5 and 3.6, it is understood that magnitudes of both the mean streamwise velocity gradient $|\partial\langle u\rangle/\partial y|$ and viscous shear stress τ_{12} are the largest near the rib crest at $x'/\delta = 0.4$ in all three rib cases. A large value of the mean streamwise velocity gradient often leads to high turbulent production rate and TKE level. In view of this, in the remainder of our analysis, we pay close attention to this special relative streamwise location $x'/\delta = 0.4$. Also, it is noticed that this particular relative streamwise position was also used by Coletti et al. (2012) in their PIV experimental study of turbulent flow and structures in a ribbed duct with and without system rotations.

To understand the influence of secondary motions on the mean streamwise velocity field, figure 3.7 demonstrates the contours of the non-dimensionalized mean streamwise vorticity (defined as $\langle \omega_x \rangle = \partial \langle w \rangle / \partial y - \partial \langle v \rangle / \partial z$) and the magnitude of the non-dimensionalized mean streamwise velocity $\langle u \rangle / U_b$ (superimposed with the mean spanwise-vertical velocity vectors) in the cross-stream (y-z) plane located at $x'/\delta = 0.4$. Given the central symmetry of the flow field, only one half of the cross-stream domain is shown. As is evident from the mean velocity vector map shown in figure 3.7, in all three rib cases, there exists one large streamwise-elongated vortex on each side of the duct. The appearance of this pair of large vortices is a reflection of the mean secondary flows in the cross-stream plane. The centers of these two vortices can be located using the vector map and are marked using white dots in figure 3.7. The mean secondary flows exhibit two apparent trends as the rib height increases. Firstly, the vortex center shifts upwards and transversely to the sidewalls as the rib height increases. Specifically, the center of the vortex lies at $(y/\delta, z/\delta) = (-0.01, 0.64)$ for $Br = 0.05$, but moves to (0.32, 0.55) and (0.42, 0.51) as the blockage ratio increases to $Br = 0.1$ and 0.2, respectively. Secondly, the impingement region on the sidewalls occurs at a higher elevation as the rib height increases. The secondary flow patterns demonstrated using the non-dimensionalized mean streamwise vorticity $\langle \omega_x \rangle / (U_b/\delta)$ in figures 3.7(a)-3.7(c) are consistent with those shown using the mean spanwise-vertical velocity vectors. However, the criterion of based on $\langle \omega_x \rangle / (U_b/\delta)$ is advantageous in differentiating vortices of opposite rotating directions. Figures 3.7(a)-3.7(c) also show that the magnitude of $\langle \omega_x \rangle / (U_b/\delta)$ decreases near the bottom corner of the ducts as the blockage ratio increases; however,

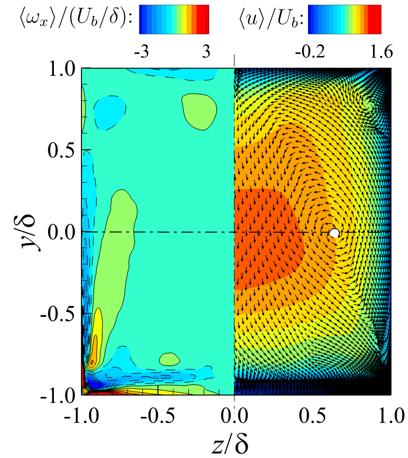

(a) $Br = 0.05$

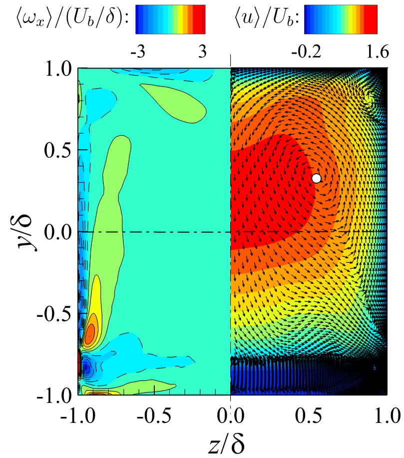

(b) $Br = 0.1$

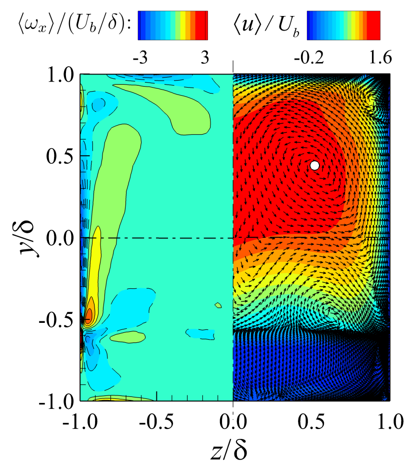

(c) $Br = 0.2$

Figure 3.7: Contours of non-dimensionalized mean streamwise vorticity $\langle\omega_x\rangle/(U_b/\delta)$ (left), and the magnitude of the non-dimensionalized mean streamwise velocity $\langle u\rangle/U_b$ superimposed with the mean spanwise-vertical velocity vectors (right) in the (y-z) plane at the relative streamwise location $x'/\delta = 0.4$ for different blockage ratios. White dots denote the center of the secondary flow vortex. The vectors are displayed at every four spanwise grid points and every three vertical points to ensure a clear view of the velocity field.

the magnitude of $\langle\omega_x\rangle/(U_b/\delta)$ in regions adjacent to the side and top walls increases monotonically with an increasing rib height. For example, in the region close to the vertical sidewall (for $-1.0 < z/\delta < -0.95$), the strength of $\langle\omega_x\rangle/(U_b/\delta)$ for the case

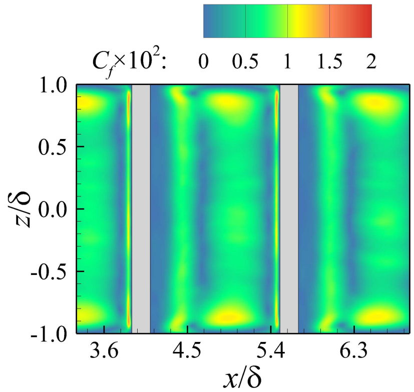

(a) $Br = 0.05$

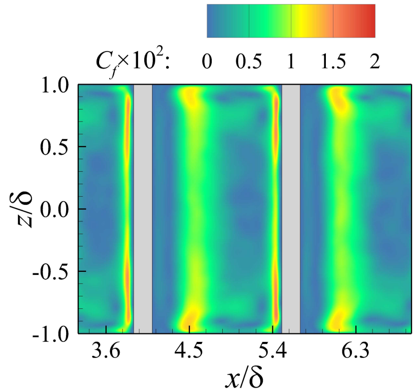

(b) $Br = 0.1$

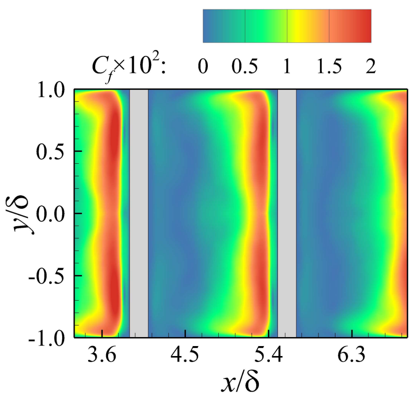

(c) $Br = 0.2$

Figure 3.8: Contours of the skin friction coefficient C_f in the (x-z) plane on the bottom wall located at $y/\delta = -1.0$ for three different rib cases.

of $Br = 0.2$ is approximately 1.7 and 1.4 times larger than those of $Br = 0.05$ and 0.1, respectively.

3.3.2 Viscous and pressure drags

To better understand the effects of rib height on the mean flow, the distributions of the skin friction and pressure coefficients are demonstrated in the (x-z) plane (located below the rib height) in figures 3.8 and 3.9, respectively. The skin friction and pressure coefficients are defined as $C_f = \tau_w/(\rho U_b^2/2)$ and $C_p = \langle p \rangle/(\rho U_b^2/2)$

respectively, where τ_w represents the local total wall friction stress calculated as $\tau_w = \mu[(\partial\langle u\rangle/\partial y)^2 + (\partial\langle w\rangle/\partial y)^2]_w^{1/2}$. Figure 3.8 clearly shows that the formed mean flow structures affect considerably the spatial distribution of the skin friction coefficient. From this figure, it is clear that the highest value of C_f occurs around the leeward and windward faces of the ribs corresponding to the cores of the recirculation bubble B and upstream vortex E, respectively (see, figure 3.4). As also shown in this figure, the effects of sidewalls on the corner vortex A and recirculation bubble B are found to be negligible in the central region (for $-0.5 < z/\delta < 0.5$), leading to a uniform spanwise distribution of C_f in this region. However, as the sidewall is approached, the value of C_f enhances significantly to reflect the boundary-layer effect near the two sideswalls of the duct (see, figure 3.7). This result is consistent with the findings of Casarsa and Arts (2005) who conducted a PIV experimental study of turbulent flow in a square duct with square rib bars (of a high blockage ratio of $Br = 0.3$) mounted on one wall in a wind tunnel.

In figure 3.9, the spatial distribution of pressure coefficient C_p for the three ribbed duct cases is plotted in the (x-z) plane located at the middle height of the rib. As is clear in this figure, the pressure drag is mostly contributed by the pressure difference between the windward and leeward faces of the rib. From figures 3.9(a)-3.9(c), it is observed that the magnitude of C_p near the windward face of the rib increases with an increasing rib height, indicating an enhanced impinging effect of the flow. The variation of the mean pressure value with the blockage ratio shown in figure 3.9 is consistent with the vortex pattern of the mean flow exhibited in figure 3.4. As the blockage ratio increases from $Br = 0.05$ to 0.1, the size of vortex E increases, which results in a stronger impinging effect on the windward rib face. However, as the Br value further increases from 0.1 to 0.2, the mechanism underlying the vortex impinging effect changes fundamentally. By comparing figures 3.4(c) with 3.4(b), it is clear that the size of vortex B (instead of vortex E) increases significantly as the blockage ratio increases from $Br = 0.1$ to 0.2, and consequently, the impinging

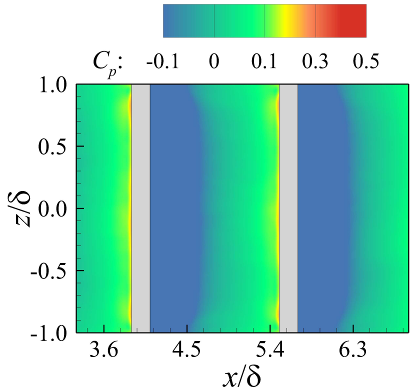

(a) $Br = 0.05$ at $y/\delta = -0.95$

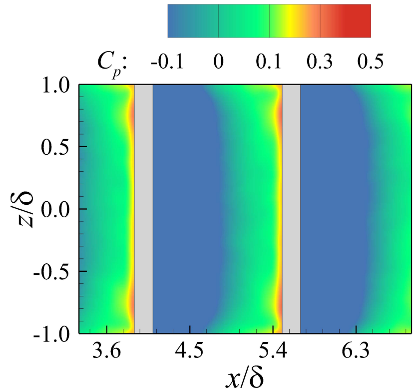

(b) $Br = 0.1$ at $y/\delta = -0.9$

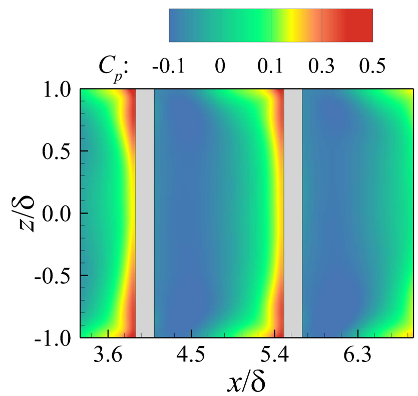

(c) $Br = 0.2$ at $y/\delta = -0.8$

Figure 3.9: Contours of the pressure coefficient C_p in the (x-z) plane at half rib height for three different rib cases.

effect of the flow on the windward face of the rib is dominated by vortex B instead of vortex E.

3.3.3 Turbulent stresses

Figure 3.10 compares the contours of "instantaneous turbulent kinetic energy" (defined as $k_t = (u'^2 + v'^2 + w'^2)/2$, following the approach of Ikeda and Durbin (2007) and Ismail et al. (2018)) in the central (x-y) plane of different rib cases. From the qualitative results shown in the figure, it is intuitive that the characteristic length

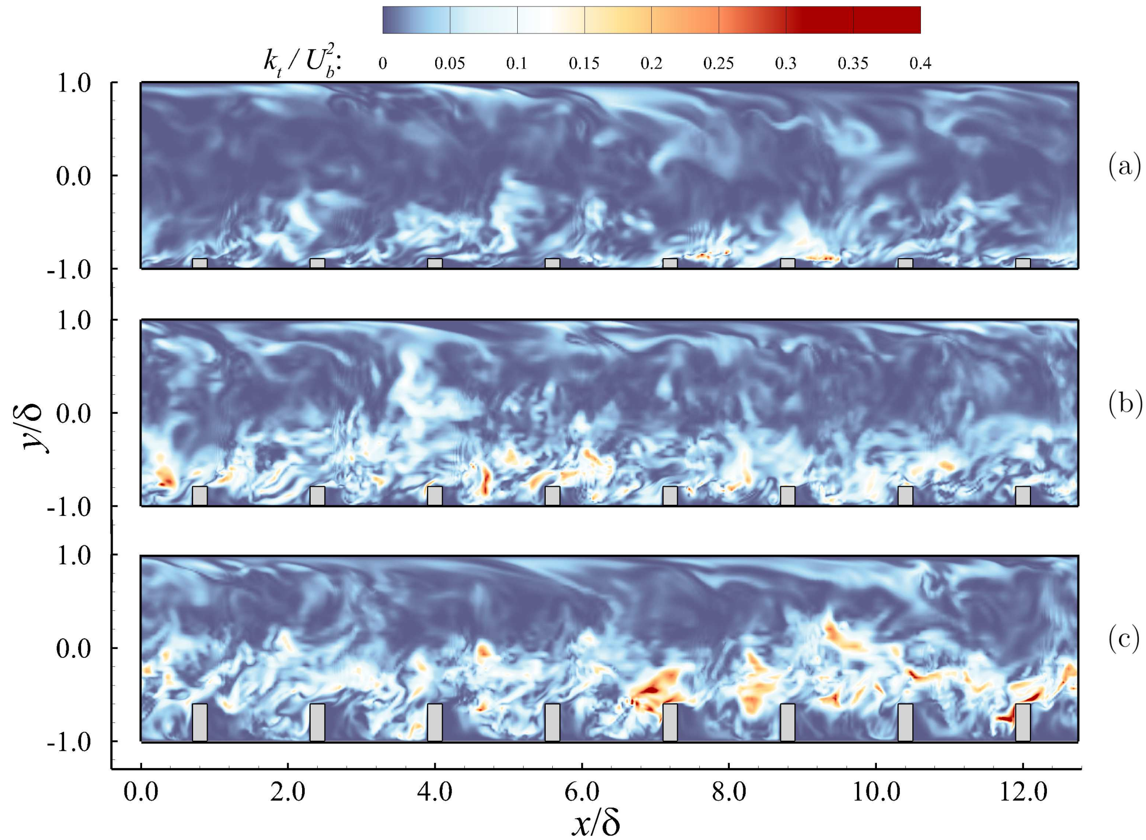

Figure 3.10: Contours of the instantaneous turbulent kinetic energy $k_t = (u'^2 + v'^2 + w'^2)/2$ (non-dimensionalized using U_b^2) in the central (x-y) plane located at $z/\delta = 0.0$ for three different rib cases. (a) $Br = 0.05$, (b) $Br = 0.1$, and (c) $Br = 0.2$.

scales of turbulence are sensitive to the rib height. From figure 3.10, it is evident that owing to the disturbances from the ribs, the magnitude of k_t in all three rib cases is greatly enhanced on the ribbed bottom wall side than on the smooth top wall side. Near the rib crest, unsteady eddies are triggered, which shed into the flow above the rib crest and then are convected downstream. From figure 3.10, it is clear that although the TKE production rate is the highest at the rib crest, the k_t value is actually low in the vicinity of the rib crest (due to the no-slip boundary condition). Owing to the strong streamwise convection, the instantaneous TKE level is typically higher downstream of the rib crest. Clearly, as the blockage ratio increases from

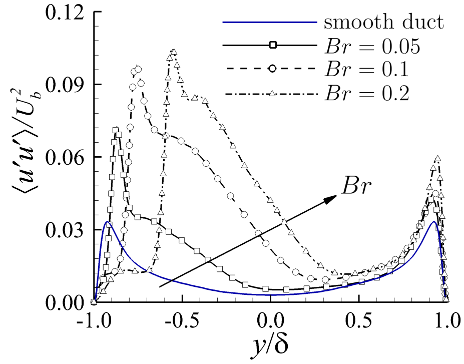

(a) Profiles of $\langle u'u' \rangle$

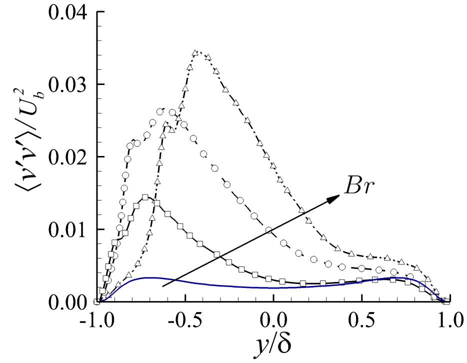

(b) Profiles of $\langle v'v' \rangle$

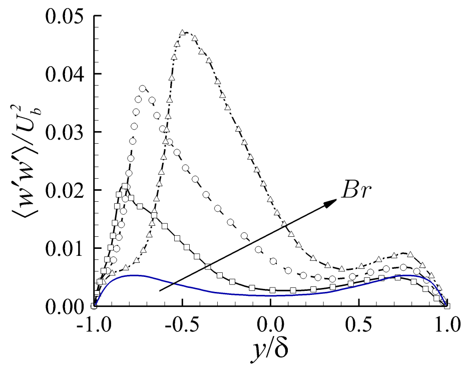

(c) Profiles of $\langle w'w' \rangle$

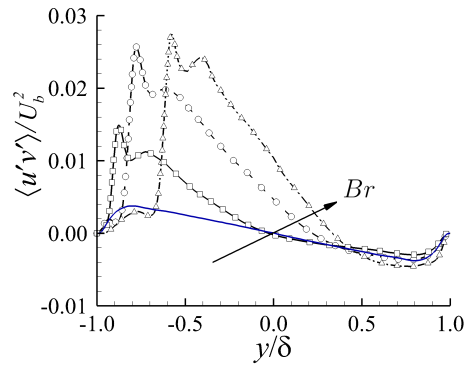

(d) Profiles of $-\langle u'v' \rangle$

Figure 3.11: Vertical profiles of Reynolds normal ($\langle u'u' \rangle$, $\langle v'v' \rangle$, and $\langle w'w' \rangle$) and shear ($-\langle u'v' \rangle$) stresses along the vertical line positioned at $(x'/\delta, z/\delta) = (0.4, 0.0)$ for three ribbed square duct flows of different blockage ratios (of $Br = 0.05$, 0.1 and 0.2), in comparison with those of the smooth duct flow.

$Br = 0.05$ to 0.2, the intensity of the spanwise vortices generated near the rib crest increases, resulting in an enhancement of local turbulent transport of momentum and energy between the ribbed bottom wall and duct center.

Figure 3.11 compares the vertical profiles of Reynolds stresses of three rib cases along the central vertical line located at $(x'/\delta, z/\delta) = (0.4, 0.0)$. The results of three rib cases are compared against that of the smooth duct in the central vertical plane located at $z/\delta = 0$. Characteristic of a smooth duct flow, the profiles of the Reynolds normal and shear stresses are symmetrical and anti-symmetrical about the duct center

($y/\delta = 0$), respectively. By contrast, the profiles of all Reynolds stress components are asymmetrical in all three rib cases due to the presence of the ribs. As is evident in figure 3.11, in general, the magnitudes of the Reynolds normal and shear stresses of the ribbed duct flows are much larger than those of the smooth duct flow due to the disturbances from the ribs. Furthermore, it is apparent the turbulence level as indicated by the magnitudes of the Reynolds normal and shear stresses are much larger on the ribbed bottom wall side than on the smooth top wall side. From figure 3.11(d), it is clear that the value of Reynolds shear stress $\langle u'v' \rangle / U_b^2$ of the three ribbed cases is comparable to that of the smooth square duct flow in the central vertical plane. However, the magnitude of $\langle u'v' \rangle / U_b^2$ is much smaller near the smooth top wall than near the ribbed bottom wall. This observation is consistent with the findings of Wang et al. (2007), Coletti et al. (2012) and Fang et al. (2015) who conducted PIV experiments of ribbed duct flows of a similar setup, and with the LES results of ribbed square duct flows of Xun and Wang (2016) and Fang et al. (2017).

For all three rib cases, the highest Reynolds stress levels occur slightly above the rib crest, where the shear effect (as indicated by the magnitude of the vertical mean velocity gradient $\partial \langle u \rangle / \partial y$, see figure 3.5) is the greatest. Specifically, for the $\langle u'u' \rangle$, $\langle w'w' \rangle$ and $-\langle u'v' \rangle$ components, their peak values on the ribbed wall side occur around $y/\delta = -0.86$, -0.76, and -0.56 for $Br = 0.05$, 0.1 and 0.2, respectively. As clearly shown in this figure, the peak values of the Reynolds normal ($\langle u'u' \rangle$, $\langle v'v' \rangle$, and $\langle w'w' \rangle$) and shear ($-\langle u'v' \rangle$) stress components are progressively enhanced near the rib crest with an increasing rib height, a feature that is fully consistent with the qualitative result shown in figure 3.10. This enhancement is mainly owing to the promotion of the shear layer strength emanating from the rib crest, which further augments the TKE production term, $-\langle u_i'u_j' \rangle \partial \langle u_i \rangle / \partial x_j$. This observation is also consistent with the DNS result of Nagano et al. (2004), who studied the effects of rib height on the turbulence statistics in a 2-D plane-channel flow. They reported that the high level of turbulence energy is attributed to large values of blockage ratios. From figures 3.11(a)-

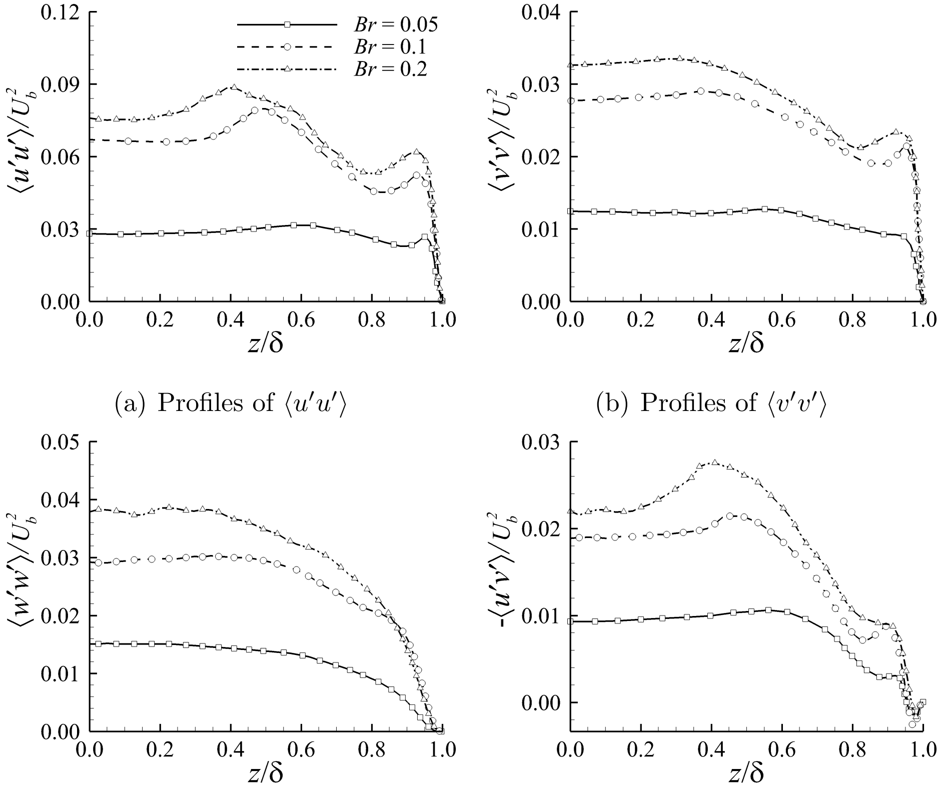

(a) Profiles of $\langle u'u' \rangle$

(b) Profiles of $\langle v'v' \rangle$

(c) Profiles of $\langle w'w' \rangle$

(d) Profiles of $-\langle u'v' \rangle$

Figure 3.12: Spanwise profiles of Reynolds normal ($\langle u'u' \rangle$, $\langle v'v' \rangle$, and $\langle w'w' \rangle$) and shear ($-\langle u'v' \rangle$) stresses along elevated lines positioned at $(x'/\delta, y/\delta) = (0.4, -0.6)$, $(0.4, -0.5)$, and $(0.4, -0.3)$ for three blockage ratios of $Br = 0.05$, 0.1 and 0.2, respectively. Given the difference in rib heights, these three positions correspond to the same relative elevation that is 0.3δ above the rib crest in each case. Owing to spanwise symmetry, only one half of the duct is plotted.

3.11(c), it is evident that the magnitudes of normal components decrease as the duct center is approached. Furthermore, it is interesting to observe that the discrepancies between the streamwise, vertical and spanwise Reynolds normal stresses near the rib crest decrease monotonically as the blockage ratio increases from $Br = 0.05$ to 0.2, leading to an enhanced degree of isotropy. As is evident in figure 3.11(d), similar to the normal components, the magnitude of the Reynolds shear stress component $-\langle u'v' \rangle$ also becomes insignificant upon approaching the duct center. Because the value of $-\langle u'v' \rangle$ is contributed by the ejection and sweep events, this indicates that the strength of these events decreases significantly in the central region, especially for $0.0 < y/\delta < 0.5$. As the smooth top wall is approached, the Reynolds normal and shear stress profiles displayed in figure 3.11 become increasingly similar to those of the classical turbulent channel flow (Kim et al., 1987). Later in subsections 3.3.6 and 3.3.7, we will refine our discussion by examining the blockage effects on the Reynolds stress anisotropy tensor and by conducting a quadrant analysis of the ejection and sweep events.

To demonstrate the 3-D effects of the ribbed duct flow, figure 3.12 compares the spanwise profiles of the Reynolds normal ($\langle u'u' \rangle$, $\langle v'v' \rangle$, and $\langle w'w' \rangle$) and shear ($-\langle u'v' \rangle$) stresses along elevated lines positioned at $(x'/\delta, y/\delta) = (0.4, -0.6)$, $(0.4, -0.5)$, and $(0.4, -0.3)$ for three blockage ratios of $Br = 0.05, 0.1$ and 0.2, respectively. Given the different heights of ribs in the three test cases, these three positions are all at the same relative elevation that is 0.3δ (or, $0.15D$) above the rib crest in each case. As shown in figure 3.12, the maximum intensity of $\langle u'u' \rangle$ occurs in a region between the sidewall and center of the duct (e.g., for the $Br = 0.2$ case, the profile peaks at $z/\delta \approx \pm 0.4$). Furthermore, it is seen that the peak position of $\langle u'u' \rangle$ shifts towards the duct center as the rib height increases, a pattern that is consistent with the qualitative results shown in figure 3.10. As is clearly seen from figure 3.12(a)-3.12(c), for the three rib cases tested, the magnitude of $\langle u'u' \rangle$ is much larger than those of $\langle v'v' \rangle$ and $\langle w'w' \rangle$, making the largest contribution to the value of TKE among the three Reynolds normal stress components. Figure 3.12(d) displays the spanwise profile of the Reynolds shear stress $-\langle u'v' \rangle$, which exhibits a similar trend to that for the streamwise Reynolds normal stress $\langle u'u' \rangle$. Owing to the cross-stream secondary flow motion, the profile of $-\langle u'v' \rangle$ peaks in the region between the sidewall and duct center. Also, as is evident from figure 3.12, at the same elevation relative to the rib crest, the magnitude of $-\langle u'v' \rangle$ increases with the increase of blockage ratio. In fact, from figures 3.11 and 3.12, it is clear that the turbulence level as indicated by the magnitudes of Reynolds normal and shear stresses all increase monotonically as the rib height increases in the central region of the duct.

3.3.4 Effect of rib height on non-equilibrium turbulence

To further understand the impact of the rib height on the turbulence statistics discussed in subsection 3.3.3, the vertical profiles of the TKE production rate, $P_k = -\langle u_i' u_j' \rangle \partial \langle u_i \rangle / \partial x_j$, dissipation rate, $\varepsilon_k = \nu \langle \partial u_i' / \partial x_j \partial u_i' / \partial x_j \rangle$, and their ratio, P_k/ε_k, are plotted in figure 3.13 along the same central vertical line as for displaying Reynolds stress profiles in figure 3.11. From figures 3.13(a) and 3.13(b), it is clear the production rate P_k and dissipation rate ε_k are significantly higher on the ribbed wall side than on the smooth top wall side in all three test cases. The high TKE production and dissipation rates on the ribbed side of the duct are indeed characteristics of this rib-roughened 3-D duct flow, which features strong secondary flows that facilitate transport of TKE in the cross-stream directions. Similar observations were noted by Hirota et al. (1992), who conducted LDV measurements of turbulent flows in a square duct with ribs mounted on one wall. Both P_k and ε_k peak around the rib crest, and their magnitude increases monotonically with the Br value. The appearance of this TKE production peak is due to the strong shear layer formed immediately above the rib crest, where the level of the mean spanwise vorticity (i.e., $\langle \omega_z \rangle = \partial \langle v \rangle / \partial x - \partial \langle u \rangle / \partial y$) is significantly augmented. This peak of P_k coincides with that in the Reynolds stress profiles shown previously in figure 3.11. Furthermore, the presence of ribs in the duct imposes significant inhomogeneities on the turbulence field such that the TKE production rate P_k is not balanced by its dissipation rate ε_k (i.e., $P_k/\varepsilon_k \neq 1$). Figure 3.13(c) compares the ratio of the production to dissipation of TKE along the vertical line located at $(x'/\delta, z/\delta) = (0.4, 0.0)$ for the three different rib cases. As shown in this figure, the maximum value of P_k/ε_k occurs slightly above the rib crest, creating a zone of strong non-equilibrium turbulence. Furthermore, as shown in figure 3.13(c), as the rib height increases, the degree of non-equilibrium as

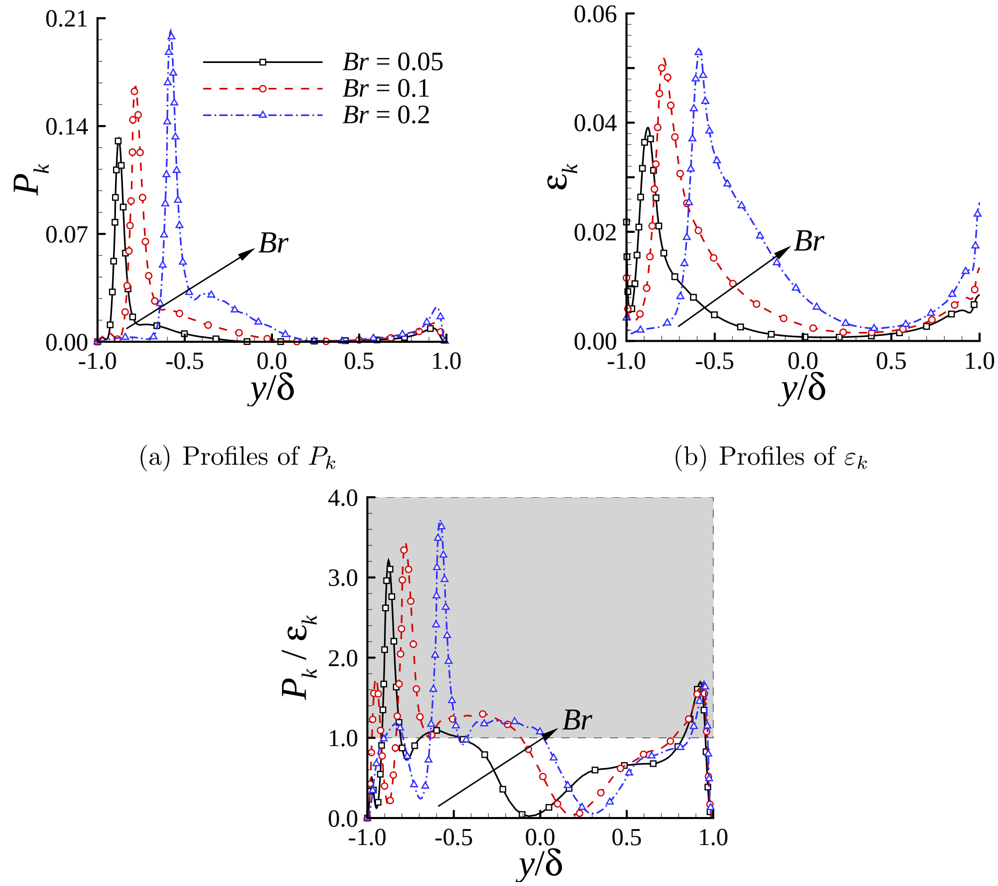

(a) Profiles of P_k

(b) Profiles of ε_k

(c) Profiles of P_k/ε_k

Figure 3.13: Vertical profiles of the TKE production term (P_k), dissipation term (ε_k), and their ratio (P_k/ε_k) along the central vertical line located at $(x'/\delta, z/\delta) = (0.4, 0.0)$ for different blockage ratios. The values of P_k and ε_k are non-dimensionalized using the duct half-height, δ, and bulk velocity, U_b. The gray area shown in panel (c) pertains to the non-equilibrium region in which $P_k/\varepsilon_k > 1$.

indicated by the peak value of P_k/ε_k increases on the ribbed bottom wall side, but remains invariant on the smooth top wall side. Specifically, close to the rib crest, the rib case with $Br = 0.2$ exhibits a maximum value of P_k/ε_k that is approximately 16% and 9% higher than those of $Br = 0.05$ and 0.1, respectively. Figure 3.13(c) also indicates that in all three rib cases, the magnitude of P_k/ε_k decreases significantly upon approaching the duct center where P_k/ε_k almost vanishes. This reduction is

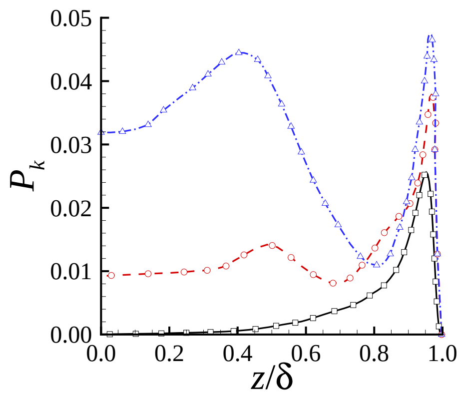

(a) Profiles of P_k

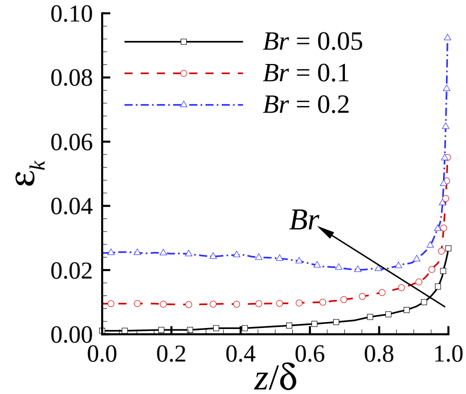

(b) Profiles of ε_k

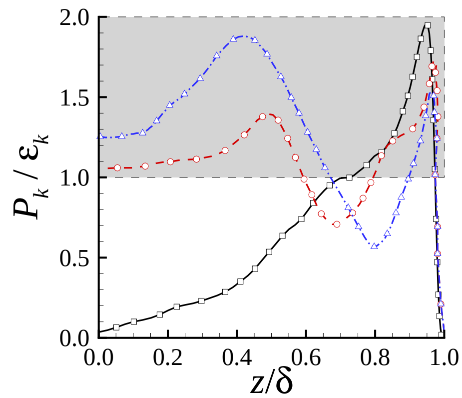

(c) Profiles of P_k/ε_k

Figure 3.14: Spanwise profiles of the TKE production term (P_k), dissipation term (ε_k), and their ratio (P_k/ε_k) along elevated lines positioned at $(x'/\delta, y/\delta) = (0.4, -0.6)$, $(0.4,\ -0.5)$, and $(0.4,\ -0.3)$ for three blockage ratios of $Br = 0.05, 0.1$ and 0.2, respectively. Given the difference in rib heights, these three positions correspond to the same relative elevation that is 0.3δ above the rib crest in each case. Owing to spanwise symmetry, only one half of the duct is plotted. The values of P_k and ε_k are non-dimensionalized using the duct half-height, δ, and bulk velocity, U_b. The gray area shown in panel (c) pertains to the non-equilibrium region in which $P_k/\varepsilon_k > 1$.

ultimately attributed to the more rapid decrease in the value of P_k compared to the decrease in the value of ε_k in central regions well above the ribs and below the top smooth wall.

Figure 3.14 compares the spanwise profiles of P_k, ε_k, and P_k/ε_k for the three rib cases. As is clear in figure 3.14(a), the profile of P_k exhibits two distinct peaks, one near the sidewall and one distant from the sidewall at about $z/\delta = 0.4$. These two peaks reflect the wall-anisotropic effect and the occurrence of the secondary flow pattern in the cross-stream direction demonstrated previously figure 3.7, respectively. Consistent with the pattern shown in figures 3.12(a) and 3.12(d), turbulence of high-level TKE and TKE production rate is convected towards the ribbed wall due to the increasingly stronger secondary flow as the blockage ratio increases from $Br = 0.05$ to 0.2. By contrast, as shown in figure 3.14(b), although the magnitude of the dissipation rate ε_k increases as the Br value increases, it is less sensitive to the rib height, especially in the central region of the channel. Consequently, the profile of P_k/ε_k displayed in figure 3.14(c) exhibits a similar trend to that of P_k. From figure 3.14(c), it is also seen that the value of P_k/ε deviates from unity on most occasions at all three rib cases, which is a clear indication of non-equilibrium turbulence characteristic of a ribbed duct flow.

3.3.5 Effect of rib height on TKE budget

To further understand the rib effects on turbulence energy transfer in the vertical direction, the transport equation of TKE (defined as $k = \langle u_i'u_i'\rangle/2$) for a statistically stationary flow can be studied, which reads

$$\underbrace{\langle u_j\rangle\frac{\partial k}{\partial x_j}}_{C_k} = \underbrace{-\frac{1}{\rho}\frac{\partial\langle p'u_j'\rangle}{\partial x_j}}_{\Pi_k} \underbrace{-\frac{1}{2}\frac{\partial\langle u_i'u_i'u_j'\rangle}{\partial x_j}}_{T_k} + \underbrace{\nu\frac{\partial^2 k}{\partial x_j^2}}_{D_k} \underbrace{-\langle u_i'u_j'\rangle\frac{\partial\langle u_i\rangle}{\partial x_j}}_{P_k} \underbrace{-\nu\langle\frac{\partial u_i'}{\partial x_j}\frac{\partial u_i'}{\partial x_j}\rangle}_{\varepsilon_k} \quad , \tag{3.4}$$

where C_k, Π_k, T_k, and D_k represent the convection, pressure diffusion, turbulent diffusion and viscous diffusion, respectively. Figure 3.15 shows the vertical profiles of the budget terms of TKE along the central vertical line positioned at $(x'/\delta, z/\delta) = (0.4, 0.0)$ for the smooth duct case and all three rib cases. The profiles of the TKE budget terms of the smooth square duct flow are plotted in figure 3.15(a), which shows that the budget balance of TKE is dominated by viscous diffusion T_k and viscous

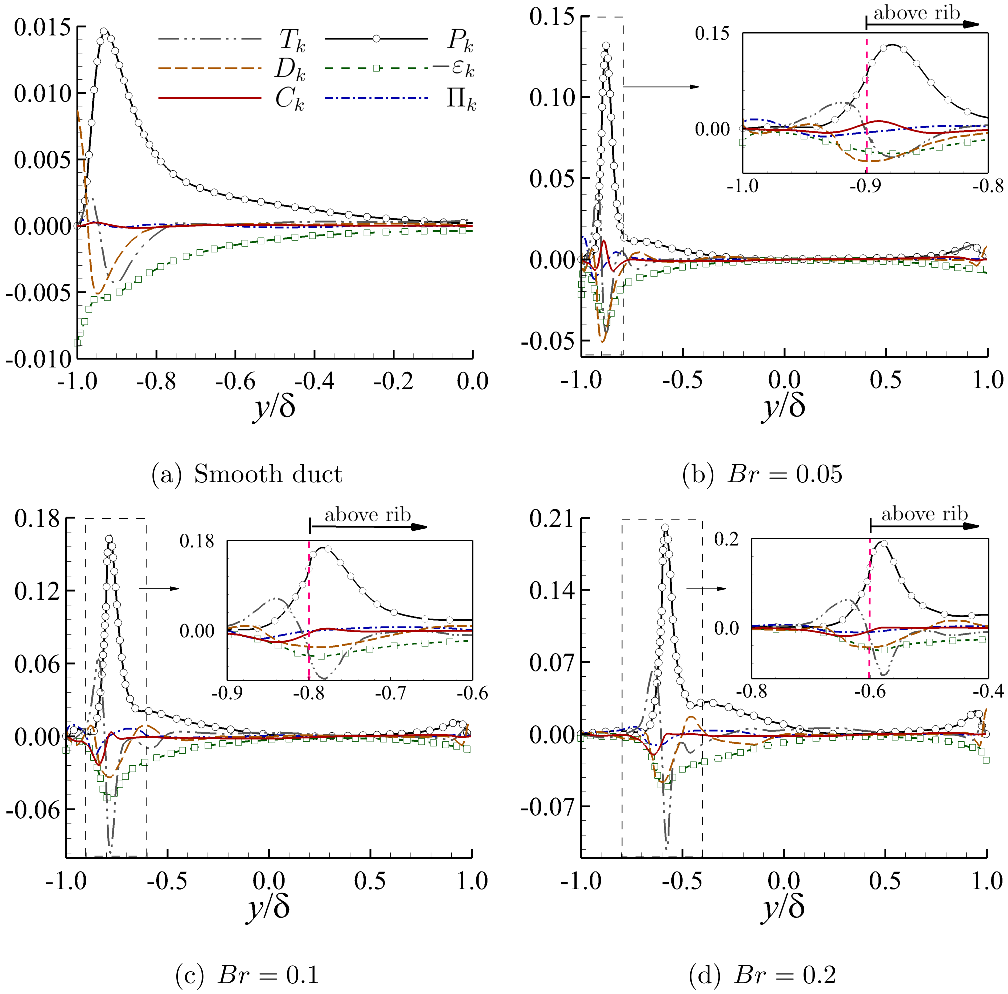

(a) Smooth duct

(b) $Br = 0.05$

(c) $Br = 0.1$

(d) $Br = 0.2$

Figure 3.15: Vertical profiles of budget terms of the TKE transport equation along the vertical line positioned at $(x'/\delta, z/\delta) = (0.4, 0.0)$ for the smooth duct flow and three ribbed duct flows of different blockage ratios. The budget terms are non-dimensionalized using the duct half-height, δ, and bulk velocity, U_b. In panel (a), for the smooth duct case, only one-half the duct is plotted due to vertical symmetry. For the three rib duct cases, in order to show clearly the profiles of the budget terms around the rib crest, they are partially enlarged and replotted in inset graphs in panels (b)-(d). The vertical pink dashed line demarcates the rib crest in inset graphs.

dissipation ε_k in the vicinity of the wall as the source and sink terms, respectively. The turbulent diffusion term T_k is zero at the wall, becomes positively-valued in the vicinity of the wall (for $y/\delta < -0.95$), and then changes its sign and reaches its negatively-valued peak at $y/\delta = -0.9$. At this elevation $y/\delta = -0.9$, the primary source of TKE is the production term P_k, which is mainly balanced by three sinks, i.e., viscous dissipation ε, viscous diffusion D_k, and turbulent diffusion T_k. As the duct center is approached, the magnitudes of all budget terms diminish, although the balance is primarily between P_k and ε (which are almost mirror images of each other). The characteristics of the TKE budget terms analyzed here are consistent with those of Vinuesa et al. (2014), who conducted DNS study of duct flows at a similar Reynolds number.

By comparing figures 3.15(b)-3.15(d) with figure 3.15(a), it is apparent that the budget balances of the three rib cases exhibit more complex patterns than that of the smooth duct flow, especially around the rib crest. Furthermore, owing to the fact the vertical profiles of the budget terms are asymmetrical in the vertical direction due to the presence of ribs, the entire vertical profiles between the ribbed and smooth walls need to be plotted in figures 3.15(b)-3.15(d). In comparison with the smooth duct flow, the dominant source term is still the production term P_k, which peaks at a position that is slightly above rib crest in all three rib cases (as shown in the inset graphs). By comparing figures 3.15(b)-3.15(d), it is seen that the magnitudes of the three sinks (D_k, T_k and ε) around the rib crest are comparable at $Br = 0.05$; however, the turbulent diffusion term T_k becomes increasingly dominant as the blockage ratio increases to $Br = 0.1$ and 0.2. By comparing the three rib cases with the smooth duct case, it is observed that the convection of TKE by the mean flow is vanishingly small as the convention term C_k does not make a remarkable contribution to the budget balance of TKE in the smooth duct flow. By contrast, as shown in figures 3.15(b)-3.15(d), the effect of the convection term C_k becomes more pronounced due to the complex mean flow pattern and high TKE level around the rib crest in all three rib cases. From figures 3.15(b)-3.15(d), it is clear that the magnitudes of the budget terms are much larger on the ribbed bottom wall side than on the smooth top wall side. A careful perusal of figures 3.15(b)-3.15(d) further indicates that the profile patterns of the budget terms on the smooth top wall side are, actually, similar to those of the smooth duct flow shown in figure 3.15(a).

3.3.6 Effect of rib height on turbulence anisotropy

The effects of rib height on turbulence anisotropy can be studied through the Reynolds stress anisotropy tensor, defined as (Pope, 2000)

$$b_{ij} = \frac{\langle u_i' u_j' \rangle}{\langle u_k' u_k' \rangle} - \frac{1}{3}\delta_{ij} \quad . \tag{3.5}$$

Previous studies of turbulence anisotropy in 2-D turbulent plane-channel flows with surface-mounted perpendicular ribs (Krogstad and Antonia, 1994; Keirsbulck et al., 2002; Krogstad et al., 2005) showed that the anisotropic states of turbulence become less apparent near the rough wall. However, Mazouz et al. (1998) showed that the degree of anisotropy enhances with the use of k-type surface roughness in a 3-D duct flow. These results indicate that turbulence anisotropy varies with not only roughness configurations but also the 2-D or 3-D flow conditions. The profiles of the Reynolds stress anisotropy tensor components (b_{11}, b_{22}, b_{33} and b_{12}) are plotted in figure 3.16 for all three rib cases along the central vertical line positioned at $(x'/\delta, z/\delta) = (0.4, 0.0)$. To facilitate our study of the rib height effect on the flows, the position of the rib crest is demarcated using a vertical dashed line in figure 3.16 for each rib case. By comparing figures 3.16(a)-3.16(c), it is observed that the value of b_{11} is larger than those of b_{22} and b_{33} in the region between the rib crest and the smooth top wall ($y/\delta = 1.0$), which is a clear indication of turbulence anisotropy. From figure 3.16(a), it is evident that the value of b_{11} peaks immediately above the rib crest whose magnitude decreases monotonically as the blockage ratio increases from $Br = 0.05$ to 0.2. Because the value of b_{11} is larger than those of b_{22} and b_{33} in the region immediately above the rib crest, a reduction in the peak value of b_{11} with Br reduces the degree of turbulence anisotropy. This can be further understood from figures 3.10 and 3.11, which show that as the rib height increases, the strength of

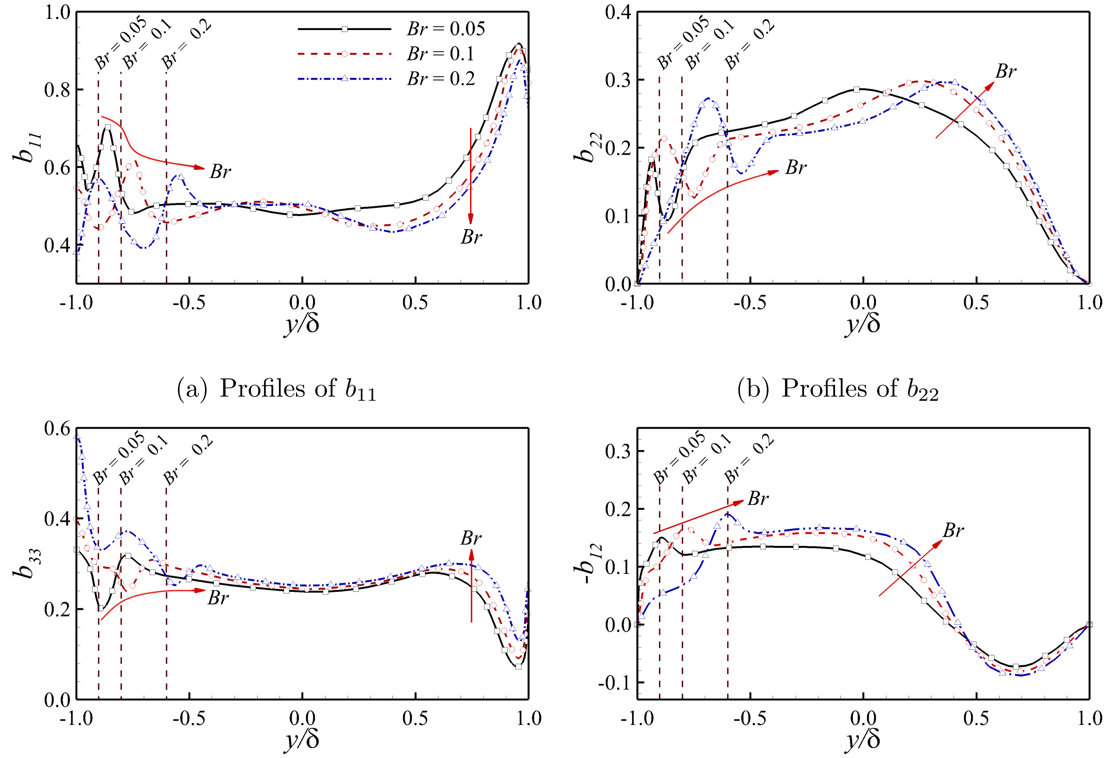

(a) Profiles of b_{11}

(b) Profiles of b_{22}

(c) Profiles of b_{33}

(d) Profiles of $-b_{12}$

Figure 3.16: Vertical profiles of Reynolds stress anisotropy tensor components (b_{11}, b_{22}, b_{33} and b_{12}) along the central vertical line positioned at $(x'/\delta, z/\delta) = (0.4, 0.0)$ for different blockage ratios. The vertical dashed lines demarcate the rib crests for test cases of $Br = 0.05$, 0.1 and 0.2. The red arrow shows the trend how the value of b_{ii} varies monotonically with an increasing Br value.

induced disturbances by the rib elements increases, making turbulence more isotropic. From figure 3.16(a), it is seen that the magnitude of b_{11} reaches its maximum near the smooth top wall ($y/\delta = 1.0$) in all the three rib cases. This is consistent with the observation of the near-wall peak value of $\langle u'u' \rangle$ on the smooth top wall side shown previously in figure 3.11(a). The wall-anisotropy as represented by the peak values of b_{11} and $\langle u'u' \rangle$ near the smooth top wall is similar to those of a smooth plane-channel flow observed by Kim et al. (1987) and Lamballais et al. (1997).

From figures 3.16(a)-3.16(c), it is clear that on the smooth top wall side, the value of b_{11} decreases monotonically with an increasing value of Br; however, those of b_{22} and b_{33} increase monotonically. These trends reflect the fact that as the rib height increases, the flow becomes more disturbed by the rib elements. The highly disturbed turbulence generated around the rib crest spreads to the smooth top wall side of the duct through mechanisms such as vortex shedding and secondary flows. As such, TKE is more evenly distributed among the three normal components, which leads to a decrease in the degree of turbulence anisotropy. From figure 3.16(d), it is observed that similar to the trends of b_{22} and b_{33}, the value of $-b_{12}$ increases monotonically as the rib height increases from $Br = 0.05$ to 0.2 in the region immediately above the rib crest. This phenomenon is strongly associated with the enhanced strength of the shear layer developed over the rib crest.

In order to study the effect of rib height on small-scale turbulence anisotropy, the following anisotropy tensor of the dissipation rate can be calculated (Speziale and Gatski, 1997)

$$d_{ij} = \frac{\varepsilon_{ij}}{2\varepsilon_k} - \frac{1}{3}\delta_{ij} \quad , \tag{3.6}$$

where ε_{ij} represents the dissipation tensor, defined as

$$\varepsilon_{ij} = 2\nu \left\langle \frac{\partial u_i'}{\partial x_k} \frac{\partial u_j'}{\partial x_k} \right\rangle \quad . \tag{3.7}$$

Figure 3.17 displays the vertical profiles of the dissipation anisotropy tensor components (d_{11}, d_{22}, d_{33} and d_{12}) along the central vertical line positioned at $(x'/\delta, z/\delta) = (0.4, 0.0)$. From figure 3.17(a), it is clear that for all three rib cases, the magnitude of d_{11} peaks around the rib crest, which decreases monotonically as the rib height increases. By comparing figures 3.17 and 3.16, it is observed that the profiles of d_{ij} feature a similar shape to that of b_{ij}, especially in terms of their peak positions around the rib crest and trends on the smooth top wall side. This is not surprising from the point of view of energy conservation, as the strength of the local TKE dissipation rate is often consistent with that of local TKE and TKE production rate. In fact, from the

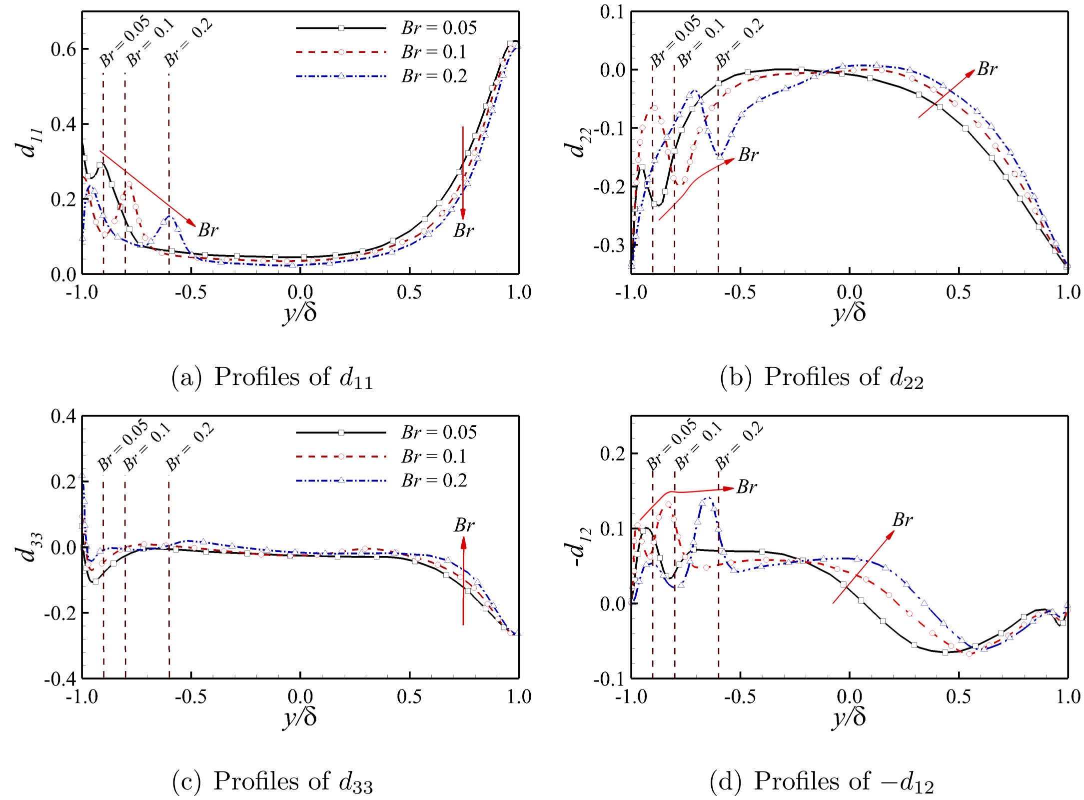

Figure 3.17: Vertical profiles of the anisotropy of the Reynolds stress dissipation rate (d_{11}, d_{22}, d_{33} and d_{12}) tensors along the central vertical line positioned at $(x'/\delta, z/\delta) = (0.4, 0.0)$ for different blockage ratios. The vertical dashed lines demarcate the rib crests for test cases of $Br = 0.05$, 0.1 and 0.2. The red arrow shows the trend how the value of d_{ii} varies monotonically with an increasing Br value.

point view of spectral analysis, the TKE dissipation rate is dominated by small scales of turbulence, and by contrast, the magnitude of Reynolds stresses is dominated by relatively large scales characteristic of the most energetic eddies. Therefore, a similar pattern between b_{ij} and d_{ij} indicates that the rib elements in the square duct have a profound influence on both the small- and large-scale structures in terms of their reflections of the degree of local turbulence anisotropy. From figures 3.17(a)-3.17(c), it is seen that the magnitude of d_{11} is larger than those of d_{22} and d_{33} around the rib crest. Furthermore, from figures 3.17(a) and 3.17(b), it is evident that as the Br value increases, the peak value around the rib crest decreases monotonically for

d_{11} but increases monotonically for d_{22}. This helps to reduce the differences between the magnitudes of d_{11}, d_{22} and d_{33}, and therefore, reducing the degree of turbulence anisotropy. From figures 3.17(a)-3.17(c), it is interesting to observe that the magnitudes of the normal components of the dissipation anisotropy tensor, d_{11}, d_{22} and d_{33}, are close to zero in the duct center for $-0.5 < y/\delta < 0.5$. By contrast, as shown in figures 3.16(a)-3.16(c), the values of the normal components of the Reynolds stress anisotropy tensor, b_{11}, b_{22} and b_{33} deviate apparently from zero in the same region. This indicates that small-scale structures exhibit a stronger "return to isotropy" tendency compared to the large-scales in the duct center. As is clear from figure 3.17(d), similar to the trend of $-b_{12}$ shown in figure 3.16(d), the anisotropy of the dissipation rate tensor component $-d_{12}$ peaks around the rib crest for all three Br numbers tested. Furthermore, the peak value increases monotonically as the rib aspect ratio increases from $Br = 0.05$ to 0.2, suggesting an increase of TKE dissipation at small scales due to the shear layer generated by the rib elements.

3.3.7 Third-order moments of velocity fluctuations and quadrant analysis

It is well-established (Andreopoulos and Bradshaw, 1981; Krogstad and Antonia, 1999; Hurther et al., 2007) that turbulent transport of TKE can be better elucidated by examining velocity triple correlations as compared to the second-order statistical moments. For instance, Hurther et al. (2007) measured TKE fluxes in a rough wall open channel flow using an acoustic Doppler velocity profiler (ADVP). They reported that high-order statistical moments of the flow are highly sensitive to the wall roughness in both the inner and outer regions of the boundary layer, and the difference between the production and dissipation rates in the rough-wall region is responsible for the intensification of TKE fluxes. In this part of the study, our attention is paid to the influence of rib height on the third-order statistics and the crossing point between

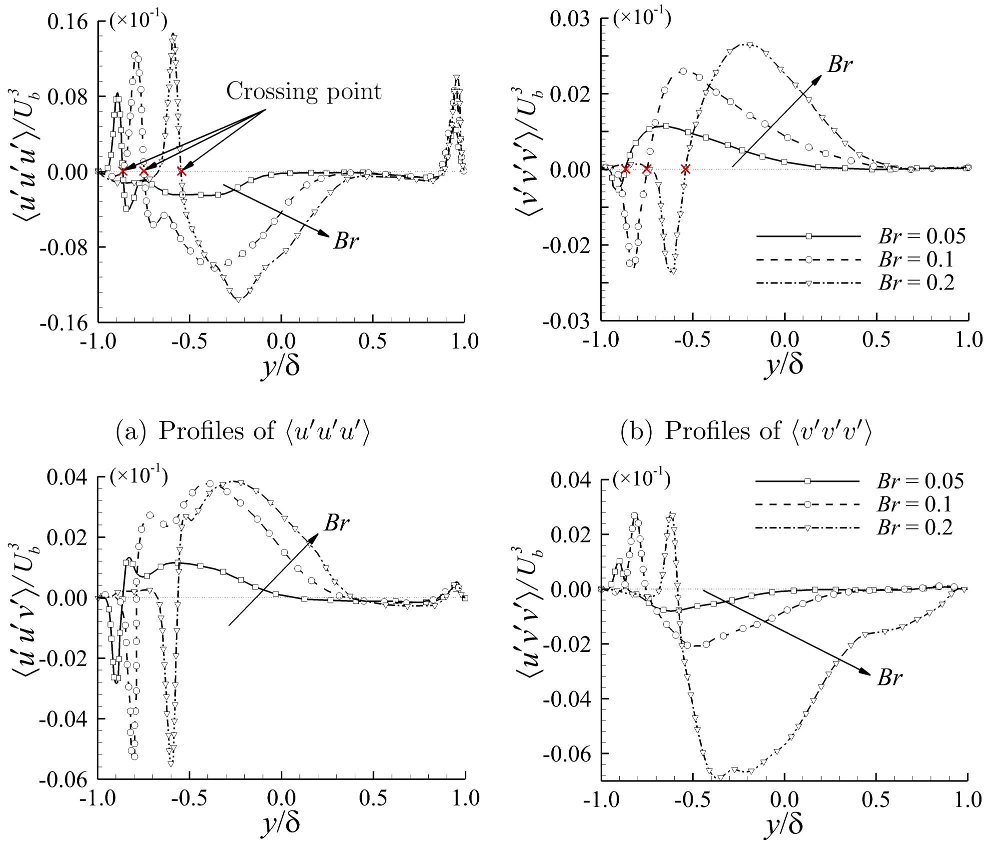

(a) Profiles of $\langle u'u'u' \rangle$ (b) Profiles of $\langle v'v'v' \rangle$

(c) Profiles of $\langle u'u'v' \rangle$ (d) Profiles of $\langle u'v'v' \rangle$

Figure 3.18: Vertical profiles of $\langle u'u'u' \rangle$, $\langle v'v'v' \rangle$, $\langle u'u'v' \rangle$, and $\langle u'v'v' \rangle$ along the central vertical line positioned at $(x'/\delta, z/\delta) = (0.4, 0.0)$ for different blockage ratios. The crossing points are marked using red cross symbol '$\times$', where $\langle u'u'u' \rangle = 0$ and $\langle v'v'v' \rangle = 0$ (in particular, when the sign of $\langle u'u'u' \rangle$ changes from positive to negative and the sign of $\langle v'v'v' \rangle$ changes from negative to positive). The crossing point occurs at elevation $y/\delta = -0.88$, -0.78 and -0.58 for $Br = 0.05$, 0.1 and 0.2, respectively.

ejections and sweeps, where the signs of $\langle u'u'u' \rangle$ and $\langle v'v'v' \rangle$ change in the vertical direction.

In figure 3.18, the non-dimensional vertical profiles of fluctuating velocity triple product components $\langle u'u'u' \rangle/U_b^3$, $\langle v'v'v' \rangle/U_b^3$, $\langle u'u'v' \rangle/U_b^3$, and $\langle u'v'v' \rangle/U_b^3$ are plotted along the central vertical line located at $(x'/\delta, z/\delta) = (0.4, 0.0)$ for three rib cases. Figures 3.18(a) and 3.18(b) show the progressive enhancement of both $\langle u'u'u' \rangle$ and

$\langle v'v'v' \rangle$ in the vicinity of the rib crest as the rib height increases. This enhancement of triple correlations results in a delayed appearance of the crossing point in the sense that it occurs at a higher elevation as the rib height increases. In figures 3.18(a) and 3.18(b), the crossing points are marked using red cross symbol '$\times$', where $\langle u'u'u' \rangle = 0$ and $\langle v'v'v' \rangle = 0$ (in particular, where the sign of $\langle u'u'u' \rangle$ changes from positive to negative and the sign of $\langle v'v'v' \rangle$ changes from negative to positive). The crossing point occurs at elevations of $y/\delta = -0.88$, -0.78 and -0.58 for $Br = 0.05$, 0.1 and 0.2, respectively. In the region near the rib crest below the crossing point, positive-valued peaks of $\langle u'u'u' \rangle$ clearly demonstrate the occurrence of high-speed streaks, which are reinforced as the rib height increases. Furthermore, as seen in figures 3.18(a) and 3.18(b), the values of $\langle u'u'u' \rangle$ and $\langle v'v'v' \rangle$ are positive and negative near the rib crest, respectively, which clearly indicate that the turbulent flow is strongly influenced by the flapping motions of the shear layer, leading to enhanced sweeping activities. In consequence, a considerable amount of high momentum fluid is swept into the inter-rib region (below the rib height). By contrast, in the region above the crossing point, the trends of $\langle u'u'u' \rangle$ and $\langle v'v'v' \rangle$ are entirely opposite, and an enhancement of the ejection mechanism is observed. This results in enhanced transport of low-momentum fluids towards the upper half of the duct due to the existence of local spanwise swirling motions. This observation is consistent with the results of Keirsbulck et al. (2002) who studied the 2-D turbulent boundary layer over a k-type rough wall using PIV measurements. Because $\langle u'u'v' \rangle$ and $\langle u'v'v' \rangle$ dominate the other turbulent diffusion terms, only the vertical turbulent transports of $\langle u'u' \rangle$ and $\langle u'v' \rangle$ (embodied by the profiles of $\langle u'u'v' \rangle$ and $\langle u'v'v' \rangle$) are shown in figures 3.18(c) and 3.18(d), respectively. As shown in figure 3.18(c), $\langle u'u'v' \rangle$ is negatively valued below the crossing point. Therefore, there exists a strong turbulent diffusion of energy (or, vertical flux of $\langle u'u' \rangle$) towards the bottom wall near the rib crest with a streamwise acceleration (owing to the positive sign of $\langle u'u'u' \rangle$). By contrast, above the crossing point, the sign of $\langle u'u'v' \rangle$ switches from negative to positive, indicating the turbulent diffusion

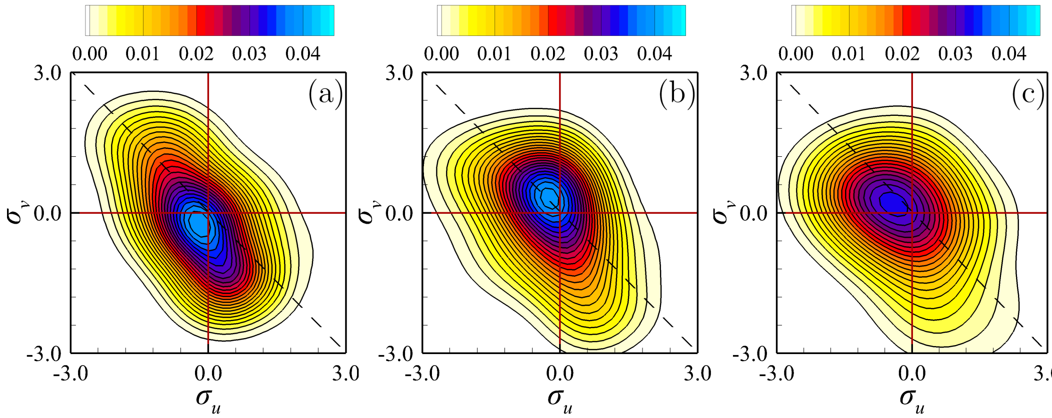

Figure 3.19: Contours of JPDF of σ_u and σ_v of the smooth square duct flow at three elevated points along the central vertical line located at $z/\delta = 0.0$. Corresponding to panels (a), (b) and (c), the elevation is $y/\delta = -0.95$, -0.9 and -0.8, respectively.

is outwards with a streamwise deceleration due to the negative values of $\langle u'u'u' \rangle$. On the opposite trend of $\langle u'u'v' \rangle$, figure 3.18(d) shows that the magnitude of $\langle u'v'v' \rangle$ increases and a positively-valued peak occurs near the rib crest due to enhanced sweep motions. However, the value of $\langle u'v'v' \rangle$ switches its sign from positive to negative in the region above the rib crest, associated with a strong outward flux of $\langle u'v' \rangle$ due to enhanced ejection motions.

To further understand the effects of rib height on Reynolds stresses, the JPDF of $\sigma_u = u'/u_{rms}$ and $\sigma_v = v'/v_{rms}$ is calculated in the central vertical line located at $(x'/\delta, z/\delta) = (0.4, 0.0)$. The JPDF of σ_u and σ_v for the smooth duct flow is used as a baseline comparison case, which is shown in figure 3.19, and those of the three ribbed duct flows are displayed in figure 3.20. Three different elevations (of $y/\delta = -0.95$, -0.9 and -0.8) are compared for each case of the smooth and ribbed duct flows. The choice of these three elevations of the smooth duct is not arbitrary, as they correspond to the mid height of the rib in three ribbed ducts of $Br = 0.05$, 0.1 and 0.2. From figure 3.19, it is seen that the streamwise velocity fluctuations synchronize well with the vertical velocity fluctuations in all three elevations, as the plotted JPDF patterns exhibit a tendency to be aligned approximately at 135° throughout quadrants II and

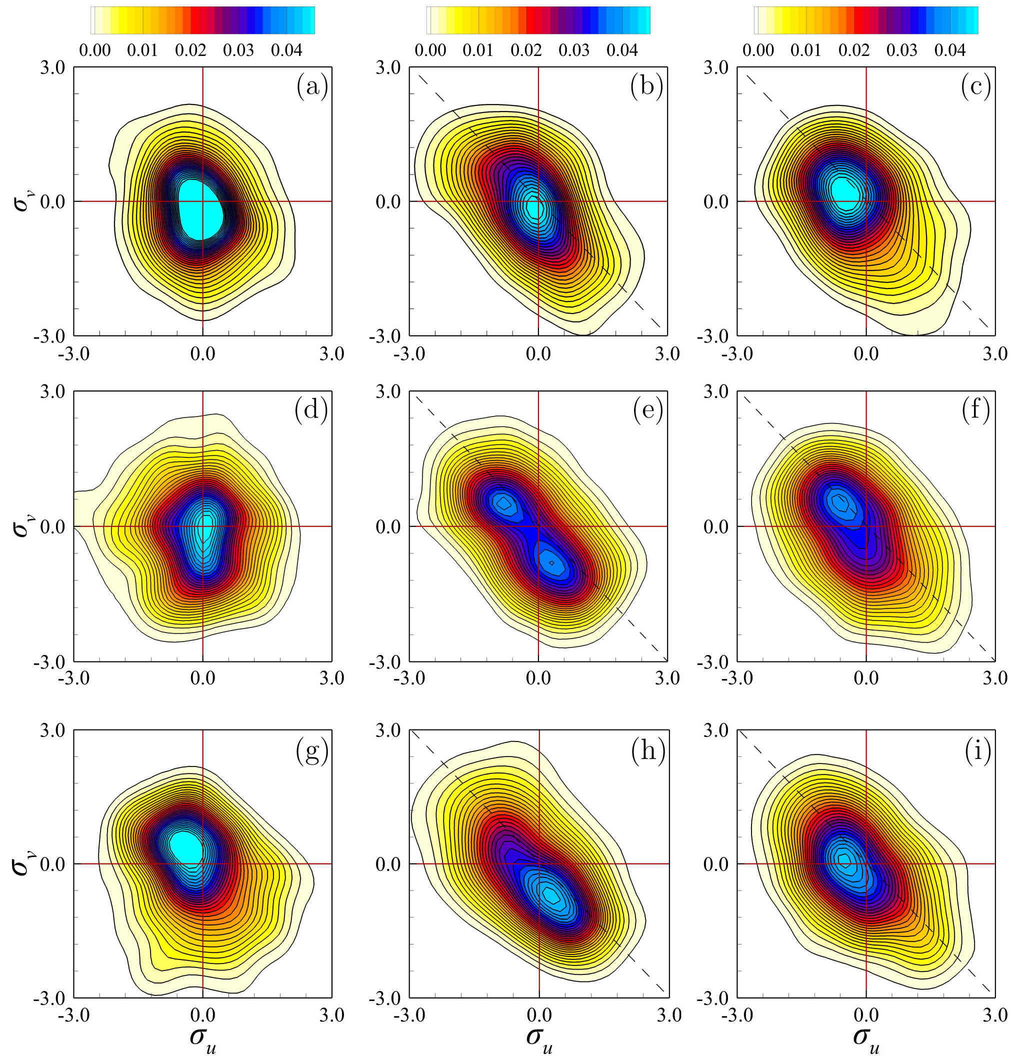

Figure 3.20: Contours of JPDF of σ_u and σ_v at three elevated points along the central vertical line located at $(x'/\delta, z/\delta) = (0.4, 0.0)$ for three different blockage ratios. The elevated points are located at the mid height of the rib, immediately above the rib crest, and above the crossing point for each test case of a specific blockage ratio. In panels (a), (b) and (c), the elevation is $y/\delta = -0.95$, -0.86, -0.4 for $Br = 0.05$; in panels (d), (e) and (f), the elevation is $y/\delta = -0.9$, -0.76, -0.4 for $Br = 0.1$; and in panels (g), (h) and (i), the elevation is $y/\delta = -0.8$, -0.56, -0.4 for $Br = 0.2$.

IV (i.e., "Q2" and "Q4", respectively). This indicates a preference for the ejection events (featuring $u' < 0$ and $v' > 0$ associated with Q2) and sweeping events (featuring $u' > 0$ and $v' < 0$ associated with Q4) at all three elevations near the bottom wall. The explanation for this preference is a well-known conclusion of the classical boundary-layer theory. According to Adrian (2007), Reynolds stress $-\langle u'v' \rangle$ is positively valued in the near-wall region due to the dominance of the ejection and sweep events.

By comparing figure 3.20 with figure 3.19, it is clear that there are differences between the JPDF patterns of three rib cases and those of the smooth duct flow. In order to facilitate a fair comparison between the smooth and ribbed duct flows, the JPDFs in figures 3.20(a), 3.20(d) and 3.20(g) are calculated at the mid rib height in each ribbed duct case (at $y/\delta = -0.95$, -0.9 and -0.8, respectively). These three elevations are exactly the same as those for figures 3.19(a), 3.19(b) and 3.19(c) for the smooth duct flow. By comparing figures 3.20(a) and 3.20(d) with figures 3.19(a) and 3.19(b), respectively, it is clear that both ejection and sweeping motions are significantly reduced at the mid height of ribs in ribbed duct flow cases of $Br = 0.05$ and 0.1. This indicates that the distribution and intensity of the JPDF is approximately identical for each quadrant at the mid rib height, where u' and v' are essentially uncorrelated, causing arbitrary occurrence of either ejection or sweeping events with no obvious directional tendency. However, for the $Br = 0.2$ case as shown in figure 3.20(g), the tendency toward ejection motion is observed at the mid rib height. As shown in figures 3.20(b), 3.20(e) and 3.20(h), near the rib crest, it is observed that the sweep and ejection events are dominant, which are mainly attributed to the large-scale flapping motions in this region. Consistent with the quadrant analysis of Reynolds shear stresses reviewed by Adrian (2007), these turbulent motions associated with the Q2 and Q4 events result in a negatively-valued Reynolds shear stress $\langle u'v' \rangle$ close to the rib crest (see, figure 3.11(d)). The thick black dashed line at the 135° angle indicates a high correlation between components at the reference point. Figures 3.20(c), 3.20(f), and 3.20(i) show that in the region above the crossing point ($y/\delta = -0.4$), the JPDF distribution prefers the Q2 events. This turbulent flow is strongly influenced by the presence of unsteady large-scale swirling flow structures, which lead to an augmentation of ejection activities.

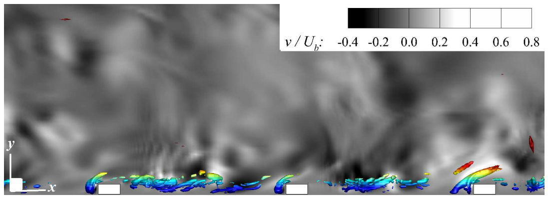

(a) $Br = 0.05$

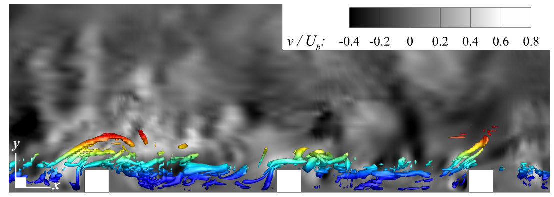

(b) $Br = 0.1$

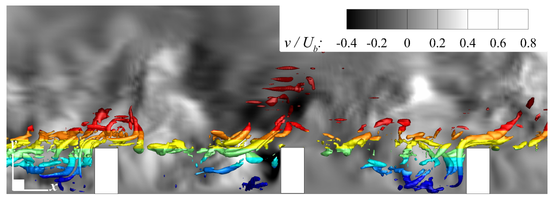

(c) $Br = 0.2$

Figure 3.21: Iso-surfaces of the swirling strength λ_{ci} around ribs, colored with non-dimensional elevation y/δ, with background contours of the instantaneous vertical velocity v/U_b in the central vertical plane (located at $z/\delta = 0$) of the domain for three blockage ratios.

3.4 Flow structures near the rib-roughened wall

The presence of ribs and four walls has a significant impact on the turbulent flow statistics and structures. In this section, we focus on the study of turbulent structures through a qualitative approach based on visualizations using the instantaneous fluctuating flow field and the λ_{ci}-criterion, and through a quantitative approach based on analysis of temporal auto-corrections, temporal spectra, and the spatial two-point auto-correlations of the turbulence field.

3.4.1 Turbulence structures in the x-y plane

In order to demonstrate the effect of ribs on near-wall turbulence structures, figure 3.21 shows the iso-surfaces of the swirling strength, λ_{ci}, superimposed onto instantaneous vertical velocity contours in the central (x-y) plane (located at $z/\delta = 0.0$) for different blockage ratios. From figure 3.21, it is clear that both the strength and size of turbulent structures induced by rib elements increase as the rib height increases, an observation that is consistent with the pattern of turbulence fluctuations shown in figure 3.10 and the trend of TKE production rate P_k demonstrated in figure 3.13(a). As the rib height increases, the sweeping or ejection activities ("splashing effects") near the leading corner of the rib element enhance, which drastically deflect the vortical structures away from the ribs, shedding into the central region of the duct. This further results in an enhancement in the local Reynolds normal and shear stress levels and TKE production rate. This physical feature is also consistent with the previous analysis of figures 3.16 and 3.17 in the sense that the local isotropy for both large- and small-scales of turbulence near the rib crest becomes increasingly apparent as the blockage ratio increases from $Br = 0.05$ to 0.2.

To develop a deeper understanding of the effect of rib height on the size and inclination angle α of turbulence structures near the rib crest, the 2-D spatial two-point auto-correlation function of velocity fluctuations can be studied. For a ribbed flow, it is defined as (Volino et al., 2009)

$$R^s_{ij}(x'_{ref}, y_{ref}, x', y) = \frac{\langle u'_i(x', y) u'_j(x'_{ref}, y_{ref})\rangle}{\sqrt{\langle u'^2_i(x', y)\rangle \langle u'^2_j(x'_{ref}, y_{ref})\rangle}} \quad , \tag{3.8}$$

where $(x'_{ref},\ y_{ref})$ are the coordinates of the reference point and superscript "s" denotes a spatial correlation. The relative streamwise coordinate of the reference point is fixed at $x'_{ref}/\delta = 0.4$, while its vertical coordinate y_{ref}/δ is determined based on the peak locations of the two Reynolds stress components $\langle u'u'\rangle$ and $-\langle u'v'\rangle$ observed in figure 3.11, both of which occur at elevations $y/\delta = -0.86$, -0.76 and -0.56 for $Br = 0.05, 0.1$ and 0.2, respectively. Figure 3.22 plots the isopleths of the spatial two-point auto-correlation coefficients of the three velocity components (R^s_{uu}, R^s_{vv} and R^s_{ww}) for the three rib cases. As clearly shown in the figure, there is an inclination angle between the tilted major axis of the isopleths and the streamwise direction. This observation is consistent with the study of 2-D turbulent boundary-layer flows over ribbed flat plates of Volino et al. (2009) and Leonardi et al. (2004),

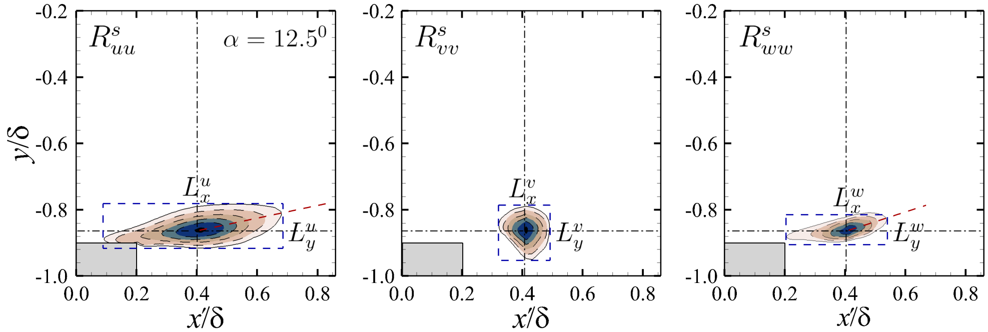

(a) $Br = 0.05$

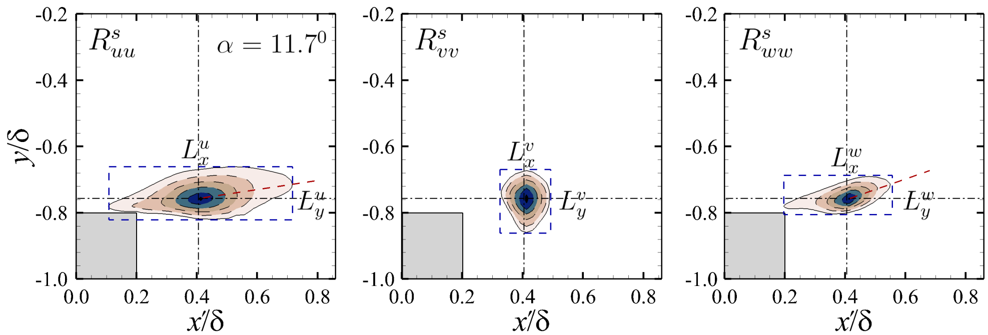

(b) $Br = 0.1$

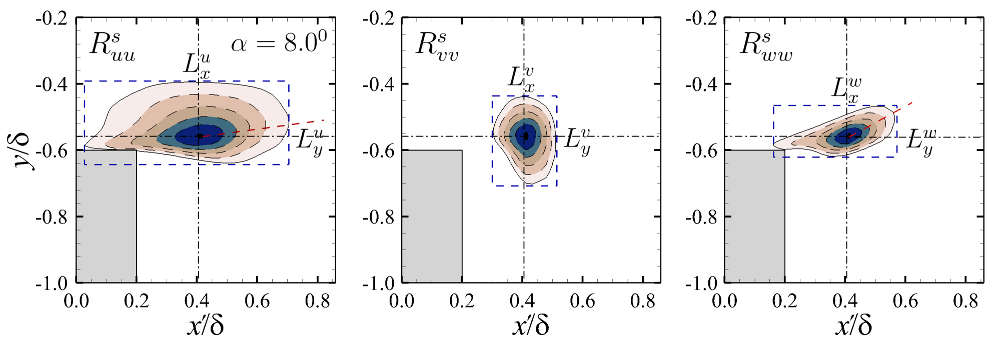

(c) $Br = 0.2$

Figure 3.22: Isopleths of two-point auto-correlation $R^s_{ii}(x'/\delta, y/\delta)$ of three velocity components displayed in the central vertical plane located at $z/\delta = 0$ for different blockage ratios. The relative streamwise coordinate of the reference point is fixed at $x'_{ref}/\delta = 0.4$, while the vertical coordinate of the reference point is $y_{ref}/\delta = -0.86$, -0.76 and -0.56 for $Br = 0.05, 0.1$ and 0.2, respectively. The isopleth value ranges from 0.5 to 1.0, with the outermost and innermost isopleths corresponding to $R^s_{ii} = 0.5$ and 1.0, respectively. The increment between two adjacent isopleths is 0.1 for all three rib cases. The dashed box contains exactly the outermost isopleth, with side-lengths of L^u_x and L^u_y for R^u_{ii}, L^v_x and L^v_y for R^v_{ii}, and L^w_x and L^w_y for R^w_{ii}.

who indicated that this inclination angle is characteristic of hairpin vortices developed over the rib crest. From figure 3.22, it is evident that the inclination angle of the isopleths of R^s_{uu} decreases monotonically from $\alpha = 12.5^\circ$ to 8.0° as the rib height increases. This physical feature can be explained on the basis that the hairpin vortices are rotated towards the streamwise and vertical directions by the asymmetric part of the shear stress tensor and the self-induction of quasi-streamwise vortices (or, hairpin legs) associated with the ejection events (Adrian et al., 2000). Indeed, from previous analysis of figures 3.20(b), 3.20(e) and 3.20(h), it is understood that as the rib height increases, the flow becomes increasingly dominated by the sweep events around the rib height. As such, along with the relative reduction in the strength of ejection events, the inclination angle decreases. To demonstrate the rib height effects on the size of hairpin structures, we compare the streamwise and vertical length scales of the outermost isopleth of the spatial two-point correlation coefficients (R^s_{uu}, R^s_{vv} and R^s_{ww}), indicated using the side-lengths of dashed boxes in figure 3.22. By comparing figures 3.22(a)-3.22(c), it is evident that as the rib height increases, both L^u_x and L^u_y (associated with R^s_{uu}) increase in value. This indicates that both the hairpin structures and streamwise streaks appearing near the rib crest increase in size with an increasing rib height. Similar to the isopleth pattern of R^s_{uu}, the major axis of the isopleth of R^s_{ww} also exhibits an inclined angle near the rib crest. Also similar to R^s_{uu}, the streamwise and vertical length scales (L^w_x and L^w_y, respectively) of the outermost isopleth of R^s_{ww} increase as the rib height increases. Although the three spatial two-point auto-correlation coefficients R^s_{uu}, R^s_{vv} and R^s_{ww} are closely related, all influenced by the turbulence structures at the rib crest, they are different in values. From figure 3.22, it is apparent that in all three rib cases, the extent of the isopleth of R^s_{uu} is greater than those of R^s_{vv} and R^s_{ww}, suggesting that the high- and low-speed streamwise streaks associated with the hairpin legs are the dominant flow structural features around the rib crest. Furthermore, in comparison with R^s_{uu} and R^s_{ww}, the isopleths of R^s_{vv} show a more isotropic distribution. Clearly, the streamwise and

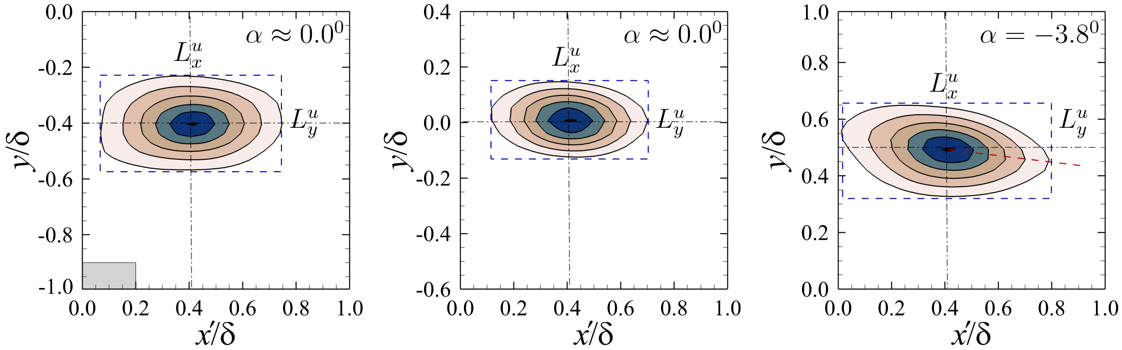

(a) $Br = 0.05$ at $y_{ref}/\delta = -0.4$ (b) $Br = 0.05$ at $y_{ref}/\delta = 0.0$ (c) $Br = 0.05$ at $y_{ref}/\delta = 0.5$

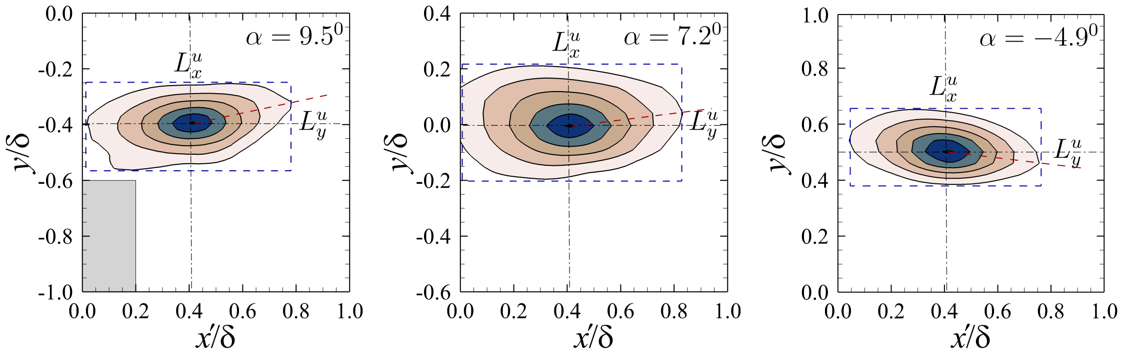

(d) $Br = 0.2$ at $y_{ref}/\delta = -0.4$ (e) $Br = 0.2$ at $y_{ref}/\delta = 0.0$ (f) $Br = 0.2$ at $y_{ref}/\delta = 0.5$

Figure 3.23: Isopleths of streamwise two-point auto-correlation $R^s_{uu}(x'/\delta, y/\delta)$ calculated at three reference points of different elevations in the central vertical plane located at $z/\delta = 0$. The comparison of the two ribbed flow cases (of $Br = 0.05$ and 0.2) is conducted at three identical reference points, with the relative streamwise coordinate fixed at $x'_{ref}/\delta = 0.4$, while the vertical coordinate being $y_{ref}/\delta = -0.4$, 0 and 0.5. The isopleth value ranges from 0.5 to 1.0, with the outermost and innermost isopleths corresponding to $R^s_{uu} = 0.5$ and 1.0, respectively. The increment between two adjacent isopleths is 0.1 for the two rib cases. The dashed box contains exactly the outermost isopleth, with side-lengths of L^u_x and L^u_y.

vertical length scales of the turbulent flow structures as indicated by the outermost isopleth of R^s_{vv}, L^v_x and L^v_y, are comparable in value and both increase as the rib height increases.

The above analysis of the isopleths of two-point auto-correlations based on figure 3.22 was conducted at the reference points of different elevations. Indeed, more degrees of freedom are involved in the analysis of a 3-D ribbed duct (in comparison with a 2-D boundary-layer flow), the turbulence structures in the three ribbed ducts of different blockage ratios can be compared from a different angle. Figure 3.23 compares the 2-D spatial two-point auto-correlation function of streamwise velocity fluctuations at three identical elevations in the central (x-y) plane ($z/\delta = 0$) for two rib cases of $Br = 0.05$ and 0.2. The comparison of these two ribbed duct cases is made at three identical reference points, with the relative streamwise coordinate fixed at $x'_{ref}/\delta = 0.4$, while the vertical coordinate being $y_{ref}/\delta = -0.4$, 0 and 0.5. A non-trivial value of the inclination angle α (as shown in figure 3.23) is a reflection of the near-wall ejection events. From figure 3.23, it is seen that the inclination angle α is negatively-valued on the smooth top wall side (at $y_{ref}/\delta = 0.5$). This is simply because the normal direction of the smooth top wall is pointing downwards, and therefore, ejection events near the smooth top wall are associated with downwash flows towards the ribbed bottom wall. By comparing figures 3.23(a)-3.23(c) with figures 3.23(d)-3.23(f), respectively, it is clear that the inclination angle α of the isopleths of R^S_{uu} increases monotonically as the Br value increases from 0.05 to 0.2, resulting in an enhanced flow interaction between the ribbed bottom wall and smooth top wall. Furthermore, from figures 3.23(a) and 3.23(d), it appears that the length scales of turbulence structures are comparable in both the streamwise and vertical directions, indicating that the rib effect on the size of turbulence structures is reduced considerably at an elevation well above the ribs.

Besides the spatial scales of turbulence structures analyzed above, the temporal scales of turbulent motions can also be investigated by using the temporal auto-correlation function of velocity fluctuations, defined as

$$R^t_{ij}(t) = \frac{\langle u'_i(t)u'_j(t_{ref})\rangle}{\sqrt{\langle u'^2_i\rangle\langle u'^2_j\rangle}} \quad , \tag{3.9}$$

where t_{ref} represents the reference time origin, and superscript "t" denotes a temporal correlation. In figure 3.24, the temporal auto-correlations of all three velocity

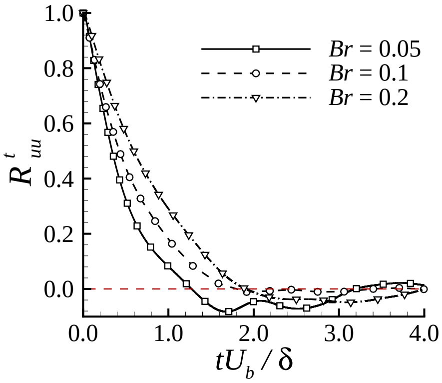

(a) Profiles of R^t_{uu}

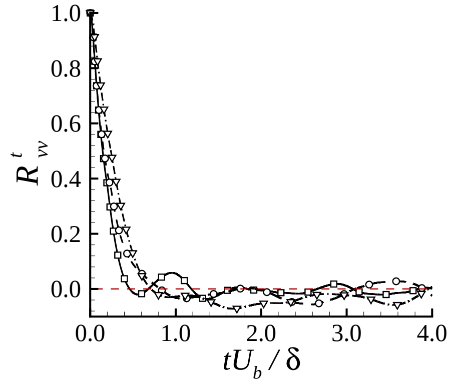

(b) Profiles of R^t_{vv}

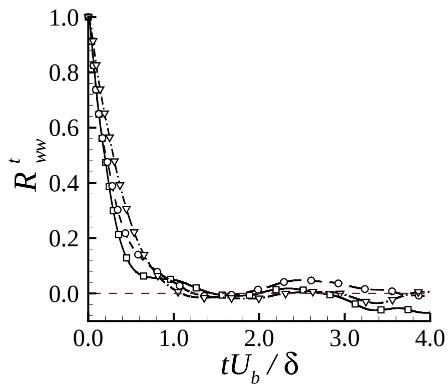

(c) Profiles of R^t_{ww}

Figure 3.24: Temporal auto-correlations of velocity fluctuations for different blockage ratios at the elevation that is slightly above the rib crest (the spatial reference point is identical to that used in figure 3.22).

components for different rib cases are compared at the elevation that is slightly above the rib crest. The spatial reference points used here are the same as in figure 3.22 for the calculation of the spatial two-point auto-correlations. From figure 3.24, it is evident that in all three cases, the temporal integral scale (as indicated by the intercept of time axis) of the streamwise velocity is longer than those of the other two components. This characteristic of the temporal scale of turbulent flow structures is consistent with the previous analysis of figure 3.22 in the sense that the largest scale of turbulence structures is associated with the streamwise velocity fluctuations. Both

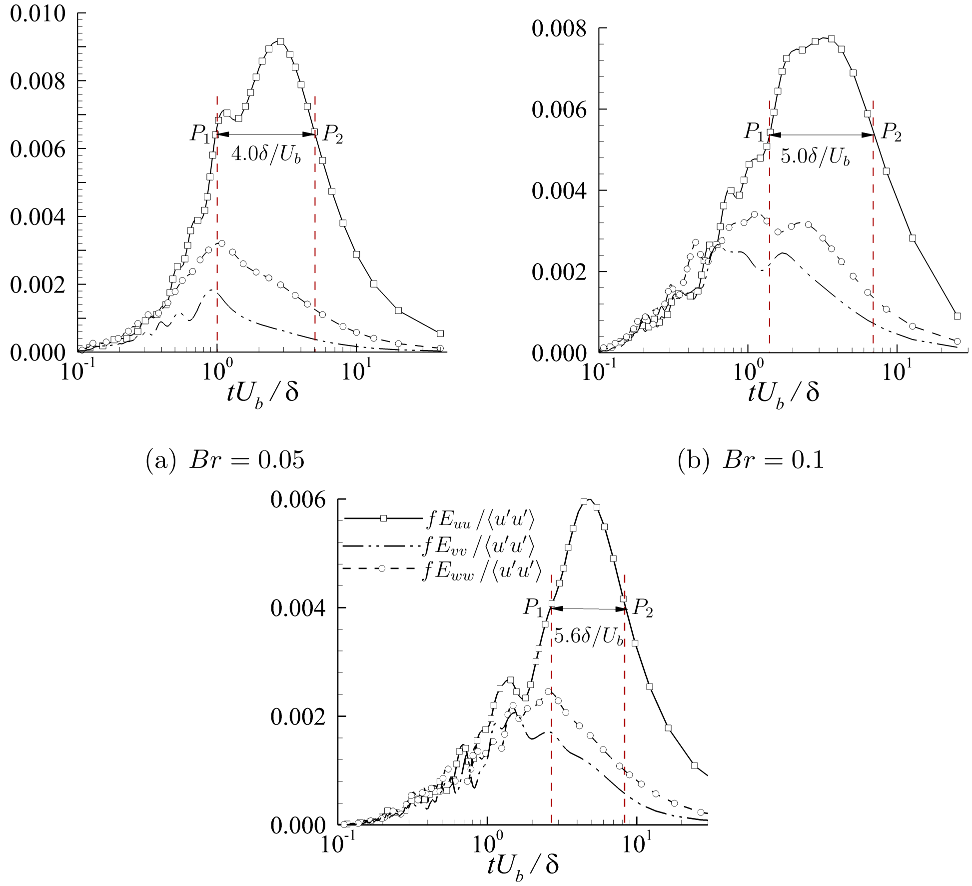

(a) $Br = 0.05$ (b) $Br = 0.1$

(c) $Br = 0.2$

Figure 3.25: Comparison of the premultiplied energy spectra, $fE_{ii}/\langle u'u'\rangle$, of the three components of velocity fluctuations for different blockage ratios at the elevation that is slightly above the rib crest (the spatial reference point is identical to that used in figure 3.22).

spatial and temporal auto-correlations shown in figures 3.22 and 3.24 clearly indicate that turbulence length scales become larger in the region immediately above the rib crest as the rib height increases.

The effects of rib height on the temporal scales of turbulent flow structures can be further quantified using the premultiplied energy spectra ($fE_{ii}/\langle u'u'\rangle$). Figure 3.25 compares the premultiplied energy spectra of all three components of velocity fluctuations. From figures 3.25(a)-3.25(c), it is observed that the characteristic temporal scale of turbulence structures increases as the rib height increases, an observation that is consistent with the previous analysis of figures 3.22 and 3.24. For example, the mode of $fE_{ii}/\langle u'u'\rangle$ occurs at the non-dimensional temporal scale of $tU_b/\delta \approx 2.77$ in the case of $Br = 0.05$, but at $tU_b/\delta \approx 3.12$ and 4.82 in the cases of $Br = 0.1$ and 0.2, respectively. The properties of these characteristic temporal scales can be further understood by defining the energy-containing range based on the temporal scales possessing premultiplied energy spectra that are at least 70% of the peak value (bounded by the vertical dashed lines "P_1" and "P_2" in figure 3.25). By comparing figures 3.25(a)-3.25(c), it is evident that owing to the substantial changes in the temporal scales induced by the rib elements, the difference between the lower (P_1) and upper (P_2) temporal thresholds increases monotonically from $4.0\delta/U_b$ to $5.6\delta/U_b$ as the blockage ratio increases from $Br = 0.05$ to 0.2. This clearly indicates that not only the mode but also the range of the temporal scales of energetic turbulent motions progressively increase as the rib height increases.

3.4.2 Turbulence structures in the x-z plane

As dominant flow structures in near-wall turbulence, streaks play a significant role in the transport of momentum and TKE, and have been well studied in the context of 2-D turbulent boundary layers developed over flat plates (see, e.g., Chernyshenko and Baig, 2005; Adrian, 2007). In the current test case of 3-D turbulent flow in a ribbed duct, the streamwise streaky structures exhibit interesting features that are qualitatively different from those in canonical 2-D turbulent boundary layers. In particular, the streak structures in a ribbed duct are sensitive to not only the rib height but also the boundary layers developed over the two vertical sidewalls of the duct. To demonstrate the rib height effects on the development of streaky structures, contours of the non-dimensionalized instantaneous streamwise velocity fluctuations, u'/U_b, are plotted in figure 3.26 in the (x-z) plane located at $y/\delta = -0.86, -0.76$ and -0.56 for $Br = 0.05, 0.1$ and 0.2, respectively. As shown previously in figures 3.11

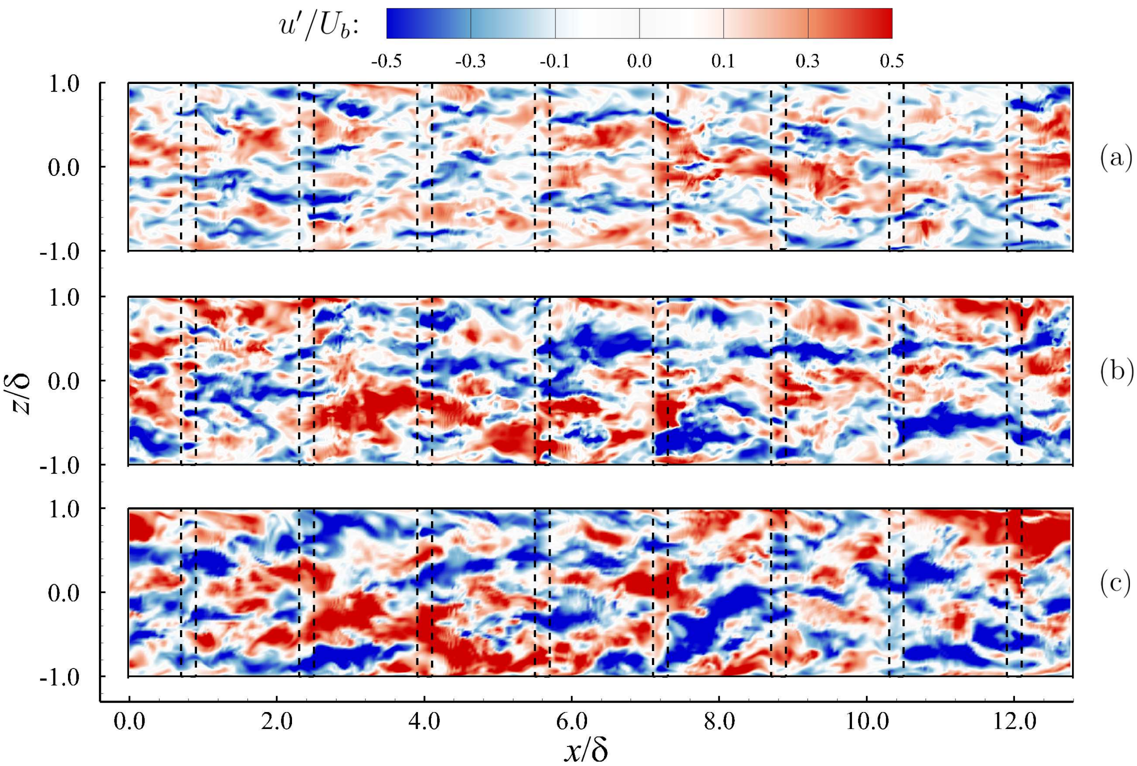

Figure 3.26: Contours of the non-dimensionalized instantaneous streamwise velocity fluctuations u'/U_b in the (x-z) plane of different elevations immediately above the rib crest for three rib cases. (a) at $y/\delta = -0.86$ and $Br = 0.05$, (b) at $y/\delta = -0.76$ and $Br = 0.1$, and (c) at $y/\delta = -0.56$ and $Br = 0.2$.

and 3.13, at these elevations, both the Reynolds stresses and TKE production rate peak. From figures 3.26(a)-3.26(c), it is seen that both the characteristic length scales and the strengths of low- and high-speed streaks are influenced apparently by the rib height. From the previous analysis (figures 3.10, 3.11 and 3.13), it is understood that as the rib height increases, the magnitudes of both turbulence intensity and TKE production rate increase near the rib crest. Correspondingly, the induced turbulence perturbations by rib elements are enhanced, leading to an increased streak strength immediately above the rib crest. Clearly, as Br increases from 0.05 to 0.2, the size of the streaky structures increases, and furthermore, the spanwise spacing between neighboring low- and high-speed streaks also increases. An enhanced strength of

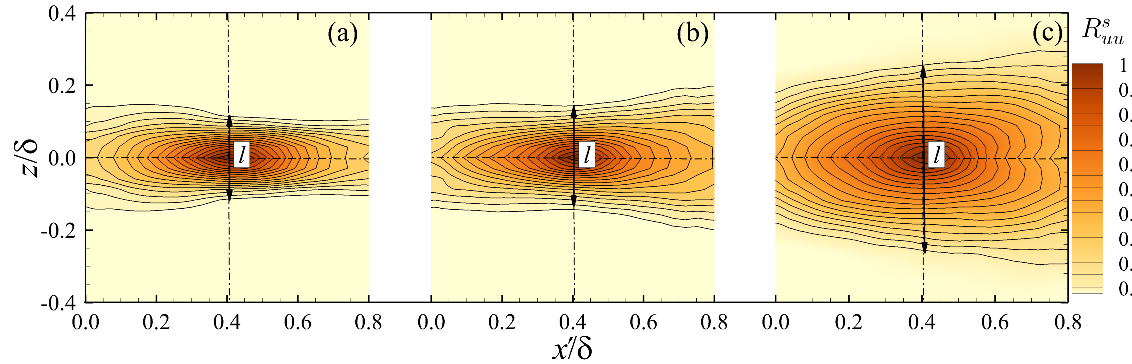

Figure 3.27: Contours of the spatial two-point auto-correlation of streamwise velocity fluctuations R^s_{uu} in the (x-z) plane for different blockage ratios. The reference point is located in the central vertical plane at $x'_{ref}/\delta = 0.4$ and $z/\delta = 0$ as in figure 3.22. The isopleth value of R^s_{uu} ranges within $[0.1, 1.0]$, with an increment of 0.05 between two adjacent isopleths. The characteristic spanwise size of the streaks is denoted as l, which is represented by the spanwise separation between two outmost isopleths across the reference point. (a) at $y/\delta = -0.86$ and $Br = 0.05$, (b) at $y/\delta = -0.76$ and $Br = 0.1$, and (c) at $y/\delta = -0.56$ and $Br = 0.2$.

streaky structures in the region immediately above the ribs is consistent with our previous observation of reduced turbulent anisotropy detailed in subsection 3.3.6. In the following, the rib height effect on the spanwise separation between the streaks will be further investigated using spatial two-point auto-correlation coefficients.

Figure 3.27 shows the isopleths of the 2-D two-point auto-correlation of streamwise velocity fluctuations in the (x-z) plane of different elevations for three rib cases. The results are obtained at the same reference points as in figure 3.22. The spanwise characteristic size of the streaks is denoted as l in the figure, which is represented by the spanwise separation between two outermost isopleths (for $R^s_{uu} = 0.1$) across the reference point. From figures 3.27(a)-3.27(c), it is clear that the value of l increases monotonically as the rib height increases. Specifically, at the reference point (which is slightly above the rib crest), the spanwise characteristic scale of streaks is about one-eighth and one-sixth of the duct width (i.e., $l = D/8$ and $D/6$) for $Br = 0.05$ and 0.1, respectively. However, as Br increases to 0.2, the value of l increases significantly to

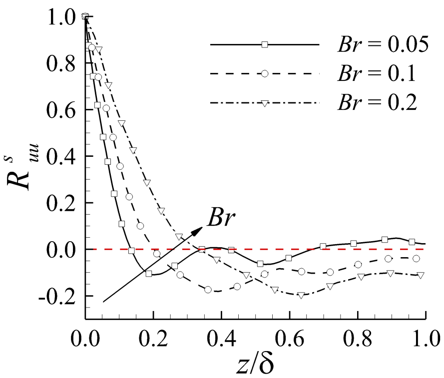

(a) Profiles of R^s_{uu}

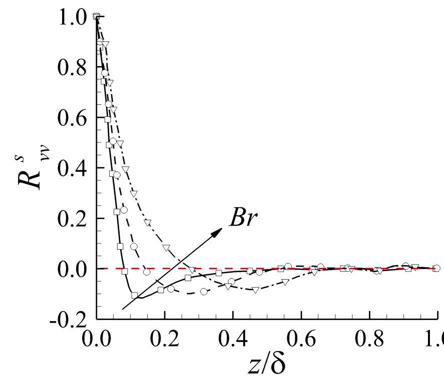

(b) Profiles of R^s_{vv}

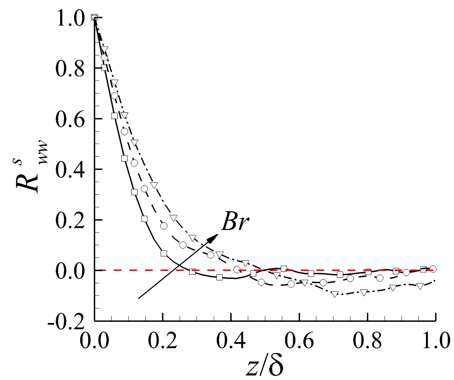

(c) Profiles of R^s_{ww}

Figure 3.28: Spanwise profiles of the spatial two-point auto-correlations for three different rib cases. The reference point is located in the central vertical plane at $z_{ref}/\delta = 0$ and $x'_{ref}/\delta = 0.4$, and the value of y_{ref}/δ is identical to that in figure 3.22.

about one-fourth of the duct width (i.e., $l = D/4$). This well explains the qualitative results shown previously in figure 3.26 that the elongated streaks tend to be stretched in the spanwise direction and be intensified with an increasing rib height.

To refine the study, figure 3.28 compares the 1-D spanwise profiles of the two-point auto-correlation coefficients of the three velocity components (R^s_{uu}, R^s_{vv} and R^s_{ww}) for the three rib cases. Given the finite size of the spanwise domain of the duct (bounded by two vertical sidewalls), the values of R^s_{uu} and R^s_{ww} do not vanish at $z/\delta = 1.0$, a feature that is drastically different from that of a canonical 2-D plane-channel flow of an infinite spanwise domain size. The spanwise characteristic length scale of streaks can be defined based on either the 2-D contours of R^s_{uu} shown in figure 3.27 or the 1-D profile of R^s_{uu} shown in figure 3.28(a). The spanwise separation between the low- and high-speed streaks can be determined precisely based on the position of the negatively-valued peak of R^s_{uu} in figure 3.28(a), which is commonly used for evaluating the spanwise characteristic length scale of streaks. From figure 3.28(a), it is evident that the decaying rate of R^s_{uu} becomes increasingly slower as the rib height increases. Consequently, the spanwise characteristic size of the streaky structures (as represented by the spanwise separation between the low- and high-speed streaks) increases monotonically from $z/\delta = 0.2$ to 0.6 as the blockage ratio increases from $Br = 0.05$ to 0.2. As such, the average spanwise streak spacing at $Br = 0.2$ is approximately three and two times larger than those at $Br = 0.05$ and 0.1, respectively. Furthermore, it is observed that the magnitude of R^s_{uu} corresponding to the characteristic spanwise scale of the streaks also increases slightly with an increasing rib height, indicating a monotonic increase in the streaky structure strength above the rib elements, a conclusion that is consistent with qualitative results shown figure 3.26. The mode corresponding to the negative peak of R^s_{vv} indicates the diameter of streamwise vortices (streaks). Figure 3.28(b) shows that near the rib crest, the mean diameter of the streamwise streaks increases monotonically; and consequently, the negative peak in the profile of R^s_{vv} shifts from $z/\delta \approx 0.12$ to 0.44 as the rib height increases from $Br = 0.05$ to 0.2. This leads to an interesting conclusion that the mean diameter of streamwise streaks is comparable to the height of the rib elements (which is $H/\delta = 0.1$ and 0.4 for $Br = 0.05$ and 0.2, respectively). By comparing figure 3.28(c) with 3.28(a), it is clear that the profiles of R^s_{ww} are similar to those of R^s_{uu}, both indicating that the spanwise characteristic scale of streaks increases monotonically as the rib height increases. In view of this, it can be concluded that the scales of streamwise streaks, in terms of their width and diameter, increase with an increasing rib height.

3.5 Chapter summary

Direct numerical simulations of fully-developed turbulent flow through ribbed square ducts are performed to investigate the effects of rib height on the statistical moments of the velocity field, secondary flow motions, and turbulence structures. The pitch-to-height ratios of the three rib cases under the investigation are $P/H = 16$, 8 and 4 (for $Br = 0.05$, 0.1 and 0.2, respectively). In order to identify the rib effects on the velocity field, an additional DNS of a smooth duct flow is conducted at the same Reynolds number of $Re_b = 5600$, which is used as a baseline comparison case in our study. The turbulence field and flow structures of the rib cases are influenced by not only the aspect ratio of the ribs but also the four sidewalls of the duct. A ribbed duct flow is intrinsically 3-D and statistically inhomogeneous in all three directions, which is qualitatively different from the classical case of a 2-D rough-wall boundary-layer flow.

The mean flow patterns of cases of $Br = 0.05$ and 0.1 are typical of k-type rough-wall flows, but that of $Br = 0.2$ exhibits features that are characteristic of a d-type rough-wall flow. Furthermore, under the 3-D flow conditions, organized secondary flows appear in the cross-stream directions whose strength decreases monotonically near the bottom corner of the ducts but increases monotonically near the side and top walls as the blockage ratio increases. The spatial distributions of the local skin friction coefficient C_f and pressure coefficient C_p are influenced significantly by the complex geometry of the domain and the secondary flow pattern in the cross-stream directions. The values of both C_f and C_p maintain approximately constant in the spanwise direction in central region of the duct. In the streamwise direction, however, the highest value of C_f occurs around the leeward and windward faces of the ribs corresponding to the cores of the recirculation bubble and upstream vortex, respectively. The magnitude of C_p is the highest near the windward face of the ribs, and increases as the rib height increases as a result of an enhanced impinging effect of the flow.

Characteristic of a smooth duct flow, the profiles of the Reynolds normal and shear stresses are symmetrical and anti-symmetrical about the duct center ($y/\delta = 0$), respectively. By contrast, the profiles of all Reynolds stress components are asymmetrical in the three rib cases due to the presence of ribs. In general, the magnitudes of the Reynolds normal and shear stresses of the ribbed duct flows are much larger than those of the smooth duct flow due to the disturbances from the ribs. The magnitudes of Reynolds shear stresses and TKE enhance as the rib height increases. For all three rib cases, the highest Reynolds stress levels occur slightly above the rib crest, where the shear effect is the greatest. For the three rib cases tested, the magnitude of $\langle u'u' \rangle$ is much larger than those of $\langle v'v' \rangle$ and $\langle w'w' \rangle$, making the largest contribution to the value of TKE among the three Reynolds normal stress components. Owing to the cross-stream secondary flow motions, the profile of $-\langle u'v' \rangle$ peaks in the region between the sidewall and duct center. In fact, the turbulence level as indicated by the magnitudes of Reynolds normal and shear stresses all increase monotonically as the rib height increases in the central region of the duct.

The maximum value of the TKE production rate over the dissipation rate P_k/ε_k occurs immediately above the rib crest and in the region between the sidewall and duct center, creating a zone of strong non-equilibrium turbulence. In the streamwise-vertical directions, high-intensity vortices are generated at the leading edge of the ribs, which then shed into the central core region of the duct. Concurrently, in the spanwise-vertical directions, secondary flow motions carry these highly energetic vortices from the duct center sideways to the two vertical walls, resulting in an increase in the value of P_k/ε_k. The transport equation of TKE is studied to further understand the rib effects on turbulence energy transfer. The budget balances of the three rib cases exhibit more complex patterns than that of the smooth duct flow, especially around the rib crest. In comparison with the smooth duct flow, the dominant source term is still the production term P_k, which peaks at a position that is slightly above rib crest in all three rib cases. Although the magnitudes of the three sinks (D_k, T_k

and ε) around the rib crest are comparable at $Br = 0.05$, the turbulent diffusion term T_k becomes increasingly dominant as the blockage ratio increases to $Br = 0.1$ and 0.2. The convection term C_k does not make a remarkable contribution to the budget balance of TKE in a smooth duct flow. By contrast, the effect of the convection term C_k becomes more pronounced due to the complex mean flow pattern and high TKE level around the rib crest in all three rib cases.

The study of turbulence anisotropy at both large- and small-scales indicates that the degree of turbulence anisotropy is sensitive to the rib height. In the region between the rib crest and the smooth top wall, there is a clear indication of turbulence anisotropy based on the study of the anisotropy tensors of the Reynolds normal stresses and dissipation rates, b_{ii} and d_{ii}, respectively. This is because the magnitude of b_{11} is larger than those of b_{22} and b_{33}; and similarly, the magnitude of d_{11} is greater than those of d_{22} and d_{33} in this region. Furthermore, it is interesting to observe that as the blockage ratio increases from $Br = 0.05$ to 0.2, the peak values of the dominant streamwise components, b_{11} and d_{11}, decrease monotonically near the rib crest. This is because the disturbances from the ribs become stronger as the rib height increases, which facilitates distribution of TKE to all three directions, therefore reducing the degree of turbulence anisotropy. It is interesting to observe that the magnitudes of the normal components of the dissipation anisotropy tensor, d_{11}, d_{22} and d_{33}, are close to zero in the duct center for $-0.5 < y/\delta < 0.5$. This indicates that small-scale structures exhibit a stronger "return to isotropy" tendency compared to the large-scale structures in the duct center.

The turbulent flow structures are further studied using the JPDF of the streamwise and vertical velocity fluctuations, λ_{ci}-criterion, temporal auto-corrections, temporal spectra, and spatial two-point auto-correlations of the turbulence field. The results show that an increase of the rib height exerts stronger disturbances to the flow field, which are subsequently deflected to the duct center. This phenomenon leads to the formation of incoherent structures and the generation of violent ejection and sweep motions just above the rib elements, giving rise to an increase of the local TKE production rate. Based on the analysis of the 2-D spatial two-point auto-correlation function of velocity fluctuations, it is discovered that in the region slightly above the rib crest, the inclination angle of the isopleths of R^s_{uu} decreases monotonically from $\alpha = 12.5°$ to $8.0°$ as the blockage ratio increases from $Br = 0.05$ to 0.2. This monotonic trend with respect to Br is also evident from the JPDF analysis, which shows that the turbulent flow becomes increasingly dominated by the sweep events near the rib crest; and as a result, a lower magnitude of the inclination angle is observed around the rib height. However, based on the analysis of R^s_{uu} of different rib cases at the same elevation, it is observed that the inclination angle α increases monotonically as the Br value increases at an elevation well above the ribs, resulting in an enhanced flow interaction between the ribbed bottom wall and the smooth top wall. It is interesting to observe that both temporal and spatial characteristic scales of turbulence increase monotonically as the rib height increases around the rib crest. Furthermore, based on an analysis of the non-dimensionalized streamwise premultiplied temporal spectrum $fE_{ii}/\langle u'u' \rangle$ of velocity fluctuations, it is observed that the range of temporal scales of the most energetic turbulence motions (with the value of $fE_{ii}/\langle u'u' \rangle$ being at least 70% of its peak value) also expands monotonically around the rib height as the rib height increases. In addition, both the spanwise characteristic size of the streaks and the diameter of streamwise vortices increase monotonically as the rib height increases. More specifically, the non-dimensional diameter of streamwise vortices increases from $z/\delta = 0.12$ to 0.44 as the blockage ratio increases from $Br = 0.05$ to 0.2, comparable in value to the height of the rib elements (i.e., $H/\delta = 0.1$ and 0.4 for $Br = 0.05$ and 0.2, respectively).

Chapter 4

Direct numerical simulation of turbulent heat transfer in a square duct with transverse ribs mounted on one wall

4.1 Introduction

In this chapter, a comparative DNS is performed to study the effects of rib height on the first- and second-order statistical moments of the temperature field, the spectral characteristics of temperature fluctuations, and coherent structures that facilitate the turbulent transport of thermal energy. In order to examine the rib effects on the turbulent heat transfer, the results of the three ribbed duct cases are compared with those of a heated smooth square duct flow at the same bulk Reynolds number. The fluid dynamics of rib-roughened square duct flows of different blockage ratios have been thoroughly analyzed in Mahmoodi-Jezeh and Wang (2020). In view of this, we concentrate our attention on the analysis of the temperature field related to turbulent heat transfer in this chapter. In regards to this topic, the remainder of this paper is organized as follows. In section 4.2, the governing equations, numerical procedure, as well as test cases are described. In section 4.3, detailed result analysis is presented. The impacts of rib aspect ratios on heat transfer and flow structures are investigated through vortex identifiers, joint probability density function (JPDF) of the velocity and temperature fluctuations, temporal auto-correlation functions, two-point cross-correlations functions, and pre-multiplied energy spectra. Finally, in section 4.4, major findings of this chapter are summarized.

4.2 Test case and numerical algorithm

The length of the square duct is $6.4D$ long and consists of eight rib periods, where D is the duct width. In the current study, three blockage ratios ($Br = 0.05, 0.1$ and 0.2) are compared, while the width and streamwise period of the bars are kept constant with $W = 0.1D$ and $P = 0.8D$, respectively. The flow field is fully-developed, and periodic boundary conditions are applied to the streamwise direction. A no-slip boundary condition is imposed on all solid walls for the velocity field. The Reynolds number is fixed at $Re_b = U_b D/\upsilon = 5600$, where U_b represents the average bulk mean velocity over the streamwise direction of the ribbed duct. The flow is inhomogeneous in all three directions in a ribbed duct. The Reynolds number of the flow can be assessed based on the mean streamwise wall friction velocities of the smooth top and ribbed bottom walls (i.e., $u_{\tau S}$ and $u_{\tau R}$, respectively) in the central vertical (x-y) plane located at $z/\delta = 0$. Under the testing condition, the Reynolds numbers (defined as $Re_{\tau S} = \delta u_{\tau S}/\nu$ and $Re_{\tau R} = \delta u_{\tau R}/\nu$) based on the friction velocities are $Re_{\tau S} = 183$, 208 and 236, and $Re_{\tau R} = 280, 346$ and 406 for the three ribbed duct cases of $Br = 0.05, 0.1$ and 0.2, respectively. Here, $\delta = D/2$ is one-half the duct width. For details of the calculation of the values of $Re_{\tau S}$ and $Re_{\tau R}$, the reader is referred to Mahmoodi-Jezeh and Wang (2020). The three ribbed duct flow cases are compared

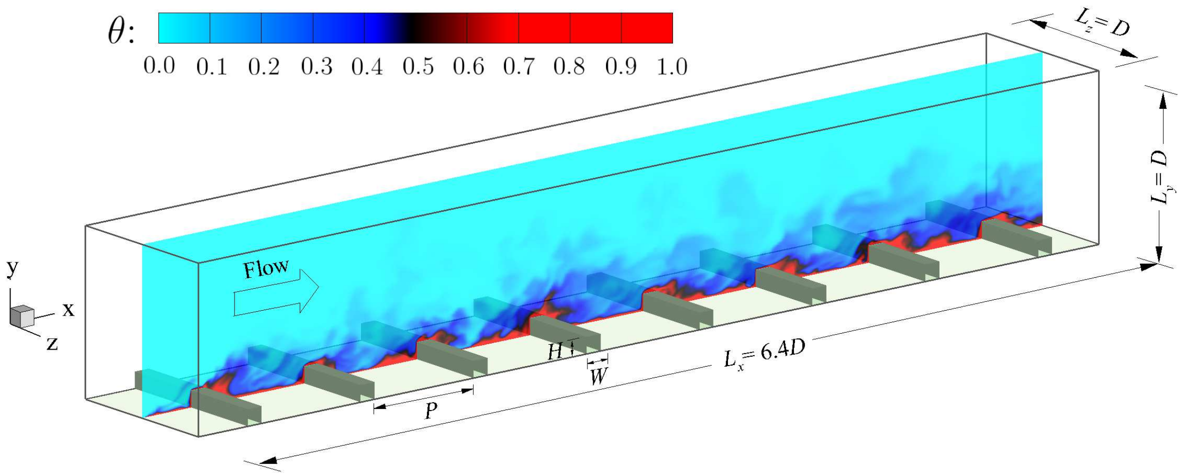

Figure 4.1: Schematic of a square duct with transverse ribs mounted on one wall, computational domain and coordinate system. Contours of instantaneous non-dimensional temperature are displayed in the central plane (located at $z/\delta = 0.0$) of the computational domain.

with a heated smooth duct flow of the same Reynolds number of $Re_b = 5600$ in this study. Given that the flow is homogeneous in the streamwise direction in a smooth duct flow, its mean friction velocity can be calculated based on peripheral averaging over four identical sidewalls of the smooth duct following the approach of Huser and Biringen (1993), Pinelli et al. (2010b), and Pirozzoli et al. (2018). The Reynolds number based on the peripherally-averaged mean friction velocity $u_{\tau P}$ and half duct width δ is $Re_{\tau P} = 180$ for the smooth duct flow. For the temperature field, it is assumed that the flow enters the duct at an inlet temperature, $T_{in} = 300K$. The Prandtl number is $Pr = 0.71$, which is typical for passive heat transfer in air and many gases. The temperature of the heated wall and ribs is maintained constant at $T_w = 350K$, while the top and side walls are assumed to be adiabatic. Also, a zero-Neumann boundary condition is prescribed over the outlet plane. The temperature field is treated as a passive scalar and is non-dimensionalized using the inlet and bottom temperature difference, i.e., $\theta = (T - T_{in})/(T_w - T_{in})$. For the smooth square duct, the domain size is given as $L_x \times L_y \times L_z = 6\pi\delta \times 2\delta \times 2\delta$ in the streamwise, vertical and spanwise directions, respectively. The streamwise computational domain L_x is identical to that used in Pirozzoli et al. (2018). In comparison with the smooth duct case, the heated surface area increases 12.5%, 25% and 50% (over a rib period of $P = 0.8D$) in the three ribbed duct cases of $Br = 0.05$, 0.1 and 0.2, respectively. The application background of this study is internal turbine blade cooling, which often feature high rib blockage ratios. By comparing these idealized benchmark test cases of ribbed square ducts with a smooth square duct, it is clear that the effective heat transfer area increases significantly due to the presence of the rib elements. It should be indicated here that the numerical treatment of the thermal energy equation based on a body-fitted mesh and the temperature boundary condition implemented in this DNS study represent a conventional approach, which is different from that used in Pirozzoli et al. (2016), MacDonald et al. (2019a) and MacDonald et al. (2019b), who introduced a "body forcing" source term in the thermal energy equation, such that the time-averaged bulk mean temperature does not vary with time, and the heat added to the fluid through the body forcing instantly equals to the heat loss from the walls at any time step.

An in-house computer code is used for conducting DNS. In this computer code, the continuity, momentum and thermal energy equations are discretized based on a general curvilinear coordinate system (ξ_1, ξ_2, ξ_3), which take the following form for an incompressible flow:

$$\frac{1}{J}\frac{\partial\left(\beta_i^k u_i\right)}{\partial \xi_k} = 0 \quad , \tag{4.1}$$

$$\frac{\partial u_i}{\partial t} + \frac{1}{J}\frac{\partial}{\partial \xi_k}\left(\beta_j^k u_i u_j\right) = -\frac{1}{J\rho}\frac{\partial\left(\beta_i^k p\right)}{\partial \xi_k} - \frac{1}{\rho}\Pi\delta_{1i} + \frac{\nu}{J}\frac{\partial}{\partial \xi_p}\left(\frac{1}{J}\beta_j^p\beta_j^q\frac{\partial u_i}{\partial \xi_q}\right) \quad , \tag{4.2}$$

$$\frac{\partial T}{\partial t} + \frac{1}{J}\frac{\partial}{\partial \xi_k}\left(\beta_j^k T u_j\right) = \frac{\alpha}{J}\frac{\partial}{\partial \xi_p}\left(\frac{1}{J}\beta_j^p\beta_j^q\frac{\partial T}{\partial \xi_q}\right) \quad , \tag{4.3}$$

where u_i, p, T, ν, ρ, α and δ_{ij} represent the velocity, pressure, temperature, kinematic viscosity, density, thermal diffusivity, and Kronecker delta, respectively. Also, Π is the required streamwise pressure gradient that keeps a constant flow rate. Here, β_i^j and J denote the cofactor and Jacobian of tensor $\partial x_i/\partial \xi_j$, respectively. The above governing equations are represented using tensor notations, and the streamwise (x), vertical (y), and spanwise (z) coordinates shown in figure 4.1 are denoted using x_i for $i = 1, 2$, and 3, respectively. It should be indicated that this computer code is developed for a general purpose of dealing with complex computational domains of curved boundaries using body-fitted mesh. Specific to the present numerical simulation of the flow through a square duct with straight rectangular ribs mounted on the bottom wall, the cofactor and Jacobian degenerate to Kronecker Delta and unity, respectively.

The computer code was developed using the FORTRAN 90/95 programming language and parallelized following the message passing interface (MPI) standard. The numerical algorithm is based on a finite-volume method in which a second-order accuracy is achieved with respect to both spatial and temporal discretizations. For both the momentum and thermal energy equations, a collocated second-order central differencing scheme was used to discretize the spatial derivatives. As such, all the physical variables (velocity components, temperature and pressure) were stored at the centroids of control volumes. An explicit two-step Runge-Kutta scheme was utilized to discretize the temporal derivative. The advection-diffusion equation that governs the temperature field was implemented after the solution of the momentum equations at each time step. A thorough description of the numerical method and validations of the DNS approach can be found in Mahmoodi-Jezeh and Wang (2020). The convergence of the solver is considered once the averaged residue of a discretized algebraic equation drops below 10^{-6}. The time step is fixed at $\Delta t U_b/\delta = 2 \times 10^{-4}$, and correspondingly, the CFL number is approximately 0.2. The precursor simulation was run for an extended duration of 73 flow-through times (i.e., $930\delta/U_b$) until the turbulent flow field becomes fully-developed and statistically stationary. Then, turbulence statistics were collected for a time period over approximately 110 flow-through times (i.e., $1400\delta/U_b$). All the simulations were conducted using the WestGrid (Western Canada Research Grid) supercomputers. For each simulated case, approximately 548,000 CPU hours were spent on solving the velocity and temperature fields and for collecting the flow statistics.

The simulations were conducted based on $1280 \times 148 \times 152$ body-fitted grid points in the x-, y-, and z-directions, respectively. The mesh is non-uniform in all three directions, and is refined near all solid surfaces. To ensure the quality of DNS, the mesh must be fine enough to resolve the smallest scales of turbulence. More specifically, in their DNS study of turbulent plane-channel flows, Moser and Moin (1987) indicated that the grid size needs to be of the same order of the Kolmogorov length scale (i.e., $O(\Delta/\eta) \sim 1$) in order to accurately simulate the turbulence dynamics and capture the turbulence kinetic energy (TKE) level in DNS. Figure 4.2 shows the ratio of the maximum grid size to the Kolmogorov length scale (Δ_{max}/η) in both the central (located at $z/\delta = 0.0$) and cross-stream (located at $x/\delta = 9.1$) planes for the rib case of $Br = 0.1$. Here, the maximum grid size is calculated as $\Delta_{max} = \max(\Delta_x, \Delta_y, \Delta_z)$ and the Kolmogorov length scale is defined as $\eta = (\nu^3/\varepsilon_k)^{0.25}$, where ε_k is the local dissipation rate of TKE, i.e., $\varepsilon_k = \nu\langle\partial u_i'/\partial x_j \partial u_i'/\partial x_j\rangle$. In our analysis of the turbulent flow field, the instantaneous velocity u_i is decomposed as $u_i = \langle u_i\rangle + u_i'$, where $\langle u_i\rangle$ denotes the mean velocity averaged over time and eight rib periods, and u_i' represents the velocity fluctuations. From figure 4.2(a), it is seen that the maximum of Δ_{max}/η occurs at two different positions, one near the leading edge of rib elements and the other between two adjacent ribs (below the rib crest), which is approximately 6.2 and 4.7, respectively. However, as shown in figure 4.2(b), the maximum of Δ_{max}/η occurs close to the two vertical sidewalls, which is found to be around 5.8. Other than these special locations, the value of Δ_{max}/η never exceeds 4.5 over the entire computational domain. Besides the case of $Br = 0.1$ investigated through figure 4.2, the value of Δ_{max}/η is also examined for the other two test cases of $Br = 0.05$ and 0.2. In fact, for all three test cases, the value of Δ_{max}/η is limited to 4.5. The non-dimensional spatial

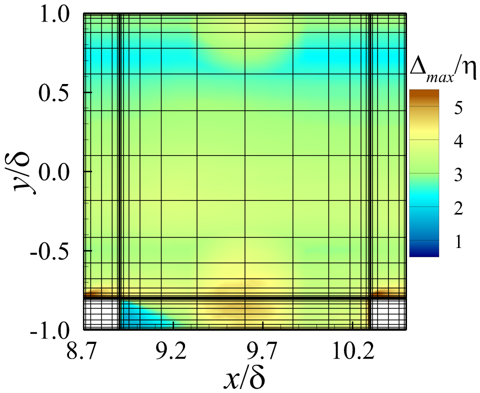

(a) Central (x-y) plane

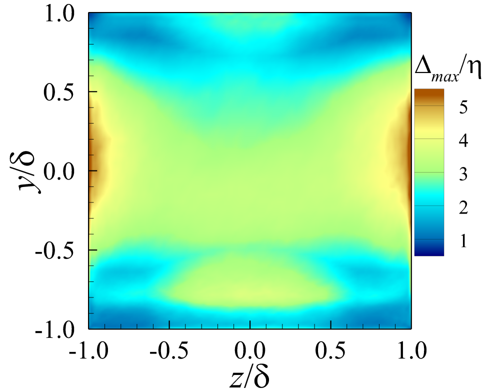

(b) Cross-stream (y-z) plane

Figure 4.2: Contours of the ratio of the grid size to the Kolmogorov length scale (Δ_{max}/η) for the rib case with $Br = 0.1$. (a) In the central (x-y) plane (located at $z/\delta = 0.0$) and (b) in the cross-stream (y-z) plane (located at $x/\delta = 9.1$). In order to show the stretched structured grid, the non-uniform mesh is also shown in panel (a). In this panel, only 20% of grid points are displayed to make the figure readable.

resolution in the streamwise direction (Δx^+) is within the ranges $[0.65, 6.5]$, $[0.69, 7.7]$ and $[0.73, 8.9]$ for $Br = 0.05$, 0.1 and 0.2, respectively. Here, Δx^+ is defined based on the mean streamwise wall friction velocity of the smooth top wall ($u_{\tau S}$) in the central vertical (x-y) plane located at $z/\delta = 0.0$.

4.3 Results and discussions

4.3.1 Mean flow and temperature fields

Figure 4.3 compares the contours of the mean temperature field superimposed with in-plane streamlines in the central plane located at $z/\delta = 0.0$ for the three blockage ratios studied. By comparing figures 4.3(a)-4.3(c), it is observed that the size of the corner vortex (marked with "I") immediately behind a rib increases monotonically as the rib height increases. The reason that the corner vortex I is the smallest for the case of $Br = 0.05$ (shown in figure 4.3(a)) is that the rib height is too small to cause

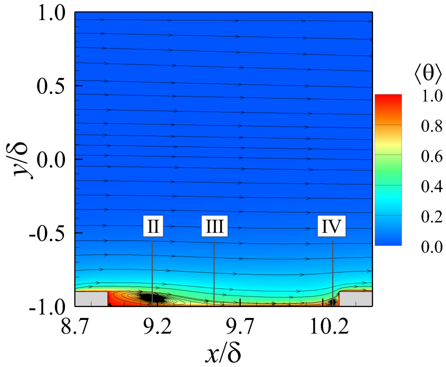

(a) $Br = 0.05$

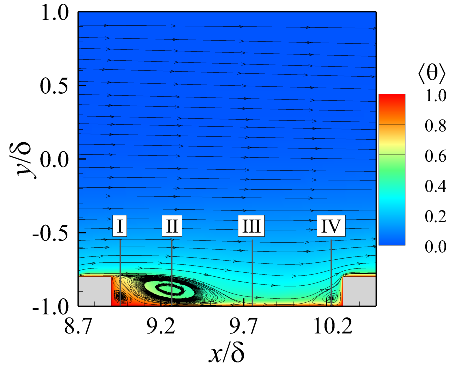

(b) $Br = 0.1$

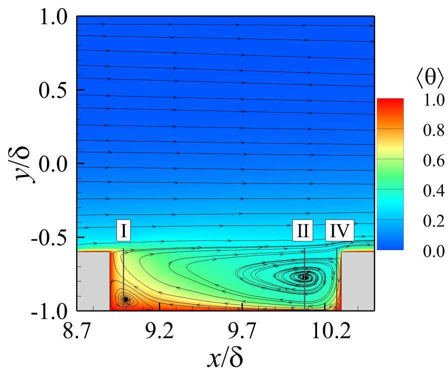

(c) $Br = 0.2$

Figure 4.3: Contours of the mean temperature, $\langle\theta\rangle$, superimposed with in-plane streamlines in the central x-y plane (located at $z/\delta = 0.0$) for different blockage ratios.

significant sudden expansion of the flow in the lee of the rib. From figures 4.3(a)-4.3(c), it is also clear that a large recirculation bubble (marked with "II") is present between two adjacent ribs whose size is also sensitive to the Br value. As the Br value increase from 0.05 to 0.1, the reattachment point (marked with "III") shifts from $x/\delta = 0.7$ to 1.1. However, as the Br value further increases from 0.1 to 0.2, the reattachment of the mean flow occurs on the windward face of the rib elements (instead of the bottom wall). Downstream of the reattachment point, a new boundary layer starts to build up and impinges onto the next rib which leads to the generation of an upstream vortex (at point "IV"). Vertical motion of this type of vortex forces cold flow towards the ribbed wall thereby affecting the heat transfer performance. The variation of the mean flow structures with the blockage ratio is further reflected in the spatial distribution of both the local drag and heat transfer coefficients on the ribbed bottom wall, which will be discussed separately later in this section.

To assess the effects of blockage ratio on the temperature field, the non-dimensional temperature profiles at four streamwise locations are plotted in figure 4.4. The results of three ribbed duct cases at four streamwise locations (for $x/\delta = 2.7, 5.9, 9.1$ and 12.3) are compared with those of the smooth duct case at $x/\delta = 15$ in the central vertical line located at $z/\delta = 0.0$. For the smooth duct case, this particular streamwise location is chosen because the temperature field reaches a fully-developed condition at $x/\delta = 15$. As is evident in figure 4.4, in the near-wall region below the rib height, the strength of the vertical gradient of the mean temperature ($d\langle\theta\rangle/dy$) for the smooth duct flow is greater than those of the ribbed duct flows, resulting in a larger magnitude of production term (i.e., $-\langle u_j'\theta'\rangle\partial\langle\theta\rangle/\partial x_j$) in the transport equation of the temperature variance. Furthermore, it is apparent that as the rib height increases, the fluid temperature in the region below the rib height becomes closer to that of the isothermal wall ($\theta = 1$), which further leads to a reduction in the heat transfer rate. From this figure, it is observed that in all three ribbed duct cases, the magnitude of the mean temperature $\langle\theta\rangle$ increases monotonically as the distance downstream of the inlet ($x/\delta = 0$) increases, reflecting the fact that the flow is continuously heated by the ribbed wall. Furthermore, as is evident from figure 4.4, more than six rib periods are required for the temperature field to reach the fully-developed condition in all three ribbed duct cases. This is because a small discrepancy between the vertical profiles of the mean temperature at $x/\delta = 9.1$ and at $x/\delta = 12.3$ is still visible for all three ribbed duct cases. As shown in figures 4.4(a)$-$4.4(c), the mean temperature gradient becomes zero as the smooth top wall is approached due to the prescribed adiabatic condition.

In order to investigate the effects of the secondary flow motions on heat transfer,

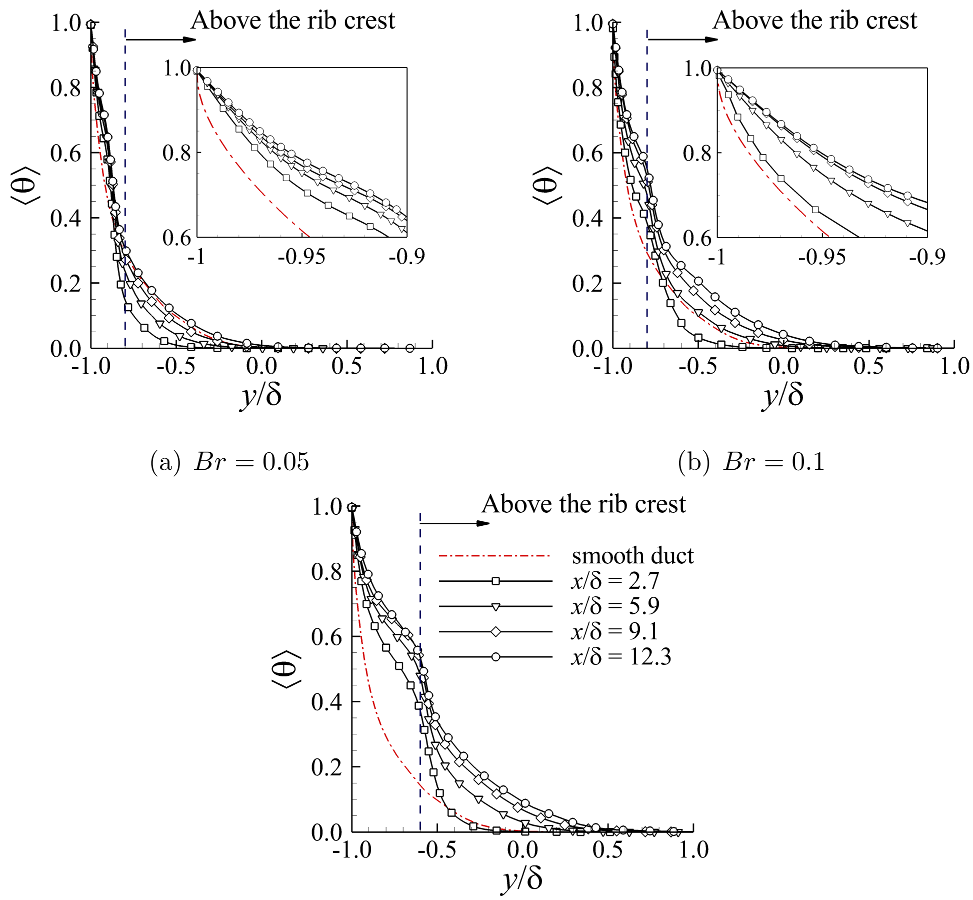

(a) $Br = 0.05$

(b) $Br = 0.1$

(c) $Br = 0.2$

Figure 4.4: Comparison of the non-dimensionalized mean temperature profiles at four streamwise locations (for $x/\delta = 2.7, 5.9, 9.1$ and 12.3) in the central plane (located at $z/\delta = 0$) of the ribbed square duct flows with that of the smooth square duct flow at $(x/\delta, z/\delta) = (15, 0.0)$. For the smooth duct case, the temperature field reaches a fully-developed condition at $x/\delta = 15$. The vertical blue dashed line demarcates the rib crest.

figure 4.5 shows the contour patterns of the secondary flow strength S and the mean spanwise-vertical velocity streamlines together with the magnitude of the mean temperature in the cross-stream (y-z) plane located at $x/\delta = 15$ for the smooth duct flow and at $x/\delta = 9.1$ for the three ribbed duct flows of different blockage ratios. Given the central symmetry of the flow field, only one half of the cross-stream domain is shown.

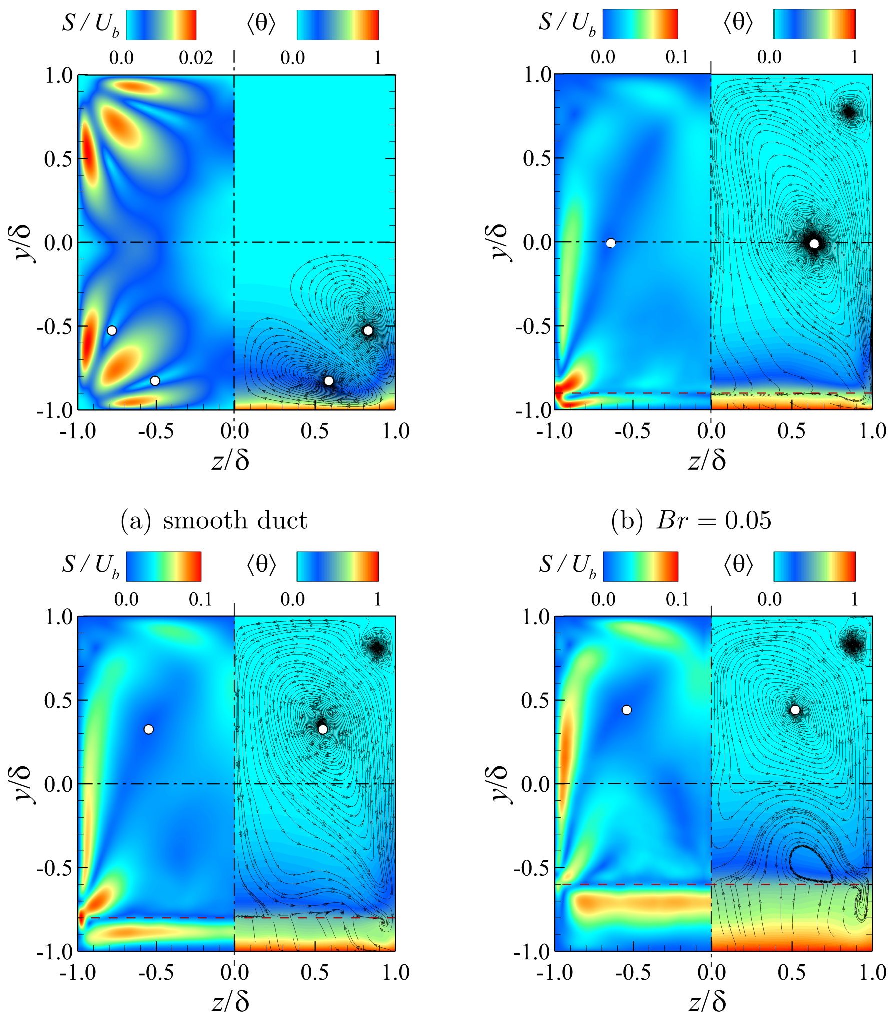

(a) smooth duct (b) $Br = 0.05$

(c) $Br = 0.1$ (d) $Br = 0.2$

Figure 4.5: Contours of the secondary flow strength S (left), and the mean spanwise-vertical velocity streamlines superimposed with the magnitude of the mean temperature (right) in the y-z plane at positions $x/\delta = 15$ and 9.1 for the smooth duct flow and three ribbed duct flows, respectively. White dots denote the center of the mean secondary flow vortex. The horizontal red dashed line demarcates the rib crest.

Here, the secondary flow strength is defined as $S = \sqrt{\langle v \rangle^2 + \langle w \rangle^2}$, following the approach of Macfarlane et al. (1998) and Noorani et al. (2016), who investigated the effects of aspect ratio on the strength of secondary flow in a smooth square duct. As is evident in figure 4.5, both the pattern and strength of the cross-stream secondary flow of the ribbed duct flow cases are considerably different from those of the smooth duct flow. From figure 4.5(a), it is seen that for the smooth duct case, the secondary flow appears as four pairs of counter-rotating vortices in the cross-stream plane. These characteristics of the secondary flow patterns in a smooth square duct are consistent with the observations of Gavrilakis (1992), Pinelli et al. (2010b), Vinuesa et al. (2014), and Pirozzoli et al. (2018). However, as shown in figures 4.5(b)-4.5(d), for the ribbed duct cases, only one pair of large dominant counter-rotating vortices can be observed in the cross-stream plane whose size is apparently influenced by the rib height. Furthermore, it is clear that in the region near the sidewalls, the secondary flow strength of three ribbed duct cases is approximately four times larger than that of the smooth duct case. From figures 4.5(b)-4.5(d), it is evident that for the ribbed duct cases, the vortex center (demarcated using a white dot) of the mean flow shifts upwards monotonically as the rib height increases, which has a significant influence on the distribution of the mean temperature $\langle\theta\rangle$. This secondary flow is mainly responsible for transporting the relatively cooler fluid from the center of the duct to the heated bottom wall, giving rise to a region with high Nu values. Figures 4.5(b)-4.5(d) also show that the strength of the secondary flow, S, decreases near the bottom corner of the duct as the blockage ratio increases; however, the magnitude of S in regions adjacent to the side and top walls as well as the rib crest increases monotonically with an increasing rib height.

To gain more insights into the influence of the secondary flow structures on the heat transfer rate, figure 4.6 shows the distribution of the non-dimensionalized local Nusselt number in the (x-z) plane located at $y/\delta = -1.0$. The Nusselt number is defined as $Nu = q_w D/\lambda(T_w - T_b)$, where the bulk temperature is calculated as $T_b = \int_0^D \int_0^D \int_0^{L_x} T|\langle u\rangle| dxdydz / \int_0^D \int_0^D \int_0^{L_x} |\langle u\rangle| dxdydz$. In this comparative study, Nu is further divided by the value calculated using the semi-empirical Dittus-Boelter equation (i.e. $Nu_0 = 0.023Re^{0.8}Pr^{0.4}$) originally developed for a smooth wall. From figure 4.6, it is clear that the value of Nu on the windward side of the rib is larger

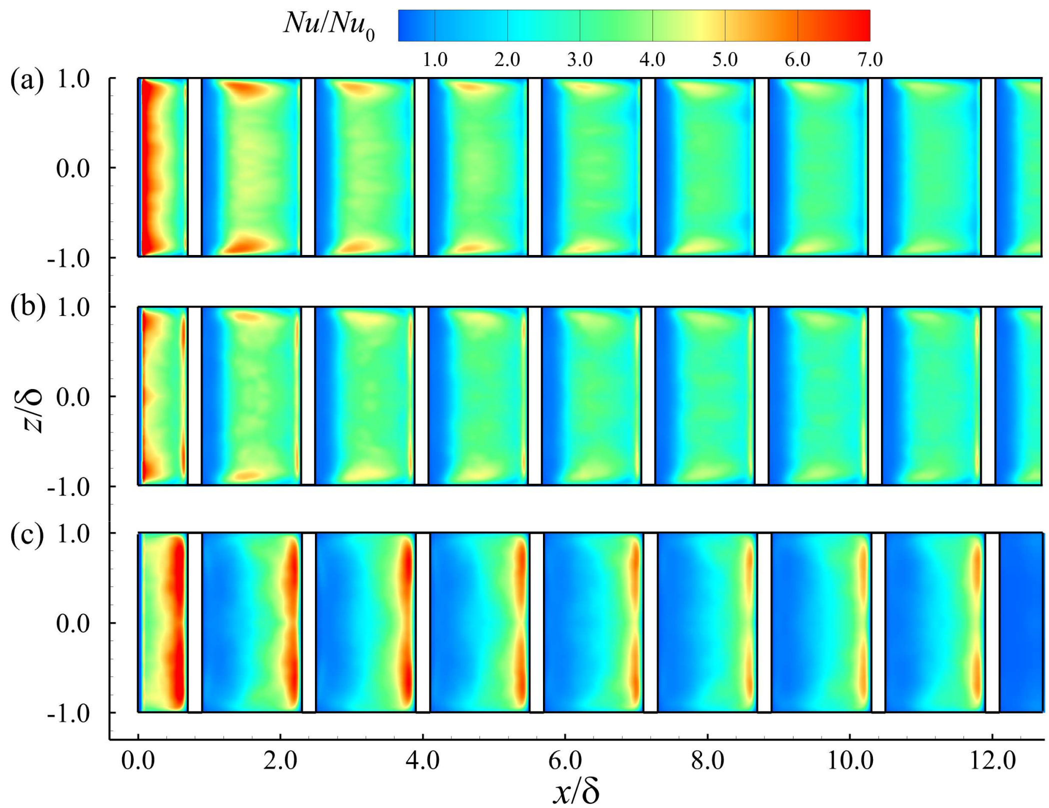

Figure 4.6: Distribution of the local non-dimensionalized Nusselt number, Nu/Nu_0, on the bottom wall located at $y/\delta = -1.0$ for three different rib cases. (a) $Br = 0.05$, (b) $Br = 0.1$, and (c) $Br = 0.2$.

in the case of $Br = 0.2$ than in the cases of $Br = 0.05$ and 0.1. This is because the recirculation vortex II (see, figure 4.3) induces a strong streamwise impingement (associated with an enhanced dynamic pressure) onto the windward face of the rib, thereby enhancing the mixing and heat transfer rate in that region. By comparing Figs. 4.6(a)-4.6(c), it is also apparent that as the Br value increases from 0.05 to 0.2, the value of Nu decreases near the two vertical sidewalls. This spanwise trend of Nu can be well explained from figure 4.5, which shows that the upward-moving impingement region near both sidewalls elevates with an increasing rib height, resulting in a lower magnitude of Nu near the two sidewalls of the square duct. Furthermore, as a result of the developing temperature field (in conjunction with a fully-developed turbulent flow field), the Nusselt number decays streamwise until the temperature

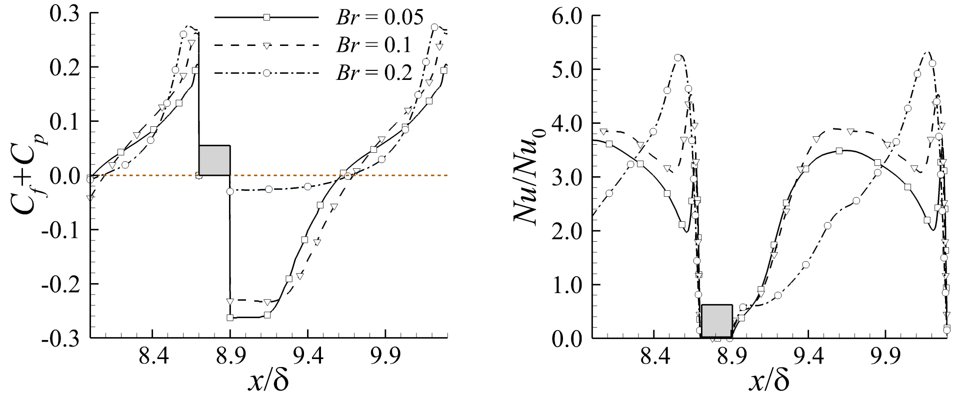

(a) Profiles of $C_f + C_p$ (b) Profiles of Nu/Nu_0

Figure 4.7: Streamwise profiles of non-dimensionalized total drag coefficient, $C_f + C_p$, and Nusselt number, Nu/Nu_0, of different blockage ratios along a central line of the bottom wall located at $(z/\delta,\, y/\delta) = (0.0,\, -1.0)$.

field reaches a fully-developed state. It is also observed that the contour pattern of the local Nusselt number becomes increasingly similar after the sixth rib, which indicates a quasi self-similar state. Although the velocity field is statistically steady and fully developed in the streamwise direction, the temperature field is developing in the streamwise direction.

To understand the effects of the mean flow field on heat transfer, figure 4.7 compares the streamwise profiles of the total drag coefficient, $C_f + C_p$, and Nusselt number, Nu/Nu_0, at $(z/\delta,\, y/\delta) = (0.0,\, -1.0)$ in the central (x-y) plane for the three different ribbed duct cases. The skin friction and pressure coefficients are defined as $C_f = \tau_w/(\rho U_b^2/2)$ and $C_p = \langle p \rangle/(\rho U_b^2/\,2)$, respectively, where τ_w represents the local total wall friction stress calculated as $\tau_w = \mu \left[(\partial \langle u \rangle / \partial y)^2 + (\partial \langle w \rangle / \partial y)^2 \right]_{wall}^{1/2}$. As seen in figure 4.7(a), for all three ribbed duct cases, the level of total drag coefficient ($C_f + C_p$) near the windward face of the rib increases monotonically as the rib height increases. This can be explained from figure 4.3, which shows that the size and strength of the recirculation bubble II increase when the rib height is augmented; and as a result, a higher magnitude of drag is observed in that region. Figure 4.7(b) highlights the fact that the temperature field and heat transfer rate respond differently to the mean flow structure patterns. For example, in the region downstream of the rib, the peak of Nu lies at the reattachment point III and immediately upstream of the rib (labeled as point IV in figure 4.3) for the cases of $Br = 0.05$ and 0.1; however, in the case of $Br = 0.2$, a sole peak is situated at the latter position (point IV, see figure 4.3). This leads to the conclusion that at a sufficiently high Br value, the streamwise impingement onto the windward face of the downstream rib, gives rise to not only an augmentation of the stagnation pressure but also an amplified magnitude of Nusselt number Nu. To refine the study, the average Nusselt number (defined as $Nu_{av} = 1/L_{x,av} \int_0^{L_{x,av}} Nu dx$) is calculated in the central vertical (x-y) plane located at $z/\delta = 0.0$ for all three ribbed duct cases. Here, $L_{x,av}$ is the horizontal distance between sixth and eighth ribs (i.e., $8.7 \leq L_{x,av} \leq 12.1$), where the local Nu exhibits a consistent self-similar pattern (see, figure 4.6). From the equation, it is understood that the magnitude of Nu_{av}/Nu_0 increases from 2.3 to 2.7 as the blockage ratio increases from $Br = 0.05$ to 0.1. However, as the Br value further increases from 0.1 to 0.2, the magnitude of Nu_{av}/Nu_0 decreases and reaches at 2.08.

4.3.2 Temperature variance and turbulent heat fluxes

Figures 4.8(a) and 4.8(b) show the vertical profiles of TKE, $k = \langle u_i' u_i' \rangle/2$, and temperature variance, $\langle \theta' \theta' \rangle$, for different blockage ratios along a central vertical line located at $(x/\delta, z/\delta) = (9.1, 0.0)$, respectively. The results of the three ribbed duct cases are compared against those of the smooth duct case in the central vertical line located at $(x/\delta, z/\delta) = (15, 0.0)$. Figure 4.8(a) clearly shows that due to the disturbances from the ribs, the magnitude of the TKE k of the ribbed duct flows is much larger than that of the smooth duct flow. From figure 4.8(a), it is also clear that owing to the presence of a strong shear layer, the value of TKE progressively increases with an increasing rib height in the region immediately above the rib crest. However, in contrast to this trend of TKE, the value of temperature variance decreases as

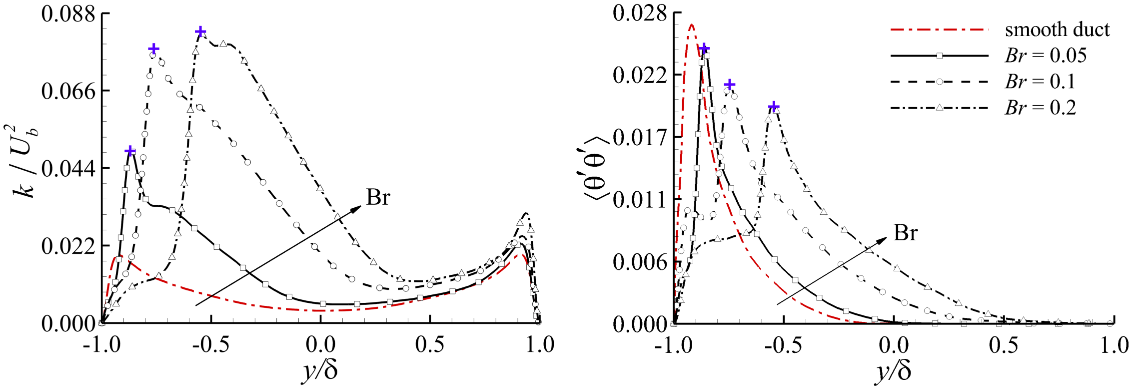

(a) Profile of k/U_b^2

(b) Profile of $\langle\theta'\theta'\rangle$

Figure 4.8: Vertical profiles of non-dimensionalized TKE k and temperature variance $\langle\theta'\theta'\rangle$ along the central vertical lines located at $(x/\delta,\ y/\delta) = (15, 0.0)$ and $(9.1, 0.0)$ for the smooth duct case and ribbed duct cases, respectively. Symbol '+' demarcates the peak position of k or $\langle\theta'\theta\rangle$ for the three ribbed duct cases. The vertical locations of these peaks correspond to $y/\delta = -0.86, -0.76$ and -0.56 for test cases of $Br = 0.05, 0.1$ and 0.2, respectively.

the rib height increases in that region. Although an increase of rib height causes a decrease in the magnitude of $\langle\theta'\theta'\rangle$ close to the ribbed bottom wall, it should not be regarded as the main reason for the reduction in the peak value of $\langle\theta'\theta'\rangle$ because the pitch-to-height ratio also has a significant impact on the turbulence statistics, which decreases monotonically with an increasing rib height. This observation is consistent with the DNS result of Nagano et al. (2004), who studied the effects of rib height on both the velocity and temperature fields in a 2-D plane-channel flow. They observed a low level of temperature variance under the condition of large blockage ratios. From figures 4.8(a) and 4.8(b), the values of both k and $\langle\theta'\theta'\rangle$ peak at $y/\delta = -0.86$, -0.76 and -0.56 in the three ribbed duct cases of $Br = 0.05$, 0.1 and 0.2, respectively. In fact, these three special vertical positions correspond to the same relative elevation that is 0.04δ immediately above the rib crest in each ribbed duct case. In term of wall units, this relative elevation corresponds to $0.04\delta u_{\tau R}/\nu = 11.2, 13.7$ and 16.2 for $Br = 0.05, 0.1$ and 0.2, respectively. The wall shear effect generated by the rib crest is

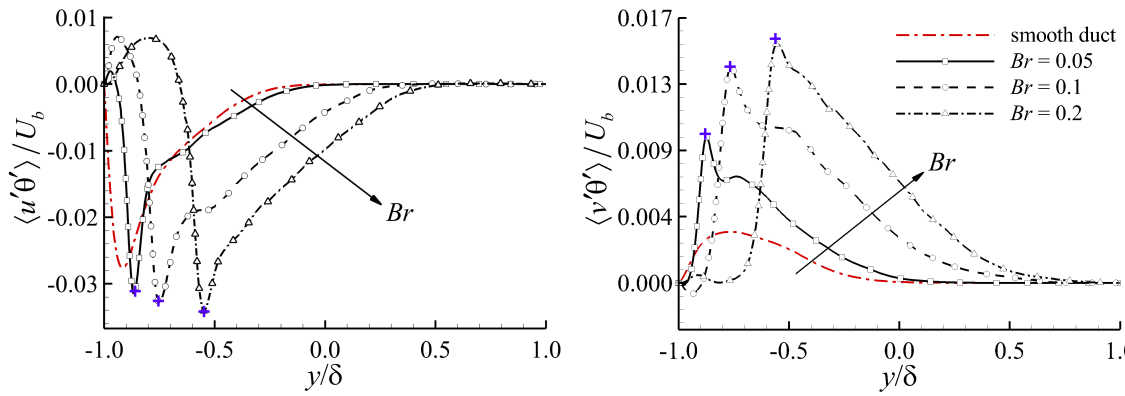

(a) Profiles of $\langle u'\theta' \rangle$

(b) Profiles of $\langle v'\theta' \rangle$

Figure 4.9: Vertical profiles of non-dimensionalized streamwise and vertical turbulent heat fluxes ($\langle u'\theta' \rangle$ and $\langle v'\theta' \rangle$, respectively) along the central vertical lines located at $(x/\delta, y/\delta) = (15, 0.0)$ and $(9.1, 0.0)$ for the smooth duct case and ribbed duct cases, respectively. Symbol '+' demarcates the peak position of $\langle u'\theta' \rangle$ and $\langle v'\theta' \rangle$ for the three ribbed duct cases. The vertical locations of these peaks correspond to $y/\delta = -0.86, -0.76$ and -0.56 for test cases of $Br = 0.05, 0.1$ and 0.2, respectively. Because temperature θ is non-dimensional by definition, turbulent heat fluxes are non-dimensionalized using the bulk mean velocity U_b only.

very strong at this relative elevation either immediately above the ribs or downstream of the ribs due to streamwise convection. In the following analysis, we will pay careful attention to the velocity and temperature statistics at these three special elevations.

Figure 4.9 compares the vertical profiles of streamwise and vertical turbulent heat fluxes (i.e., $\langle u'\theta' \rangle$ and $\langle v'\theta' \rangle$, respectively) of three ribbed duct cases along the same central vertical line as in figure 4.8. The results of the three ribbed duct cases are compared against those of the smooth duct flow in the central vertical plane located at $(x/\delta, z/\delta) = (15, 0.0)$. By comparing figures 4.9(a) and 4.9(b) with figure 4.8(a), it is seen that the trends in the magnitudes of these two turbulent heat fluxes are similar to that of TKE, highlighting the fact that the wall-mounted rib elements impose a strong disturbance near the ribbed bottom wall, leading to an increase in the magnitudes of not only the TKE but also the streamwise and vertical turbulent heat fluxes in the region immediately above the rib crest.

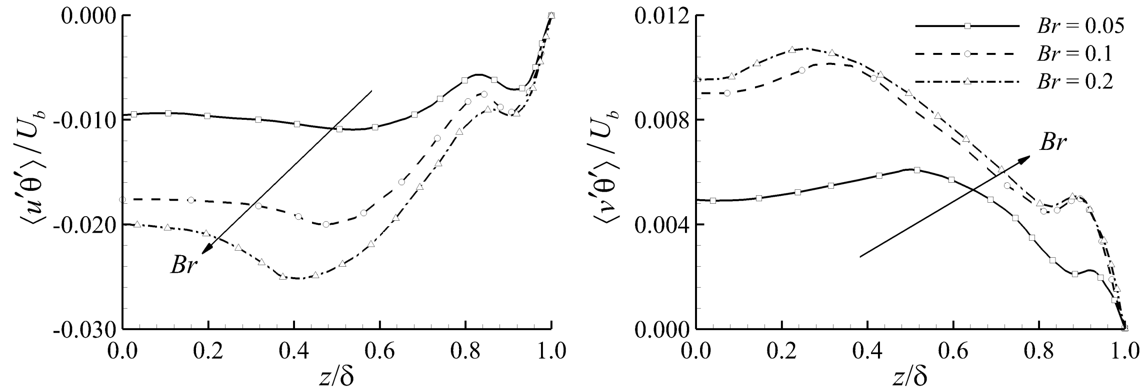

(a) Profiles of $\langle u'\theta'\rangle$ (b) Profiles of $\langle v'\theta'\rangle$

Figure 4.10: Spanwise profiles of non-dimensionalized streamwise and vertical turbulent heat fluxes ($\langle u'\theta'\rangle$ and $\langle v'\theta'\rangle$, respectively) each along an elevated line positioned at $(x/\delta, y/\delta) = (9.1, -0.6)$, $(9.1, -0.5)$, and $(9.1, -0.3)$ for three blockage ratios of $Br = 0.05$, 0.1 and 0.2, respectively. Given the difference in rib heights, these three positions correspond to the same relative elevation that is 0.3δ above the rib crest in each case. Owing to spanwise symmetry, only one half of the duct is plotted. Because temperature θ is non-dimensional by definition, turbulent heat fluxes are non-dimensionalized using the bulk mean velocity U_b only.

To demonstrate the 3-D effects of the ribbed duct flow, figure 4.10 compares the spanwise profiles of the streamwise and vertical turbulent heat fluxes each along an elevated line positioned at $(x/\delta, y/\delta) = (9.1, -0.6)$, $(9.1,\ -0.5)$, and $(9.1,\ -0.3)$ for three blockage ratios of $Br = 0.05, 0.1$ and 0.2, respectively. Given the different heights of ribs in the three test cases, these three vertical are all at the same relative elevation that is 0.3δ (or, $0.15D$) above the rib crest in each case in order to facilitate a fair comparison. As is shown in figures 4.10(a) and 4.10(b), both $\langle u'\theta'\rangle$ and $\langle v'\theta'\rangle$ peak in a region between the sidewall and the center of the duct (e.g., for the $Br = 0.2$ case, the profiles of these two turbulent heat fluxes peak at $z/\delta \approx \pm 0.4$). Furthermore, it is observed that as the rib height increases, the peak positions of $\langle u'\theta'\rangle$ and $\langle v'\theta'\rangle$ shift towards the duct center. This is because of the cross-stream secondary flow motions, which facilitate turbulent transport of TKE and thermal energy by carrying highly energetic vortices from the duct center towards the vertical sidewalls.

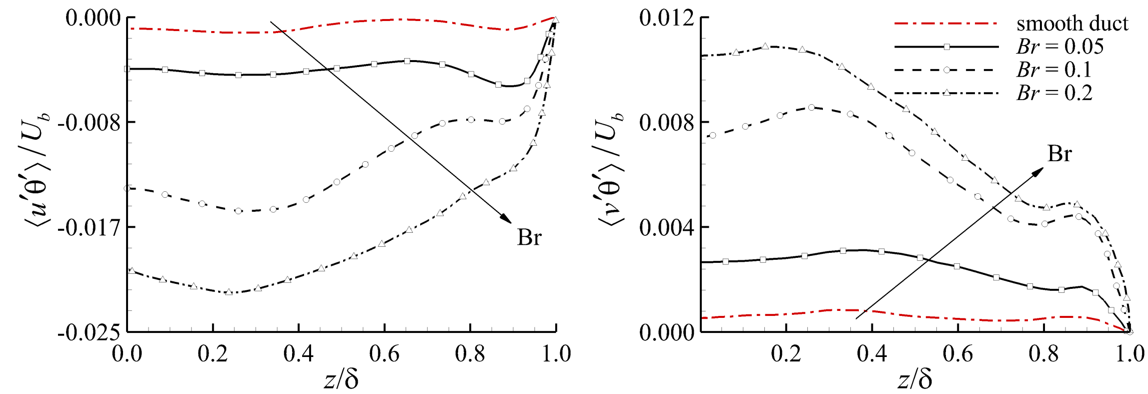

(a) Profiles of $\langle u'\theta' \rangle$

(b) Profiles of $\langle v'\theta' \rangle$

Figure 4.11: Spanwise profiles of non-dimensionalized streamwise and vertical turbulent heat fluxes ($\langle u'\theta' \rangle$ and $\langle v'\theta' \rangle$, respectively) along an elevated line positioned at $(x/\delta, y/\delta) = (15, -0.4)$ and $(9.1, -0.4)$ for smooth and ribbed duct cases, respectively. The comparison of the profiles of turbulent heat fluxes are made at the elevation of $y/\delta = -0.4$. Owing to spanwise symmetry, only one half of the duct is plotted. Because temperature θ is non-dimensional by definition, turbulent heat fluxes are non-dimensionalized using the bulk mean velocity U_b only.

The above analysis of the turbulent heat fluxes based on figure 4.10 was conducted at the same relative elevation above the rib crest (while the absolute elevations are different) for the three ribbed duct cases. To refine the comparative study of the rib effects on turbulent heat transfer, figure 4.11 compares the spanwise profiles of the streamwise and vertical turbulent heat fluxes along an elevated line positioned at $(x/\delta, y/\delta) = (15, -0.4)$ and $(9.1, -0.4)$ for the smooth duct flow and three ribbed duct flows, respectively. The comparison of these square duct cases (either smooth or ribbed) is conducted at an identical elevation of $y/\delta = -0.4$. From figure 4.11, it is clear that both the streamwise and vertical turbulent heat fluxes peak around the sidewalls and duct center. The magnitudes of these increase monotonically as the Br value increases. The appearance of a local maximum in the profile of turbulent heat fluxes near the duct center results from the fact that in the (x-y) plane, high-intensity vortices are generated near the ribs and spread to higher elevations through

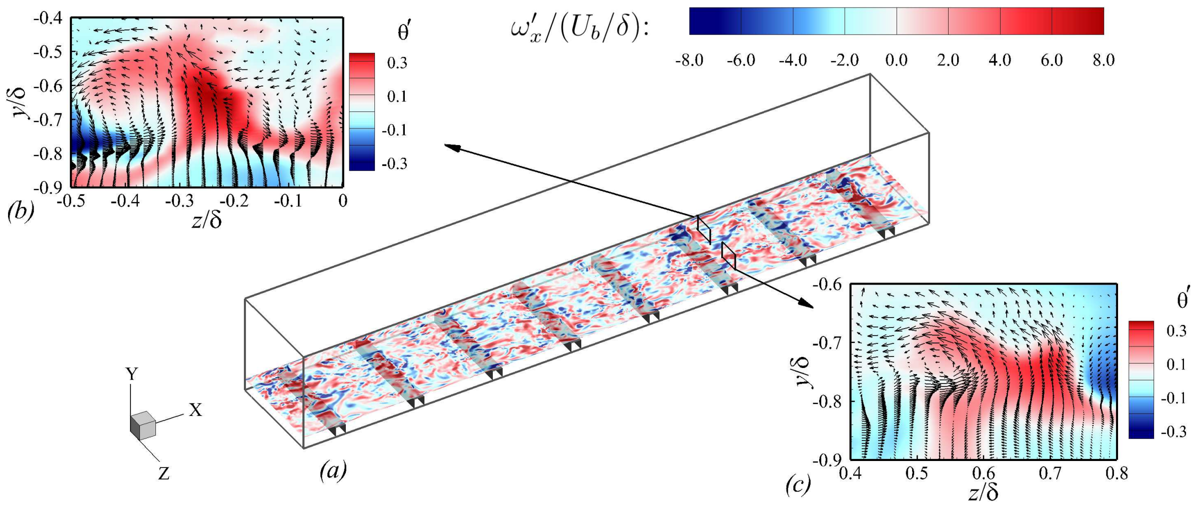

Figure 4.12: Coherent flow structures demonstrated using instantaneous streamwise vorticity fluctuations ω_x' for the case of $Br = 0.1$. The value of ω_x' has been non-dimensionalized by U_b/δ. (*a*) contours of the instantaneous ω_x' in the x-z plane located at $y/\delta = -0.76$. (*b*) and (*c*) contours of instantaneous temperature fluctuations θ' superimposed with instantaneous velocity fluctuations (v', w') in two arbitrary cross-stream planes extracted from the 3D domain at streamwise location $x/\delta = 9.1$.

the shedding of shear layer structures triggered by the rib crest. Simultaneously, strong secondary flows in the (y-z) plane carry these vortices from the duct center and run into the sidewalls of the duct, resulting in large magnitudes of turbulent heat fluxes (near the sidewalls).

4.3.3 Turbulence structures and heat transfer near the ribbed wall

To refine our understanding of the turbulent transport processes of momentum and thermal energy in a ribbed duct, it is useful to analyze the effects of rib height on both the instantaneous streamwise vorticity ω_x' and temperature fluctuations θ' near the rib-roughened bottom wall. Figure 4.12(a) shows the contours of ω_x' in the (x-z) plane (at $y/\delta = -0.76$) above the rib height for the ribbed duct case of

$Br = 0.1$. This particular vertical location is chosen because the magnitudes of $\langle\theta'\theta'\rangle$, $\langle u'\theta'\rangle$ and $\langle v'\theta'\rangle$ peak around $y/\delta = -0.76$ for this blockage ratio (see figures 4.8(b), 4.9(a) and 4.9(b)). As shown in figure 4.12(a), it is clear that instantaneous elongated eddy motions are indicated by positively- and negatively-valued contours of $\omega'_x/(U_b/\delta)$, which alternate in the spanwise direction and meander in the streamwise direction. Due to the presence of the ribs, streaky structures are broken up, which cause amplified streamwise vorticity fluctuations, leading to a high peak value of TKE shown previously in figure 4.8(a). In general, the streaky structure patterns of this 3-D ribbed duct flow as exhibited in figure 4.12(a) are qualitatively different from those in a canonical 2-D turbulent boundary layer (Chernyshenko and Baig, 2005; Adrian, 2007). Figures 4.12(b) and 4.12(c) show the two snapshots of the captured streamwise-elongated vortices, using the vectors of instantaneous fluctuating velocities (v', w') in two cross-stream (y-z) planes at $x/\delta = 9.1$. To demonstrate the role of these vortices in turbulent transport of thermal energy, the contours of temperature fluctuations θ' are also displayed in figures 4.12(b) and 4.12(c). From these two figures, it is evident that violent ejection and sweep motions (represented by blue and red colored contours of θ', respectively) occur near the rib crest (around $y/\delta = -0.8$). It is further observed that ejection events are associated with positively-valued θ', whereas sweep events are coupled with negatively-valued θ'. As such, both ejection and sweep events contribute to the positively- and negatively-valued $\langle v'\theta'\rangle$ and $\langle u'\theta'\rangle$, respectively (see, figures 4.9(b) and 4.9(a)) in the vicinity of the rib crest.

To develop a deeper understanding of the effects of sweep and ejection events on turbulent heat transfer in the region slightly above the rib crest, JPDF of $\sigma_u = u'/u_{rms}$, $\sigma_v = v'/v_{rms}$ and $\sigma_\theta = \theta'/\theta_{rms}$ is calculated for the ribbed duct case of $Br = 0.1$ at the location $(x/\delta, y/\delta) = (9.1, -0.76)$ in the central vertical plane (at $z/\delta = 0.0$), where the peaks of $\langle\theta'\theta'\rangle$, $\langle u'\theta'\rangle$, and $\langle v'\theta'\rangle$ occur. Figures 4.13(a) and 4.13(b) show that there exists a strong negative correlation between u' and θ', and a positive correlation between v' and θ', respectively. The black dash line at 135° indicates a high

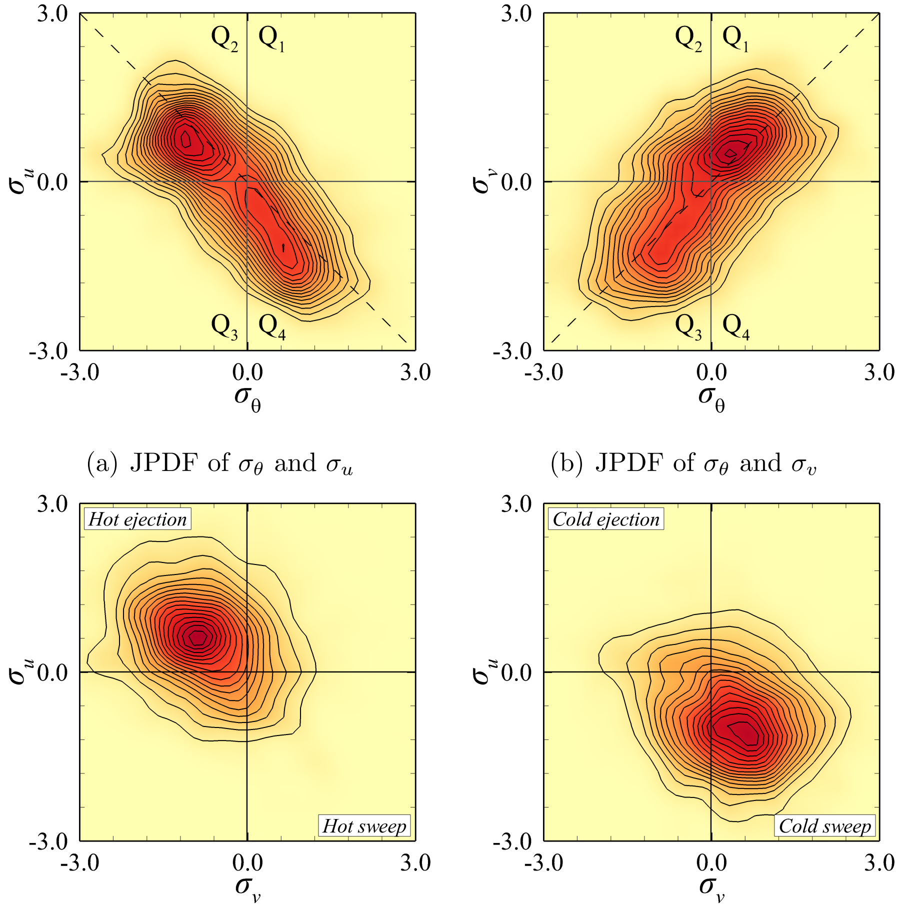

(a) JPDF of σ_θ and σ_u (b) JPDF of σ_θ and σ_v

(c) JPDF of σ_u and σ_v ($\theta' > 0$) (d) JPDF of σ_u and σ_v ($\theta' < 0$)

Figure 4.13: JPDF of σ_θ, σ_u and σ_v at the location $(x/\delta, y/\delta) = (9.1, -0.76)$ in the central vertical plane located at $z/\delta = 0$ for the case of $Br = 0.1$. Contours vary with incremental JPDF value of 0.0035.

correlation between two components at the reference point. For the JPDF between σ_θ and σ_u, there is an apparent preference for the second (Q_2) and fourth (Q_4) quadrant events, which lead to a negatively valued streamwise turbulent heat flux $\langle u'\theta' \rangle$ near the rib crest as shown previously in figure 4.9(a). In contrast, the JPDF of σ_θ and σ_v shows a tendency towards the first (Q_1) and third (Q_3) events leading to positive-valued vertical turbulent heat flux $\langle v'\theta' \rangle$ in figure 4.9(b). The obtained results of the JPDF analysis at the reference point indicate that the ejection (featuring $u' < 0$ and $v' > 0$ associated with Q2) and sweep (featuring $u' > 0$ and $v' < 0$ associated

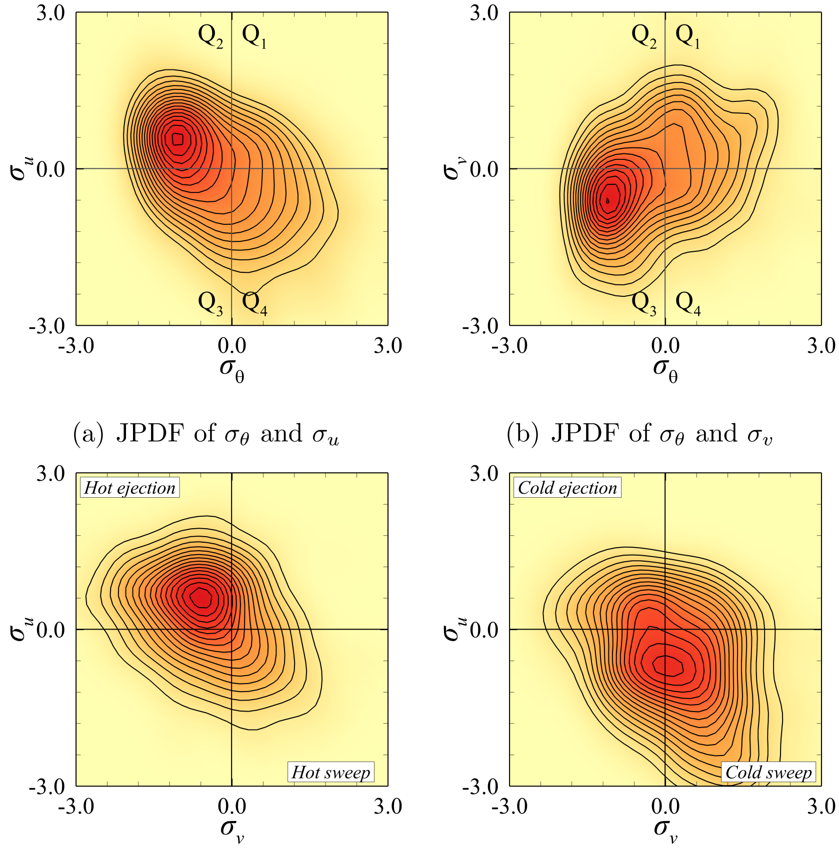

(a) JPDF of σ_θ and σ_u (b) JPDF of σ_θ and σ_v

(c) JPDF of σ_u and σ_v ($\theta' > 0$) (d) JPDF of σ_u and σ_v ($\theta' < 0$)

Figure 4.14: JPDF of σ_θ, σ_u and σ_v at the location $(x/\delta, y/\delta) = (15, -0.76)$ in the central vertical plane located at $z/\delta = 0.0$ for the smooth square duct case. Contours vary with incremental JPDF value of 0.0017.

with Q4) events are dominant near the rib crest, which are mainly attributed to the unsteady large-scale motions in this region, an observation that is consistent with the previous analysis of figures 4.12(b) and 4.12(c). Figures 4.13(c) and 4.13(d) show the occurrence of hot ejection-like and cold sweep-like motions in the region slightly above the rib crest. From this discussion, it can be concluded that in the region near the rib crest, lower momentum fluid packets ($u' < 0$) with higher temperatures ($\theta' > 0$) are ejected into the duct center, meanwhile higher momentum fluid packets ($u' > 0$) with lower temperatures ($\theta' < 0$) sweep towards the ribbed bottom wall.

When these fluid packets interact with the recirculation zone, both $\langle u'\theta' \rangle$ and $\langle v'\theta' \rangle$ increase significantly in their magnitudes near the rib crest.

The physical mechanisms underlying the JPDF patterns of the ribbed duct flow shown in figure 4.13 can be better understood by comparing them with those of a smooth duct flow. Figure 4.14 shows the JPDF of σ_u, σ_v and σ_θ for the smooth duct flow case at the location $(x/\delta, y/\delta) = (15, -0.76)$ in the central vertical plane $(z/\delta = 0.0)$. The reference point is positioned at the same elevation $(y/\delta = -0.76)$ as in figure 4.13 for the ribbed flow case. By comparing figures 4.14 and 4.13, it is observed that despite the differences in the JPDF patterns of the ribbed and smooth duct flow cases, they exhibit a general tendency towards ejection and sweep motions in the near-wall region for both smooth and ribbed duct cases. These turbulent motions cause the values of $\langle u'\theta' \rangle$ and $\langle v'\theta' \rangle$ to become negative and positive at the reference point, respectively (see figure 4.9).

Figure 4.15 shows the iso-surfaces of the swirling strength, λ_{ci}, superimposed onto instantaneous temperature contours in the central vertical plane $(z/\delta = 0.0)$ of the domain for three different rib cases. From figure 4.15, it is observed that as the blockage ratio increases from $Br = 0.05$ to 0.2, the dynamics of turbulence structures near the ribbed bottom wall become more intensified, characterized by enhanced spread and shedding of vortices in the region immediately above the rib crest. This further leads to an enhanced strength of turbulence motions in that region, as well indicated by the magnitude of TKE in figure 4.8(a). From figure 4.13, it is known that the temperature fluctuations are highly correlated with the streamwise and vertical velocity fluctuations near the rib crest, and therefore, the magnitudes of turbulent heat fluxes $\langle u'\theta' \rangle$ and $\langle v'\theta' \rangle$ are greatly enhanced with an increasing Br value, a pattern that is evident in figures 4.9(a) and 4.9(b).

Figure 4.16 shows the iso-surfaces of the instantaneous streamwise vorticity ω_x superimposed onto instantaneous temperature θ contours in the cross-stream y-z plane (located at $x/\delta = 9.1$) for three different rib cases. From figure 4.16, it is

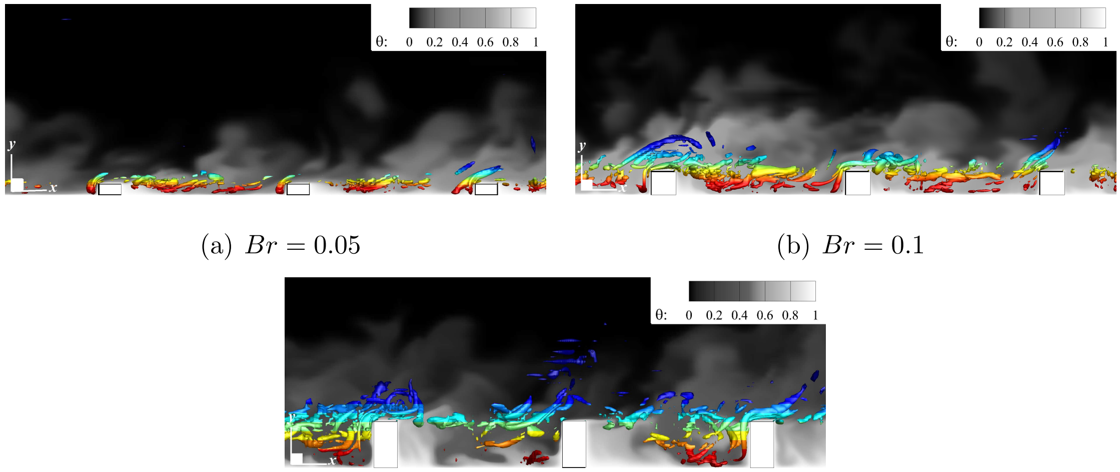

(a) $Br = 0.05$

(b) $Br = 0.1$

(c) $Br = 0.2$

Figure 4.15: Iso-surfaces of the swirling strength λ_{ci} around ribs, colored with $(1 - y/\delta)$, superimposed on the background instantaneous temperature field θ (shown using grey-scaled contours) in the central plane (located at $z/\delta = 0$) for three different rib cases.

evident that owing to the disturbances from the ribs, the energetic vortical structures in all three rib cases are densely populated on the ribbed bottom wall side than on the smooth top wall side. Clearly, as the blockage ratio increases from $Br = 0.05$ to 0.2, the strength of these disturbances becomes more apparent (see figure 4.8(a)); and as a result, more streamwise vortices are generated near the rib crest. This phenomenon results in an enhanced local turbulent transport of momentum and energy between the ribbed bottom wall and duct center. By comparing figures 4.16(a)-4.16(c), it is seen that below the rib height, vortical structures become less populated as the rib height increases, which results in lower heat transfer rate near the leeward face of the ribs as shown previously in figure 4.6. This is a reflection of the fact that as the rib height increases, the recirculation bubble behind a rib increases in size (see figures 4.3 and 4.15), preventing the cold fluid from effectively contacting the heated bottom wall.

Since the streaky structures in a 3-D ribbed duct are sensitive to not only the rib

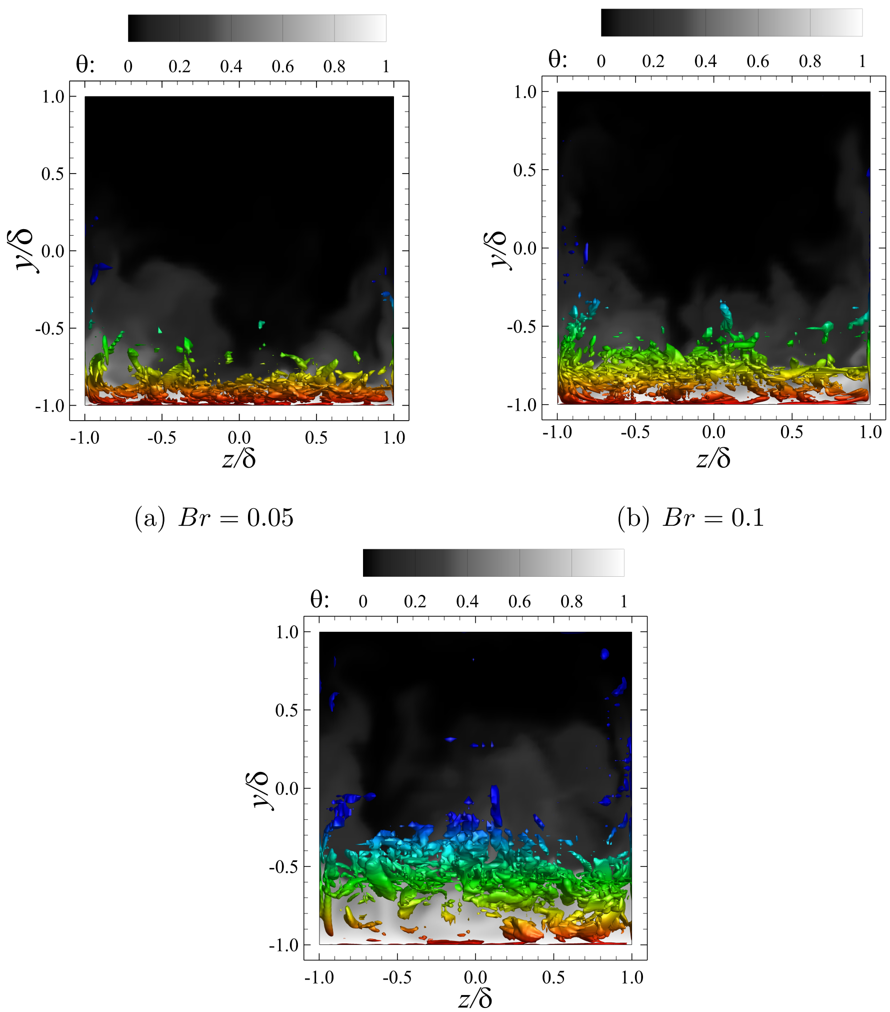

(a) $Br = 0.05$

(b) $Br = 0.1$

(c) $Br = 0.2$

Figure 4.16: Iso-surface instantaneous streamwise vorticity ω_x at the level of $4.5U_b$ in the cross-stream (y-z) plane at $x/\delta = 9.1$ superimposed on to the background instantaneous temperature field θ (shown using grey-scaled contours) for different rib cases. The value of ω_x has been non-dimensionalized by U_b/δ. The iso-surfaces of instantaneous streamwise vorticity are colored using non-dimensionalized elevation $(1 - y/\delta)$.

height but also the boundary layers developed over the two vertical sidewalls of the duct, it would be interesting to investigate the riblet effect on the turbulence structures associated with temperature fluctuations in this peripherally confined space. To

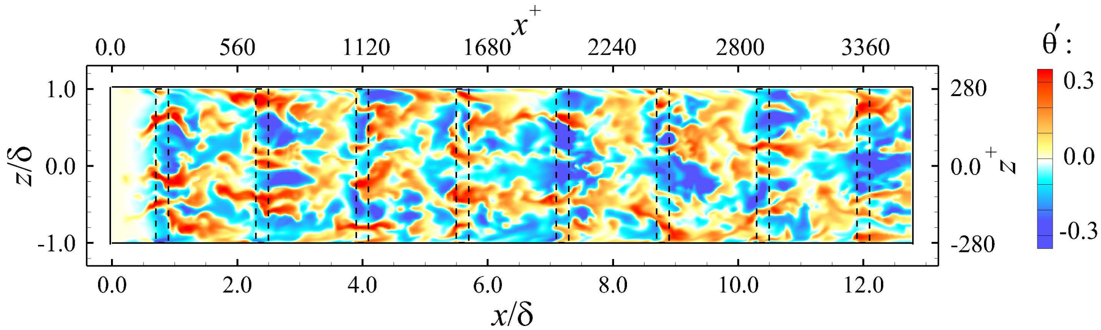

(a) $Br = 0.05$

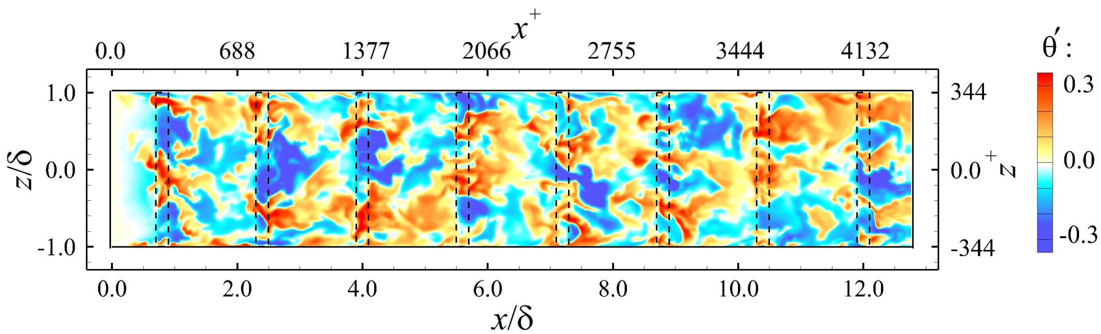

(b) $Br = 0.1$

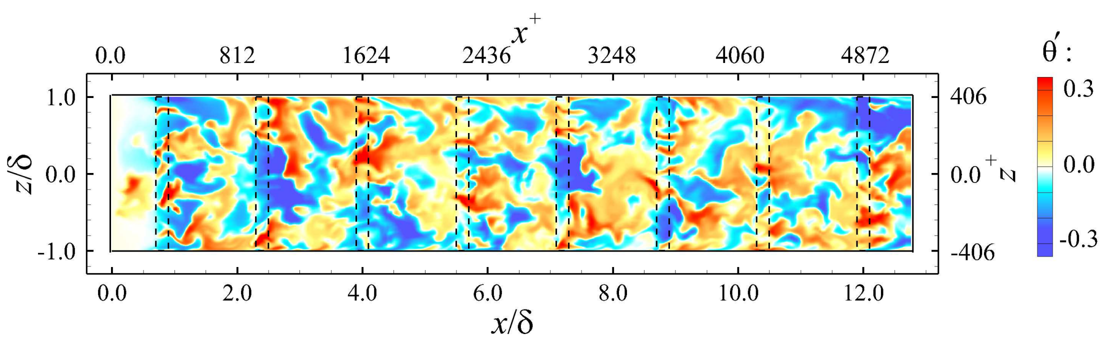

(c) $Br = 0.2$

Figure 4.17: Contours of non-dimensionalized instantaneous temperature fluctuations θ' in the x-z plane immediately above the rib crest for three rib cases. (a) at $y/\delta = -0.86$ for $Br = 0.05$, (b) at $y/\delta = -0.76$ for $Br = 0.1$, and (c) at $y/\delta = -0.56$ for $Br = 0.2$. Given the difference in rib heights, these three vertical positions (i.e., $y/\delta = -0.86$, -0.76 and -0.56 for the three rib cases) correspond to the same relative elevation that is 0.04δ immediately above the rib crest in each rib case, where the value of $\langle\theta'\theta'\rangle$ peaks. In each figure panel, the streamwise coordinate is given both as x/δ (bottom) and as x^+ (top). Similarly, the spanwise coordinate is given both as z/δ (left) and as z^+ (right). The wall units x^+ and z^+ are calculated based on $u_{\tau R}$.

this purpose, contours of the non-dimensionalized instantaneous temperature fluctuations θ' are plotted in figure 4.17 in the x-z plane located at $y/\delta = -0.86, -0.76$ and -0.56 for $Br = 0.05, 0.1$ and 0.2, respectively. As explained above, these three special vertical positions correspond to the same relative elevation that is 0.04δ immediately above the rib crest in each rib case, where the value of $\langle\theta'\theta'\rangle$ peaks. As shown previously in figures 4.9(a) and 4.9(b), at these elevations, both the streamwise and vertical turbulent heat fluxes reach their maxima. From figures 4.17(a)-4.17(c), it is observed that the characteristic length scales and strengths of temperature streaks are sensitive to the rib height. For the rib case of $Br = 0.05$, the streaky structures associated with temperature fluctuations are more elongated in the streamwise direction and are more similar to those of a classical turbulent plane-channel flow (e.g., Kim and Moin, 1989). However, as the rib height increases, the strength of induced disturbances by the rib elements increases (see figure 4.8(a)). Consequently, the streaky structures associated with temperature fluctuations violently break up and the flow becomes increasingly "patchy" in the exhibited x-z plane.

To refine our study of the effects of rib height on turbulence structures and associated temporal scales, the spatial two-point cross-correlation coefficients between the streamwise velocity and temperature fluctuations can be analyzed, which is defined as

$$R^s_{u\theta}(x_{ref}, y_{ref}, x, y) = \frac{\langle\theta'(x,y)u'(x_{ref}, y_{ref})\rangle}{\sqrt{\langle\theta'^2(x,y)\rangle\langle u'^2(x_{ref}, y_{ref})\rangle}} \quad , \tag{4.4}$$

where (x_{ref}, y_{ref}) are the coordinates of the reference point and superscript "s" denotes spatial correlation. The streamwise coordinate of the reference point is fixed at $x_{ref}/\delta = 9.1$, while the vertical coordinate being $y_{ref}/\delta = -0.86$ and -0.4 (for the rib case of $Br = 0.05$) and $y_{ref}/\delta = -0.56$ and -0.4 (for the rib case of $Br = 0.2$). From figure 4.18, it is seen that the cross-correlation coefficient $R^s_{u\theta}$ is larger at the reference point near the rib crest and smaller at the reference point far above the rib crest. More specifically, the value of $R^s_{u\theta}$ decreases by 27% and 15% as y_{ref}/δ increases from -0.86 and -0.56 to -0.4 for cases of $Br = 0.05$ and 0.2, respectively. This feature is consistent with the observation in figure 4.13(a) that the streamwise velocity fluctuations synchronize well with the temperature fluctuations in the region immediately above the rib element, such that the value of $\langle u'\theta' \rangle$ reaches its maximum near the rib crest as shown in figure 4.9(a). From this figure, it is also observed that similar to the trend of $R^s_{u\theta}$, the value of the inclination angle α of turbulence structures decreases as y/δ increases. This implies that the hot ejection motions become less violent as the vertical distance from the rib crest increases. By comparing figures 4.18(a) and 4.18(b) with figures 4.18(c) and 4.18(d), respectively, it is clear that the value of $R^s_{u\theta}$ decreases as a result of an increasing rib height; however, the inclination angle α of the isopleths of $R^s_{u\theta}$ increases considerably. From this discussion, it can be concluded that owing to the intensification by the disturbances from the ribs with an increasing rib height, the Reynolds analogy between turbulent transport of momentum and that of thermal energy (indicated by u' and θ') becomes less applicable as the Br value increases.

The above analysis of spatial scales of the turbulent velocity and temperature fields were conducted in the physical space based on the two-point cross-correlation coefficients. Alternatively, the analysis can be performed in a spectral space based on the energy spectrum, which are the counterparts of two-point auto-correlation coefficients in Fourier transform. Although the results of two-point auto-correlation coefficients have the advantage of being very intuitive, more precise information on turbulence energy level, and temporal frequencies and scales can be obtained through a spectral analysis. The temporal energy spectra and pre-multiplied energy spectra of the streamwise and temperature fluctuations are shown in figure 4.19. The comparison of the two ribbed flow cases (of $Br = 0.05$ and 0.2) is conducted at the elevation that is slightly above the rib crest (with the spatial reference point being identical to that used in figures 4.18(a) and 4.18(c)). From figures 4.19(a) and 4.19(b), it is clear that for a wide range of temporal frequencies (measured using Strouhal number $f\delta/U_b$), the spectral difference between the non-dimensionalized streamwise velocity

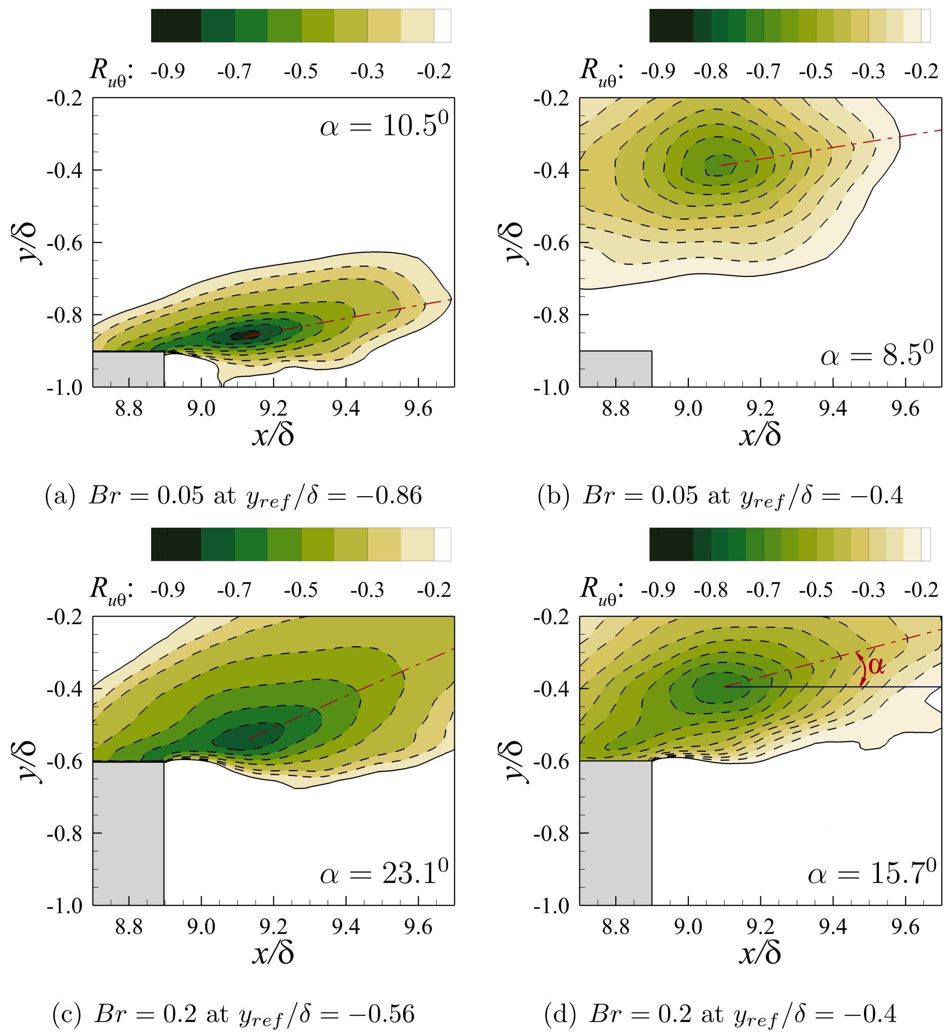

(a) $Br = 0.05$ at $y_{ref}/\delta = -0.86$

(b) $Br = 0.05$ at $y_{ref}/\delta = -0.4$

(c) $Br = 0.2$ at $y_{ref}/\delta = -0.56$

(d) $Br = 0.2$ at $y_{ref}/\delta = -0.4$

Figure 4.18: Isopleths of two-point cross-correlations of the fluctuating streamwise velocity and temperature calculated at two reference points of different elevations at the streamwise location of $x_{ref}/\delta = 9.1$ in the central vertical plane located at $z/\delta = 0.0$. Note that the reference points at $y_{ref}/\delta = -0.86$ and -0.56 coincide with the peaks positions of $\langle\theta'\theta'\rangle$, $\langle u'\theta'\rangle$, and $\langle v'\theta'\rangle$ for $Br = 0.05$ and 0.2 cases, respectively. The isopleth value ranges from -0.2 to -1.0, with the outermost and innermost isopleths corresponding to $R^s_{u\theta} = -0.2$ and -1.0, respectively.

and temperature fluctuations (i.e., $E_{uu}U_b/(\delta\langle u'u'\rangle)$ and $E_{\theta\theta}U_b/(\delta\langle\theta'\theta'\rangle)$, respectively) is minimal. However, as the Br value increases from 0.05 to 0.2, difference between these two energy spectrum terms can be observed in figure 4.19(b), especially at low frequencies (corresponding to large temporal scales). Furthermore, it is apparent the

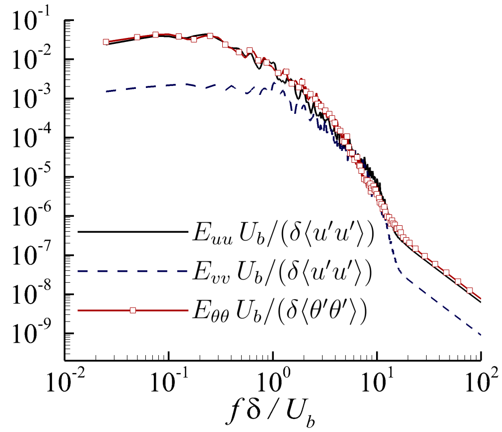

(a) Temporal energy spectra ($Br = 0.05$)

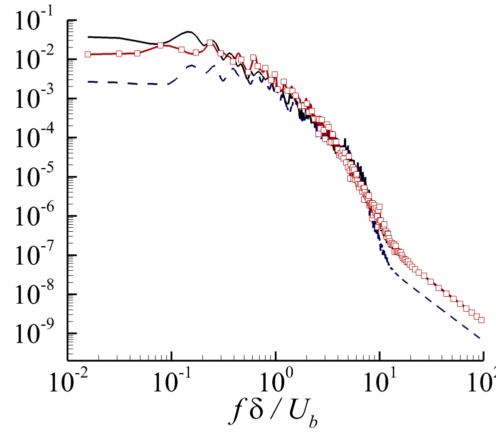

(b) Temporal energy spectra ($Br = 0.2$)

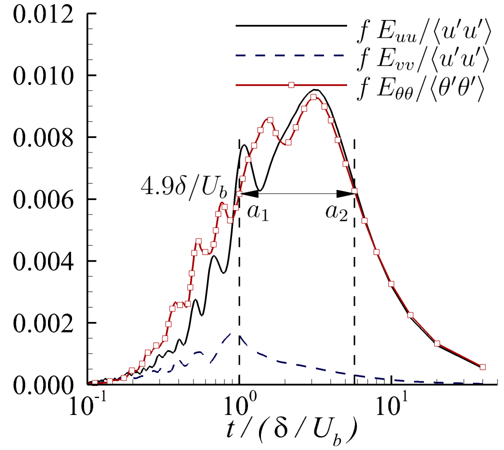

(c) Pre-multiplied energy spectra (Br = 0.05)

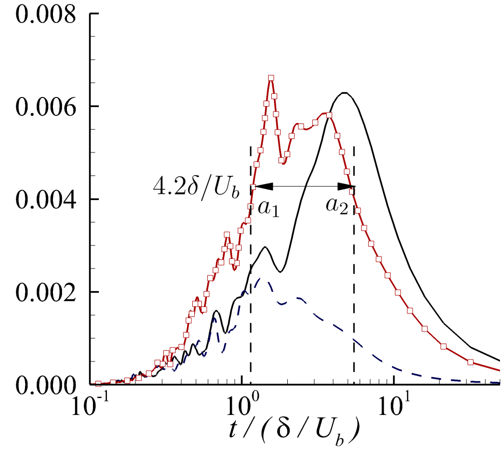

(d) Pre-multiplied energy spectra (Br = 0.2)

Figure 4.19: Non-dimensionalized temporal energy spectra and pre-multiplied energy spectra of the streamwise and vertical velocity fluctuations and temperature fluctuations for two different rib cases of $Br = 0.05$ and 0.2. The comparison of the two ribbed flow cases is conducted at the elevation that is slightly above the rib crest (with the spatial reference point being identical to that used in figures 4.18(a) and 4.18(b)).

energy spectrum level of temperature fluctuations as indicated by the magnitude of $E_{\theta\theta}U_b/(\delta\langle\theta'\theta'\rangle)$ decreases slightly with an increasing rib height. This is also consistent with the observation in figure 4.8(b) that the level of temperature variance $\langle\theta'\theta'\rangle$

monotonically decreases as the rib height increases in the region immediately above the rib crest. As is evident in figures 4.19(c) and 4.19(d), similar to the temporal energy spectra, the discrepancies between the non-dimensionalized pre-multiplied energy spectra of streamwise velocity and temperature fluctuations (i.e., $fE_{uu}/\langle u'u'\rangle$ $fE_{\theta\theta}/\langle \theta'\theta'\rangle$, respectively) increase near the rib crest as the blockage ratio increases. Furthermore, by comparing figures 4.19(c) with 4.19(d), it is observed that as the rib height increases, the characteristic temporal scales of turbulence structures (as indicated by the modes of $fE_{uu}/\langle u'u'\rangle$ and $fE_{vv}/\langle u'u'\rangle$) increase, whereas the temporal scale of thermal structures (as indicated by the mode of $fE_{\theta\theta}/\langle \theta'\theta'\rangle$) decreases monotonically. For example, the mode of $fE_{\theta\theta}/\langle \theta'\theta'\rangle$ occurs at the non-dimensional temporal scale of $t/(\delta/U_b) \approx 3.1$ in the case of $Br = 0.05$, but at $t/(\delta/U_b) \approx 1.8$ in the case of $Br = 0.2$. The energetic turbulence scales associated with the temperature fluctuations near the rib crest can be further quantified by defining the energy-containing range which possesses premultiplied energy spectra that are at least 70% of the peak value (bounded by the vertical dashed lines "a_1" and "a_2" in figures 4.19(c) and 4.19(d)). By comparing 4.19(c) and 4.19(d), it is observed that owing to the significant changes in the temporal scales generated by the rib elements, the energy-containing range narrows monotonically from $4.9\delta/U_b$ to $4.2\delta/U_b$ as the blockage ratio increases from $Br = 0.05$ to 0.2.

To further investigate the temporal scales of turbulent motions in the three ribbed duct flow cases, the temporal auto-correlation the function of velocity and temperature fluctuations should be examined, which is defined as

$$R^t_{\phi\phi}(t) = \frac{\langle \phi(t)\phi(t_{ref})\rangle}{\sigma_\phi \sigma_\phi} \quad , \tag{4.5}$$

where, t_{ref} denotes the reference time origin, superscript "t" represents temporal correlation, and "σ_ϕ" denotes the root mean square (r.m.s.) value of ϕ. In figure 4.20, the temporal auto-correlations of the streamwise and vertical velocity fluctuations and temperature fluctuations for three different ribbed duct cases are compared at

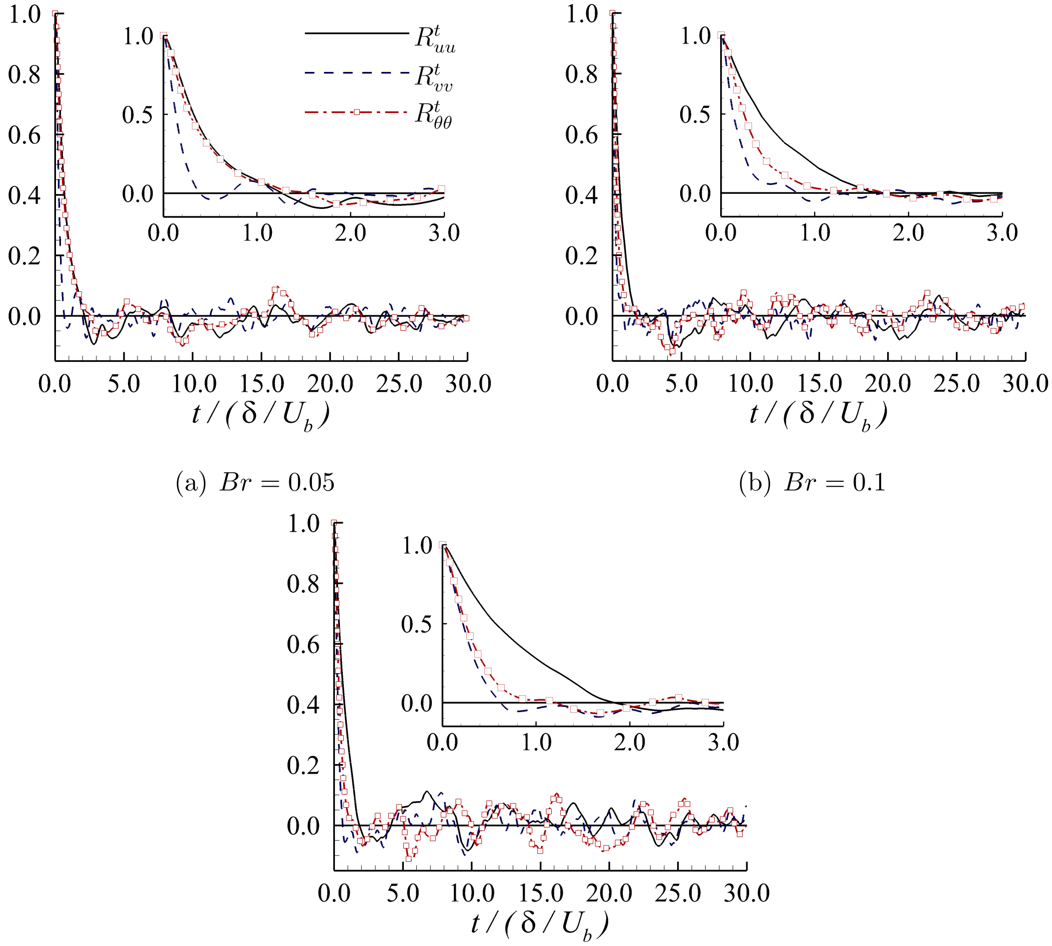

(a) $Br = 0.05$

(b) $Br = 0.1$

(c) $Br = 0.2$

Figure 4.20: Temporal auto-correlations $R^t_{\phi\phi}(t)$ of the streamwise and vertical velocities fluctuations and temperature fluctuations displayed in the central vertical plane located at $(x/\delta, z/\delta) = (9.1, 0.0)$ for different blockage ratios. The vertical coordinate of the reference point is $y_{ref}/\delta = -0.86$, -0.76 and -0.56 for $Br = 0.05, 0.1$ and 0.2, respectively. For all three rib cases, in order to show clearly the profiles of the temporal auto-correlation function $R^t_{\phi\phi}(t)$ around the reference time origin, they are partially enlarged and replotted in inset graphs.

the elevation that is slightly above the rib crest. By comparing figures 4.20(a)–4.20(c), it is evident that the trends of temporal auto-correlation coefficient become increasingly different between the streamwise velocity and temperature fluctuations as the rib height increases. From figure 4.20, it is observed that the decaying rate of the

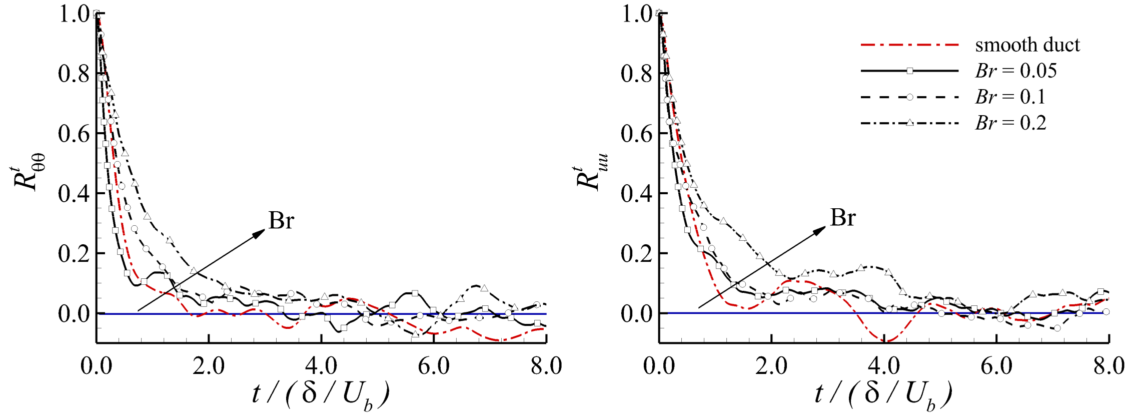

(a) Profiles of $R_{\theta\theta}$ (b) Profiles of R_{uu}

Figure 4.21: Temporal auto-correlations of the streamwise velocity fluctuations and temperature fluctuations (R^t_{uu} and $R^t_{\theta\theta}$, respectively) displayed in the central vertical plane located at $(x/\delta,\ z/\delta) = (15, 0.0)$ and $(9.1, 0.0)$ for the smooth duct case and ribbed duct cases, respectively. The comparison of these square duct cases (either smooth or ribbed) is conducted at the same elevation of $y/\delta = -0.4$.

auto-correlation function $R^t_{\theta\theta}$ becomes faster with an increasing rib height, indicating a trend of increasingly shortened temporal scales associated with instantaneous temperature fluctuations. However, in contrast to the trend of $R^t_{\theta\theta}$, the decaying rate of R^t_{uu} becomes slower as the rib height increases. This implies that the temporal scales of the turbulent motions near the rib crest increase as a result of an increasing rib height. This conclusion is consistent with our previous analysis of pre-multiplied energy spectra of u' and θ' on figures 4.19(c) and 4.19(d).

The above discussion of the temporal auto-correlations $R^t_{\phi\phi}$ is based on the same relative elevation that is 0.04δ immediately above the rib crest in each ribbed duct flow case. To refine our analysis, the temporal auto-correlation of the streamwise velocity and temperature fluctuations (i.e., R^t_{uu} and $R^t_{\theta\theta}$, respectively) are plotted in figure 4.21 in the central vertical plane at the same elevation of $y/\delta = -0.4$ for all three ribbed duct cases. Furthermore, the results of three ribbed duct flow cases are compared against that of a heated smooth duct flow case. As shown in figure 4.21, the decaying rates of $R^t_{\theta\theta}$ and R^t_{uu} of the two ribbed duct flow cases of lower blockage ratios (of $Br = 0.05$ and 0.5) are close to those of the smooth duct flow case. From figure 4.21, it is also evident that the characteristic temporal scales of both turbulence structures and thermal structures (as indicated by the magnitudes of R^t_{uu} and $R^t_{\theta\theta}$, respectively) increase as the Br value increases at an elevation well above the bottom wall. This result is consistent with our previous observation (Mahmoodi-Jezeh and Wang, 2020), in the sense that the spatial length scales of turbulent motions also become larger at the same elevation (of $y/\delta = -0.4$) as the Br value increases.

4.4 Chapter summary

Direct numerical simulation is performed to study turbulent heat transfer in ribbed square duct flows of three different blockage ratios. In order to examine the effects of ribs on the turbulent heat transfer, the results of the three ribbed duct cases are compared with those of a smooth square duct flow case at the same bulk Reynolds number of $Re_b = 5600$. The effect of sidewalls and ribs on the statistical moments of the temperature field and coherent structures is investigated. In contrast to the 2-D rib-roughened boundary-layer flow over a flat plate, turbulent transport of momentum and thermal energy is influenced by not only rib-induced disturbances but also strong secondary flows in the cross-stream directions of the duct. As a result, both the flow and temperature fields are intrinsically 3-D and statistically inhomogeneous in all three directions.

It is observed that the mean flow patterns in the inter-rib region under the rib height are qualitatively different for different Br values. For the ribbed duct cases of $Br = 0.05$ and 0.1, the reattachment point III occurs in between the two adjacent ribs. However, for the ribbed duct case with $Br = 0.2$, the recirculation vortex II occupies almost the entire cavity between the two ribs (under the rib height), such that the reattachment point is non-present and the mean flow “skims” over the two ribs and the cavity between them. Furthermore, owing to the confinement of the four sidewalls of the duct, strong organized secondary flows appear in the cross-stream directions, which drastically influence the mean temperature field and distribution of Nusselt number near the two sidewalls of the square duct. The magnitude of the total drag coefficient $(C_f + C_p)$ is also observed to be strongly influenced by the rib height. The level of $(C_f + C_p)$ increases monotonically near the windward face of the rib with an increasing rib height. This phenomenon leads to an enhanced impinging effect of the flow onto the windward face of the rib, which further leads to an amplified magnitude of Nusselt number Nu.

Owing to the strong shear layer generated by the rib crest, the value of TKE k progressively increases with an increase of rib height in the region immediately above the rib crest. However, in contrast to this trend of TKE, the value of temperature variance $\langle \theta'\theta' \rangle$ decreases as the rib height increases in the same region. The magnitudes of streamwise and vertical turbulent heat fluxes (i.e., $\langle u'\theta' \rangle$ and $\langle v'\theta' \rangle$, respectively) enhance as the rib height increases. For all three ribbed duct cases, the highest turbulent heat fluxes levels occur slightly above the rib crest, where the levels of both TKE k and temperature variance $\langle \theta'\theta' \rangle$ are the greatest. Owing to the cross-stream secondary flow motions, both profiles of $\langle u'\theta' \rangle$ and $\langle v'\theta' \rangle$ peak in the region between the sidewall and duct center. The magnitudes of turbulent heat fluxes $\langle u'\theta' \rangle$ and $\langle v'\theta' \rangle$ increase monotonically as the rib height increases in the central region of the duct.

The influence of turbulence structures on the temperature field near the rib crest is analyzed using the JPDF of the streamwise velocity and temperature fluctuations, λ_{ci}-criterion, temporal auto-corrections, temporal spectra, and spatial two-point cross-correlations of the turbulence field. The results show that owing to the disturbances from the ribs, energetic vortical structures in all three ribbed duct cases are more densely populated on the ribbed bottom wall side than on the smooth top wall side. Furthermore, the strengths of both rib-generated disturbances and structures enhance as the rib height increases. This leads to the formation of incoherent structures and the occurrences of violent ejection and sweep events. The ejection and sweep events are coupled with positively- and negatively-valued temperature fluctuations θ', respectively, in the region immediately above the rib elements. In fact, based on an analysis of the instantaneous streamwise vorticity fluctuations and JPDF, it is observed that in the region near the rib crest, lower momentum fluid packets ($u' < 0$) with higher temperatures ($\theta' > 0$) are ejected into the duct center, meanwhile higher momentum fluid packets ($u' > 0$) with lower temperatures ($\theta' < 0$) sweep towards the ribbed bottom wall. When these fluid packets interact with the recirculation zone, both $\langle u'\theta' \rangle$ and $\langle v'\theta' \rangle$ increase significantly in their magnitudes near the rib crest. The existence of hot ejection and cold sweep motions make significant contributions to the sustained levels of negatively- and positively-valued of streamwise and vertical turbulent heat fluxes near the rib crest, respectively.

The study of spatial two-point cross-correlations of the streamwise velocity and temperature fluctuations indicates that as the rib height increases, the Reynolds analogy between turbulent transport of momentum and that of thermal energy (indicated by u' and θ') becomes less applicable. Specifically, close to the rib crest, the value of $R^s_{u\theta}$ decreases by 16% as the Br value increases from 0.05 to 0.2. Based on the analysis of the pre-multiplied energy spectra of streamwise velocity and temperature fluctuations (i.e., $fE_{uu}/\langle u'u' \rangle$ and $fE_{\theta\theta}/\langle \theta'\theta' \rangle$, respectively), it is discovered that the spectral difference between the non-dimensionalized streamwise velocity and temperature fluctuations increases near the rib crest as the blockage ratio increases. It is also observed that the range of temporal scales of the most energetic turbulent motions associated with the temperature fluctuations (with the value of $fE_{\theta\theta}/\langle \theta'\theta' \rangle$ being at least 70% of its peak value) narrows around the rib height as the blockage ratio increases. Based on an analysis the temporal auto-correlations, it is observed that the temporal scales associated with temperature fluctuations decrease with an increasing rib height in a region slightly above the rib crest. However, the trend reverses at an elevation well above the rib crest.

Finally, it should be indicated that compared to the classical 2-D ribbed boundary-layer flows developing over flat plates, DNS study of turbulent heat and fluid flows in a 3-D ribbed duct is still relatively new. In this DNS study, we have investigated the effects of the blockage ratio ($Br = H/D$) and pitch-to-height ratio P/H on turbulent heat transfer, and compared three ribbed duct flow cases with a smooth duct case. However, there are other important parameters that also influence the velocity and temperature fields in a ribbed duct, including the duct aspect ratio L_y/L_z, width-to-pitch ratio of the rib W/P, Reynolds number, and streamwise domain length L_x (which affects the predictive accuracy of DNS in terms of the captured characteristic streamwise length scales of the most energetic turbulence structures). The physics of this type of turbulent heat and fluid flow in a ribbed duct will be better understood as more DNS studies appear in literature.

Chapter 5

Direct numerical simulation of turbulent duct flow with inclined or V-shaped ribs mounted on one wall

5.1 Introduction

In this chapter, highly-disturbed turbulent flow with distinct three-dimensional characteristics in a square duct with inclined or V-shaped ribs mounted on one wall is investigated using direct numerical simulation. The Reynolds number based on the bulk mean velocity is fixed at $Re_b = 7000$ for both ribbed duct cases, while the Reynolds number based on the mean streamwise wall friction velocity of the ribbed bottom wall is $Re_{\tau R} = 642$ and 1294 for the inclined and V-shaped rib cases, respectively. The turbulent flow in either an inclined or a V-shaped rib-roughened duct is strongly inhomogeneous in all three directions, influenced by not only the rib elements but also the four duct sidewalls. As a result, although both inclined and V-shaped rib elements exert significant disturbances to the flow field, the effects of these two types of rib elements are different in terms of the distribution of the mean streamwise and vertical velocities, mean and turbulent secondary flows, the pressure and viscous drag coefficients, Reynolds stresses, the budget balance of TKE, coherent flow structures, as well as the spatial and temporal scales of turbulence. In regards to this topic, the remainder of this paper is organized as follows. In section 5.2, the governing equations, numerical algorithms, and test cases are described. Also in this section, a detailed study of the minimal computational domain required for accurately capturing turbulent flow structures in a square duct with either inclined or V-shaped ribs mounted on one wall is conducted. In section 5.3, the influence of both sidewalls and ribs on the statistically averaged quantities are analyzed, including the mean flows, the pressure and viscous drag coefficients, Reynolds stresses, as well as budget balance of TKE. Furthermore, the TKE production term is decomposed into an "active" and an "inactive" components, following the proposal of Hinze (1972). This decomposition further allows us to determine whether the difference in the magnitude of the TKE production term is caused by large- or small-scale eddies. In section 5.4, the effects of rib geometry on turbulent flow structures are investigated using multiple tools such as vortex identifiers, joint probability density functions (JPDF) of streamwise and vertical velocity fluctuations, two-point auto-correlation functions, and premultiplied energy spectra. In section 5.5, major conclusions of this research are summarized.

5.2 Test case and numerical procedure

Figure 5.1 shows the geometry of the computational domain and body-fitted mesh used in our DNS. The streamwise, vertical and spanwise domain sizes for the current study are set to $L_x \times L_y \times L_z = 64H \times 10H \times 10H$, respectively. Both cross-sections of the duct and ribs are square-shaped, with the side lengths H and D ($L_y = L_z = D$), respectively. The distance between the ribs (P) in the streamwise direction is $8.0H$,

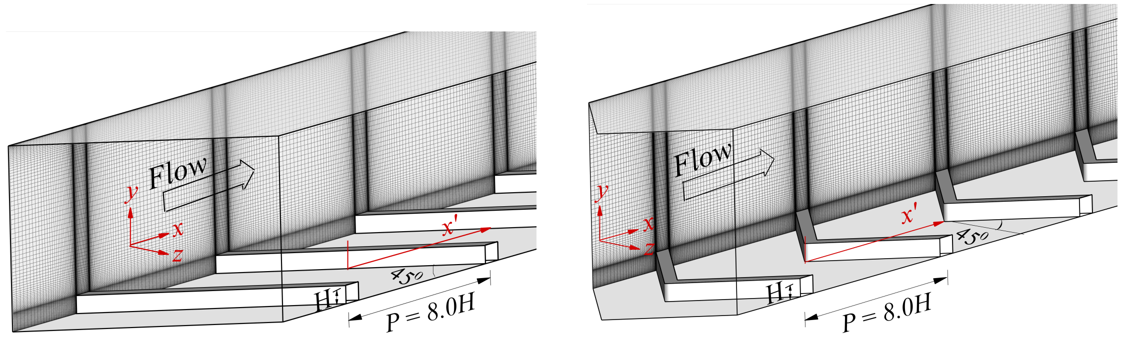

(a) $Br = 0.05$ (b) $Br = 0.2$

Figure 5.1: Schematic of the 3-D duct with the different rib geometries, coordinates and grid system. The side length of the square-shaped rib and duct is H and D, respectively. The origin of the absolute coordinate system $[x, y, z]$ is located at the centre of the inlet (y-z) plane. Eight rib periods are simulated in this DNS study. To facilitate the analysis of each rib period, the relative streamwise coordinate x' is defined, with its origin located at the windward face of each rib.

and both height and width of the rib are 10% of the duct height (i.e., $H = 0.1D$). This same rib height has been also used for the rib-roughened duct flows in the PIV studies of Wang et al. (2010), Coletti et al. (2013) and Fang et al. (2015), and in the LES studies of Sewall et al. (2006) and Fang et al. (2017). Periodic boundary conditions are prescribed for velocity components in the streamwise direction and a no-slip boundary condition is applied to all solid walls. The mass flow rate is kept constant, which offers a fixed-valued bulk Reynolds number (Re_b) for both rib cases. This is similar to the study of Fang et al. (2015) and Coletti et al. (2012), who conducted an experimental study of rib-roughened duct flows based on a constant bulk Reynolds number Re_b. The Reynolds number is $Re_b = U_b D/\nu = 7000$, where U_b denotes the average bulk mean velocity over the streamwise direction.

Table 5.1 shows the key parameters involved in our comparative study of inclined and V-shaped ribbed duct flow test cases. The Reynolds number based on the rib height is defined as $H^+ = Hu_{\tau R}/\nu$. Alternatively, the Reynolds number can be defined based on the mean streamwise wall friction velocities of the smooth top and

Table 5.1: Key flow parameters of the inclined and V-shaped test cases.

Case	D_v/D_p	D_t ($\mathrm{m^2 s^{-2}}$)	H^+	$Re_{\tau R}$	$Re_{\tau S}$	Re_b
inclined	14.6	3.35×10^{-2}	128	641	288	7000
V-shaped	4.72	1.37×10^{-1}	259	1294	300	7000

ribbed bottom walls (i.e., $Re_{\tau S} = \delta u_{\tau S}/\nu$ and $Re_{\tau R} = \delta u_{\tau R}/\nu$, respectively) in the central vertical (x-y) plane located at $z/\delta = 0.0$. Here, $\delta = D/2$ is the half side length of the square duct, which is defined in an analogy to the usual convention used in the study of a 2-D smooth or ribbed plane-channel flow. For a smooth wall, the friction velocity ($u_{\tau S}$) is directly defined as the mean streamwise velocity gradient (i.e., $u_{\tau S} = (\nu \partial \langle u \rangle / \partial y)^{1/2}$). However, calculation of the friction velocity on a ribbed wall is complex as it is determined by both viscous and pressure drags as $u_{\tau R} = (D_p + D_v)^{1/2}$. This method for calculating $u_{\tau R}$ follows the approach of Leonardi and Castro (2010) and Ismail et al. (2018) in their DNS study of 2-D ribbed turbulent channel flows and Mahmoodi-Jezeh and Wang (2020) in their DNS study of turbulent flow in a 3-D square duct with transverse ribs mounted on one wall. Here, D_p and D_v represent the pressure and viscous drag forces in the central (x-y) plane, defined as $D_p = 1/(\rho L_x) \sum_{n=1}^{N} \int_0^H (\langle P_{wind} \rangle - \langle P_{lee} \rangle) dy$ and $D_v = \mu/(\rho L_x) \int_0^{L_x} (\partial \langle u \rangle / \partial y)_w \, dx$, respectively. In these equations, subscript 'w' denotes either the bottom wall or top of the rib elements, N is the total number of rib elements, $\langle \cdot \rangle$ denotes averaging over time and over the eight rib periods, and P_{wind} and P_{lee} represent the pressure on the windward and leeward faces of a rib, respectively. The total drag forcing term is $D_t = D_p + D_v$ in the central (x-y) plane. Given the 3-D nature of the flow, the evaluation of the characteristic values of the mean wall friction velocities ($u_{\tau R}$ and $u_{\tau S}$) and drag forces (D_p and D_v) are done in the central (x-y) plane here, simply because these values vary in the spanwise direction. Different from a conventional 2-D ribbed flow over a flat plate, the 3-D ribbed duct flows studied here is statistically inhomogeneous in all three directions.

From table 5.1, it is clear that a significant fraction of the friction velocity on the ribbed bottom wall $u_{\tau R}$ is contributed by pressure drag D_p, as the ratio of the friction drag D_v to the pressure drag D_p is 14.6% and 4.72% for the inclined and V-shaped rib cases, respectively. This implies that there exists a significant pressure difference between the windward and leeward faces of the inclined and V-shaped ribs (as will be further discussed in section 3.2). Furthermore, it is observed that the value of D_t in the inclined rib case is one order of magnitude smaller than that in the V-shaped rib case, resulting in a smaller magnitude of the mean friction velocity $u_{\tau R}$ on the ribbed bottom wall.

An in-house computer code was developed using FORTRAN 90/95 to solve the governing equations, and Message passing interface (MPI) libraries were used to parallelize the code. In order to simulate the turbulent fluid flow over non-orthogonal ribs within a square duct, the continuity and momentum equations in this computer code are discretized based on a general curvilinear coordinate system (ξ_1, ξ_2, ξ_3), which take the following form in the context of an incompressible fluid:

$$\frac{1}{J}\frac{\partial\left(\beta_i^k u_i\right)}{\partial \xi_k} = 0 \quad , \tag{5.1}$$

$$\frac{\partial u_i}{\partial t} + \frac{1}{J}\frac{\partial}{\partial \xi_k}\left(\beta_j^k u_i u_j\right) = -\frac{1}{J\rho}\frac{\partial\left(\beta_i^k p\right)}{\partial \xi_k} - \frac{1}{\rho}\Pi\delta_{1i} + \frac{\nu}{J}\frac{\partial}{\partial \xi_p}\left(\frac{1}{J}\beta_j^p \beta_j^q \frac{\partial u_i}{\partial \xi_q}\right) \quad . \tag{5.2}$$

Here, governing equations are expressed using tensor notations, and the streamwise (x), vertical (y), and spanwise (z) coordinates shown in figure 5.1 are denoted using x_i for $i = 1, 2,$ and 3, respectively. In the above equations, p, ν, ρ and δ_{ij} represent the pressure, kinematic viscosity, density of the fluid, and Kronecker delta, respectively. In equation (2.2), Π is a constant pressure gradient that drives the flow, and β_i^j and J are the cofactor and Jocobian of tensor $\partial x_i/\partial \xi_j$, respectively.

The numerical algorithm is based on a finite-volume method in which a second-order accuracy is achieved with respect to both spatial and temporal discretizations. Within each sub-step of the second-order Runge-Kutta scheme, a fractional-step method is applied and a pressure correction equation is solved using the parallel algebraic multigrid solver (AMG). For time advancement, the Courant-Friedrichs-Lewy (CFL) number is kept approximately at 0.2. A momentum interpolation approach is used to obtain the cell-face velocity components and based on the velocity and pressure values in two adjacent control volumes in order to avoid a potential checkerboard problem of the pressure field. The simulation started with an initial laminar flow solution superimposed with artificial perturbations to trigger turbulence. The precursor simulation was run for an extended duration of 61 flow-through times (i.e., $780\delta/U_b$) until the turbulent flow field becomes fully-developed and statistically stationary. Then, turbulence statistics were collected for a time period over approximately 55 flow-through times (i.e., $704\delta/U_b$). All the simulations were conducted using the WestGrid (Western Canada Research Grid) supercomputers. For each simulated case, 254 cores were used for performing DNS, and approximately 520,000 CPU hours were spent for solving the velocity field and for collecting the flow statistics after the flow becomes fully developed and statistically stationary.

5.2.1 Streamwise domain-size study

In order to accurately predict statistical moments of the velocity field, the streamwise computational domain size L_x must be held sufficiently large such that all dominant coherent flow structures may fully evolve in the streamwise direction and their wavelengths can be captured in a numerical simulation. To this purpose, the spatial two-point correlation function of streamwise velocity fluctuation (R_{uu}) is calculated for both ribbed duct cases at two streamwise locations. For a ribbed duct flow, the streamwise two-point auto-correlation coefficient is defined as (Townsend, 1980; Volino et al., 2009)

$$R_{uu}(x_{ref}, \Delta x) = \frac{\langle u'(x_{ref})u'(x_{ref} + \Delta x)\rangle}{\sqrt{\langle u'^2(x_{ref})\rangle\langle u'^2(x_{ref} + \Delta x)\rangle}} \quad , \tag{5.3}$$

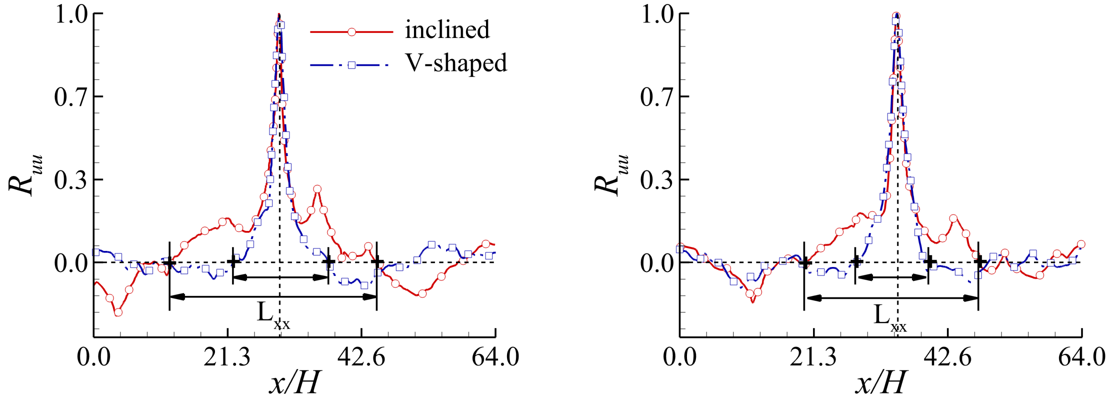

(a) $x_{ref}/h = 29.0$ (b) $x_{ref}/h = 34.0$

Figure 5.2: Streamwise profiles of two-point auto-correlations for ribbed duct flows of two rib cases at different streamwise locations (x/H). The streamwise coordinate of the reference points are $x_{ref}/H = 29.0$ and 34.0, while the vertical coordinate of the reference points is fixed at $y_{ref}/H = -3.8$. In terms of the relative streamwise coordinate, the reference points are located near the leeward and windward of a rib at $x'_{ref}/H = 2.0$ and 7.0, respectively. The characteristic streamwise length scale (L_{xx}) determined based on the streamwise two-point auto-correlation coefficient.

where u' represents the streamwise velocity fluctuations, and Δx denotes the relative displacement from the reference point located at x_{ref}, such that $x = x_{ref} + \Delta x$. The streamwise coordinate of the reference points are $x_{ref}/H = 29.0$ and 34.0, while the vertical coordinate of the reference points is fixed at $y_{ref}/H = -3.8$. In terms of the relative streamwise coordinate, the reference points are located near the leeward and windward sides of a rib at $x'_{ref}/H = 2.0$ and 7.0, respectively.

Figure 5.2 shows that for both rib cases, the profile of R_{uu} drops drastically to almost zero at the two ends. This indicates that the velocity statistics are not affected by the streamwise domain size, such that a domain size of $L_x = 64H$ is sufficiently large for capturing the characteristic length scales of dominant turbulence structures in the streamwise direction. From figure 5.2, it is also evident that the decaying rates of R_{uu} in the inclined rib case are slower than those of V-shaped rib case at both reference points ($x_{ref}/H = 29.0$ and 34.0), indicating that the streamwise length

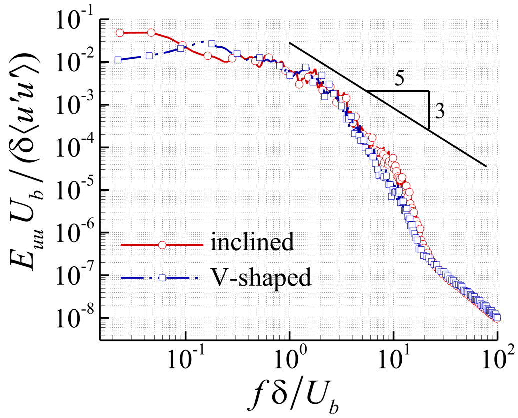

(a) $x_{ref}/h = 29.0$

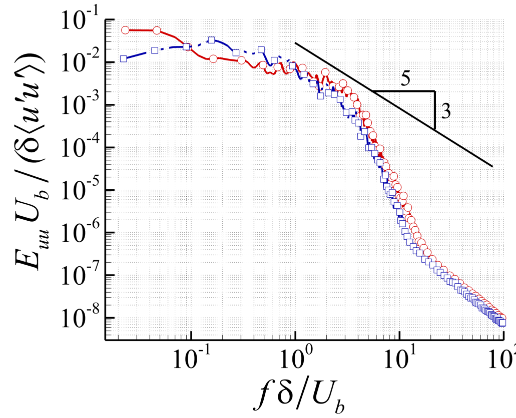

(b) $x_{ref}/h = 35.0$

Figure 5.3: Non-dimensionalized temporal energy spectra of streamwise velocity fluctuations for both inclined and V-shaped rib cases. The comparison of the two ribbed flow cases is conducted at the elevation that is slightly above the rib crest (with the spatial reference point being identical to that used in figures 5.2(a) and 5.2(b)).

scales of turbulent eddies of the inclined rib case are larger than those of the V-shaped rib case. By comparing figure 5.2(a) with 5.2(b), it is apparent that the decaying rate of R_{uu} is slightly slower at the reference point near the leeward face of the rib ($x_{ref}/H = 29.0$) than at the reference point near the windward face of the rib ($x_{ref}/H = 34.0$). More specifically, the value of the streamwise integral length scale (i.e., $L_{xx} = \int_0^\infty R_{uu}(x)dx$) decreases by 16.5% and 4.7% as x_{ref}/H increases from 29.0 to 34.0 in the inclined and V-shaped rib cases, respectively.

Figure 5.3 shows the temporal energy spectra of the streamwise velocity fluctuations. The spatial reference points considered here are the same as in figure 5.2 for the calculation of the streamwise two-point auto-correlation coefficient. Figure 5.3 shows that for both inclined and V-shaped rib cases, the difference between the highest and lowest frequencies is of the order of four. This implies that the statistical sampling range is deemed to be sufficient to resolve all significant temporal scales of the studied turbulent flows. From figure 5.3, it is also observed that the energy spectrum is strongly influenced by the rib geometry, as the $-5/3$ slope (which is a

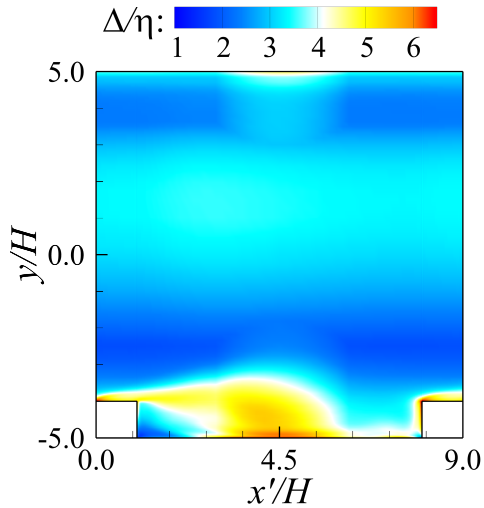

(a) inclined rib case

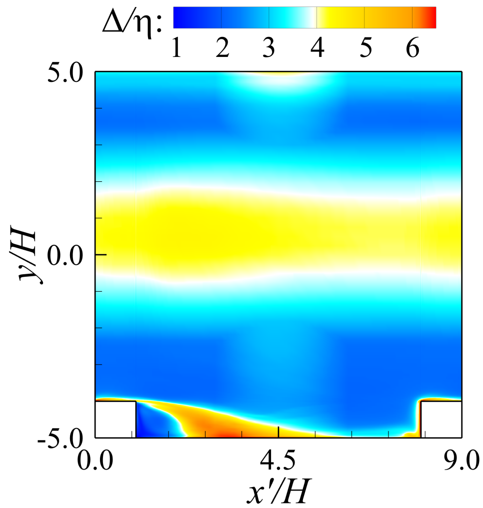

(b) V-shaped rib case

Figure 5.4: Contours of the ratio between the grid resolution and Kolmogorov length scale (Δ/η) in the central plane at $z/H = 0.0$ for two rib cases

characteristic of equilibrium turbulence regime, Pope, 2000) is apparently absent near the leeward and windward faces of the rib (at $x_{ref}/H = 29.0$ and 34.0, respectively). This indicates the presence of small-scale structures with a high degree of anisotropy due to the disturbances from the ribs.

5.2.2 Grid resolution

The number of body-fitted grid points used in the current simulations are $N_x \times N_z \times N_y = 1424 \times 168 \times 162$ in the streamwise, vertical and spanwise directions, respectively. The mesh is non-uniform in all three directions, and is refined near all solid surfaces. To ensure that the local resolution of this grid is sufficient for conducting DNS of turbulent flow over different rib geometries, the contours of the ratio between the maximal dimension of a grid cell in all three directions (i.e., $\Delta = \max(\Delta_x, \Delta_y, \Delta_z)$) and Kolmogorov length scale, $\eta = (\nu^3/\varepsilon)^{0.25}$, in the central ($x$-$y$) plane located at $z/H = 0.0$ are plotted in figure 5.4. Here, $\varepsilon = \nu\langle a'_{ij}a'_{ij}\rangle$ is the TKE dissipation rate, with $a'_{ij} = \partial u'_i/\partial x_j$ being the fluctuating velocity gradient tensor. In their DNS study of turbulent channel flows, Moser and Moin (1987) indicated that the grid size requires to be of the same order as the Kolmogorov length scale (i.e., $O(\Delta/\eta) \sim O(1)$) in order to accurately capture the TKE dissipation pertaining to the smallest scales of turbulence.

Figure 5.4 shows that the maximum magnitude of $\Delta_{\max}/\eta$ occurs in the inter-rib region under the rib height, which is approximately 5.3 and 6.3 for inclined and V-shaped rib cases, respectively. It is therefore expected that the mesh resolutions employed suffice to capture small turbulence motions at the Kolmogorov scale level in the two rib cases. From figure 5.4, it is evident that the appearance of a local maximum in the contours of $\Delta_{\max}/\eta$ is associated with a destruction mechanism of the upstream flow structures near the rib elements. A detailed explanation of the rib geometry effects on turbulence structures will be provided in section 5.4. The spatial resolutions used in this research are comparable to those used by Ismail et al. (2018), who conducted a DNS study of turbulent flows in a channel with rough-to-smooth step changes based on a second-order accurate finite-difference computer code.

5.3 Statistics of the velocity field

5.3.1 Mean velocity field

Figure 5.5 shows the time-averaged streamlines superimposed onto the mean streamwise velocity field in the central vertical (x-y) plane located at $z/H = 0.0$ for two rib cases. From figure 5.5, it is observed that both the contours of $\langle u\rangle/U_b$ and the mean streamlines are influenced significantly by the rib geometries. This inevitably leads to changes in the spatial distribution of skin friction and pressure coefficients, which will be discussed separately in this section. From figure 5.5(a), it is seen that for the inclined rib case, no apparent separation bubbles are present in

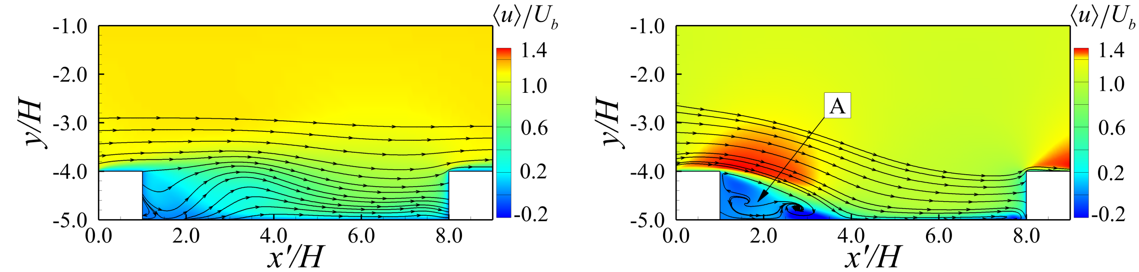

(a) inclined rib case

(b) V-shaped rib case

Figure 5.5: Contours of the mean streamwise velocity $\langle u \rangle/U_b$ superimposed with in-plane mean streamlines in the central (x-y) plane (located at $z/H = 0.0$) for two rib cases.

the near-wall region below the rib height. This phenomenon is mainly attributed to the occurrence of large vortices unique for the inclined rib flow case, which reduce the tendency of generating separation bubbles in the leeward side of the rib. These large vortices will be investigated thoroughly later in section 3.2. These physical features are consistent with the observations of Bonhoff et al. (1999) who studied the effects of inclined ribs on the turbulence statistics in a rectangular duct flow using a planar PIV. By contrast, for the V-shaped rib case as shown in figure 5.5(b), a large single separation bubble (marked with "A") exists in the inter-rib region below the rib height. From figure 5.5(b), it is observed that due to the downdraft of the mean flow, the separation bubble behind the rib is squeezed towards the leeward face of the V-shaped rib, which further leads to the formation of a region of high pressure values. This well explains the pressure drag difference between the inclined and V-shaped rib cases shown previously in table 5.1. By comparing figures 5.5(a) with 5.5(b), it is seen that for the inclined rib case, the highest streamwise momentum level as indicated by the magnitude of $\langle u \rangle/U_b$ appears in regions well above the rib crest (for $y/H > -3.7$), whereas for the V-shaped rib cases, the maximum value of $\langle u \rangle/U_b$ occurs near the rib crest due to an enhanced pressure difference.

Figure 5.6 compares the vertical profiles of the non-dimensionalized mean stream-

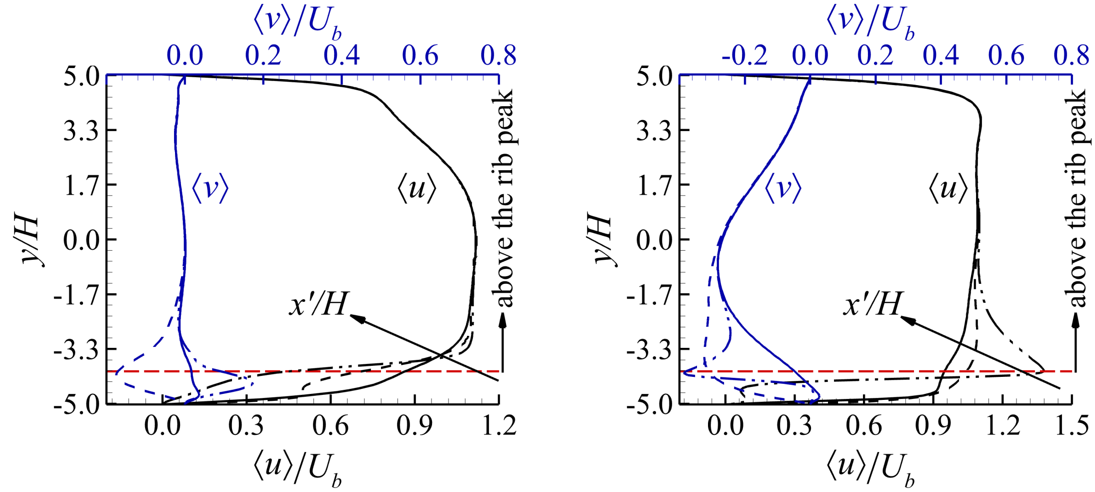

(a) inclined rib case

(b) V-shaped rib case

Figure 5.6: Comparison of the non-dimensionalized mean streamwise and vertical velocity profiles (indicated by the black and blue colors, respectively) at three relative downstream locations from the rib (for $x'/H = 2.0$ (dash-dot-dot), 4.5 (dashed) and 7.0 (solid)) in the central plane (located at $z/H = 0$) for two ribbed duct flows. The horizontal red dashed line demarcates the rib crest.

wise and vertical velocity profiles (i.e., $\langle u \rangle / U_b$ and $\langle v \rangle / U_b$, respectively) of the two rib cases along the central vertical lines located at $(x'/H, z/H) = (2.0, 0.0)$, (4.5, 0.0) and (7.0, 0.0). From figure 5.6, it is evident that the maximum value of $\langle u \rangle / U_b$ in both rib cases occurs above the rib height and then decreases monotonically as the relative downstream distance from the rib (x'/H) increases from 2.0 to 7.0, a pattern that is remarkably different from those in a canonical 2-D turbulent boundary layer over a flat plate (Miyake et al., 2001; Leonardi et al., 2004; Ikeda and Durbin, 2007; Burattini et al., 2008; Volino et al., 2009) or in a transverse rib-roughened duct flow (Coletti et al., 2012; Labbé, 2013; Mahmoodi-Jezeh and Wang, 2020). As an example, for the 2-D riblet flow over a flat plate, the magnitude of $\langle u \rangle / U_b$ reaches its maximum near the central region of the channel (Miyake et al., 2001; Volino et al., 2009). The existence of this mean streamwise velocity peak further causes the appearance of the strong shear layers (as indicated by the magnitude of mean streamwise velocity gradient $d\langle u\rangle/dy$ near the rib crest), which is often accompanied by an increase in the value of the TKE production rate (i.e., $-\langle u_i'u_j'\rangle\partial\langle u_i\rangle/\partial x_j$). From figure 5.6, it is also clear that for both ribbed duct cases, the vertical gradient of $\langle u\rangle$ is positive in the region near the ribbed bottom wall (for $-5.0 < y/H < -4.0$), which indicates an acceleration of the mean flow in the downstream direction. However, as the duct centre is approached, the vertical gradient of $\langle u\rangle$ becomes negligible and negative in the inclined and V-shaped rib cases, respectively. In contrast to the monotonic variation of the mean streamwise velocity $\langle u\rangle/U_b$ with an increasing relative streamwise distance x'/H, the mean vertical velocity $\langle v\rangle/U_b$ exhibits a complex behavior near the ribbed bottom wall. As demonstrated in figure 5.6, in the region near the rib crest at $x'/H = 2.0$, the value of $\langle v\rangle/U_b$ is positive and negative in the inclined and V-shaped rib cases, respectively. This further confirms that the mean flow field is sensitive to the rib geometry. As seen in figure 5.6(a), the magnitude of $\langle v\rangle/U_b$ in the inclined rib case remains unchanged as the vertical distance from the rib crest increases. However, as is clear in figure 5.6(b), the magnitude of $\langle v\rangle/U_b$ in the V-shaped rib case decreases as the duct center approaches, a feature that is consistent with the qualitative results shown previously in figure 5.5(b). From figures 5.5 and 5.6, it is understood that the magnitude of the mean streamwise velocity gradient $|d\langle u\rangle/dy|$ reaches its maximum near the rib crest (in the vertical direction) and at the relative streamwise location $x'/H = 2.0$ in the two ribbed cases. In view of this, in the remainder of our analysis, we need to pay a close attention to the flow physics occurring at this special relative streamwise location $x'/H = 2.0$.

Figure 5.7 shows the contours of non-dimensionalized mean streamwise vorticity (defined as $\langle\omega_x\rangle = \partial\langle w\rangle/\partial y - \partial\langle v\rangle/\partial z$) superimposed with the mean spanwise-vertical velocity streamlines in the (y-z) plane at the relative streamwise location $x'/H = 2.0$ for two ribbed duct cases. From figure 5.7, it is seen that the pattern of the secondary flow is strongly influenced by the rib geometry, causing substantial variations in momentum transfer in the cross-stream plane. As is evident in figure 5.7(a), for

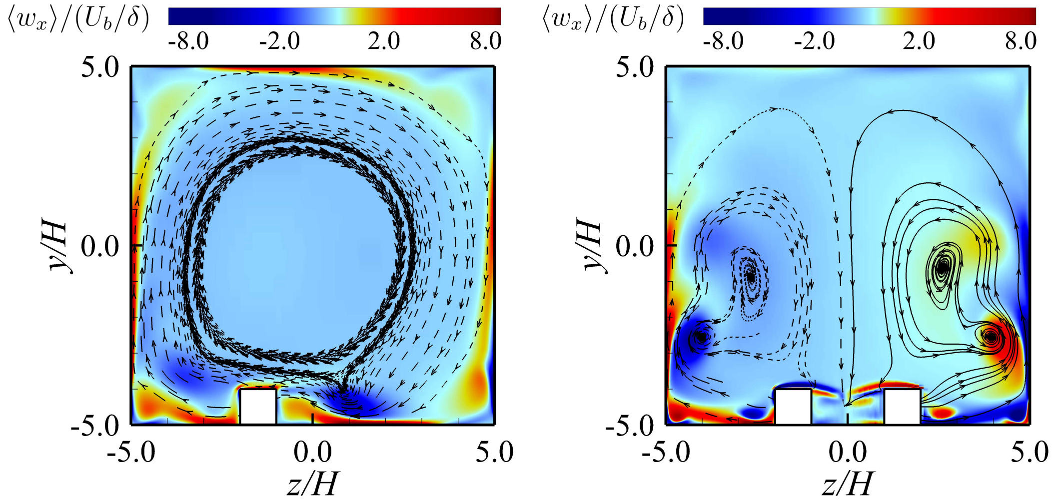

(a) inclined rib case (b) V-shaped rib case

Figure 5.7: Contours of non-dimensionalized mean streamwise vorticity ($\langle \omega_x \rangle/(U_b/\delta)$) superimposed with the mean spanwise-vertical velocity streamlines in the (y-z) plane at the relative streamwise location $x'/H = 2.0$ for two ribbed cases.

the inclined rib case, the secondary flow appears as a large streamwise-elongated vortex, which occupies almost the entire cross-section of the square duct. Owing to the interaction between this large-scale circulation of the fluid with the four boundary layers developed over the duct walls, high-level positively-valued mean streamwise vorticity $\langle \omega_x \rangle$ appears near all four sidewalls. From figure 5.7(b), it is clear that the vortex pattern of the mean flow in the V-shaped rib case is drastically different from that in the inclined rib case since the secondary flow develops into a pair of large symmetrical counter-rotating vortices in the cross-stream directions. This figure also shows that due to the angled ribs in the V-shaped rib case, the mean streamwise vorticity generated in the near-rib region is convected sideways and upwards by the secondary flow, interacting with the boundary layers over the two vertical sidewalls, and creating a region with high values of $\langle \omega_x \rangle$ near the sidewalls above the rib height ($y/H = -2.5$).

Figure 5.8 compares the spanwise profiles of non-dimensionalized mean stream-

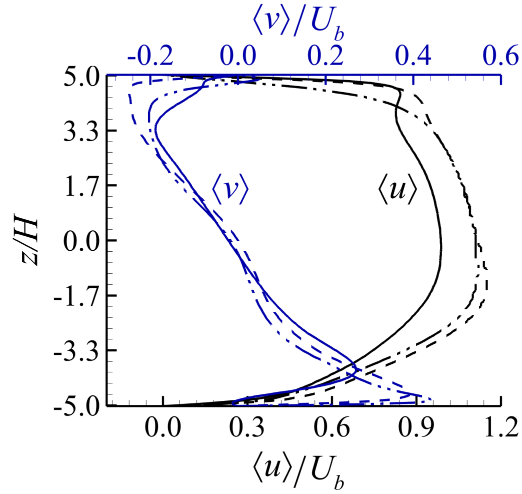

(a) inclined rib case

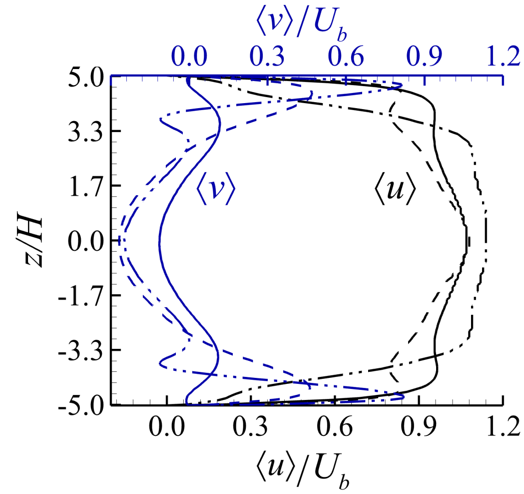

(b) V-shaped rib case

Figure 5.8: Spanwise profiles of the non-dimensionalized mean streamwise and vertical velocity profiles (indicated by the black and blue colors, respectively) along three elevated lines positioned at $y/H = -3.8$ (dash-dot-dot), -2.5 (dashed) and 0.0 (solid) for two ribbed cases. The relative streamwise coordinate of the point is fixed at $x'/H = 2.0$.

wise and vertical velocity profiles (i.e., $\langle u \rangle/U_b$ and $\langle v \rangle/U_b$, respectively) along three elevated lines positioned at $(x'/H, y/H) = (2.0, -3.8)$, $(2.0, -2.5)$, and $(2.0, 0.0)$ of the two ribbed duct cases. From figure 5.8, it is clear that the profiles of $\langle u \rangle/U_b$ and $\langle v \rangle/U_b$ for the inclined rib case are asymmetrical in the cross-stream directions, but symmetrical for V-shaped rib case at all three vertical locations. Figure 5.8 also shows that the presence of the cross-stream secondary flow motion influences significantly the spanwise distributions of both $\langle u \rangle/U_b$ and $\langle v \rangle/U_b$. From figure 5.8(a), it is seen that for the inclined rib case, the spanwise profile of $\langle u \rangle/U_b$ at all three vertical locations is skewed to one side of the duct, with its magnitude peaks approximately at $z/H = -1.7$. However, for the V-shaped rib case as shown in figure 5.8(b), the profile of $\langle u \rangle/U_b$ peaks not only at the duct center but also near the two vertical sidewalls (located at $z/H = \pm 5.0$). By comparing figure 5.8(a) with 5.8(b), it is apparent that the highest value of $\langle u \rangle/U_b$ occurs at $y/H = -2.5$ in the inclined rib case, and at $y/H = -3.8$ in the V-shaped rib case, indicating that the highest level of streamwise momentum occurs in the lower half duct (for $y/H < 0.0$) in both rib cases. This observation is consistent with the previous analysis of figure 5.5 and with the observations of Gao and Sundén (2004b) and Fang et al. (2015), who conducted PIV experiments of ribbed duct flows with a similar geometrical setup.

For the mean vertical flow motion, figure 5.8(a) shows that the profile of $\langle v \rangle / U_b$ in the inclined rib case manifests two distinct peaks, one positively- and one negatively-valued, located at $z/H = -5.0$ and 5.0, respectively. This clearly indicates upward- and downward-moving of the flow near the sidewalls of the duct, which is a direct consequence of the appearance of the mean secondary flows in the cross-stream plane (see, figure 5.7(a)). However, as shown in figure 5.8(b), the magnitude of $\langle v \rangle / U_b$ in the V-shaped rib case peaks close to the two vertical sidewalls of the duct. Furthermore, the peak magnitude $\langle v \rangle / U_b$ decreases as the distance from the sidewalls increases. This trend reflects the fact that the mean flow near the sidewalls is pushed upwards (corresponding to the positive sign of $\langle v \rangle / U_b$) and then convected downwards near the central region (corresponding to the negative sign of $\langle v \rangle / U_b$). From figure 5.8, it is observed that for both rib cases, the secondary flow effect on the mean flow field is the largest at $y/H = -2.5$, hence, our study needs to be refined to investigate the influence of secondary flow on the major characteristics of the flow field at this specific vertical position later in subsection 5.3.3.

5.3.2 Viscous and pressure drags

The effects of rib geometry on the mean flow field can be further investigated through an analysis of the skin friction and pressure coefficients, defined as $C_f = \tau_w / (\rho U_b^2 / 2)$ and $C_p = \langle p \rangle / (\rho U_b^2 / 2)$, respectively, where τ_w represents the local total wall friction stress calculated as $\tau_w = \mu [(\partial \langle u \rangle / \partial y)^2 + (\partial \langle w \rangle / \partial y)^2]_w^{1/2}$. Figure 5.9 shows the distributions of the skin friction C_f on the bottom wall located at $y/H = -0.5$ for two ribbed duct cases. To explain the influence of the mean flow structures

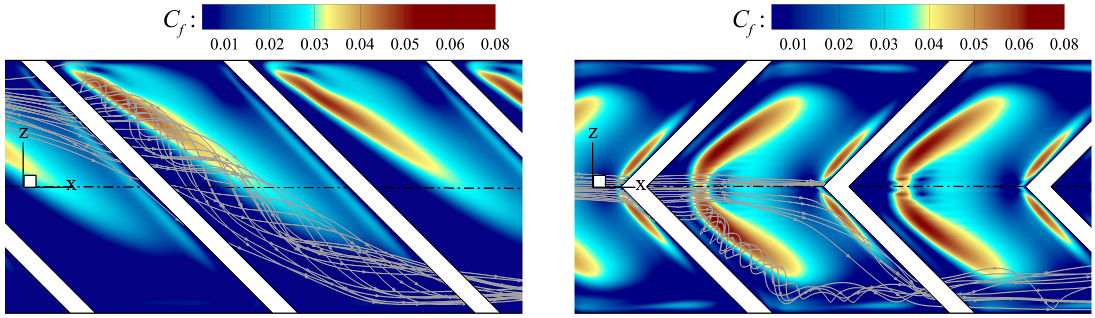

(a) inclined rib case

(b) V-shaped rib case

Figure 5.9: Contours of the skin friction coefficient C_f displayed in the (x-z) plane on the bottom wall located at $y/H = -5.0$ for two ribbed cases. The presentation of the contour plots of C_f is superimposed with the mean velocity streamlines.

on the local C_f value, the mean velocity streamlines are also superimposed. From figure 5.9, it is evident that owing to the presence of ribs and strong secondary flows, the magnitude of C_f varies considerably along the cross-stream directions, indicating that this 3-D rib-roughened duct flow is remarkably inhomogeneous in the spanwise direction. As seen in figure 5.9(a), the highest value of C_f in the inclined rib case appears at the corner on the leeward side of the upstream ribs near the vertical sidewall of the duct (at $z/H = 5.0$). This is due to the fact that the secondary flow induces a strong downwash of mean flows towards the ribbed bottom wall (see figures 5.7(a) and 5.8(a)), further resulting in a large magnitude of the streamwise velocity gradient in the vertical direction. By contrast, in the V-shaped rib case as shown in figure 5.9(b), the highest friction coefficient values appear near the leeward face of the rib elements in the central region (for $-2.5 < z/H < 2.5$). This peak of C_f coincides exactly with the core of the vortex A exhibited previously in figure 5.5(b). Furthermore, it is apparent that both streamlines and vortex A (featuring high values of C_f) evolve along the V-shaped ribs and then become aligned with the main stream in regions near the sidewalls.

Figure 5.10 compares the spatial distributions of pressure coefficient C_p of the

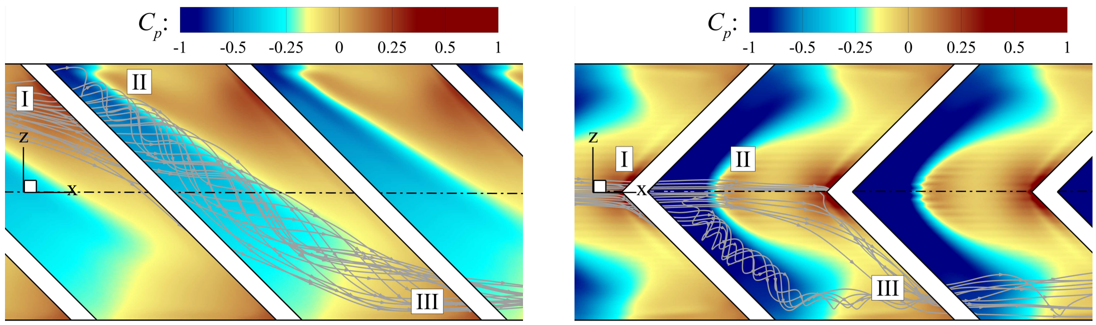

(a) inclined rib case

(b) V-shaped rib case

Figure 5.10: Contours of the pressure coefficient C_p displayed in the (x-z) plane on the bottom wall located at $y/H = -5.0$ for two ribbed cases. The presentation of the contour plots of C_p is superimposed with the mean velocity streamlines.

two ribbed duct cases over the ribbed bottom wall located at $y/H = -5.0$. From figures 5.10(a) and 5.10(b), it is evident that similar to the skin friction coefficient, both the pressure coefficient level and its spatial distribution are sensitive to the rib geometry. Figure 5.10(a) clearly demonstrates the spatial evolution of the streamlines of the mean flow and shows how the flow turns as it passes over the inclined ribs. First, flow intensively interacts with the windward face of the upstream rib near the vertical sidewall of the duct (at $z/H = 5.0$), causing the flow to become stagnant and create a high pressure region (marked with "I"), then the flow in the inter-rib region is driven toward the other sidewall (at $z/H = -5.0$) and impinges onto the windward side of the downstream rib, which results in the generation of the second and third high-pressure regions (marked with "II" and "III", respectively). From figure 5.10(b), it is observed that the mean streamline topology in the V-shaped rib case is substantially different from that of the inclined rib case. Figure 5.10(b) shows that the magnitude of C_p reaches its maximum near the windward face of the V-shaped ribs (marked with "I") and near the reattachment point (marked with "II"). Furthermore, owing to the angled ribs in the V-shaped rib case, the mean streamlines diverge from the duct midspan towards the sidewalls below the rib height and impinge on the two vertical sidewalls of the duct, leading to the formation of a region with high values of C_p (marked with "III"). By comparing figures 5.9 with 5.10, it is concluded that the pressure difference between the windward and leeward faces of the ribs greatly contribute to increasing the total drag (see table 5.1). Furthermore, if we compare the mean flow features of the full inclined ribbed duct shown in figure 5.10(a) with that of one-half the V-shaped duct (for $z/H = -5.0$) shown in figure 5.10(b), certain similarity can be observed in terms of the streamline and C_p contour patterns. More specifically, the mean flow pattern exhibited in the V-shaped ribbed duct is almost a pair of mirror reflections of that of the inclined rib case. The same can be concluded by comparing figures 5.9(a) and 5.9(b) with respect to the spatial distribution of the C_f values.

5.3.3 Reynolds stress distributions

Figure 5.11 compares the contours of the non-dimensionalized mean Reynolds normal stress components ($\langle u'u' \rangle/U_b^2$, $\langle v'v' \rangle/U_b^2$ and $\langle w'w' \rangle/U_b^2$) in the central ($x$-$y$) plane (located at $z/H = 0.0$) for two rib cases. From figure 5.11(a), it is seen that for the inclined rib case, the magnitude of the streamwise Reynolds normal stress $\langle u'u' \rangle$ peaks in the neighborhood of the rib crest and then decreases as the downstream distance from the leading edge of the rib ($x'/H = 0.0$) increases. This enhancement in the magnitude of $\langle u'u' \rangle$ immediately downstream of the rib crest is a result of the occurrence of the boundary-layer separation near the leading edge of the rib, which also produces strong spanwise vortex shedding. However, as shown in figure 5.11(b), the primary peak of $\langle u'u' \rangle$ in the V-shaped case occurs in the inter-rib region (below the rib height) in the lee of the ribs. This is due to the negative values of $\langle v \rangle/U_b$ induced by the secondary flows, which results in a downwash of high momentum flow from duct center to the ribbed wall (see figures 5.5(b), 5.6(b) and 5.7(b)). By comparing figure 5.11(c) with 5.11(d), it is observed that the highest levels of the vertical Reynolds normal stress $\langle v'v' \rangle$ in the inclined rib case are mainly

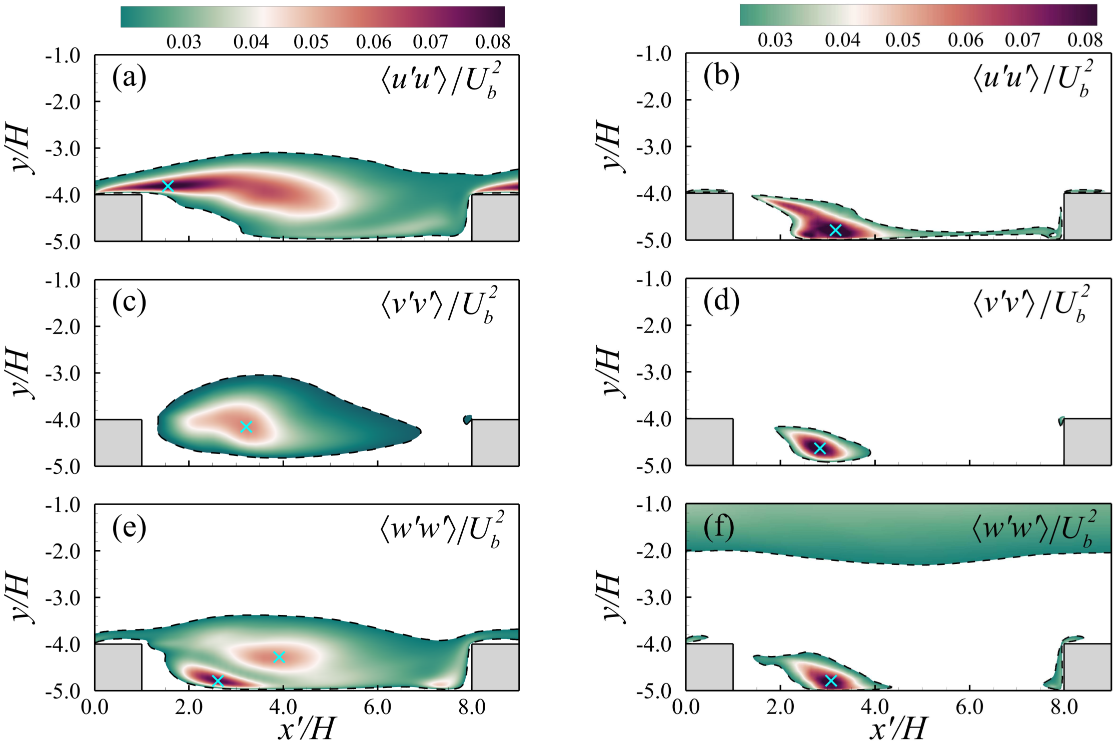

Figure 5.11: Contours of non-dimensionalized Reynolds normal stress components ($\langle u'u'\rangle/U_b^2$, $\langle v'v'\rangle/U_b^2$ and $\langle w'w'\rangle/U_b^2$) in the central ($x$-$y$) plane for the inclined rib case (a, c and e) and V-shaped rib case (b, d and f). To facilitate a clear visual comparison, contour values less than 20% of the peak value of Reynolds normal stresses are clipped off. Cross symbol $\times$ marks the local peak positions of Reynolds normal stresses.

concentrated around the rib height; however, in the V-shaped rib case, large values of $\langle v'v'\rangle$ are primarily confined within a small region below the rib height. As is seen clearly in figure 5.11(e), in the inclined rib case, the contours of the spanwise Reynolds normal stress $\langle w'w'\rangle$ exhibit two distinct peaks, one in the near-wall region below the rib height and one near the rib height. The occurrence of these two peaks is a unique feature of the inclined rib-roughened duct flow. By contrast, in the V-shaped rib case, the maximum value of $\langle w'w'\rangle$ is only observed within the cavity (for $2.0 < x'/H < 4.0$), which nearly coincides with those of $\langle u'u'\rangle$ and $\langle v'v'\rangle$ shown in figures 5.11(b) and 5.11(d), respectively.

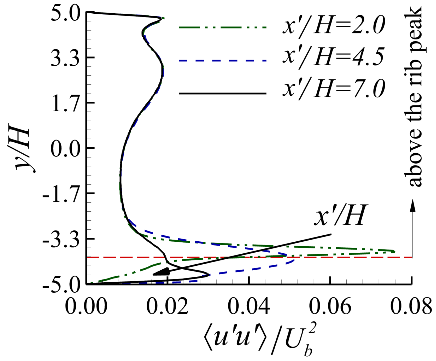

(a) inclined rib case

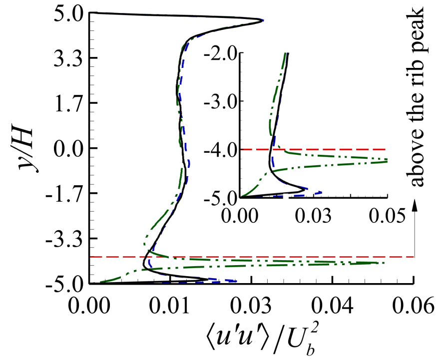

(b) V-shaped rib case

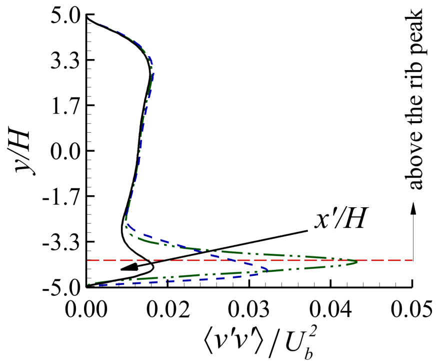

(c) inclined rib case

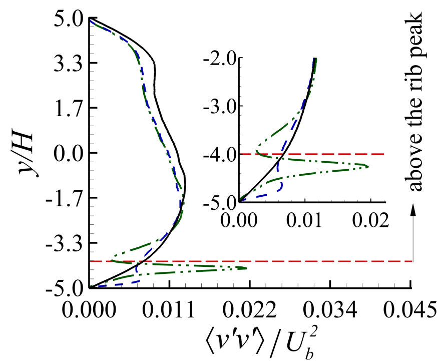

(d) V-shaped rib case

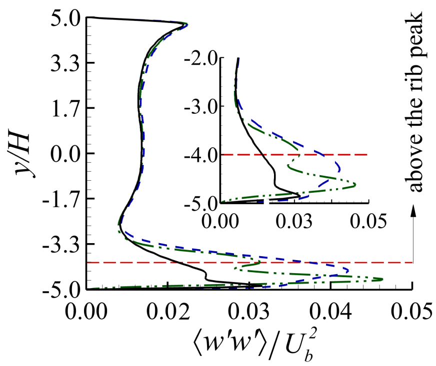

(e) inclined rib case

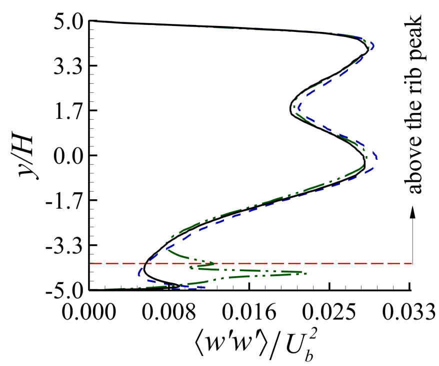

(f) V-shaped rib case

Figure 5.12: Comparison of the non-dimensionalized Reynolds normal stress components ($\langle u'u'\rangle/U_b^2$, $\langle v'v'\rangle/U_b^2$ and $\langle w'w'\rangle/U_b^2$) at three relative streamwise locations (for $x'/H = 2.0$, 4.5 and 7.0) in the central vertical plane (located at $z/H = 0$) for the inclined rib case (a, c and e) and V-shaped rib case (b, d and f). The horizontal red dashed line demarcates the rib crest. In order to show clearly the profiles of the Reynolds stresses below the rib crest, they are partially enlarged and replotted in inset graphs in panels (b), (d) and (e).

To further investigate the effects of rib geometry on the velocity field, figure 5.12 compares the vertical profiles of non-dimensionalized Reynolds normal stresses ($\langle u'u' \rangle / U_b^2$, $\langle v'v' \rangle / U_b^2$ and $\langle w'w' \rangle / U_b^2$) of two rib cases along the central vertical lines located at $(x'/H, z/H) = (2.0, 0.0)$, (4.5, 0.0) and (7.0, 0.0). From figure 5.12, it is observed that for both ribbed duct cases, the highest turbulent levels (as indicated by the magnitudes of Reynolds normal stresses) occur around the rib height at the relative streamwise location $x'/H = 2.0$, where the shear strength is the largest (see figure 5.6). The shear layer generated over the rib crest separates immediately after of the rib, shedding downstream energetically and causing an enhancement in the variance of velocity fluctuations. Furthermore, it is observed that for both rib cases, the peak value of all the three Reynolds stress components reduces monotonically near the rib crest as x'/H increases from 2.0 to 7.0. From figure 5.12, it is clear that owing to the disturbances from the ribs, the magnitudes of Reynolds normal stresses in both inclined and V-shaped rib cases are significantly amplified on the ribbed bottom wall side than on the smooth top wall side. Also, it is apparent that although there exists a drastic difference in the patterns of the Reynolds normal stresses profiles below the rib height ($y/H < -4.0$) between these two ribbed duct cases, they all collapse to a single profile above the rib height ($y/H > -4.0$). From figures 5.12(a), 5.12(c) and 5.12(e), it is evident that for the inclined rib case, the magnitudes of normal components reduce considerably as the duct center is approached, especially on the ribbed side. By contrast, for the V-shaped rib case as shown in figures 5.12(b), 5.12(d) and 5.12(f), the magnitudes of normal components increase and peak near the duct center, contributing to a local enhancement of TKE.

Figure 5.13 compares the vertical profiles of Reynolds shear stress ($\langle u'v' \rangle / U_b^2$) along the central vertical lines located at $(x'/H, z/H) = (2.0, 0.0)$, (4.5, 0.0) and (7.0, 0.0) for the two ribbed duct flow cases. From figure 5.13, it is seen that similar to the trend of $\langle u'u' \rangle$ shown previously in figures 5.12(a) and 5.12(b) (for inclined and V-shaped rib cases, respectively), the Reynolds shear stress component $\langle u'v' \rangle$ peaks

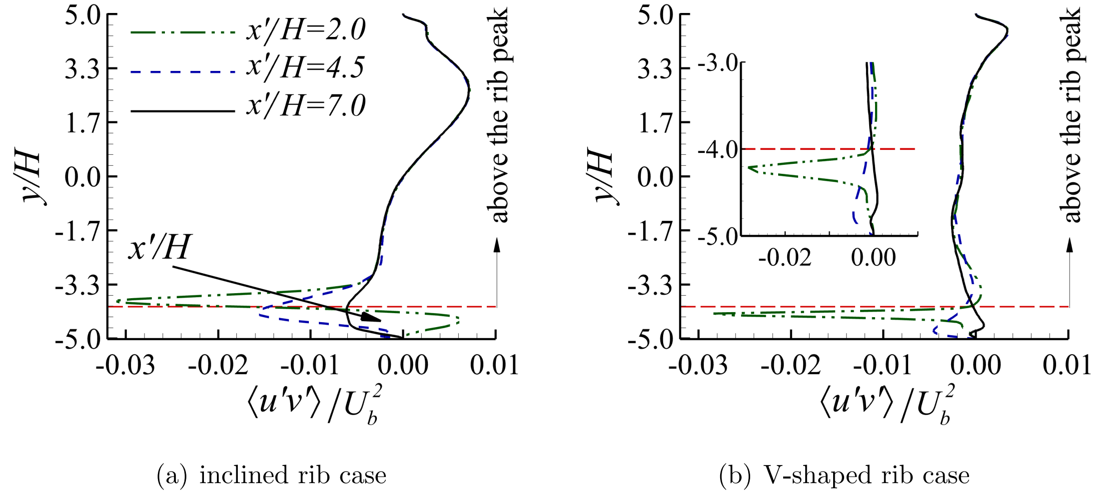

Figure 5.13: Profiles of the non-dimensionalized Reynolds shear stress ($\langle u'v'\rangle/U_b^2$) at three relative streamwise locations (for $x'/H = 2.0$, 4.5 and 7.0) in the central vertical plane (located at $z/H = 0$) for two ribbed cases. The horizontal red dashed line demarcates the rib crest.

around the rib height for both rib cases, with the magnitude decreasing progressively as the relative streamwise distance x'/H increases. Since the Reynolds shear stress is a reflection of the sweeping or ejection events, it implies that the strength of both events is significant near the rib crest but becomes trivial as x'/H increases from 2.0 to 7.0. Later in section 5.4, we will refine our study by examining the rib geometry effects on turbulent motions through a quadrant analysis of the ejection and sweep events. From figure 5.13(a), it is clear that as the duct centre is approached, the magnitude of $\langle u'v'\rangle$ gradually increases and a positive peak occurs in its profile at $y/H = 2.3$ in the inclined rib case. By contrast, for the V-shaped rib case as seen from figure 5.13(b), the magnitude of $\langle u'v'\rangle$ in all three streamwise locations becomes trivial in the central region of the duct. In fact, the profile of $\langle u'v'\rangle$ in the V-shaped rib case becomes almost a vertical straight line with a small magnitude in the region $-4.0 < y/H < 4.0$.

Figure 5.14 compares the spanwise profiles of the Reynolds normal ($\langle u'u'\rangle$, $\langle v'v'\rangle$ and $\langle w'w'\rangle$) and shear ($\langle u'v'\rangle$) stresses along an elevated line positioned at

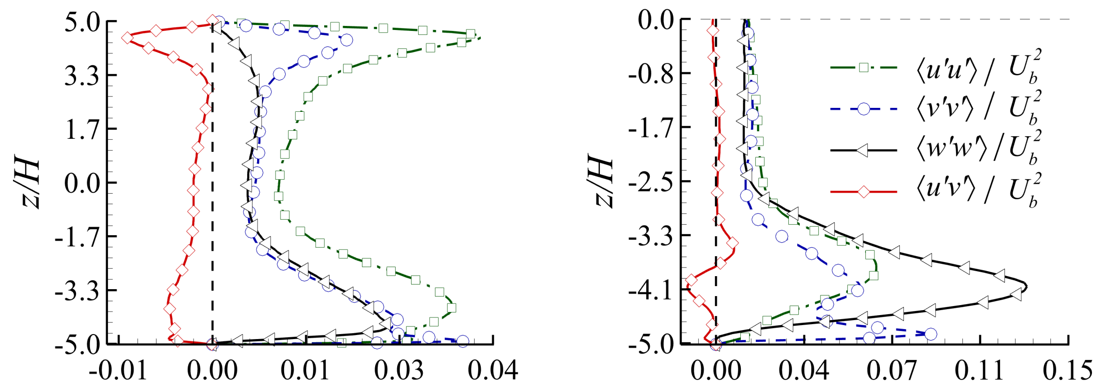

(a) inclined rib case

(b) V-shaped rib case

Figure 5.14: Spanwise profiles of Reynolds normal ($\langle u'u' \rangle$, $\langle v'v' \rangle$, and $\langle w'w' \rangle$) and shear ($\langle u'v' \rangle$) stresses along an elevated line positioned at $(x'/H, y/H) = (2.0, -2.5)$ for two ribbed cases. In panel (b), for the V-shaped rib-roughened duct, only one-half the duct is plotted given the vertical symmetry of the profiles (the horizontal dashed line on the top of the domain demarcates the symmetric center).

$(x'/H, y/H) = (2.0, -2.5)$ for the two rib cases. From figure 5.14, it is evident that for both inclined and V-shaped rib cases, the highest Reynolds stress levels appear near the vertical sidewalls and decay in magnitude as the duct center is approached. This physical feature is mainly attributed to the difference of the rib geometries and associated secondary flow patterns in the cross-stream plane shown previously in figure 5.7. Figure 5.14(a) shows that for the inclined rib case, the magnitudes of the three normal components are comparable in value near the sidewall (located at $z/H = -5.0$), indicating that turbulence tends to be locally isotropic in this region. However, the three Reynolds normal stress magnitudes are significantly different near the other sidewall (located atat $z/H = 5.0$), with the magnitude of $\langle u'u' \rangle$ being approximately 1.9 and 8.7 times larger than those of $\langle v'v' \rangle$ and $\langle w'w' \rangle$, respectively. This implies that $\langle u'u' \rangle$ makes the primary contribution to the TKE among the three Reynolds normal stress components and also indicates the anisotropic states of turbulence in this region (near the side wall located at $z/H = 5.0$). Given spanwise symmetry of the mean flow field in the V-shaped ribbed duct case, only one-half of the Reynolds stress profiles are displayed in figure 5.14(b). From figure 5.14(b), it is seen that near the two vertical sidewalls, the magnitude of $\langle w'w' \rangle$ is larger than those of $\langle u'u' \rangle$ and $\langle v'v' \rangle$ in the V-shaped rib case. This phenomenon reflects the fact that TKE is mostly contributed by $\langle w'w' \rangle$ (instead of $\langle u'u' \rangle$ and $\langle v'v' \rangle$), a physical feature that is drastically different from that of an inclined ribbed duct flow.

5.3.4 TKE budget analysis near the rib-roughened wall

To further elucidate the effects of the rib geometry on the turbulence stresses discussed in subsection 5.3.3, the turbulent transport of TKE (defined as $k = \langle u'_i u'_i \rangle / 2$) can be studied, which reads as follows:

$$0 = \Pi_k + T_k + D_k + P_k + \varepsilon_k + C_k \quad . \tag{5.4}$$

Here, $\Pi_k, T_k, D_k, P_k, \varepsilon_k$ and C_k denote the pressure diffusion term, turbulence diffusion term, viscous diffusion term, turbulent production term, dissipation term, and mean convection term, defined as

$$\Pi_k = -\frac{1}{\rho}\frac{\partial \langle p'u'_j \rangle}{\partial x_j}, \;\; T_k = -\frac{1}{2}\frac{\partial \langle u'_i u'_i u'_j \rangle}{\partial x_j}, \qquad D_k = \nu \frac{\partial^2 k}{\partial x_j^2} \quad ,$$
$$P_k = -\langle u'_i u'_j \rangle \frac{\partial \langle u_i \rangle}{\partial x_j}, \;\; \varepsilon_k = -\nu \langle \frac{\partial u'_i}{\partial x_j}\frac{\partial u'_i}{\partial x_j} \rangle, \;\; C_k = -\langle u_j \rangle \frac{\partial k}{\partial x_j} \quad ,$$

respectively. Figure 5.15 shows the profiles of TKE budget terms along the central vertical line positioned at $(x'/H, z/H) = (2.0, 0.0)$ for the two rib cases. In order to clearly demonstrate the profiles of the budget terms around the rib crest, they are plotted partially in figure 5.15. From the figure, it is clear that the turbulence energy transfer in the vertical direction is sensitive to the rib geometry, as the TKE budgets of these two rib cases are not only different in values but also dissimilar in patterns. As shown in figure 5.15(a), for the inclined rib case, the budget balance of TKE in the inter-rib region (for $-5.0 < y/H < -4.5$) is dominated by viscous diffusion D_k and turbulence diffusion T_k as the source terms; and by convection C_k,

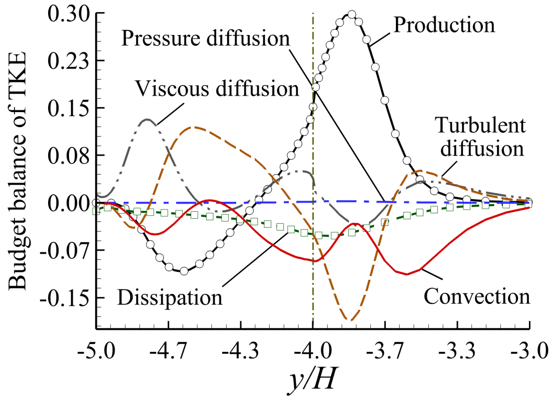

(a) inclined rib case

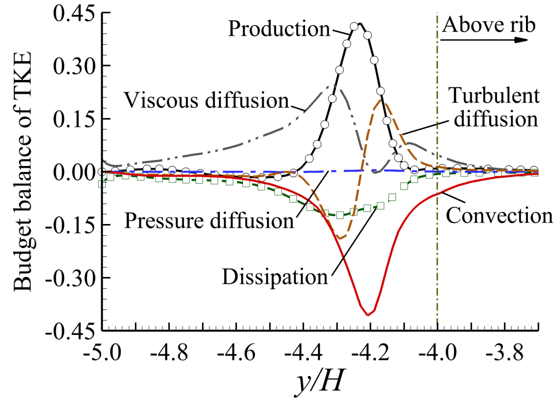

(b) V-shaped rib case

Figure 5.15: Vertical profiles of the budget terms of the TKE transport equation along the central vertical line positioned at $(x'/H, z/H) = (2.0, 0.0)$ for both ribbed cases. The budget terms are non-dimensionalized using the duct half-height, δ, and bulk velocity, U_b. In order to show clearly the profiles of the budget terms around the rib crest, they are plotted partially in panels (a) and (b). The vertical dash-dotted line demarcates the position of the rib crest.

production P_k and dissipation ε_k as the sink terms. Furthermore, it is observed from figure 5.15(a) that the turbulence diffusion term T_k changes its sign four times near the ribbed bottom wall (for $-5.0 < y/H < -3.0$), indicating that this term can be either a source or a sink in the inclined ribbed duct flow case. The appearance of large positively-valued turbulent diffusion term T_k below and above the rib height (at $y/H = -4.6$ and -3.5, respectively) clearly indicates that highly-turbulent fluid is transported away from these regions. From figure 5.15(a), it is also apparent that owing to the disturbances from the ribs, a dominant TKE source (as indicated by a distinct peak of turbulent production term P_k) appears above the rib crest, which is primarily balanced by the four sink terms (i.e., by turbulence diffusion, dissipation, convection, and viscous diffusion). This peak of P_k coincides with that in the streamwise normal stress $\langle u'u' \rangle$ shown previously in figure 5.12(a). By contrast, as shown in figure 5.15(b), in the V-shaped rib case, all dominant TKE budget terms peak in a region below the rib height. This feature is fully consistent with the quantitative results shown in figures 5.12(b), 5.12(d), and 5.12(f), in the sense that high levels of Reynolds normal stress components are also mainly concentrated in the region slightly below the rib crest. In the region very close to the ribbed bottom wall (for $-5.0 < y/H < -4.7$), the TKE budget in the V-shaped rib case is primarily balanced between the viscous diffusion and dissipation terms (i.e., D_k and ε_k), as the source and sink terms, respectively. However, as the distance from the bottom wall increases in the vertical direction (for $-4.4 < y/H < -4.0$), the magnitudes of D_k and P_k become increasingly dominant TKE sources and reach their maxima just below the rib height, balanced by the dissipation term ε_k, convection term C_k and turbulent diffusion term T_k. From figure 5.15, it is apparent that among all the six TKE budget terms, Π_k makes the smallest contribution to the TKE balance in both ribbed cases. It can be therefore concluded that near the rib elements, the five calculated terms in equation 5.4 contribute significantly to the TKE balance and the production and dissipation are not the only dominant terms.

It is well established (Wang et al., 2007; Coletti et al., 2012; Mahmoodi-Jezeh and Wang, 2020) that the presence of ribs in a 3-D square duct imposes remarkable changes to turbulence length scales compared to those of a conventional 2-D ribbed boundary-layer flow over a flat plate. This inevitably impacts the mechanism underlying the TKE production rate. In order to determine whether the difference in the magnitude of TKE production term is caused by large- or the small-scale eddies, the method of Hinze (1972) are followed through an analysis of active, $-\varepsilon_{ijk}\langle u'_j\omega'_k\rangle$, and inactive, $(\partial\langle u'_ju'_j\rangle/\partial x_i)/2$, modes of Reynolds shear stresses $\partial\langle u'_iu'_j\rangle/\partial x_i$. The active motion is rotational and causes shear stresses, with positive values representing energy attained from small-scale eddies and negative values representing energy being lost to small-scale eddies (Hinze, 1972). However, inactive motion is irrotational and acts through the pressure field, which mainly pertains to large-scale structures from a spectral analysis point of view (Townsend, 1961; Hinze, 1972). Furthermore, inactive motion does not directly create shear stresses for a flow that is homogeneously turbulent in the

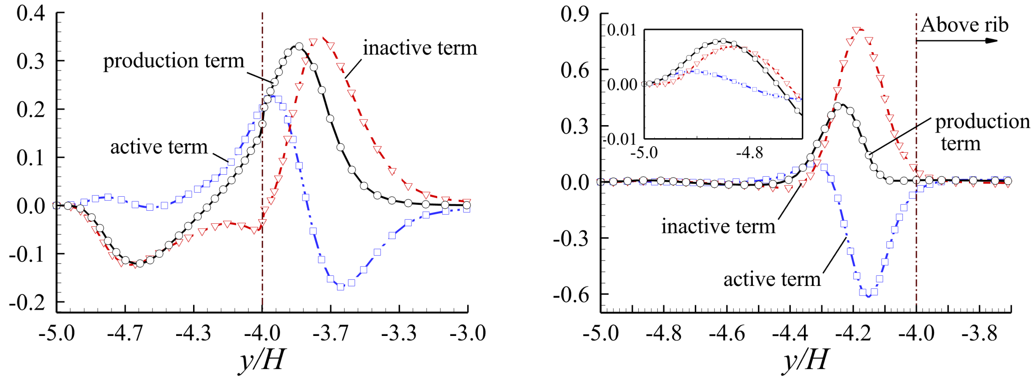

(a) inclined rib case

(b) V-shaped rib case

Figure 5.16: Vertical profiles of the TKE production P_k, and its active (P_{ka}) and inactive (P_{ki}) components along the central vertical line positioned at $(x'/H, z/H) = (2.0, 0.0)$ for both ribbed cases. These budget terms are non-dimensionalized using the duct half-height, δ, and bulk velocity, U_b. In order to show clearly the profiles of the budget terms around the rib crest, they are plotted partially in panels (a) and (b). The vertical dash-dotted line demarcates the position of the rib crest.

streamwise direction (Bradshaw, 1967; Orlandi et al., 2006). However, in the present study, the flow is strongly inhomogeneous in all three directions due to the presence of ribs and peripheral confinement of the duct. The physics of the turbulent flow in both ribbed duct cases can be better understood by examining the effects of the active and inactive turbulent motions on the TKE production rate. On the other side, it would be interesting to investigate the impact of rib geometry on both the rotational and irrotational turbulent motions. The TKE production rate $P_k = -\langle u_i'u_j'\rangle\partial\langle u_i\rangle/\partial x_j)$ can be decomposed into an active production part (defined as $P_{ka} = \varepsilon_{ijk}\langle u_i\rangle\langle u_j'\omega_k'\rangle$) and an inactive production part (defined as $P_{ki} = -\langle u_j'u_j'\rangle/2 \cdot \partial\langle u_i\rangle/\partial x_i$), viz. $P_k = P_{ka} + P_{ki}$, or,

$$P_k = \varepsilon_{ijk}\langle u_i\rangle\langle u_j'\omega_k'\rangle - \frac{\partial\langle u_i\rangle}{\partial x_i}\frac{\langle u_j'u_j'\rangle}{2} \quad . \tag{5.5}$$

Figure 5.16 compares the vertical profile of the TKE production rate P_k with those of the active and inactive production components (P_{ka} and P_{ki}, respectively) in the central (x-y) plane located at $(x'/H, z/H) = (2.0, 0.0)$. From figure 5.16(a), it is seen that in the region below the inclined rib height (for $y/H < -4.0$), the magnitude of the active term P_{ka} becomes insignificant, while the magnitude of the inactive term P_{ki} reaches its minimum. In fact, the negatively-valued peak of P_{ki} occurs at $y/H = -4.7$, directly resulting in a local minimum in the profile of P_k in the same region. From figure 5.16(a), it is also observed that the active term P_{ki} peaks in the region slightly above the rib crest at $y/H = -3.9$, which signifies the transfer of TKE from small- to large-scales, leading to an enhanced magnitude of P_k. However, as the vertical distance from the rib crest increases, TKE starts to be drained from large- to small-scales of turbulence. Inevitably, the magnitude of the active term P_{ka} switches its sign from being positive to being negative, and reaches its minimum (or, negatively-valued peak) at $y/H = -3.6$. Thus, at this elevation of $y/H = -3.6$, the main source of TKE production term is the inactive term P_{ki}. The inactive term P_{ki} is associated with swirling motions caused by the attached eddies of large sizes (Townsend, 1961). Specifically, for the V-shaped rib case, it is evident from figure 5.16(b) that in the region just below the rib height, both the TKE production term P_k and its inactive component P_{ki} are maximized, whereas its active component P_{ka} reaches a minimum (or, a negatively-valued peak). This phenomenon can be explained by the fact that highly energetic shedding vortices generated from the top surface of the sharp-angled V-shaped ribs induce a strong shear layer (see figure 5.6(b) and figures 5.12(b), 5.12(d) and 5.12(f)), leading to an augmentation in both magnitudes of the inactive and TKE production rates. Concurrently, the interaction of turbulent structures with the V-shaped ribs cause turbulent structures to break up, leading to a loss of energy and formation of small-scale structures, as portrayed by a negatively-valued peak of the active component P_{ki} in figure 5.16(b).

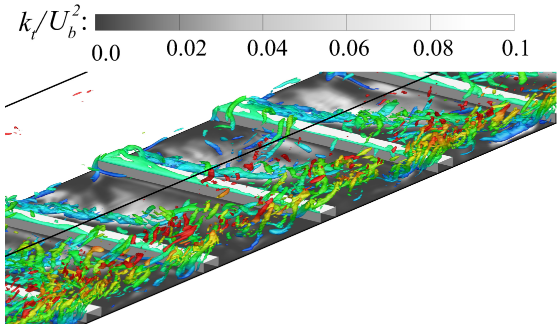

(a) inclined rib case

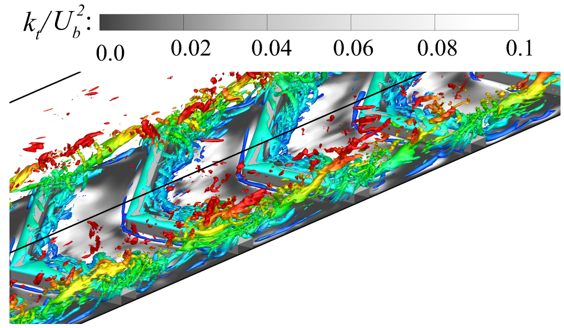

(b) V-shaped rib case

Figure 5.17: Isosurfaces of the swirling strength λ_{ci} around ribs superimposed with background contours of the instantaneous turbulent kinetic energy (i.e., $k_t = (u'^2 + v'^2 + w'^2)/2$) in the $(x$-$z)$ plane located at $y/H = -5.0$ for two ribbed cases. The iso-surfaces of swirling strength are colored using non-dimensionalized elevation y/H.

5.4 Effects of rib geometry on turbulence structures

To better understand the effects of rib geometry on near-wall turbulence structures, figure 5.17 demonstrates the iso-surfaces of the swirling strength, λ_{ci} (Zhou et al., 1999), superimposed onto the contours of the 'instantaneous TKE' (defined as $k_t = (u'^2 + v'^2 + w'^2)/2$) in the $(x$-$z)$ plane located at $y/H = -5.0$ for the two rib cases. This figure vividly shows the effects of the rib geometry on the vortical structures in the inclined and V-shaped ribbed duct flow cases. From figure 5.17(a), it is apparent that due to the inclination angle of the ribs, the energetic vortical structures are deflected towards only one side of the duct (located at $z/H = -5.0$), where the secondary flow motion pushes the fluid to move upward as previously shown in figure 5.7(a). The interactions between these turbulent eddies with the boundary layer developed over the sidewall are the underlying physical causes of the appearance of a local maximum in the profiles of Reynolds stresses and TKE production rate. However, as shown in figure 5.17(b), the turbulence structures in the V-shaped rib case

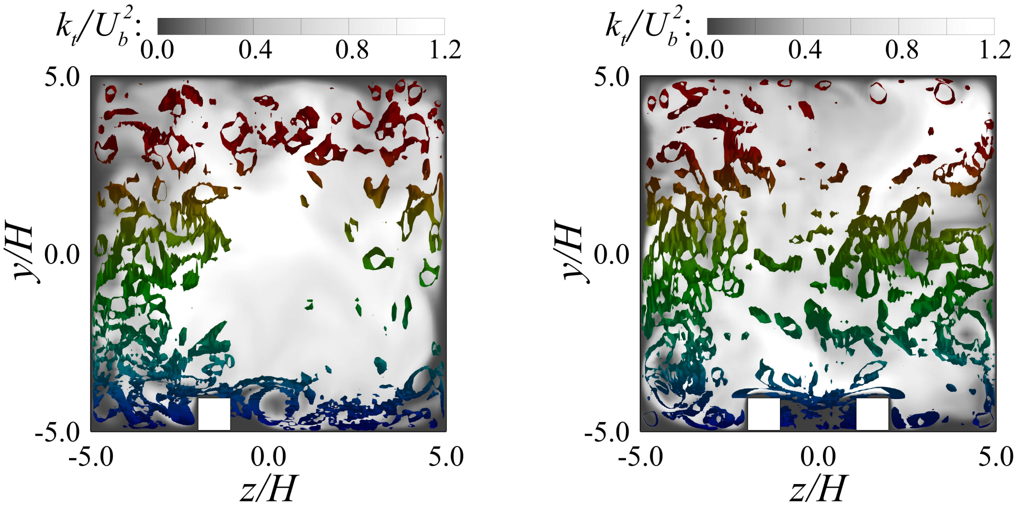

(a) inclined rib case (b) V-shaped rib case

Figure 5.18: Iso-surface of the swirling strength λ_{ci} in the cross-stream (y-z) plane at the relative streamwise location $x'/H = 2.0$ superimposed onto the background instantaneous turbulent kinetic energy k_t (shown using grey-scaled contours) for two ribbed cases. The iso-surfaces of swirling strength are colored using non-dimensionalized elevation y/H.

divert from the duct center sideways towards both sidewalls (located at $z/H = \pm 5.0$); and as a result, a significant fraction of these vortical structures are concentrated near the two vertical sidewalls. From figures 5.17(a) and 5.17(b), it is seen that in comparison with the inclined rib case, V-shaped rib case induces stronger disturbances to the velocity field as turbulence structures apparently become more broken down, and as a result, more vortical structures are generated near the ribbed bottom wall in the V-shaped ribbed duct flow. This physical feature is consistent with the previous analysis of figure 5.2, in the sense that the length scales of turbulent eddies of the V-shaped rib case are smaller than those of the inclined rib case.

Figure 5.18 shows the contours of the non-dimensionalized instantaneous TKE k_t/U_b^2 superimposed with the iso-surfaces of the swirling strength λ_{ci} in the cross-stream (y-z) plane located at $x'/H = 2.0$ downstream of the rib. As is clear in figure 5.18, turbulent eddies induced by rib elements are influenced significantly by the secondary flow in the cross-stream directions. From figure 5.18(a), it is seen that in the inclined rib case, the energetic vortical structures around the rib elements recirculate within the closed square cross-section of the duct due to the presence of secondary flow, which further facilitates the distribution of turbulence energy in the cross-stream directions. As is evident in figure 5.18(b), for the V-shaped rib case, turbulent eddies are mostly confined near the ribbed bottom wall and the two vertical sidewalls of the duct, a pattern that is consistent with the spatial distributions of the swirling strength iso-surfaces shown in figure 5.17(b). Clearly, energetic turbulent eddies in the duct center are carried by the cross-stream secondary flow motion towards each vertical sidewall (for the mean secondary flow pattern, see figure 5.7(b)), giving rise to a high local Reynolds stress value (see figure 5.14).

To further understand the effects of rib geometry on the length scale and inclination angle (α) of turbulence structures near the ribbed bottom wall, the 2-D spatial two-point auto-correlation function of streamwise velocity fluctuations can be investigated, which is defined as

$$R_{ij}(x'_{ref}, y_{ref}, x', y) = \frac{\langle u'_i(x', y) u'_j(x'_{ref}, y_{ref})\rangle}{\sqrt{\langle u'^2_i(x', y)\rangle \langle u'^2_j(x'_{ref}, y_{ref})\rangle}} \quad , \tag{5.6}$$

where (x'_{ref}, y_{ref}) are the coordinates of the reference point. The comparison of these two ribbed duct cases is conducted at three reference points with different relative streamwise coordinates (for $x'_{ref}/H = 2.0, 4.5$ and 7.0) and a common vertical coordinate fixed at $y_{ref}/H = -3.8$. This particular vertical position is chosen to sensitize the vortex shedding events over the rib crest and is due to the fact that the shear effect is the largest in this region (see, figure 5.6). As is evident in figure 5.19, for both rib cases, there exists a small angle α between the direction of stretched isopleths and the streamwise direction at all three reference points. This angle α is mainly a reflection of the inclination angle of hairpin packets near the rib crest (Christensen and Adrian, 2001; Adrian, 2007; Volino et al., 2009). Furthermore, it is observed that near the leeward face of the rib (at $x'_{ref}/H = 2.0$), the value of α

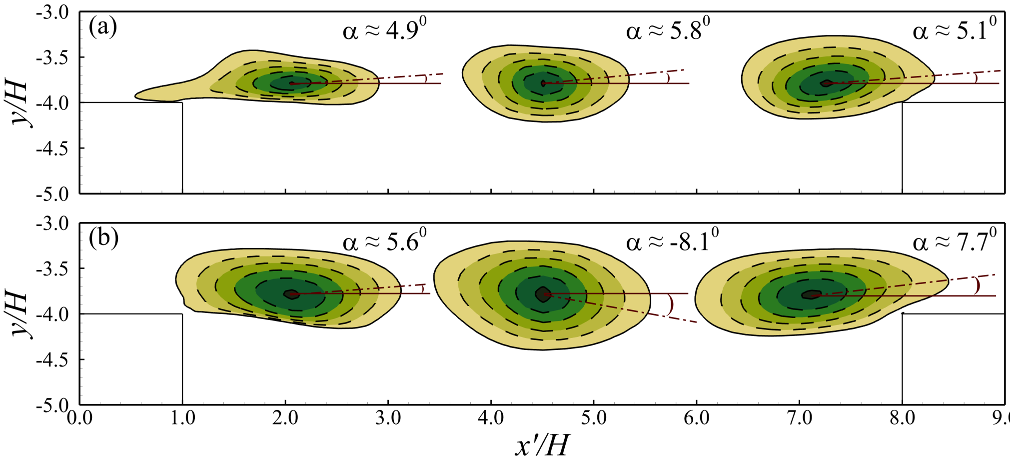

Figure 5.19: Isopleths of two-point auto-correlation R_{uu} with respect to the reference points at $(x'_{ref}/H, y_{ref}/H) = (2.0, -3.8), (4.5, -3.8)$ and $(7.0, -3.8)$ in the central vertical plane located at $z/H = 0.0$. The isopleth value ranges from 0.5 to 1.0, with the outermost and innermost isopleths corresponding to $R_{uu} = 0.5$ and 1.0, respectively. The increment between two adjacent isopleths is 0.1 for the two rib cases. (a) inclined rib case and (b) V-shaped rib case.

is smaller than that near the windward face of the rib (at $x'_{ref}/H = 7.0$) in both ribbed duct cases. By comparing figure 5.19(a) with 5.19(b), it is clear that near the leeward and windward faces of the ribs (at $x'_{ref}/H = 2.0$ and 7.0. respectively), the inclination angle α of the V-shaped rib case is greater than that of the inclined rib case, leading to an increase in the communication between the flow near the ribbed bottom wall and that near the smooth top wall. Furthermore, in comparison with the inclined rib case, the characteristic length of the streamwise correlation (as indicated by the length of the outermost isopleth of R_{uu}) in the V-shaped rib cases is larger than that in the inclined rib case at all the three reference points. This physical feature is inconsistent with the observation of figure 5.2 in the sense that the value of the integral length scale L_{xx} in the inclined rib case is larger than that in the V-shaped rib case. As is evident in figure 5.19(b), with a reference point between two adjacent ribs $(x'_{ref}/H, y_{ref}/H) = (4.5, -3.8)$, the value of the inclination angle in the V-shaped rib case becomes negative (i.e., $\alpha = -8.1°$), indicating a downwash of the

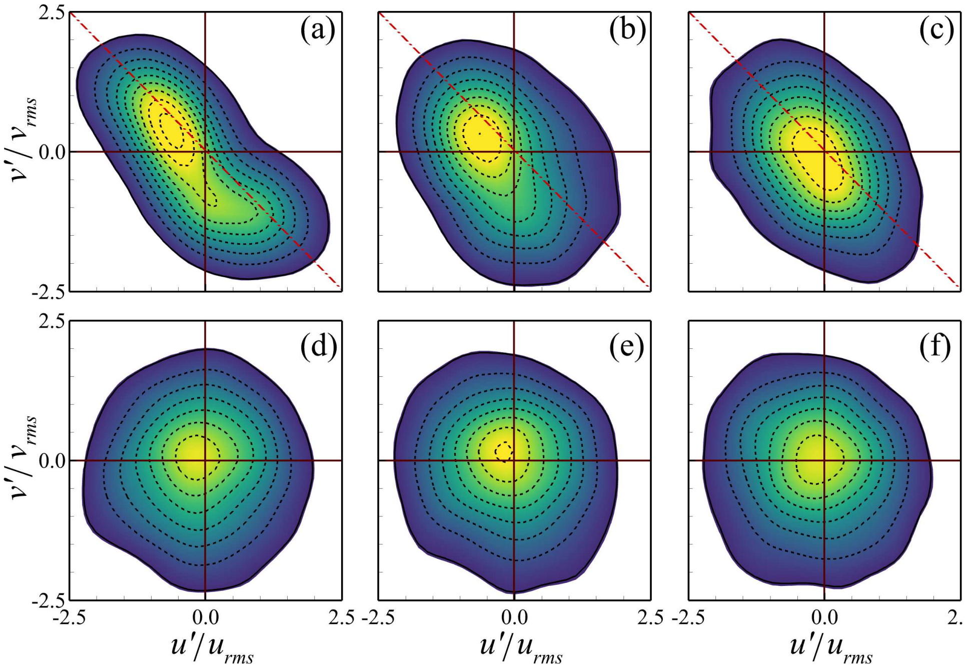

Figure 5.20: Contours of JPDF of u'/u_{rms} and v'/v_{rms} at three different relative streamwise locations ($x'_{ref}/H = 2.0, 4.0$ and 7.0) in the central vertical plane located at $z/H = 0.0$. The comparison of the two ribbed flow cases is conducted at the elevation that is slightly above the rib crest (with the reference points being identical to those used in figures 5.19). Contours vary with incremental JPDF value of 0.0035. Panels (a), (b) and (c) correspond to the inclined rib case, and panels (d), (e) and (f) correspond to the V-shaped rib case. In panels (a) and (d), the relative streamwise coordinate of the reference point is $x'_{ref}/H = 2.0$, in panels (b) and (e), the relative streamwise coordinate of the reference point is $x'_{ref}/H = 4.5$, and in panels (c) and (f), the relative streamwise coordinate of the reference point is $x'_{ref}/H = 7.0$.

mean flow into the inter-rib region (below the rib height) by the secondary flow (see, figures 5.5(b) and 5.6(b)).

Figure 5.20 compares the distributions of the JPDF of u'/u and v'/v downstream of the rib crest (at the same reference points as in figure 5.19) for both rib cases. From figures 5.20(a)-5.20(c), it is clear that in the inclined rib case, the isopleths of JPDF indicate a tendency towards the second and fourth quadrant (Q2 and Q4) events (Adrian, 2007). This phenomenon implies that the ejection (featuring $u' < 0$ and $v' > 0$, associated with Q2) and sweep (featuring $u' > 0$ and $v' < 0$, associated with Q4) motions make the most contribution to the Reynolds shear stress, resulting in a negatively valued $\langle u'v' \rangle$ in the region immediately above the rib height (see, figure 5.13(a)). The preference for the diagonal direction (indicated using a red dashed-dotted line) at the 135^0 angle in the inclined rib case (in figures 5.20(a)-(c)) indicates that there exists a strong correlation between streamwise and vertical velocity fluctuations at all three reference points. By contrast, as shown in figures 5.20(d)-(f), the isopleths of JPDF in the V-shaped rib case show an isotropic distribution, which signifies that there is no apparent correlation between the streamwise and vertical velocity fluctuations in the region around the rib height. This observation also suggests an absence of vortices near the rib crest as they are commonly associated with the occurrence of multiple Q2 and Q4 events (Christensen and Adrian, 2001; Adrian, 2007). This physical feature is consistent with the previous analysis of figure 5.13(b) in the sense that the Reynolds shear stress in the V-shaped rib case is suppressed in the region above the rib crest. This observation is also consistent with the findings of Fang et al. (2015) who conducted a PIV experiment to investigate the effects of the V-shaped ribs on turbulent flow and structures in a square duct.

To refine our study of the effects of rib geometry on the temporal scales of turbulent flow structures, premultiplied energy spectra of streamwise velocity fluctuations (i.e., $fE_{uu}/\langle u'u' \rangle$) are plotted in the figure 5.21 at two different relative streamwise locations for both rib cases. The relative streamwise coordinates of the two reference points are $x'_{ref}/H = 2.0$ and 7.0, while the vertical coordinate of the reference point is fixed at $y_{ref}/H = -3.8$. From figure 5.21, it is seen that in the lee of the rib (at $x'_{ref}/H = 2.0$), the temporal scale of turbulence structures is larger than that in the windward of the rib (at $x'_{ref}/H = 7.0$) in both ribbed duct cases. More specifically, the mode of $fE_{uu}/\langle u'u' \rangle$ (as indicated by the vertical dashed lines "a_1" and "a_2" in figure 5.21) decreases by 15% and 9% as x'/H increases from 2.0 to 7.0 in the inclined and V-shaped ribbed duct cases, respectively. By comparing figures 5.2 and 5.21, it is understood that both spatial and temporal scales of turbulence at $x'_{ref}/H = 2.0$

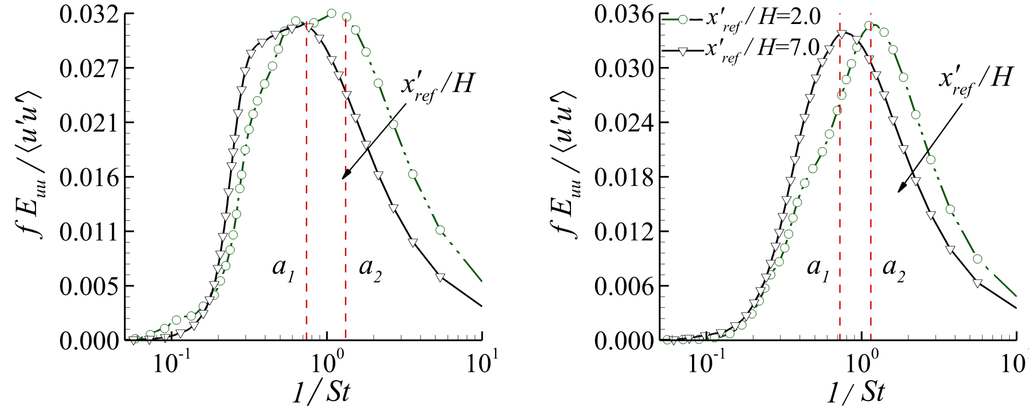

(a) inclined rib case

(b) V-shaped rib case

Figure 5.21: Comparison of the premultiplied temporal energy spectra, $fE_{uu}/\langle u'u' \rangle$, of streamwise velocity fluctuations for the two ribbed cases. The relative streamwise coordinate of the reference points are $x'_{ref}/H = 2.0$ and 7.0, while the vertical coordinate of the reference point is fixed at $y_{ref}/H = -3.8$. The red vertical dashed lines "a_1" and "a_2" demarcate the modes of the premultiplied energy spectra at $x'_{ref}/H = 2.0$ and 7.0, respectively.

are larger than those at $x'_{ref}/H = 7.0$ for both ribbed duct cases. By comparing figure 5.21(a) with 5.21(b), it is apparent that the temporal scale of turbulent eddies in the inclined rib case is slightly larger than that in the V-shaped rib case. For example, at a reference point near the leeward face of a rib (at $x'_{ref}/H = 2.0$), the mode of $fE_{ii}/\langle u'u' \rangle$ corresponds to a non-dimensional temporal scale of $t_c = 1/St \approx 1.37$ in the inclined rib case, whereas $t_c \approx 1.14$ in the V-shaped rib case. Here, $St = f\delta/U_b$ is the Strouhal number.

In view of that turbulence structures in a 3-D ribbed duct undergo significant changes in both patterns and sizes due to the presence of the ribs and appearance of the cross-stream secondary flows, it is worthwhile to investigate the rib geometry effects on the streamwise streaky structures in this peripherally-confined duct space. To this purpose, contours of non-dimensionalized instantaneous streamwise velocity fluctuations u'/U_b are plotted in figure 5.22 in the (x-z) plane located at $y/H = -3.8$ for both rib cases. From figure 5.22(a), it is evident that owing to the inclination

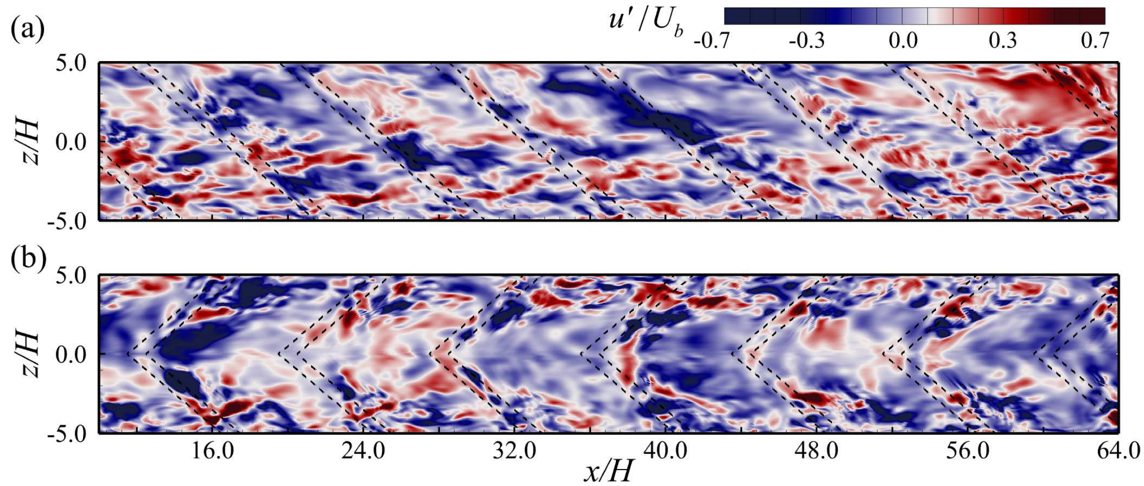

Figure 5.22: Contours of non-dimensionalized instantaneous streamwise velocity fluctuations u'/U_b in the (x-z) plane for two ribbed cases at the elevation that is slightly above the rib crest for $y/H = -3.8$ (the vertical coordinate of the reference point is identical to that used in figure 5.19). (a) inclined rib case, and (b) V-shaped rib case.

angle of the ribs and the circular movement of the secondary flow in the cross-stream directions (see, figures 5.7(a) and 5.18(a)), the streaky structures in regions slightly above the rib crest are advected from one side of the duct (at $z/H = 5.0$) to the other side of the duct (at $z/H = -5.0$). As a result, the streaky structures in the inclined rib case tend to concentrate near the vertical sidewall at $z/H = -5.0$ and no apparent streaky structures are observed at $z/H = 5.0$, a conclusion that is consistent with qualitative results shown previously in figure 5.17(a). By contrast, as shown in figure 5.22(b), the streaky structures in the V-shaped rib case are mainly populated in regions near two vertical sidewalls due to sharp-angled ribs and the presence of symmetrical streamwise-elongated vortices in the cross-stream plane (see, figures 5.7(b) and 5.18(b)). From figure 5.22(b), it is also observed that the magnitude of u'/U_b in the V-shaped rib case is greatly suppressed in the inter-rib region in the duct center (for $-2.5 < z/H < 2.5$), which further leads to a reduction in the magnitudes of Reynolds shear stresses and TKE production rate (see, figures 5.14(b) and 5.15(b)).

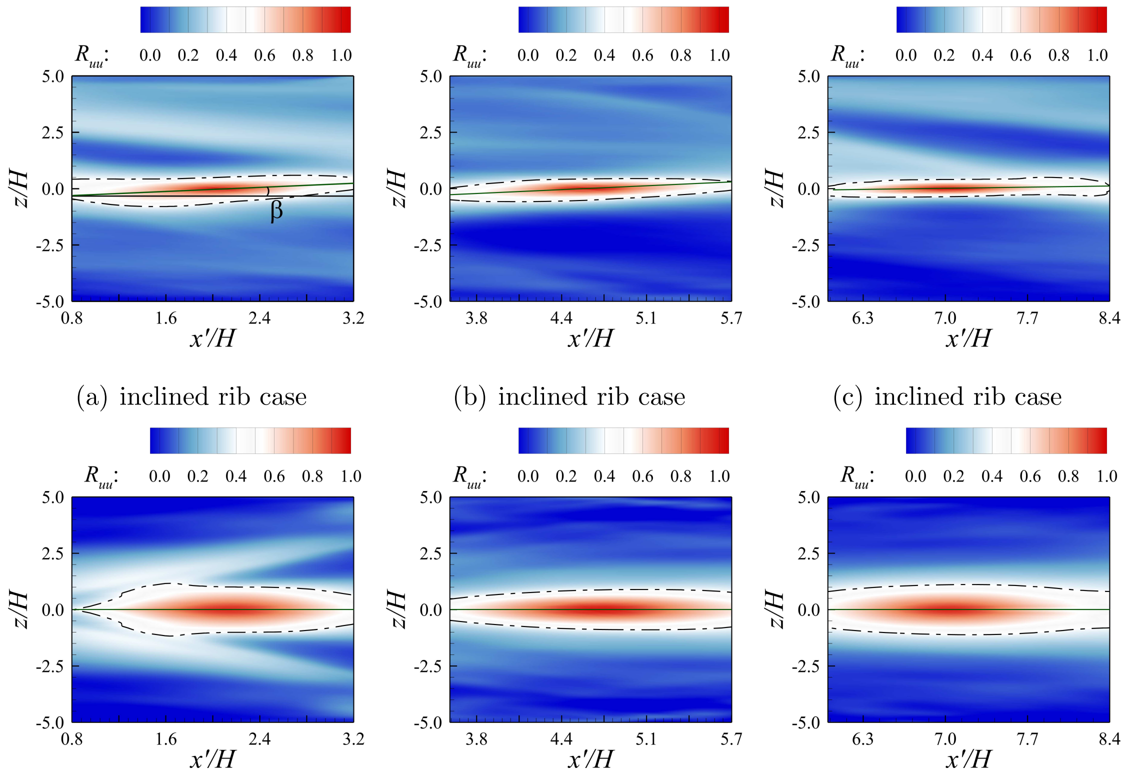

(a) inclined rib case (b) inclined rib case (c) inclined rib case

(d) V-shaped rib case (e) V-shaped rib case (f) V-shaped rib case

Figure 5.23: Contours of the two-point auto-correlation of streamwise velocity fluctuations R_{uu} calculated at three reference points of different streamwise positions and a common elevation of $y_{ref}/H = -3.8$ in the central vertical plane located at $z/H = 0.0$. The superimposed dashed-dotted line corresponds to $R_{uu} = 0.4$. In panels (a) and (d), the relative streamwise coordinate of the reference point is $x'_{ref}/H = 2.0$; in panels (b) and (e), the relative streamwise coordinate of the reference point is $x'_{ref}/H = 4.5$; and in panels (c) and (f), the relative streamwise coordinate of the reference point is $x'_{ref}/H = 7.0$.

Figure 5.23 shows the contours of the 2-D two-point auto-correlation of streamwise velocity fluctuations (R_{uu}) in the (x-z) plane of three different relative streamwise positions ($x'_{ref}/H = 2.0, 4.5$ and 7.0) for the two rib cases. The results are obtained at the same reference points as in figure 5.19. From figure 5.23, it is evident that the characteristic correlation widths and structure angles based on streamwise velocity fluctuations are influenced significantly by the complex geometry of the domain and

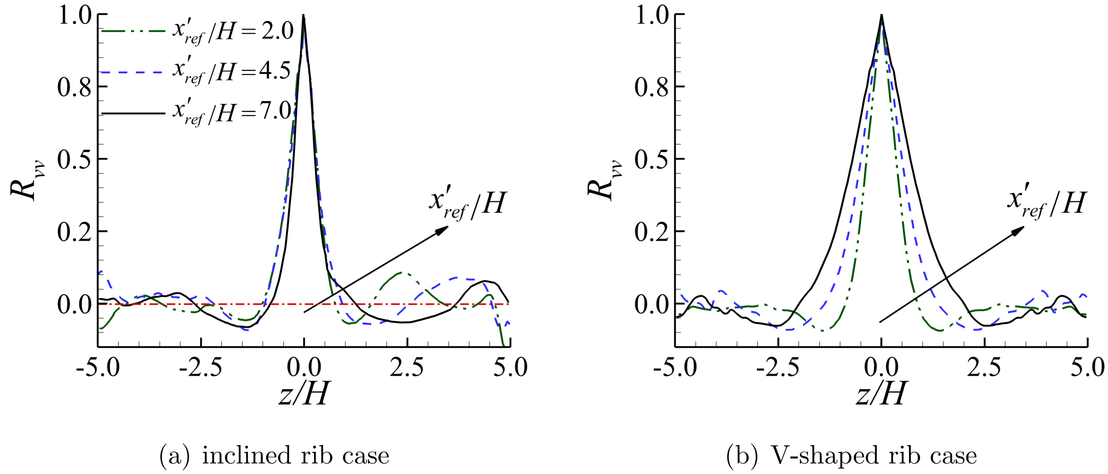

Figure 5.24: Spanwise profiles of the two-point auto-correlation of vertical velocity fluctuations (R_{vv}) at three different relative streamwise locations ($x'_{ref}/H = 2.0, 4.5$ and 7.0) for the two ribbed cases. The vertical coordinate of the reference point is fixed at $y_{ref}/H = -3.8$, as in figure 5.19.

secondary flows. Figures 5.23(a)-5.23(c) clearly indicate that in the inclined rib case, the characteristic inclination angle of the contours R_{uu} decreases from $\beta = 13.7^0$ to 4.5^0 as x'_{ref}/H increases from 2.0 to 7.0, reflecting the fact that turbulence structures are inclined towards not only the streamwise direction (see figure 5.19(a)) but also the spanwise direction. By contrast, as is shown in figures 5.23(d)-5.23(f), the contours pattern of R_{uu} in the V-shaped tib case are well elongated in the streamwise direction without any deflection towards the spanwise direction (such that $\beta \equiv 0.0$) for all three reference points. By comparing figures 5.23(a)-5.23(c) with figures 5.23(d)-5.23(f), it is evident that the spanwise characteristic size of streaks of the V-shaped rib case is larger than that of the inclined rib case.

In order to refine our study of turbulent flow structures, the spanwise 1-D two-point auto-correlation of the vertical velocity fluctuation (R_{vv}) is plotted in figure 5.24 at three different relative streamwise locations (for $x'_{ref}/H = 2.0, 4.5$ and 7.0) for the two rib cases. The vertical coordinate of the reference point is fixed at $y_{ref}/H = -3.8$. From figure 5.24, it is evident that the profile of R_{vv} is asymmetrical in the spanwise direction in the inclined rib case, but symmetrical in the V-shaped rib case at all three relative streamwise locations of $x'/H = 2.0, 4.5$ and 7.0. As shown in figure 5.24(a), the half characteristic spanwise scale (or, "diameter") of the streaky structures (as inferred from the position of the negatively-valued peak of R_{vv}) in the inclined rib case is $|\Delta z/H| = 1.4$ in one half of the duct (from $z/H = -5.0$ to 0.0) at all three streamwise locations. However, in the other half of the duct (from $z/H = 0.0$ to 5.0), the diameter of the streaky structure increases monotonically from $|\Delta z/H| = 1.05$ to 2.5 as x'/H increases from 2.0 to 7.0. As is clear from figure 5.24(b), the profile of R_{vv} in the V-shaped rib case also exhibits a monotonic trend and the diameter of streamwise streaks increases monotonically from $|\Delta z/H| = 1.35$ to 2.6 as the x'/H increases from 2.0 to 7.0. From figure 5.24, it is concluded that both the inclined and V-shaped rib elements have a deep impact not only on the size of turbulence structures (see figures 5.19 and 5.23) but also on the diameter of streamwise vortices in a square duct.

5.5 Chapter summary

Direct numerical simulations are conducted to study the effects of rib geometry on the turbulent flow field confined within a square duct. This research is carried out with the background that although there are many numerical and experimental studies focusing on turbulent flows in either smooth or transverse rib-roughened ducts, much less is documented on turbulent flows in a duct with inclined and V-shaped ribs in the current literature. Furthermore, a DNS study of inclined and V-shaped ribbed duct flows is still lacking. In contrast to the conventional 2-D rough-wall boundary-layer flow with transverse ribs mounted on a flat plate, the turbulent flow in either an inclined or a V-shaped ribbed duct studied here is statistically inhomogeneous in all three directions, influenced by not only the rib elements but also the four duct sidewalls.

Although both inclined and V-shaped rib elements exert strong disturbances to the flow field, their effects are considerably different in terms of the mean streamwise and vertical velocities, mean and turbulent secondary flows, the pressure and viscous drag coefficients, Reynolds stresses, budget balance of TKE, coherent flow structures, as well as the spatial and temporal characteristic scales of turbulence. The Reynolds number based on the bulk mean velocity is fixed at $Re_b = 7000$ for both ribbed duct cases, while the Reynolds number based on the mean streamwise wall friction velocity of the ribbed bottom wall is $Re_{\tau R} = 642$ and 1294 for the inclined and V-shaped rib cases, respectively. In the inclined ribbed duct case, no apparent separation bubbles are present in the near-wall region below the rib height and the highest streamwise momentum level as indicated by the magnitude of $\langle u \rangle / U_b$ appears in regions well above the rib crest (for $y/H > -3.7$). However, in the V-shaped ribbed duct case, a large single separation bubble exists in the inter-rib region below the rib height and the maximum value of $\langle u \rangle / U_b$ occurs near the rib crest. Owing to the confinement of the four sidewalls of the duct, secondary flows appear as large longitudinal vortices in the cross-stream plane in both inclined and V-shaped rib cases. It is observed that secondary flow in the inclined rib case appears as only one large streamwise-elongated vortex in the entire cross-stream plane, however, in the V-shaped rib case, it develops into a pair of large symmetrical counter-rotating vortices. Furthermore, given the same bulk Reynolds number tested, the pressure drag in the V-shaped rib case is approximately twice that in the inclined rib case, resulting in a drastic increase in the value of the friction velocity $u_{\tau R}$ on the ribbed bottom wall.

Investigations into the Reynolds normal and shear stress components indicate that the highest turbulence levels in the inclined rib case appear in the region slightly above the rib crest. This enhancement in the magnitude of the Reynolds stresses immediately downstream of the rib crest is a result of the occurrence of the boundary-layer separation near the leading edge of the rib, which also produces strong spanwise vortex shedding. However, in the V-shaped case, the strongest turbulent levels occur in the inter-rib region (below the rib height) in the lee of the ribs. This is due to the negative values of $\langle v \rangle / U_b$ induced by the secondary flows, which result in a downwash of high momentum flow from the duct center to the ribbed wall. Owing to the difference of the rib geometries and associated secondary flow patterns, the cross-stream distribution of Reynolds stresses in the inclined rib case is significantly different from that in the V-shaped rib case. It is observed that the magnitudes of the three normal components in the inclined rib case are comparable in value near the sidewall located at $z/H = -5.0$, while they are significantly different near the other sidewall located at $z/H = 5.0$. As such, in the inclined rib case, turbulence tends to be locally isotropic and anisotropic near the two vertical sidewalls (located at $z/H = -5.0$ and 5.0), respectively. By contrast, in the V-shaped ribbed duct case, it is seen that near the two vertical sidewalls, the magnitude of $\langle w'w' \rangle$ is larger than those of $\langle u'u' \rangle$ and $\langle v'v' \rangle$.

Through an analysis of the TKE budget terms, it is found that the turbulence energy transfer in the vertical direction is sensitive to the rib geometry, as the TKE budget terms of these two rib cases are not only different in values but also dissimilar in their profile patterns. It is seen that for the inclined rib case, the budget balance of TKE in the inter-rib region (for $-5.0 < y/H < -4.5$) is dominated by viscous diffusion D_k and turbulence diffusion T_k as the source terms; and by convection C_k, production P_k and dissipation ε_k as the sink terms. However, the TKE budget in the V-shaped rib case is primarily balanced between the viscous diffusion and dissipation terms (i.e., D_k and ε_k) as the source and sink terms, respectively, in the region very close to the ribbed bottom wall (for $-5.0 < y/H < -4.7$). To further understand the impact of rib geometry on induced turbulence perturbations by rib elements, the rotational and irrotational components of the TKE production term are investigated. It is discovered that in the region below the inclined rib height (for $y/H < -4.0$), the magnitude of the active term P_{ka} becomes insignificant, while the magnitude of the inactive term P_{ki} reaches its a negatively-valued peak at $y/H = -4.7$, directly resulting in a local minimum in the profile of the production term P_k in the same region. However, in the V-shaped rib case, both the TKE production term P_k and its inactive component P_{ki} are maximized, whereas its active component P_{ka} reaches a minimum (or, a negatively-valued peak) in the region below the rib height.

The effects of rib geometry on the scales and dynamics of coherent structures are investigated through an analysis of the λ_{ci}-criterion, spatial two-point auto-correlations of the turbulence field, JPDF of the streamwise and vertical velocity fluctuations, and premultiplied energy spectra. It is observed that in the inclined rib case the energetic vortical structures are deflected towards only one side of the duct (located at $z/H = -5.0$), where the secondary flow motion pushes the fluid to move upward. However, in the V-shaped rib case, turbulence structures divert from the duct center sideways towards both vertical sidewalls (located at $z/H = \pm 5.0$), and as a result, a significant fraction of the vortical structures are concentrated near the two sidewalls. Based on an analysis of the 2-D spatial two-point auto-correlation function of velocity fluctuations, it is seen that near the leeward and windward faces of a rib (at $x'_{ref}/H = 2.0$ and 7.0. respectively), the inclination angle α of the V-shaped rib case is greater than that of the inclined rib case, leading to an increase in the communication between the flow near the ribbed bottom wall and that near the smooth top wall. Furthermore, based on an analysis of the non-dimensionalized streamwise premultiplied temporal spectrum $fE_{ii}/\langle u'u' \rangle$ of velocity fluctuations, it is observed that the mode of $fE_{uu}/\langle u'u' \rangle$ decreases by 15% and 9% as x'/H increases from 2.0 to 7.0 for the inclined and V-shaped ribbed duct cases, respectively.

The study of spatial two-point auto-correlations in the streamwise-spanwise plane indicates that turbulence structures in the inclined rib case are considerably different from those in the V-shaped rib case in terms of their characteristic width and diameter. Specifically, in the inclined rib case, the characteristic inclination angle of the contours R_{uu} decreases from $\beta = 13.7^0$ to 4.5^0 as the x'_{ref}/H increases from 2.0 to 7.0, reflecting the fact that turbulence structures are inclined towards not only the streamwise direction but also the spanwise direction. By contrast, in the V-shaped rib case, the contours pattern of R_{uu} are well elongated in the streamwise direction without any deflection towards the spanwise direction (such that $\beta \equiv 0.0$) for all three reference points.

Finally, it should be indicated that in this research, we are motivated to conduct a detailed DNS study of inclined and V-shaped ribbed duct flows to fill the gap of literature. As the first step, our focus is on developing a fundamental understanding of the flow physics and coherent structures of these two ribbed square duct flows. Admittedly, this work has limitations, mainly because the DNS was carried out based on fixed values of Reynolds number Re_b, rib alignment angle, blockage ratio (H/D), pitch-to-height ratio (P/H), rib width-to-pitch ratio, and aspect ratio of the duct (L_y/L_z). Indeed, these are all important parameters and need to explored in future studies. Furthermore, owing to the absence of spanwise homogeneity, both inclined and V-shaped ribbed duct flows are intrinsically 3-D, and are computationally more intensive in DNS compared to the conventional 2-D rib-roughened boundary-layer flows over a flat plate. Therefore, as a moderate or long term objective, collective efforts with also possible contributions from other research groups will be needed in order to develop a systematic knowledge of the subject.

Chapter 6

Conclusions and future works

This chapter summarizes the individual contributions of the preceding chapters to illustrate how they cumulatively achieve the overall objectives of the thesis. The overall contributions of the thesis and recommendations for future work are also presented.

6.1 Conclusions

6.1.1 Summary of the influences of rib height on turbulent flow and structures in a square duct

In this research, turbulent flow in a ribbed square duct of different blockage ratios ($Br = 0.05$, 0.1 and 0.2) at a fixed Reynolds number of $Re_b = 5600$ is studied using DNS. The results are compared with those of a smooth duct flow. In contrast to the classical 2-D rib-roughened boundary-layer flow over a flat plate, the turbulence field is influenced by not only the rib elements but also the four duct sidewalls. The dynamics of coherent structures are studied by examining characteristics of the instantaneous velocity field, swirling strength, temporal auto-corrections, spatial two-point auto-correlations, and velocity spectra.

The mean flow patterns of cases of $Br = 0.05$ and 0.1 are typical of k-type rough-wall flows, but that of $Br = 0.2$ exhibits features that are characteristic of a d-type rough-wall flow. Furthermore, under the 3-D flow conditions, organized secondary flows appear in the cross-stream directions whose strength decreases monotonically near the bottom corner of the ducts but increases monotonically near the side and top walls as the blockage ratio increases. The spatial distributions of the local skin friction coefficient C_f and pressure coefficient C_p are influenced significantly by the complex geometry of the domain and the secondary flow pattern in the cross-stream directions. The values of both C_f and C_p maintain approximately constant in the spanwise direction in central region of the duct. In the streamwise direction, however, the highest value of C_f occurs around the leeward and windward faces of the ribs corresponding to the cores of the recirculation bubble and upstream vortex, respectively. The magnitude of C_p is the highest near the windward face of the ribs, and increases as the rib height increases as a result of an enhanced impinging effect of the flow.

Characteristic of a smooth duct flow, the profiles of the Reynolds normal and shear stresses are symmetrical and anti-symmetrical about the duct center ($y/\delta = 0$), respectively. By contrast, the profiles of all Reynolds stress components are asymmetrical in the three rib cases due to the presence of ribs. In general, the magnitudes of the Reynolds normal and shear stresses of the ribbed duct flows are much larger than those of the smooth duct flow due to the disturbances from the ribs. The magnitudes of Reynolds shear stresses and TKE enhance as the rib height increases. For all three rib cases, the highest Reynolds stress levels occur slightly above the rib crest, where the shear effect is the greatest. For the three rib cases tested, the magnitude of $\langle u'u' \rangle$ is much larger than those of $\langle v'v' \rangle$ and $\langle w'w' \rangle$, making the largest contribution to the value of TKE among the three Reynolds normal stress components. Owing to the cross-stream secondary flow motions, the profile of $-\langle u'v' \rangle$ peaks in the region between the sidewall and duct center. In fact, the turbulence level as indicated by the magnitudes of Reynolds normal and shear stresses all increase monotonically as the rib height increases in the central region of the duct.

The maximum value of the TKE production rate over the dissipation rate P_k/ε_k occurs immediately above the rib crest and in the region between the sidewall and duct center, creating a zone of strong non-equilibrium turbulence. In the streamwise-vertical directions, high-intensity vortices are generated at the leading edge of the ribs, which then shed into the central core region of the duct. Concurrently, in the spanwise-vertical directions, secondary flow motions carry these highly energetic vortices from the duct center sideways to the two vertical walls, resulting in an increase in the value of P_k/ε_k. The transport equation of TKE is studied to further understand the rib effects on turbulence energy transfer. The budget balances of the three rib cases exhibit more complex patterns than that of the smooth duct flow, especially around the rib crest. In comparison with the smooth duct flow, the dominant source term is still the production term P_k, which peaks at a position that is slightly above rib crest in all three rib cases. Although the magnitudes of the three sinks (D_k, T_k and ε) around the rib crest are comparable at $Br = 0.05$, the turbulent diffusion term T_k becomes increasingly dominant as the blockage ratio increases to $Br = 0.1$ and 0.2. The convection term C_k does not make a remarkable contribution to the budget balance of TKE in a smooth duct flow. By contrast, the effect of the convection term C_k becomes more pronounced due to the complex mean flow pattern and high TKE level around the rib crest in all three rib cases.

The turbulent flow structures are further studied using the JPDF of the streamwise and vertical velocity fluctuations, λ_{ci}-criterion, temporal auto-corrections, temporal spectra, and spatial two-point auto-correlations of the turbulence field. The results show that an increase of the rib height exerts stronger disturbances to the flow field, which are subsequently deflected to the duct center. This phenomenon leads to the formation of incoherent structures and the generation of violent ejection and sweep motions just above the rib elements, giving rise to an increase of the local TKE production rate. Based on the analysis of the 2-D spatial two-point auto-correlation function of velocity fluctuations, it is discovered that in the region slightly above the rib crest, the inclination angle of the isopleths of R^s_{uu} decreases monotonically from $\alpha = 12.5°$ to $8.0°$ as the blockage ratio increases from $Br = 0.05$ to 0.2. This monotonic trend with respect to Br is also evident from the JPDF analysis, which shows that the turbulent flow becomes increasingly dominated by the sweep events near the rib crest; and as a result, a lower magnitude of the inclination angle is observed around the rib height. However, based on the analysis of R^s_{uu} of different rib cases at the same elevation, it is observed that the inclination angle α increases monotonically as the Br value increases at an elevation well above the ribs, resulting in an enhanced flow interaction between the ribbed bottom wall and the smooth top wall. It is interesting to observe that both temporal and spatial characteristic scales of turbulence increase monotonically as the rib height increases around the rib crest. Furthermore, based on an analysis of the non-dimensionalized streamwise premultiplied temporal spectrum $fE_{ii}/\langle u'u' \rangle$ of velocity fluctuations, it is observed that the range of temporal scales of the most energetic turbulence motions (with the value of $fE_{ii}/\langle u'u' \rangle$ being at least 70% of its peak value) also expands monotonically around the rib height as the rib height increases. In addition, both the spanwise characteristic size of the streaks and the diameter of streamwise vortices increase monotonically as the rib height increases. More specifically, the non-dimensional diameter of streamwise vortices increases from $z/\delta = 0.12$ to 0.44 as the blockage ratio increases from $Br = 0.05$ to 0.2, comparable in value to the height of the rib elements (i.e., $H/\delta = 0.1$ and 0.4 for $Br = 0.05$ and 0.2, respectively).

6.1.2 Summary of the effects of rib height on turbulent heat transfer in a square duct

Turbulent flow structures and heat transfer in a ribbed square duct of different blockage ratios ($Br = 0.05$, 0.1 and 0.2) are investigated using DNS. The influence of sidewalls and rib height on the turbulence structures associated with temperature fluctuations are analyzed based on multiple tools such as vortex swirling strengths, temporal auto-corrections, spatial two-point cross-correlations, JPDF between the temperature and velocity fluctuations, statistical moments of different orders, and temperature spectra.

It is observed that the mean flow patterns in the inter-rib region under the rib height are qualitatively different for different Br values. For the rib cases of $Br = 0.05$ and 0.1, the reattachment point III occurs in between the two adjacent ribs, a feature that is typical of the so-called k-type rough-wall boundary-layer flow. However, for the rib case with $Br = 0.2$, the recirculation vortex II occupies almost the entire cavity between the two ribs (under the rib height), such that the reattachment point is non-present and the mean flow "skim" over the two ribs and the cavity between them. This physical feature is a characteristic of the so-called d-type rough-wall flow. Furthermore, owing to the confinement of the four sidewalls of the duct, strong organized secondary flows appear in the cross-stream directions, which drastically influence the mean temperature field and distribution of Nusselt number near the two sidewalls of the square duct. The magnitude of the total drag coefficient $(C_f + C_p)$ is also observed to be strongly influenced by the rib height, as the level of $(C_f + C_p)$ increases monotonically near the windward face of the rib with an increasing rib height. This phenomenon leads to an enhanced impinging effect of the flow onto the windward face of the rib, which further leads to an amplified magnitude of Nusselt number Nu.

Owing to the strong shear layer generated by the rib crest, the value of TKE k progressively increases with an increase of rib height in the region immediately above the rib crest. However, in contrast to this trend of TKE, the value of temperature variance $\langle \theta'\theta' \rangle$ decreases as the rib height increases in the same region. The magnitudes of streamwise and vertical turbulent heat fluxes (i.e., $\langle u'\theta' \rangle$ and $\langle v'\theta' \rangle$, respectively) enhance as the rib height increases. For all three rib cases, the highest turbulent heat fluxes levels occur slightly above the rib crest, where the levels of both TKE k and temperature variance $\langle\theta'\theta'\rangle$ are the greatest. Owing to the cross-stream secondary flow motions, both the profiles of $\langle u'\theta'\rangle$ and $\langle v'\theta'\rangle$ peak in the region between the sidewall and duct center. Indeed, levels of turbulent heat fluxes as indicated by the magnitudes of $\langle u'\theta'\rangle$ and $\langle v'\theta'\rangle$ all increase monotonically as the rib height increases in the central region of the duct.

The influence of turbulence structures on the temperature field near the rib crest is analyzed using the JPDF of the streamwise velocity and temperature fluctuations, λ_{ci}-criterion, temporal auto-corrections, temporal spectra, and spatial two-point cross-correlations of the turbulence field. The results show that owing to the disturbances from the ribs, energetic vortical structures in all three rib cases are densely populated on the ribbed bottom wall side than on the smooth top wall side. Furthermore, the strengths of both rib-generated disturbances and structures enhance as the rib height increases. This leads to the formation of incoherent structures and the occurrences of violent ejection and sweep events. The ejection and sweep events are coupled positively- and negatively-valued temperature fluctuations θ', respectively, in the region immediately above the rib elements. In fact, based on an analysis of the instantaneous streamwise vorticity fluctuations and JPDF, it is observed that in the region near the rib crest, low momentum fluid ($u' < 0$) packets with high temperature ($\theta' > 0$) are ejected into the duct center region, meanwhile high momentum fluid packets ($u' > 0$) with low temperature ($\theta' < 0$) sweep towards the ribbed bottom wall. When these fluid packets interact with the recirculation zone, both $\langle u'\theta'\rangle$ and $\langle v'\theta'\rangle$ increase significantly in their magnitudes near the rib crest. The existence of hot ejection and cold sweep motions make significant contributions to sustain the level of negatively- and positively-valued of streamwise and vertical turbulent heat fluxes near the rib crest, respectively.

The study of spatial two-point cross-correlations of the streamwise velocity and temperature fluctuations indicates that as the disturbances from the ribs become intensified as the rib height increases, the Reynolds analogy between turbulent transport of momentum and that of thermal energy (indicated by u' and θ') becomes less applicable. Specifically, close to the rib crest, the value of $R^s_{u\theta}$ decreases by 16% as the Br value increases from 0.05 to 0.2. Based on the analysis of the pre-multiplied energy spectra of streamwise velocity and temperature fluctuations (i.e., $fE_{uu}/\langle u'u'\rangle$ $fE_{\theta\theta}/\langle\theta'\theta'\rangle$, respectively), it is discovered that the spectral difference between the non-dimensionalized streamwise velocity and temperature fluctuations increases near the rib crest as the blockage ratio increases. It is also observed that the range of temporal scales of the most energetic turbulent motions associated with the temperature fluctuations (with the value of $fE_{\theta\theta}/\langle\theta'\theta'\rangle$ being at least 70% of its peak value) narrows monotonically around the rib height as the blockage ratio increases.

6.1.3 Summary of the effects of rib geometry on turbulent flow and structures in a square duct

Direct numerical simulations are conducted to study the effects of rib geometry on the turbulent flow field confined within a square duct. This research is carried out with the background that although there are many numerical and experimental studies focusing on turbulent flows in either smooth or transverse rib-roughened ducts, much less is documented on turbulent flows in a duct with inclined and V-shaped ribs in the current literature. Furthermore, a DNS study of inclined and V-shaped ribbed duct flows is still lacking. In contrast to the conventional 2-D rough-wall boundary-layer flow with transverse ribs mounted on a flat plate, the turbulent flow in either an inclined or a V-shaped ribbed duct studied here is statistically inhomogeneous in all three directions, influenced by not only the rib elements but also the four duct sidewalls.

Although both inclined and V-shaped rib elements exert strong disturbances to the flow field, their effects are considerably different in terms of the mean streamwise and vertical velocities, mean and turbulent secondary flows, the pressure and viscous drag coefficients, Reynolds stresses, budget balance of TKE, coherent flow structures, as well as the spatial and temporal characteristic scales of turbulence. The Reynolds number based on the bulk mean velocity is fixed at $Re_b = 7000$ for both ribbed duct cases, while the Reynolds number based on the mean streamwise wall friction velocity of the ribbed bottom wall is $Re_{\tau R} = 642$ and 1294 for the inclined and V-shaped rib cases, respectively. In the inclined ribbed duct case, no apparent separation bubbles are present in the near-wall region below the rib height and the highest streamwise momentum level as indicated by the magnitude of $\langle u \rangle / U_b$ appears in regions well above the rib crest (for $y/H > -3.7$). However, in the V-shaped ribbed duct case, a large single separation bubble exists in the inter-rib region below the rib height and the maximum value of $\langle u \rangle / U_b$ occurs near the rib crest. Owing to the confinement of the four sidewalls of the duct, secondary flows appear as large longitudinal vortices in the cross-stream plane in both inclined and V-shaped rib cases. It is observed that secondary flow in the inclined rib case appears as only one large streamwise-elongated vortex in the entire cross-stream plane, however, in the V-shaped rib case, it develops into a pair of large symmetrical counter-rotating vortices. Furthermore, given the same bulk Reynolds number tested, the pressure drag in the V-shaped rib case is approximately twice that in the inclined rib case, resulting in a drastic increase in the value of the friction velocity $u_{\tau R}$ on the ribbed bottom wall.

Investigations into the Reynolds normal and shear stress components indicate that the highest turbulence levels in the inclined rib case appear in the region slightly above the rib crest. This enhancement in the magnitude of the Reynolds stresses immediately downstream of the rib crest is a result of the occurrence of the boundary-layer separation near the leading edge of the rib, which also produces strong spanwise vortex shedding. However, in the V-shaped case, the strongest turbulent levels occur in the inter-rib region (below the rib height) in the lee of the ribs. This is due to the negative values of $\langle v \rangle / U_b$ induced by the secondary flows, which result in a downwash of high momentum flow from the duct center to the ribbed wall. Owing to the difference of the rib geometries and associated secondary flow patterns, the cross-stream distribution of Reynolds stresses in the inclined rib case is significantly different from that in the V-shaped rib case. It is observed that the magnitudes of the three normal components in the inclined rib case are comparable in value near the sidewall located at $z/H = -5.0$, while they are significantly different near the other sidewall located at $z/H = 5.0$. As such, in the inclined rib case, turbulence tends to be locally isotropic and anisotropic near the two vertical sidewalls (located at $z/H = -5.0$ and 5.0), respectively. By contrast, in the V-shaped ribbed duct case, it is seen that near the two vertical sidewalls, the magnitude of $\langle w'w' \rangle$ is larger than those of $\langle u'u' \rangle$ and $\langle v'v' \rangle$.

Through an analysis of the TKE budget terms, it is found that the turbulence energy transfer in the vertical direction is sensitive to the rib geometry, as the TKE budget terms of these two rib cases are not only different in values but also dissimilar in their profile patterns. It is seen that for the inclined rib case, the budget balance of TKE in the inter-rib region (for $-5.0 < y/H < -4.5$) is dominated by viscous diffusion D_k and turbulence diffusion T_k as the source terms; and by convection C_k, production P_k and dissipation ε_k as the sink terms. However, the TKE budget in the V-shaped rib case is primarily balanced between the viscous diffusion and dissipation terms (i.e., D_k and ε_k) as the source and sink terms, respectively, in the region very close to the ribbed bottom wall (for $-5.0 < y/H < -4.7$). To further understand the impact of rib geometry on induced turbulence perturbations by rib elements, the rotational and irrotational components of the TKE production term are investigated. It is discovered that in the region below the inclined rib height (for $y/H < -4.0$), the magnitude of the active term P_{ka} becomes insignificant, while the magnitude of the inactive term P_{ki} reaches its a negatively-valued peak at $y/H = -4.7$, directly resulting in a local minimum in the profile of the production term P_k in the same region. However, in the V-shaped rib case, both the TKE production term P_k and its inactive component P_{ki} are maximized, whereas its active component P_{ka} reaches a minimum (or, a negatively-valued peak) in the region below the rib height.

The effects of rib geometry on the scales and dynamics of coherent structures are investigated through an analysis of the λ_{ci}-criterion, spatial two-point auto-correlations of the turbulence field, JPDF of the streamwise and vertical velocity fluctuations, and premultiplied energy spectra. It is observed that in the inclined rib case the energetic vortical structures are deflected towards only one side of the duct (located at $z/H = -5.0$), where the secondary flow motion pushes the fluid to move upward. However, in the V-shaped rib case, turbulence structures divert from the duct center sidways towards both vertical sidewalls (located at $z/H = \pm 5.0$), and as a result, a significant fraction of the vortical structures are concentrated near the two sidewalls. Based on an analysis of the 2-D spatial two-point auto-correlation function of velocity fluctuations, it is seen that near the leeward and windward faces of a rib (at $x'_{ref}/H = 2.0$ and 7.0. respectively), the inclination angle α of the V-shaped rib case is greater than that of the inclined rib case, leading to an increase in the communication between the flow near the ribbed bottom wall and that near the smooth top wall. Furthermore, based on an analysis of the non-dimensionalized streamwise premultiplied temporal spectrum $fE_{ii}/\langle u'u' \rangle$ of velocity fluctuations, it is observed that the mode of $fE_{uu}/\langle u'u' \rangle$ decreases by 15% and 9% as x'/H increases from 2.0 to 7.0 for the inclined and V-shaped ribbed duct cases, respectively.

The study of spatial two-point auto-correlations in the streamwise-spanwise plane indicates that turbulence structures in the inclined rib case are considerably different from those in the V-shaped rib case in terms of their characteristic width and diameter. Specifically, in the inclined rib case, the characteristic inclination angle of the contours R_{uu} decreases from $\beta = 13.7^0$ to 4.5^0 as the x'_{ref}/H increases from 2.0 to 7.0, reflecting the fact that turbulence structures are inclined towards not only the streamwise direction but also the spanwise direction. By contrast, in the V-shaped rib case, the contours pattern of R_{uu} are well elongated in the streamwise direction without any deflection towards the spanwise direction (such that $\beta \equiv 0.0$) for all three reference points.

Finally, it should be indicated that in this research, we are motivated to conduct a detailed DNS study of inclined and V-shaped ribbed duct flows to fill the gap of literature. As the first step, our focus is on developing a fundamental understanding of the flow physics and coherent structures of these two ribbed square duct flows. Admittedly, this work has limitations, mainly because the DNS was carried out based on fixed values of Reynolds number Re_b, rib alignment angle, blockage ratio (H/D), pitch-to-height ratio (P/H), rib width-to-pitch ratio, and aspect ratio of the duct (L_y/L_z). Indeed, these are all important parameters and need to explored in future studies. Furthermore, owing to the absence of spanwise homogeneity, both inclined and V-shaped ribbed duct flows are intrinsically 3-D, and are computationally more intensive in DNS compared to the conventional 2-D rib-roughened boundary-layer flows over a flat plate. Therefore, as a moderate or long term objective, collective efforts with also possible contributions from other research groups will be needed in order to develop a systematic knowledge of the subject.

6.2 Future work

To continue this current study, the following research topics are suggested.

(1) Stationary Smooth and Ribbed Straight Square Ducts

Objectives: In this proposed research, there are several subtopics, including (i) DNS and LES studies of non-equilibrium 3-D ribbed duct flows, (ii) an investigation of the effects of high Reynolds number on the dynamics of both cross-stream secondary flow motions and incoherent turbulence structures (as shown in figure 3.22) near the rib-roughened wall, as well as (iii) an investigation of the effects of both sidewalls and rib elements on the mechanism underlying the organized secondary flows and their influences on turbulent heat transfer and coherent structures.

(2) Stationary Ribbed Curved Ducts

Objectives: DNS and LES studies of turbulent flow and heat transfer in curved square ribbed ducts are of direct relevance to the internal cooling of gas turbine blades. The goal of this research is to (i) study the non-equilibrium turbulent flow development, (ii) evaluate the effects of both Reynolds numbers and curvature ratio numbers on the statistical moments of the temperature field, premultiplied energy spectra of the turbulent temperature field (as depicted in figure 4.19), and turbulence structures that facilitate the turbulent transport of thermal energy, as well as (iii) provide detailed benchmark data of turbulent flow in curved square ducts with transverse ribs mounted on one wall.

(3) Rotating Ribbed Straight and Curved Ducts

Objectives: This study aims at conducing an LES study to test a wide range of rotation numbers based on a variety of SGS models. The characteristics of the flow field under system rotation will be compared against those of non-rotating flows. Furthermore, the combined effects of the Coriolis force and curvature ratio number on the mean secondary flow structures, and on large- and small-scale turbulence structures will be examined in both physical and spectral spaces.

Appendix A

Discretization of the momentum equation

In this appendix, finite volume discretization of the momentum equation and the momentum interpolation method on curvilinear collocated grids are presented.

A.1 Details of discretization in space and time

Following the method of analysis in chapter 2, the nonlinear convection term can be straightforwardly discretized as

$$
\begin{aligned}
&\int_w^e \int_s^n \int_b^t \frac{1}{J} \frac{\partial}{\partial \xi_k} \left(\rho \beta_j^k u_i u_j\right) d\xi_1 d\xi_2 d\xi_3 \\
&= \int_s^n \int_b^t \left(\rho \beta_j^1 u_i u_j\right) d\xi_2 d\xi_3 \Big|_w^e \\
&+ \int_w^e \int_b^t \left(\rho \beta_j^2 u_i u_j\right) d\xi_1 d\xi_3 \Big|_s^n \\
&+ \int_w^e \int_s^n \left(\rho \beta_j^3 u_i u_j\right) d\xi_1 d\xi_2 \Big|_b^t \\
&= \frac{1}{J} \left(\rho \beta_j^1 u_i u_j|_w^e + \rho \beta_j^2 u_i u_j|_s^n + \rho \beta_j^3 u_i u_j|_b^t\right) \\
&= \frac{1}{J} \left(m_e u_i|_e - m_w u_i|_w + m_n u_i|_n - m_s u_i|_s + m_t u_i|_t - m_b u_i|_b\right) \quad .
\end{aligned}
\tag{A.1}
$$

The pressure gradient term in equation 2.2 can be discretized as

$$\begin{aligned}\int_w^e\int_s^n\int_b^t \frac{\partial p}{\partial x_i}dx_1dx_2dx_3 =& \int_w^e\int_s^n\int_b^t \frac{1}{J}\frac{\partial(\beta_i^j p)}{\partial \xi_j}d\xi_1 d\xi_2 d\xi_3 \\ =&\frac{1}{J}\left(\beta_i^1 p|_w^e + \beta_i^2 p|_s^n + \beta_i^3 p|_b^t\right) \quad ,\end{aligned} \tag{A.2}$$

The viscous term in equation 2.2 can be discretized as

$$\begin{aligned}&\int\int\int_{\mathscr{V}} \nu\frac{1}{J}\frac{\partial}{\partial \xi_p}\left(\frac{1}{J}\beta_j^p\beta_j^q\frac{\partial u_i}{\partial \xi_q}\right)d\xi_1 d\xi_2 d\xi_3 = \\ &\nu\frac{1}{J}\left[\frac{1}{J}\beta_j^1\beta_j^q\frac{\partial u_i}{\partial \xi_q}\bigg|_w^e + \frac{1}{J}\beta_j^2\beta_j^q\frac{\partial u_i}{\partial \xi_q}\bigg|_s^n + \frac{1}{J}\beta_j^3\beta_j^q\frac{\partial u_i}{\partial \xi_q}\bigg|_b^t\right] = \\ &\nu\frac{1}{J}\left[\frac{1}{J}\beta_j^1\beta_j^1\frac{\partial u_i}{\partial \xi_1}\bigg|_w^e + \frac{1}{J}\beta_j^2\beta_j^2\frac{\partial u_i}{\partial \xi_2}\bigg|_s^n + \frac{1}{J}\beta_j^3\beta_j^3\frac{\partial u_i}{\partial \xi_3}\bigg|_b^t\right] + \\ &\nu\frac{1}{J}\left[\frac{1}{J}\beta_j^1\beta_j^2\frac{\partial u_i}{\partial \xi_2}\bigg|_w^e + \frac{1}{J}\beta_j^2\beta_j^1\frac{\partial u_i}{\partial \xi_1}\bigg|_s^n + \frac{1}{J}\beta_j^3\beta_j^1\frac{\partial u_i}{\partial \xi_1}\bigg|_b^t\right] + \\ &\nu\frac{1}{J}\left[\frac{1}{J}\beta_j^1\beta_j^3\frac{\partial u_i}{\partial \xi_3}\bigg|_w^e + \frac{1}{J}\beta_j^2\beta_j^3\frac{\partial u_i}{\partial \xi_3}\bigg|_s^n + \frac{1}{J}\beta_j^3\beta_j^2\frac{\partial u_i}{\partial \xi_2}\bigg|_b^t\right] \quad .\end{aligned} \tag{A.3}$$

It should be indicated that the cross-derivative diffusion flux in the last two brackets are zero in orthogonal grid (for chapters 3 and 4).

Eventually, the integral equation for momentum conservation on a curvilinear grid system can be expressed as:

$$\begin{aligned}&J\rho\frac{\partial u_i}{\partial t} + m_e u_i|_e - m_w u_i|_w + m_n u_i|_n - m_s u_i|_s + m_t u_i|_t - m_b u_i|_b \\ &= -\beta_i^1 p_e + \beta_i^1 p_w - \beta_i^2 p_n + \beta_i^2 p_s - \beta_i^3 p_t + \beta_i^3 p_b \\ &+\mu\left(\frac{1}{J}\beta_j^1\beta_j^1\frac{\partial u_i}{\partial \xi_1}\bigg|_w^e + \frac{1}{J}\beta_j^2\beta_j^2\frac{\partial u_i}{\partial \xi_2}\bigg|_s^n + \frac{1}{J}\beta_j^3\beta_j^3\frac{\partial u_i}{\partial \xi_3}\bigg|_b^t\right) \\ &+\mu\left(\frac{1}{J}\beta_j^1\beta_j^2\frac{\partial u_i}{\partial \xi_2}\bigg|_w^e + \frac{1}{J}\beta_j^2\beta_j^1\frac{\partial u_i}{\partial \xi_1}\bigg|_s^n + \frac{1}{J}\beta_j^3\beta_j^1\frac{\partial u_i}{\partial \xi_1}\bigg|_b^t\right) \\ &+\mu\left(\frac{1}{J}\beta_j^1\beta_j^3\frac{\partial u_i}{\partial \xi_3}\bigg|_w^e + \frac{1}{J}\beta_j^2\beta_j^3\frac{\partial u_i}{\partial \xi_3}\bigg|_s^n + \frac{1}{J}\beta_j^3\beta_j^2\frac{\partial u_i}{\partial \xi_2}\bigg|_b^t\right) \\ &+J\rho f_i \quad ,\end{aligned} \tag{A.4}$$

where $f_i = -\Pi\delta_{1i}$ denotes a constant streamwise pressure gradient that drives the flow and $J\rho\partial\bar{u}_i/\partial t$ represents the temporal derivative of momentum in the x_i direction within a control volume.

In this computer code, a fully explicit second-order Runge-Kutta method is used for the temporal discretization. The temporal discretized for equation A.4 can be written in the form:

$$\begin{aligned}
&J\rho\frac{u_i^* - u_i}{\Delta t} + m_e u_i|_e - m_w u_i|_w + m_n u_i|_n - m_s u_i|_s + m_t u_i|_t - m_b u_i|_b \\
&= -\beta_i^1 p|_w^e - \beta_i^2 p|_s^n - \beta_i^3 p|_b^t \\
&+ \mu\left(\frac{1}{J}\beta_j^1\beta_j^1\frac{\partial u_i}{\partial \xi_1}\bigg|_w^e + \frac{1}{J}\beta_j^2\beta_j^2\frac{\partial u_i}{\partial \xi_2}\bigg|_s^n + \frac{1}{J}\beta_j^3\beta_j^3\frac{\partial u_i}{\partial \xi_3}\bigg|_b^t\right) \\
&+ \mu\left(\frac{1}{J}\beta_j^1\beta_j^2\frac{\partial u_i}{\partial \xi_2}\bigg|_w^e + \frac{1}{J}\beta_j^2\beta_j^1\frac{\partial u_i}{\partial \xi_1}\bigg|_s^n + \frac{1}{J}\beta_j^3\beta_j^1\frac{\partial u_i}{\partial \xi_1}\bigg|_b^t\right) \\
&+ \mu\left(\frac{1}{J}\beta_j^1\beta_j^3\frac{\partial u_i}{\partial \xi_3}\bigg|_w^e + \frac{1}{J}\beta_j^2\beta_j^3\frac{\partial u_i}{\partial \xi_3}\bigg|_s^n + \frac{1}{J}\beta_j^3\beta_j^2\frac{\partial u_i}{\partial \xi_2}\bigg|_b^t\right) \\
&+ J\rho f_i \quad .
\end{aligned} \tag{A.5}$$

Here, u_i^* denotes an updated preliminary velocity fields. Equation A.5 can be expressed in a more compact manner as follows

$$u_i^* = H_i - \frac{\Delta t}{J\rho}\left(\beta_i^1 p|_w^e + \beta_i^2 p|_s^n + \beta_i^3 p|_b^t\right) \quad , \tag{A.6}$$

where H_i denotes all the explicit terms except for the pressure terms in equation A.5.

A.2 Momentum interpolation

In this thesis, in order to prevent the checkerboard effect in the pressure field, the momentum interpolation method of Rhie and Chow (1983) is used to establish the relation between the cell-face mass flux and the pressure in two adjacent control volumes. Specifically, each term of equation A.6 is interpolated and shifted by half a control volume to relate the pressure stored at centroids of adjacent control volumes, so that the check-board pressure solution is avoided.

The velocity components based on a general curvilinear coordinate system can be obtained from

$$
\begin{aligned}
u_{1P}^{n} &= \frac{1}{2}\Delta t H_1^*(u) + u_{1p}^{0} - \frac{\frac{1}{2}\Delta t}{J\rho}\beta_1^1 p|_w^e \quad , \\
u_{2P}^{n} &= \frac{1}{2}\Delta t H_2^*(u) + u_{2p}^{0} - \frac{\frac{1}{2}\Delta t}{J\rho}\beta_2^2 p|_n^s - \frac{\frac{1}{2}\Delta t}{J\rho}\beta_2^1 p|_w^e \quad , \\
u_{1P}^{n} &= \frac{1}{2}\Delta t H_3^*(u) + u_{3p}^{0} - \frac{\frac{1}{2}\Delta t}{J\rho}\beta_3^3 p|_t^b \quad .
\end{aligned}
\tag{A.7}
$$

It should be noted that for the transverse rib-roughened duct cases (chapters 3 and 4), the components of β_2^1 in the equation A.7 shall be deemed to equal zero. Indeed, the transverse rib case can be treated as a special case of either inclined or V-shaped rib cases.

The velocity components on the interface between adjacent control volumes can be calculated by interpolation of the momentum conservation equations:

$$
\begin{aligned}
u_{1e}^{n} &= \left(\frac{1}{2}\Delta t H_1^*(u) + u_{1P}^{0}\right)_e - \frac{\frac{1}{2}\Delta t}{J\rho}\beta_1^1 p|_P^E \quad , \\
u_{1w}^{n} &= \left(\frac{1}{2}\Delta t H_1^*(u) + u_{1P}^{0}\right)_w - \frac{\frac{1}{2}\Delta t}{J\rho}\beta_1^1 p|_W^P \quad , \\
u_{2e}^{n} &= \left(\frac{1}{2}\Delta t H_2^*(u) + u_{2P}^{0} - \frac{\frac{1}{2}\Delta t}{J\rho}\beta_2^2 p|_s^n\right)_e - \frac{\frac{1}{2}\Delta t}{J\rho}\beta_2^1 p|_P^E \quad , \\
u_{2w}^{n} &= \left(\frac{1}{2}\Delta t H_2^*(u) + u_{2P}^{0} - \frac{\frac{1}{2}\Delta t}{J\rho}\beta_2^2 p|_s^n\right)_w - \frac{\frac{1}{2}\Delta t}{J\rho}\beta_2^1 p|_W^P \quad , \\
u_{2n}^{n} &= \left(\frac{1}{2}\Delta t H_2^*(u) + u_{2P}^{0} - \frac{\frac{1}{2}\Delta t}{J\rho}\beta_2^1 p|_w^e\right)_n - \frac{\frac{1}{2}\Delta t}{J\rho}\beta_2^2 p|_P^N \quad , \\
u_{2s}^{n} &= \left(\frac{1}{2}\Delta t H_2^*(u) + u_{2P}^{0} - \frac{\frac{1}{2}\Delta t}{J\rho}\beta_2^1 p|_w^e\right)_s - \frac{\frac{1}{2}\Delta t}{J\rho}\beta_2^2 p|_S^P \quad , \\
u_{3t}^{n} &= \left(\frac{1}{2}\Delta t H_3^*(u) + u_{3P}^{0}\right)_t - \frac{\frac{1}{2}\Delta t}{J\rho}\beta_3^3 p|_P^T \quad , \\
u_{3b}^{n} &= \left(\frac{1}{2}\Delta t H_3^*(u) + u_{3P}^{0}\right)_b - \frac{\frac{1}{2}\Delta t}{J\rho}\beta_3^3 p|_B^P \quad .
\end{aligned}
\tag{A.8}
$$

In general, the velocity components, which are based on the estimated pressure field, do not satisfy the continuity equation. As such, an artificial net mass source is produced. To remove this artificial mass source, the mass fluxes on the east and west faces are corrected through

$$\begin{aligned} m_e &= \rho\beta_1^1 H_1|_e + \rho\beta_2^1 H_2|_e - \frac{\Delta t}{J}\left(\beta_1^1\beta_1^1 p|_P^E + \beta_2^1\beta_2^1 p|_P^E + \beta_2^1\beta_2^2 p|_{se}^{ne}\right) \quad , \\ m_w &= \rho\beta_1^1 H_1|_w + \rho\beta_2^1 H_2|_w - \frac{\Delta t}{J}\left(\beta_1^1\beta_1^1 p|_W^P + \beta_2^1\beta_2^1 p|_W^P + \beta_2^1\beta_2^2 p|_{sw}^{nw}\right) \quad . \end{aligned} \tag{A.9}$$

Except for the east and west faces, mass fluxes on other faces only involve the pressure at two adjacent control volumes, which are expressed as

$$\begin{aligned} m_n &= \rho\beta_2^2 H_2|_n - \frac{\Delta t}{J}\left(\beta_2^2\beta_2^2 p|_P^N\right) \quad , \\ m_s &= \rho\beta_2^2 H_2|_s - \frac{\Delta t}{J}\left(\beta_2^2\beta_2^2 p|_S^P\right) \quad , \\ m_t &= \rho\beta_3^3 H_3|_t - \frac{\Delta t}{J}\left(\beta_3^3\beta_3^3 p|_P^T\right) \quad , \\ m_b &= \rho\beta_3^3 H_3|_b - \frac{\Delta t}{J}\left(\beta_3^3\beta_3^3 p|_B^P\right) \quad . \end{aligned} \tag{A.10}$$

From equations A.9 and A.10, it is understood that the coefficient matrix of the pressure correction equation in transverse and V-shaped rib cases possess 7 and 11 nonzero diagonal bands, repectively. The pressure equation can now be solved using a variety of matrix equation solvers. In this thesis, the parallel algebraic multigrid solver BoomerAMG (Henson and Yang., 2002) provided by the Portable, Extensible Toolkit for Scientific Computation (PETSc) library (Balay et al., 2014) is used to solve this irregular matrix for the pressure correction.

Appendix B

Derivation of the Reynolds stress transport equation in a ribbed square duct

The velocity field can be decomposed into its mean and fluctuating components as $u_i = \langle u \rangle + u'$. By applying this decomposition to the transport equation of momentum, the transport equation of the Reynolds stresses can be obtained. The continuity and Naiver-Stokes equations equations that govern the turbulent flow fields for DNS can be written in the following general form in the context of an incompressible fluid:

$$\left\langle \frac{\partial u_i}{\partial x_i} \right\rangle = \left\langle \frac{\partial(\langle u_i \rangle + u_i')}{\partial x_i} \right\rangle = \left\langle \frac{\partial \langle u_i \rangle}{\partial x_i} \right\rangle + \left\langle \frac{\partial u_i'}{\partial x_i} \right\rangle = \frac{\partial \langle u_i \rangle}{\partial x_i} = 0.0 \quad , \tag{B.1}$$

$$N(u_i) = \frac{\partial u_i}{\partial t} + u_k \frac{\partial u_i}{\partial x_k} + \frac{1}{\rho} \frac{\partial p}{\partial x_i} - \nu \left(\frac{\partial^2 u_i}{\partial x_k \partial x_k} \right) = 0.0 \quad , \tag{B.2}$$

where $N(u_i)$ is referred to as a Navier-Stokes operator. Note that the average of a fluctuation quantity is zero identically. As a result, $u_j' N(u_i)$ can be determined as follows:

$$u'_j N(u_i) = u'_j \frac{\partial u_i}{\partial t} + u'_j u_k \frac{\partial u_i}{\partial x_k} + u'_j \frac{1}{\rho}\frac{\partial p}{\partial x_i} - u'_j \nu \frac{\partial^2 u_i}{\partial x_k \partial x_k}$$
$$= u'_j \frac{\partial(\langle u_i\rangle + u'_i)}{\partial t} + u'_j(\langle u_k\rangle + u'_k)\frac{\partial(\langle u_i\rangle + u'_i)}{\partial x_k} + u'_j \frac{1}{\rho}\frac{\partial(\langle p\rangle + p'_i)}{\partial x_i} - u'_j \nu \left[\frac{\partial^2(\langle u_i\rangle + u'_i)}{\partial x_k \partial x_k}\right]$$
$$= u'_j \frac{\partial\langle u_i\rangle}{\partial t} + u'_j \frac{\partial u'_i}{\partial t} + u'_j \langle u_k\rangle \frac{\partial\langle u_i\rangle}{\partial x_k} + u'_j \langle u_k\rangle \frac{\partial u'_i}{\partial x_k} + u'_j u'_k \frac{\partial\langle u_i\rangle}{\partial x_k} + u'_j u'_k \frac{\partial u'_i}{\partial x_k} + u'_j \frac{1}{\rho}\frac{\partial\langle p\rangle}{\partial x_i}$$
$$+ u'_j \frac{1}{\rho}\frac{\partial p'}{\partial x_i} - u'_j \nu \frac{\partial^2\langle u_i\rangle}{\partial x_k \partial x_k} - u'_j \nu \frac{\partial^2 u'_i}{\partial x_k \partial x_k} \quad . \tag{B.3}$$

Similart to $u'_j N(u_i)$, multiplication of the Naiver-Stokes equation equation with the fluctuating velocity $u'_i N(u_j)$ leads to

$$u'_i N(u_j) = u'_i \frac{\partial\langle u_j\rangle}{\partial t} + u'_i \frac{\partial u'_j}{\partial t} + u'_i \langle u_k\rangle \frac{\partial\langle u_j\rangle}{\partial x_k} + u'_i \langle u_k\rangle \frac{\partial u'_j}{\partial x_k} + u'_i u'_k \frac{\partial\langle u_j\rangle}{\partial x_k} + u'_i u'_k \frac{\partial u'_j}{\partial x_k}$$
$$+ u'_i \frac{1}{\rho}\frac{\partial\langle p\rangle}{\partial x_j} + u'_i \frac{1}{\rho}\frac{\partial p'}{\partial x_j} - u'_i \nu \frac{\partial^2\langle u_j\rangle}{\partial x_k \partial x_k} - u'_i \nu \frac{\partial^2 u'_j}{\partial x_k \partial x_k} \quad . \tag{B.4}$$

Then take an summation average of equations B.3 and B.4. As the summation of these two equations will be lengthy, and in the following, the derivations are done term by term. Starting from the unsteady term, we have

$$\left\langle u'_j \frac{\partial u_i}{\partial t} + u'_i \frac{\partial u_j}{\partial t}\right\rangle = \left\langle u'_j \frac{\partial\langle u_i\rangle}{\partial t} + u'_j \frac{\partial u'_i}{\partial t} + u'_i \frac{\partial\langle u_j\rangle}{\partial t} + u'_i \frac{\partial u'_j}{\partial t}\right\rangle$$
$$= \left\langle u'_j \frac{\partial\langle u_i\rangle}{\partial t}\right\rangle + \left\langle u'_j \frac{\partial u'_i}{\partial t}\right\rangle + \left\langle u'_i \frac{\partial\langle u_j\rangle}{\partial t}\right\rangle + \left\langle u'_i \frac{\partial u'_j}{\partial t}\right\rangle = \frac{\partial\langle u'_i u'_j\rangle}{\partial t} \quad . \tag{B.5}$$

Followed by the summation of convective terms, we obtain

$$\left\langle u'_j u_k \frac{\partial u_i}{\partial x_k} + u'_i u_k \frac{\partial u_j}{\partial x_k}\right\rangle = \left\langle u'_j \langle u_k\rangle \frac{\partial\langle u_i\rangle}{\partial x_k} + u'_j \langle u_k\rangle \frac{\partial u'_i}{\partial x_k} + u'_j u'_k \frac{\partial\langle u_i\rangle}{\partial x_k} + u'_j u'_k \frac{\partial u'_i}{\partial x_k}\right\rangle$$
$$+ \left\langle u'_i \langle u_k\rangle \frac{\partial\langle u_j\rangle}{\partial x_k} + u'_i \langle u_k\rangle \frac{\partial u'_j}{\partial x_k} + u'_i u'_k \frac{\partial\langle u_j\rangle}{\partial x_k} + u'_i u'_k \frac{\partial u'_j}{\partial x_k}\right\rangle$$
$$= \langle u_k\rangle \frac{\partial u'_i u'_j}{\partial x_k} + \langle u'_j u'_k\rangle \frac{\partial\langle u_i\rangle}{\partial x_k} + \langle u'_i u'_k\rangle \frac{\partial\langle u_j\rangle}{\partial x_k} + \frac{\partial u'_i u'_j u'_k}{\partial x_k} \quad . \tag{B.6}$$

The summation of the pressure strain terms result in

$$\begin{aligned}
\left\langle u_j' \frac{1}{\rho}\frac{\partial p}{\partial x_i} + u_i'\frac{1}{\rho}\frac{\partial p}{\partial x_j}\right\rangle =& \frac{1}{\rho}\left(\left\langle u_j'\frac{1}{\rho}\frac{\partial \langle p\rangle}{\partial x_i} + u_j'\frac{1}{\rho}\frac{\partial p'}{\partial x_i} + u_i'\frac{1}{\rho}\frac{\partial \langle p\rangle}{\partial x_j} + u_i'\frac{1}{\rho}\frac{\partial p'}{\partial x_j}\right\rangle\right)\\
=& \frac{1}{\rho}\left\langle \frac{\partial p'u_j'}{\partial x_i} - p'\frac{\partial u_j'}{\partial x_i} + \frac{\partial p'u_i'}{\partial x_j} - p'\frac{\partial u_i'}{\partial x_j}\right\rangle \\
=& \frac{1}{\rho}\frac{\partial}{\partial x_k}(\langle p'u_j'\rangle\delta_{ik} + \langle p'u_i'\rangle\delta_{jk}) - \frac{2}{\rho}\langle p's_{ij}'\rangle \quad .
\end{aligned} \tag{B.7}$$

Finally, the summation of the viscous terms leads to

$$\begin{aligned}
&-\left\langle u_j'\nu\frac{\partial^2 u_i}{\partial x_k\partial x_k} + u_i'\nu\frac{\partial^2 u_j}{\partial x_k\partial x_k}\right\rangle\\
=&-\left(\left\langle u_j'\nu\frac{\partial^2\langle u_i\rangle}{\partial x_k\partial x_k}\right\rangle + \left\langle u_j'\nu\frac{\partial^2 u_i'}{\partial x_k\partial x_k}\right\rangle + \left\langle u_i'\nu\frac{\partial^2\langle u_j\rangle}{\partial x_k\partial x_k}\right\rangle + \left\langle u_i'\nu\frac{\partial^2 u_j'}{\partial x_k\partial x_k}\right\rangle\right)\\
=&-\left(\left\langle\frac{\partial}{\partial x_k}\left(u_j'\nu\frac{\partial u_i'}{\partial x_k}\right)\right\rangle - \left\langle\nu\frac{\partial u_j'}{\partial x_k}\frac{\partial u_i'}{\partial x_k}\right\rangle + \left\langle\frac{\partial}{\partial x_k}\left(u_i'\nu\frac{\partial u_j'}{\partial x_k}\right)\right\rangle - \left\langle\nu\frac{\partial u_i'}{\partial x_k}\frac{\partial u_j'}{\partial x_k}\right\rangle\right)\\
=&-\nu\frac{\partial^2\langle u_i'u_j'\rangle}{\partial x_k\partial x_k} + 2\nu\left\langle\nu\frac{\partial u_i'}{\partial x_k}\frac{\partial u_j'}{\partial x_k}\right\rangle \quad .
\end{aligned} \tag{B.8}$$

From equations B.5 - B.8, we obtain

$$\begin{aligned}
\langle u_j'N(u_i) + u_i'N(u_j)\rangle =& \frac{\partial\langle u_i'u_j'\rangle}{\partial t} + \langle u_k\rangle\frac{\partial u_i'u_j'}{\partial x_k} + \langle u_j'u_k'\rangle\frac{\partial\langle u_i\rangle}{\partial x_k} + \langle u_i'u_k'\rangle\frac{\partial\langle u_j\rangle}{\partial x_k}\\
&+\frac{\partial u_i'u_j'u_k'}{\partial x_k} + \frac{1}{\rho}\frac{\partial}{\partial x_k}(\langle p'u_j'\rangle\delta_{ik} + \langle p'u_i'\rangle\delta_{jk}) - \frac{2}{\rho}\langle p's_{ij}'\rangle\\
&-\nu\frac{\partial^2\langle u_i'u_j'\rangle}{\partial x_k\partial x_k} + 2\nu\left\langle\nu\frac{\partial u_i'}{\partial x_k}\frac{\partial u_j'}{\partial x_k}\right\rangle = 0.0 \quad .
\end{aligned} \tag{B.9}$$

Rearranging the terms and taking an average of the obtained equation results in the following Reynolds stress transportation equation

$$\begin{aligned}
&\underbrace{\langle u_k\rangle\frac{\partial u_i'u_j'}{\partial x_k}}_{C_{ij}} - \underbrace{\left(-\langle u_j'u_k'\rangle\frac{\partial\langle u_i\rangle}{\partial x_k} - \langle u_i'u_k'\rangle\frac{\partial\langle u_j\rangle}{\partial x_k}\right)}_{P_{ij}} - \underbrace{\left(\frac{2}{\rho}\langle p's_{ij}'\rangle\right)}_{\Pi_{ij}} + \underbrace{\left(2\nu\left\langle\nu\frac{\partial u_i'}{\partial x_k}\frac{\partial u_j'}{\partial x_k}\right\rangle\right)}_{\epsilon_{ij}}\\
&\quad - \underbrace{\frac{\partial}{\partial x_k}\left[-\langle u_i'u_j'u_k'\rangle\frac{1}{\rho}(\langle p'u_j'\rangle\delta_{ik} + \langle p'u_i'\rangle\delta_{jk}) + \nu\frac{\partial\langle u_i'u_j'\rangle}{\partial x_k}\right]}_{D_{ij}} = 0.0 \quad .
\end{aligned} \tag{B.10}$$

Here, $C_{ij}, P_{ij}, \Pi_{ij}, \epsilon_{ij}$ and D_{ij} represent the convection, production, pressure-strain, viscous dissipation, diffusion (consisting of turbulent, pressure and viscous diffusion effects).

Bibliography

Adrian, R. J. (2007). Hairpin vortex organization in wall turbulence. *Phys. Fluids*, 19:041301.

Adrian, R. J., Meinhart, C. D., and Tomkins, C. D. (2000). Vortex organization in the outer region of the turbulent boundary layer. *J. Fluid Mech.*, 422:1–54.

Andreopoulos, J. and Bradshaw, P. (1981). Measurements of turbulence structure in the boundary layer on a rough surface. *J. Boundary-Layer Meteorol.*, 20:201–213.

Balay, S., Buschelman, K., Eijkhout, V., Gropp, W. D., Kaushik, D., Knepley, M. G., McInnes, L. C., Smith, B. F., and Zhang, H. (2014). PETSc users manual anl-95/11-revision 2.1. 5. *Argonne National Lab.*

Bandyopadhyay, P. R. (1987). Rough-wall turbulent boundary layers in the transition regime. *J. Fluid Mech.*, 180:231–266.

Bhaganagar, K. (2008). Direct numerical simulation of unsteady flow in channel with rough walls. *Phys. Fluids*, 20:101508.

Bhaganagar, K. and Chau, L. (2015). Characterizing turbulent flow over 3-D idealized and irregular rough surfaces at low Reynolds number. *Appl. Math. Modell.*, 39:6751–6766.

Bhaganagar, K., Kim, J., and Coleman, G. (2004). Effect of roughness on wall-bounded turbulence. *Flow, Turb. Combust.*, 72:463–492.

Bonhoff, B., Parneix, S., Leusch, J., Johnson, B. V., Schabacker, J., and Bölcs, A. (1999). Experimental and numerical study of developed flow and heat transfer in coolant channels with 45 degree ribs. *Int. J. Heat Fluid Flow*, 20:311–319.

Borello, D., Salvagni, A., and Hanjalić, K. (2015). Effects of rotation on flow in an asymmetric rib-roughened duct: LES study. *Int. J. Heat Fluid Flow*, 55:104–119.

Bradshaw, P. (1967). 'inactive' motion and pressure fluctuations in turbulent boundary layers. *J. Fluid Mech.*, 30:241–258.

Brundrett, E. and Baines, W. D. (1964). The production and diffusion of vorticity in duct flow. *J. Fluid Mech.*, 19:375–394.

Burattini, P., Leonardi, S., Orlandi, P., and Antonia, R. A. (2008). Comparison between experiments and direct numerical simulations in a channel flow with roughness on one wall. *J. Fluid Mech.*, 600:403–426.

Casarsa, L. and Arts, T. (2005). Experimental investigation of the aerothermal performance of a high blockage rib-roughened cooling channel. *J. Turbomach.*, 127:580–588.

Chan, L., MacDonald, M., Chung, D., Hutchins, N., and Ooi, A. (2015). A systematic investigation of roughness height and wavelength in turbulent pipe flow in the transitionally rough regime. *J. Fluid Mech.*, 771:743–777.

Chernyshenko, S. I. and Baig, M. F. (2005). The mechanism of streak formation in near-wall turbulence. *J. Fluid Mech.*, 544:99–131.

Choi, H., Moin, P., and Kim, J. (1993). Direct numerical simulation of turbulent flow over riblets. *J. Fluid Mech.*, 255:503–539.

Christensen, K. T. and Adrian, R. J. (2001). Statistical evidence of hairpin vortex packets in wall turbulence. *J. Fluid Mech.*, 431:433–443.

Coceal, O., Dobre, A., Thomas, T. G., and Belcher, S. E. (2007). Structure of turbulent flow over regular arrays of cubical roughness. *J. Fluid Mech.*, 589:375–409.

Coletti, F., Cresci, I., and Arts, T. (2013). Spatio-temporal analysis of the turbulent flow in a ribbed channel. *Int. J. Heat Fluid Flow*, 44:181–196.

Coletti, F., Lo Jacono, D., Cresci, I., and Arts, T. (2014). Turbulent flow in rib-roughened channel under the effect of Coriolis and rotational buoyancy forces. *Phys. Fluids*, 26:045111.

Coletti, F., Maurer, T., Arts, T., and Di Sante, A. (2012). Flow field investigation in rotating rib-roughened channel by means of particle image velocimetry. *Exp. Fluids*, 52:1043–1061.

Fang, X., Yang, Z., Wang, B. C., Tachie, M. F., and Bergstrom, D. J. (2015). Highly-disturbed turbulent flow in a square channel with V-shaped ribs on one wall. *Int. J. Heat Fluid Flow*, 56:182–197.

Fang, X., Yang, Z., Wang, B.-C., Tachie, M. F., and Bergstrom, D. J. (2017). Large-eddy simulation of turbulent flow and structures in a square duct roughened with perpendicular and V-shaped ribs. *Phys. Fluids*, 29:065110.

Fujita, H., Yokosawa, H., and Hirota, M. (1989). Secondary flow of the second kind in rectangular ducts with one rough wall. *Exp. Therm. Fluid Sci.*, 2:72–80.

Fukagata, K. and Kasagi, N. (2002). Highly energy-conservative finite difference method for the cylindrical coordinate system. *J. Comput. Phys.*, 181:181:478.

Gao, X. and Sundén, B. (2004a). Effects of inclination angle of ribs on the flow behavior in rectangular ducts. *J. Fluids Eng.*, 126:692–699.

Gao, X. and Sundén, B. (2004b). PIV measurement of the flow field in rectangular ducts with 60 parallel, crossed and V-shaped ribs. *Exp. Therm. Fluid Sci.*, 28:639–653.

Gavrilakis, S. (1992). Numerical simulation of low-Reynolds-number turbulent flow through a straight square duct. *J. Fluid Mech.*, 244:101–129.

Griffith, B. E. and Patankar, N. A. (2020). Immersed methods for fluid–structure interaction. *Ann. Rev. Fluid Mech.*, 52:421.

Han, J. C., Dutta, S., and Ekkad, S. (2012). *Gas Turbine Heat Transfer and Cooling Technology*. CRC press.

Hattori, H. and Nagano, Y. (2012). Structures and mechanism of heat transfer phenomena in turbulent boundary layer with separation and reattachment via DNS. *Int. J. Heat Fluid Flow*, 37:81–92.

Henson, V. E. and Yang., U. M. (2002). Boomeramg: A parallel algebraic multigrid solver and preconditioner. *Appl. Numer. Math.*, 41:155–177.

Hetsroni, G., Mosyak, A., Rozenblit, R., and Yarin, L. P. (1999). Thermal patterns on the smooth and rough walls in turbulent flows. *Int. J. Heat Mass Transfer*, 42:3815–3829.

Hinze, J. (1972). *Turbulence*. McGraw-Hill.

Hirota, M., Fujita, H., Yokosawa, H., Nakai, H., and Itoh, H. (1997). Turbulent heat transfer in a square duct. *Int. J. Heat Fluid Flow*, 18:170–180.

Hirota, M., Yokosawa, H., and Fujita, H. (1992). Turbulence kinetic energy in turbulent flows through square ducts with rib-roughened walls. *Int. J. Heat Fluid Flow*, 13:22–29.

Hurther, D., Lemmin, U., and Terray, E. A. (2007). Turbulent transport in the outer region of rough-wall open-channel flows: the contribution of large coherent shear stress structures (LC3S). *J. Fluid Mech.*, 574:465–493.

Huser, A. and Biringen, S. (1993). Direct numerical simulation of turbulent flow in a square duct. *J. Fluid Mech.*, 257:65–95.

Ikeda, T. and Durbin, P. A. (2007). Direct simulations of a rough-wall channel flow. *J. Fluid Mech.*, 571:235–263.

Ismail, U., Zaki, T. A., and Durbin, P. A. (2018). Simulations of rib-roughened rough-to-smooth turbulent channel flows. *J. Fluid Mech.*, 843:419–449.

Jackson, P. S. (1981). On the displacement height in the logarithmic velocity profile. *J. Fluid Mech.*, 111:15–25.

Keirsbulck, L., Labraga, L., Mazouz, A., and Tournier, C. (2002). Surface roughness effects on turbulent boundary layer structures. *J. Fluids Eng.*, 124:127–135.

Kim, J. and Moin, P. (1989). Transport of passive scalars in a turbulent channel flow. In *Turbulent Shear Flows 6*, pages 85–96. Springer.

Kim, J., Moin, P., and Moser, R. (1987). Turbulence statistics in fully developed channel flow at low Reynolds number. *J. Fluid Mech.*, 177:133–166.

Krogstad, P.-Å., Andersson, H. I., Bakken, O. M., and Ashrafian, A. (2005). An experimental and numerical study of channel flow with rough walls. *J. Fluid Mech.*, 530:327–352.

Krogstad, P.-Å. and Antonia, R. A. (1994). Structure of turbulent boundary layers on smooth and rough walls. *J. Fluid Mech.*, 277:1–21.

Krogstad, P.-Å. and Antonia, R. A. (1999). Surface roughness effects in turbulent boundary layers. *Exp. Fluids*, 27:450–460.

Labbé, O. (2013). Large-eddy-simulation of flow and heat transfer in a ribbed duct. *Comput. Fluids*, 76:23–32.

Lamballais, E., Lesieur, M., and Métais, O. (1997). Probability distribution functions and coherent structures in a turbulent channel. *Phys. Rev. E*, 56:6761–6766.

Lee, J. H., Sung, H. J., and Krogstad, P.-Å. (2011). Direct numerical simulation of the turbulent boundary layer over a cube-roughened wall. *J. Fluid Mech.*, 669:397–431.

Leonardi, S. and Castro, I. P. (2010). Channel flow over large cube roughness: a direct numerical simulation study. *J. Fluid Mech.*, 651:519–539.

Leonardi, S., Orlandi, P., Djenidi, L., and Antonia, R. A. (2004). Structure of turbulent channel flow with square bars on one wall. *Int. J. Heat Fluid Flow*, 25:384–392.

Leonardi, S., Orlandi, P., Djenidi, L., and Antonia, R. A. (2015). Heat transfer in a turbulent channel flow with square bars or circular rods on one wall. *J. Fluid Mech.*, 776:512–530.

Leonardi, S., Orlandi, P., Smalley, R. J., Djenidi, L., and Antonia, R. A. (2003). Direct numerical simulations of turbulent channel flow with transverse square bars on one wall. *J. Fluid Mech.*, 491:229–238.

Li, Q. X., P, M., and D., Y.-H. (2018). Turbulence modulation and heat transfer enhancement in channels roughened by cube-covered surface. *Comput. Fluids*, 165:33–42.

Liou, T. M., Wu, Y. Y., and Chang, Y. (1993). LDV measurements of periodic fully developed main and secondary flows in a channel with rib-disturbed walls. *J. Fluids Eng.*, 115:109–114.

Liu, Y. Z., Ke, F., and Sung, H. J. (2008). Unsteady separated and reattaching turbulent flow over a two-dimensional square rib. *J. Fluids Struct.*, 24:366–381.

Lohász, M. M., Rambaud, P., and Benocci, C. (2006). Flow features in a fully developed ribbed duct flow as a result of MILES. *Flow, Turb. Combust.*, 77:59–76.

MacDonald, M., Chan, L., Chung, D., Hutchins, N., and Ooi, A. (2016). Turbulent flow over transitionally rough surfaces with varying roughness densities. *J. Fluid Mech.*, 763:130–161.

MacDonald, M., Hutchins, N., and Chung, D. (2019a). Roughness effects in turbulent forced convection. *J. Fluid Mech.*, 861:138–162.

MacDonald, M., Hutchins, N., Lohse, D., and Chung, D. (2019b). Heat transfer in rough-wall turbulent thermal convection in the ultimate regime. *Phys. Rev. Fluids*, 4:071501.

Macfarlane, I., Joubert, P. N., and Nickels, T. B. (1998). Secondary flows and developing, turbulent boundary layers in a rotating duct. *J. Fluid Mech.*, 373:1–32.

Mahmoodi-Jezeh, S. V. and Wang, B.-C. (2020). Direct numerical simulation of turbulent flow through a ribbed square duct. *J. Fluid Mech.*, 900.

Mazouz, A., Labraga, L., and Tournier, C. (1998). Anisotropy invariants of Reynolds stress tensor in a duct flow and turbulent boundary layer. *J. Fluids Eng.*, 120:280–284.

Mittal, R. and Iaccarino, G. (2005). Immersed boundary methods. *Ann. Rev. Fluid Mech.*, 37:239–261.

Miyake, Y., Tsujimoto, K., and Nakaji, M. (2001). Direct numerical simulation of rough-wall heat transfer in a turbulent channel flow. *Int. J. Heat Fluid Flow*, 22:237–244.

Mompean, G., Gavrilakis, S., Machiels, L., and Deville, M. O. (1996). On predicting the turbulence-induced secondary flows using nonlinear k-ε models. *Phys. Fluids*, 8:1856–1868.

Moser, R. D. and Moin, P. (1987). The effects of curvature in wall-bounded turbulent flows. *J. Fluid Mech.*, 175:479–510.

Nagano, Y., Hattori, H., and Houra, T. (2004). DNS of velocity and thermal fields in turbulent channel flow with transverse-rib roughness. *Int. J. Heat Fluid Flow*, 25:393–403.

Noorani, A., Vinuesa, R., Brandt, L., and Schlatter, P. (2016). Aspect ratio effect on particle transport in turbulent duct flows. *Phys. Fluids*, 28:115103.

Orlandi, P., Lenoardi, S., and Antonia, R. A. (2006). Turbulent channel flow with either transverse or longitudinal roughness elements on one wall. *J. Fluid Mech.*, 561:279–305.

Perry, A. E., Schofield, W. H., and Joubert, P. N. (1969). Rough wall turbulent boundary layers. *J. Fluid Mech.*, 37:383–413.

Peskin, C. S. (1972). Flow patterns around heart valves: a numerical method. *J. Comput. Phys.*, 10:252–271.

Philips, D. A., Rossi, R., and Iaccarino, G. (2013). Large-eddy simulation of passive scalar dispersion in an urban-like canopy. *J. Fluid Mech.*, 723:404–428.

Pinelli, A., Naqavi, I. Z., Piomelli, U., and Favier, J. (2010a). Immersed-boundary methods for general finite-difference and finite-volume navier–stokes solvers. *J. Comput. Phys.*, 229:9073–9091.

Pinelli, A., Uhlmann, M., Sekimoto, A., and Kawahara, G. (2010b). Reynolds number dependence of mean flow structure in square duct turbulence. *J. Fluid Mech.*, 644:107–122.

Pirozzoli, S., Bernardini, M., and Orlandi, P. (2016). Passive scalars in turbulent channel flow at high Reynolds number. *J. Fluid Mech.*, 788:614–639.

Pirozzoli, S., Modesti, D., Orlandi, P., and Grasso, F. (2018). Turbulence and secondary motions in square duct flow. *J. Fluid Mech.*, 840:631–655.

Pope, S. B. (2000). *Turbulent Flows.* Cambridge Univ., Cambridge, UK.

Rhie, C. M. and Chow, W. L. (1983). Numerical study of the turbulent flow past an airfoil with trailing edge separation. *AIAA J.*, 21:1525–1532.

Rouhi, A., Chung, D., and Hutchins, N. (2019). Direct numerical simulation of open-channel flow over smooth-to-rough and rough-to-smooth step changes. *J. Fluid Mech.*, 866:450–486.

Ruck, S. and Arbeiter, F. (2018). Detached eddy simulation of turbulent flow and heat transfer in cooling channels roughened by variously shaped ribs on one wall. *Int. J. Heat Mass Transfer*, 118:388–401.

Scotti, A. (2006). Direct numerical simulation of turbulent channel flows with boundary roughened with virtual sandpaper. *Phys. Fluids*, 18:031701.

Sewall, E. A., Tafti, D. K., Graham, A. B., and Thole, K. A. (2006). Experimental validation of large eddy simulations of flow and heat transfer in a stationary ribbed duct. *Int. J. Heat Fluid Flow*, 27:243–258.

Shafi, H. S. and Antonia, R. A. (1997). Small-scale characteristics of a turbulent boundary layer over a rough wall. *J. Fluid Mech.*, 342:263–293.

Speziale, C. G. and Gatski, T. B. (1997). Analysis and modelling of anisotropies in the dissipation rate of turbulence. *J. Fluid Mech.*, 344:155–180.

Thom, A. S. (1971). Momentum absorption by vegetation. *Q. J. R. Met. Soc.*, 97:414–428.

Townsend, A. A. (1961). Equilibrium layers and wall turbulence. *J. Fluid Mech.*, 11:97–120.

Townsend, A. A. R. (1980). *The Structure of Turbulent Shear Flow*. Cambridge Univ., Cambridge, UK.

Vasilyev, O. (2000). High order finite difference schemes on non-uniform meshes with good conservation properties. *J. Comput. Phys.*, 157:746–761.

Vinuesa, R., Noorani, A., Lozano-Durán, A., Khoury, G. K. E., Schlatter, P., Fischer, P. F., and Nagib, H. M. (2014). Aspect ratio effects in turbulent duct flows studied through direct numerical simulation. *J. Turbul.*, 15:677–706.

Volino, R. J., Schultz, M. P., and Flack, K. A. (2009). Turbulence structure in a boundary layer with two-dimensional roughness. *J. Fluid Mech.*, 635:75–101.

Wagner, S. and Shishkina, O. (2015). Heat flux enhancement by regular surface roughness in turbulent thermal convection. *J. Fluid Mech.*, 763:109–135.

Wang, L., Hejcik, J., and Sunden, B. (2007). PIV measurement of separated flow in a square channel with streamwise periodic ribs on one wall. *J. Fluids Eng.*, 129:834–841.

Wang, L., Salewski, M., and Sundén, B. (2010). Turbulent flow in a ribbed channel: Flow structures in the vicinity of a rib. *Exp. Therm. Fluid Sci.*, 34:165–176.

Xun, Q.-Q. and Wang, B.-C. (2016). Hybrid RANS/LES of turbulent flow in a rotating rib-roughened channel. *Phys. Fluids*, 28:075101.

Yaglom, A. M. and Kader, B. A. (1974). Heat and mass transfer between a rough wall and turbulent fluid flow at high Reynolds and peclet numbers. *J. Fluid Mech.*, 62:601–623.

Yang, D. and Shen, L. (2010). Direct-simulation-based study of turbulent flow over various waving boundaries. *J. Fluid Mech.*, 650:131–180.

Yokosawa, H., Fujita, H., Hirota, M., and Iwata, S. (1989). Measurement of turbulent flow in a square duct with roughened walls on two opposite sides. *Int. J. Heat Fluid Flow*, 10:125–130.

Yuan, J. and Piomelli, U. (2014). Roughness effects on the reynolds stress budgets in near-wall turbulence. *J. Fluid Mech.*, 760:1–11.

Zhou, J., Adrian, R. J., Balachandar, S., and Kendall, T. M. (1999). Mechanisms for generating coherent packets of hairpin vortices in channel flow. *J. Fluid Mech.*, 387:353–396.